3-23-2018

Evaluation of High Velocity Wear

Armando DeLeon

INVESTIGATION OF SEVERAL METHODS OF EVALUATING WEAR IN A HIGH-SPEED ENVIRONMENT

DISSERTATION

Armando DeLeon, Lt Col, USAF

AFIT-ENY-DS-18-M-249

DEPARTMENT OF THE AIR FORCE
AIR UNIVERSITY

AIR FORCE INSTITUTE OF TECHNOLOGY

Wright-Patterson Air Force Base, Ohio

The views expressed in this dissertation are those of the author and do not reflect the official policy or position of the United States Air Force, the Department of Defense, or the United States Government.

AFIT-ENY-DS-18-M-249

INVESTIGATION OF SEVERAL METHODS OF EVALUATING WEAR IN A HIGH-SPEED ENVIRONMENT

DISSERTATION

Presented to the Faculty

Graduate School of Engineering and Management

Air Force Institute of Technology

Air University

Air Education and Training Command

in Partial Fulfillment of the Requirements for the

Degree of Doctor of Philosophy in Aeronautical Engineering

Armando DeLeon, B.S.A.E., M.S.A.E.

Lt Col, USAF

March 2018

AFIT-ENY-DS-18-M-249

INVESTIGATION OF SEVERAL METHODS OF EVALUATING WEAR IN A HIGH-SPEED ENVIRONMENT

DISSERTATION

Armando DeLeon, B.S.A.E., M.S.A.E.
Lt Col, USAF

Approved:

Anthony N. Palazotto, Ph.D. (Chairman)	Date
William P. Baker, Ph.D. (Member)	Date
Robert A. Brockman, Ph.D. (Member)	Date

Accepted:

Adedeji B. Badiru, Ph.D. Dean, Graduate School of Engineering and Management	Date

Abstract

The Holloman High Speed Test Track (HHSTT) located at Holloman Air Force Base conducts hypersonic testing in a unique way. Rather than perform cost prohibitive flight testing or hypersonic wind tunnel testing, a rocket-powered sled propels test articles down a track. This test setup has been used to test at speeds up to 2885 m/s (~Mach 8.6).

The sled is kept on the rails by utilizing slippers, fabricated to wrap around the rail[1]. This slipper design keeps the sled from separating from the rail during a test due to the airflow producing lift, in a designed effort to minimize the wear that occurs during the test run. Different sleds and rails are used at the HHSTT and thus different geometries exist [2].

The slipper material is carefully chosen in an attempt to minimize rail wear as well as to include a safety margin so that the slipper can maintain the designed load carrying capability despite material loss due to wear. Through the years, different materials were used as test velocities increased and a better understanding of the wear environment occurred.

This research investigated the wear phenomenon using three different methods, incorporating finite element mechanical modeling as well as heat transfer thermal modeling. One of the methods incorporated a three-dimensional Finite Element Model (FEM) consisting of a portion of the slipper colliding with micron sized asperities to simulate slipper-rail contact and included assumptions pertaining to that scale. The second method was a one-dimensional heat transfer model that simulated the entire time that a test run occurs. The third method was another three-dimensional FEM. As opposed to the previous FEM described, it used friction as the mechanism by which the slipper and rail interacted. These last two models were at a larger scale and their results, along with the asperity collision results, were compared to experimental data acquired from a worn slipper from an actual test at the HHSTT in 2008.

Acknowledgments

Acknowledgments I will like to express my appreciation to my research advisor, Distinguished Professor Dr. Anthony N. Palazotto, whose tireless efforts and infinite patience guided my efforts. His continued encouragement, invaluable advice, and ongoing support for this long term research project kept me on track throughout my time at AFIT. He spent many many hours explaining the finer points of underlying principles of this research. I am grateful for his mentoring and sincerely value his guidance.

I would like to extend my gratitude to Dr. William P. Baker who spent considerable time and energy with the underpinnings of this research. Without which this research would still be ongoing. Also, Dr. Robert A. Brockman for his valuable input and constructive feedback throughout my research.

To August, my wife, without her patience and support I would not have been able to undertake much less complete this work; may our continued life together offer countless opportunities to express my gratitude. My daughter and son, Autumn and Anthony who inspire me to improve in countless ways every day.

During my investigations, Maj. Oliver Easterday provided support and encouragement may he rest in peace. Lt. Col. Chad Hale provided important insight that afforded clarity on available data. Maj.(ret) Rodolfo Buentello Hernandez provided details on model use that was instrumental to this research. And many thanks to Major Geof Cox. His friendship and academic support means a great deal to me.

Finally, I extend my gratitude to the Air Force Office of Scientific Research for funding this investigation.

Armando DeLeon

Table of Contents

Page

Page

Page

List of Figures

List of Acronyms

Acronym	Definition
ALE3D	Arbitrary-Lagrange-Eulerian
AFIT	Air Force Institute of Technology
ASTM	American Society for Testing and Materials
CFD	Computational Fluid Dynamics
CTH	Three-dimensional shock hydrodynamics code
DADS	Dynamic Analysis and Design System
EOS	Equation of State
FEA	Finite Element Analysis
FEM	Finite Element Model
GPa	GigaPascal
HHSTT	Holloman High Speed Test Track
MPa	MegaPascal
PDE	Partial Differential Equation
HEL	Hugoniot Elastic Limit
SEM	Scanning Electron Microscope

Nomenclature

$\#Asp$	# of asperities per unit area
$\%Asp_{na}$	% of asperities of size n
α	partition function
α_0	initial value at time zero, assumed to be 50 %
α_m	value at time of melt, assumed to be 10%
$\Delta\varepsilon_p$	increment of equivalent plastic strain
δ	constant, based on contact %
δ_n	nodal encroachment distance
$\dot{\bar{\mathrm{v}}}$	vector, nodal temperature gradient
$\dot{\bar{\varepsilon}}_0$	reference strain rate
$\dot{\bar{\varepsilon}}_p$	equivalent plastic strain rate
$\dot{\bar{u}}_p$	rate of plastic displacement
η	nominal compressive strain
η_{hf}	user-specified inelastic heat fraction
Γ	Gruneisen ratio
Γ_0	material property
κ	thermal diffusivity

λ	ratio of specific heats
μ	coefficient of friction
μm	micrometer (10^{-6} meter)
μs	microsecond (10^{-6}) seconds
ν	kinematic viscosity
ω	scaled temperature
ω_{JC}	Johnson-Cook damage parameter
$\overline{\sigma}_y$	static yield stress
$\overline{\mathrm{v}}$	vector, nodal temperatures
$\overline{\varepsilon}_f$	strain at failure
$\overline{\varepsilon}_p$	equivalent plastic strain
$\overline{u}_p^f$	user specified effective plastic displacement
ρ	density
ρ_0	density in front of shock wave
ρ_1	density behind shock wave
ρ_r	reference density
σ	stress
σ_f	stress at failure
σ_y	yield stress

σ_{VM} Mises stress

τ_y yield stress in shear

$\theta_x, \theta_y, \theta_z$ rotations in x,y,z directions respectfully

ε strain

ξ scaled distance

c_0 reference speed of sound in the material

d_1 - d_5 Johnson-Cook fracture constants

D_{sl_I} sliding distance per velocity interval

dt increment of time

dx, dy, dz differential distance in x,y,z direction respectfully

e_H Hugoniot specific energy

E_{gen} Energy generated within control volume

E_{in} Energy entering control volume

E_{out} Energy leaving control volume

E_{st} Energy stored within control volume

k^{TC} thermal conductivity

l_{c_I} slipper length per velocity increment

m_s mass

Nu Nusselt number

q'' heat flux

$Q_x + Q_y + Q_z$ energy entering control volume through x,y,z direction respectfully

$Q_{x+dx}, Q_{y+dy}, Q_{z+dz}$ energy exiting control volume through x,y,z direction respectfully

r^{pl} heat flux per unit volume

s_H linear Hugoniot slope coefficient

t_0 initial time

u_x, u_y, u_z displacement in x,y,z directions respectfully

Vol_I Volumetric wear per unit area at velocity interval, I

$Vol_{I,na}$ simulated wear (volumetric) due to an asperity of size n at velocity increment I

w_c slipper width

w_d wear depth, 3D FEM

W_I normalized wear rate per velocity interval

%Cont percentage of time slipper-rail in contact

A Area

a defines a ratio of thermal conductivity, specific heat, density, and diffusivity length

A_c Slipper area in contact with Rail

A_H Helmholtz free energy

A_y initial yield stress

B hardening modulus

C strain rate dependent coefficient

C_d scaled conductive heat flux

C_p specific heat

C_v scaled convective heat flux

D_s sliding distance

E Young's modulus

e internal energy of the system

e_0 specific internal energy in front of shock wave

e_1 specific internal energy behind shock wave

F force

F_k frictional force

G change in thermal conductivity due to temperature changes

h convective heat transfer coefficient

k spring stiffness

k_1,k_2,k_3,k_4, slope approximations, Runga-Kutta method

k_f thermal conductivity of the fluid

L characteristic length, dependent on element type and size

l gap between slipper and rail

l_h latent heat

l_∞ freestream tube

m contact/no contact switch (1 or 0)

M_∞ Mach (freestream)

M_e Mach in the gap

m_{JC} thermal softening coefficient

N number of nodes

n work hardening exponent

N_f normal force

na size of the asperities

P pressure

P_0 pressure in front of shock wave

P_1 pressure behind shock wave

P_H Hugoniot pressure

P_{hyd} hydrostatic pressure

Pr Prandtl number for air

q_g heat generation rate

q_{vm} Von Mises stress

Re_x Reynold's number

RK_n current solution, Runga-Kutta method

RK_{n+1} next step solution, Runga-Kutta method

S entropy of the system

s ratio of speed of melt front and diffusivity length

T temperature

t time

t^* entire model run time

t^* entire model run time

T_0 transition temperature

T_a ambient temperature, 300°K

T_H Homologous temperature

T_m melt temperature

t_m time to melt

T_{aw} freestream temperature

T_{surf} temperature at surface of slipper

u_m melt depth

V volume

v_0 particle velocity in front of shock wave

v_1 particle velocity behind shock wave

v_2 airflow velocity post shock wave

v_c couette flow velocity profile

v_s shock wave velocity

v_∞ velocity (freestream)

v_e velocity in the gap

y distance into depth of slipper

y^* diffusivity length

y_{max} maximum depth into slipper

INVESTIGATION OF SEVERAL METHODS OF EVALUATING WEAR IN A HIGH-SPEED ENVIRONMENT

I. High Velocity Wear Problem Overview

1.1 Overview

The HHSTT was initially constructed in 1949. Since that time, the track was lengthened numerous times, now consisting of dual rails at a length of 51,000 feet and a monorail at 20,500 feet. In addition to increasing in length over the years, the velocities of the test runs have correspondingly been increasing. In 2003, a new world record for ground testing was performed on the dual rail setup that reached 2,885 m/s ~Mach 8.5 (6,453 mph).

As velocity requirements continue to increase, the test facility is continuously upgraded[33][34]. However, the accuracy of the wear rate prediction is a limiting factor. A slipper failure would be a catastrophic event that would destroy valuable and unique test assets and result in the loss of test time and money. Thus, the current strategy of the responsible test organization is to remain conservative and keep velocities in a range that current slippers are known capable of surviving. In addition, current slippers can only be used once since one cannot currently predict the properties of a used slipper, hence the need to increase the accuracy of the wear rate prediction.

Typically a test setup consists of a multi-stage rocket propelled sled with a test payload as depicted in Figure 1.1. Previous work at the Air Force Institute of Technology (AFIT) has focused on the dual rail sled setup depicted in Figure 1.2. As the sled system travels down the rail at high velocities it remains attached to the rail by slippers. The slipper design can be seen in Figure 1.3.

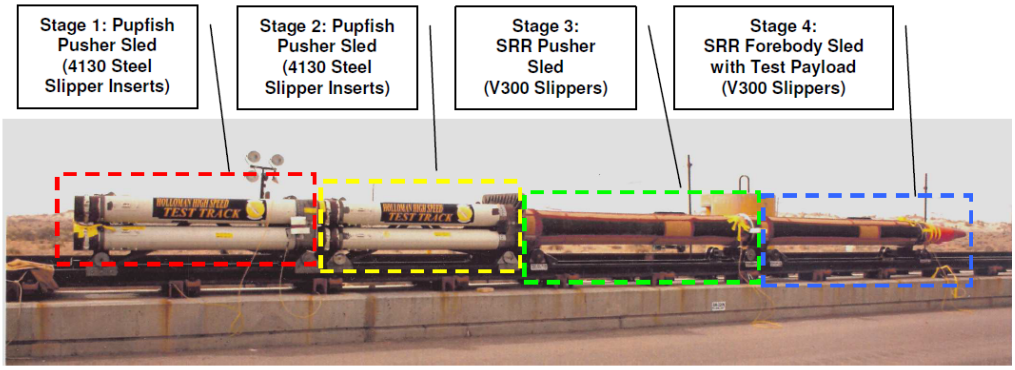

Figure 1.1: Multiple Stage Rocket Sled [3]

Figure 1.2: Dual Rail Slippers [3]

As two surfaces slide against one another wear occurs. Wear is a complex phenomenon that includes adhesion, abrasion, surface fatigue, fretting, and erosion. The environment that the slipper operates in exacerbates all of these types due to high strain rates, owing to the high velocity, as well as the thermal environment from friction, aerodynamic heating and plastic deformation. The slippers experience extreme forces including mechanical, thermal, and aerodynamic. Figure 1.3 shows a gap between the slipper and the rail. The sled is designed to produce lift in an attempt to reduce the wear on the slippers by reducing the pressure over the full test run[2]. This results in bouncing as the lift is counteracted by the wraparound slippers connecting the sled to the rails[1]. This bouncing adds further complexity as it introduces transient forces that must be taken into account to properly understand and model the slipper-rail environment. The slippers

thus endure varying loads while undergoing wear for the duration of the run. The quest to improve the durability of the slippers is an ongoing process that requires an ever better understanding of the complex wear phenomenon experienced in this extreme environment.

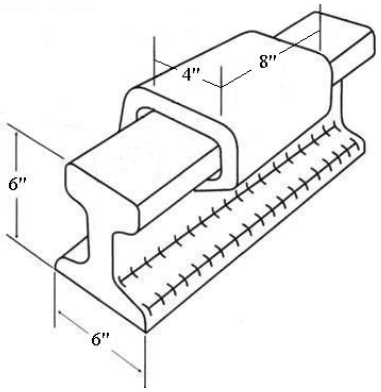

Figure 1.3: Wrap around Slipper [4]

1.2 Research Objectives

The goal of this research was to study and understand the wear of metals in contact during an event at the HHSTT in 2008. The 2008 experiment is a particular run included in the modeling and does not represent all the conditions an experiment could contain, but the investigation of its features gave many of the physical characteristics of high velocity wear. Thus, it is felt that many of the physics oriented features of this dynamic event can be observed and studied by tracing the functions of this experiment. In addition, the 2008 run had many important experimental and physical parts useful in the analysis. In order to do that, several models were developed. At the microscale, the first FEM was developed to model a portion of the slipper impacting an asperity attached to a portion of the rail. This micromechanical scaled model simulates a fraction of the test run, on the order of 10^{-7} seconds. It was used to estimate wear and to investigate several assumptions used in previous work [18][3][35].

A heat transfer model was also constructed to estimate the melt wear that occurs for the acceleration phase of the test run accomplished in 2008. The heat transfer model was

the only model used that could simulate the entire acceleration phase of the run by limiting the model to one-dimension. It also provided the initial temperature incorporated in the three-dimensional FEMs used in this work. Additionally, the heat transfer model provides insight into the temperature profile through the thickness of the slipper and how it develops over time.

Finally, a larger scaled FEM was constructed to simulate a portion of the slipper traveling down the rail while in contact at specific velocities during the acceleration phase of the test run. The output from this model provided an estimate of the wear that occurs due to wear damage. This wear was scaled to the actual slipper and then compared to the wear measured from the worn slipper taken from the 2008 test.

Several items were accomplished to achieve the research objectives and are listed below:

1. Described the general contact algorithm within ABAQUS [27].

2. Evaluated the need for and results of an equation of state at the velocities of the asperity collision modeled.

3. Examined the effects of boundary conditions that differed from previous work [18][15][3][22].

4. Evaluated the wear rate for a HHSTT test run using three numerical models based on previous work [18][15][3][22].

5. Evaluated the effects of temperature derived from a one dimensional heat transfer analysis as import to three-dimensional finite element mechanical wear estimate models.

6. Increased realism in the existing heat transfer analysis by representing varying (in place of constant) material properties.

7. Partially validated a partition function used to estimate the heat distribution between slipper and rail by making use of temperature data from a 2014 slipper experiment.

8. Evaluated the total wear for the 2008 HHSTT test run using the combined results of the macro scaled models.

1.3 Wear Overview

Wear is a complex phenomenon that encompasses many different types of surface damage. Since this research investigated two solid surfaces sliding past each other at high velocities, it was focused on what is referred to as 'abrasive wear' and thermal wear. Chemical wear is described by Kato [36] and is also present but to an unknown degree in the HHSTT scenario, it was not investigated as part of this study.

As defined by the American Society for Testing and Materials (ASTM), *wear* is the loss of material due to hard particles or hard protuberances that are forced against and move along a solid surface [37]. The ASM handbook [30] identifies several mechanisms to explain how material is removed from a surface during abrasion. These mechanisms include fracture, fatigue, and melting. Because of the complexity of abrasion, no one mechanism completely accounts for all the loss.

Most previous research focuses on pin on disk type studies. Some of the processes that are possible when a single abrasive tip traverses a surface, include plowing, wedge formation, cutting, micro fatigue, and micro cracking [30]. Plowing refers to material that has been moved to the side to create grooves. Ridges form from the displaced material. No material is lost, although the ridges could be abraded through micro fatigue. This mechanism is associated with light loading. Wedge formation is described as being similar to plowing however, the material that is displaced builds up in the groove versus on ridges. This is also associated with relatively light loading. Cutting is when material is separated from the surface of material without resulting damage in the surrounding material. The difference between plowing, wedge formation, and cutting is due to the depth

of penetration. This is the factor that separates the different mechanisms. Fragmentation also occurs in hardened steels and is similar to cutting except the surrounding material incurs additional damage in the form of localized cracks that leads to additional wear due to spalling [30]. These physical features are represented through the various models performed through the research.

By examining a worn slipper from a HHSTT test in 2008, some of these mechanisms can be identified. In Figure 1.4 three of the mechanisms can be readily seen.

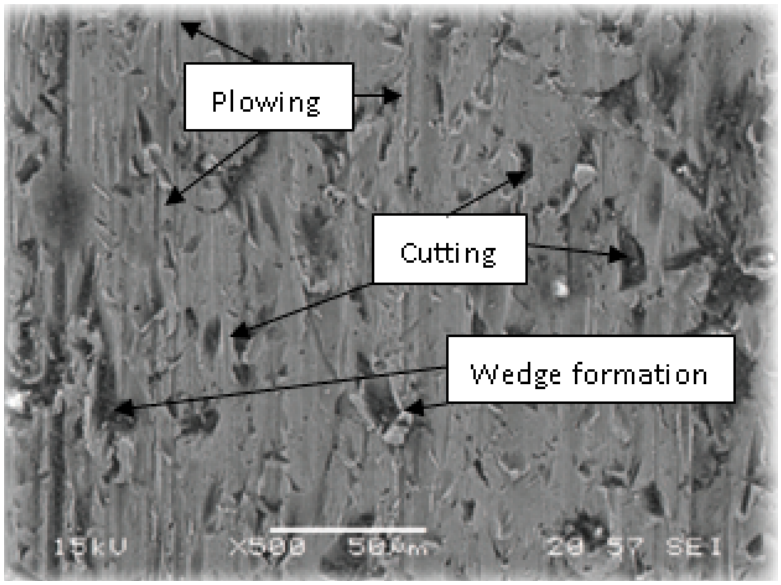

Figure 1.4: Test Slipper Surface, 500x [3]

Another factor of importance is the raised temperature that occurs due to conduction, convection, and plasticity. They affect the material and cause *melt wear*. In the scenario under study, the slipper slides on a rail at high speed. This environment leads to material melting. As melting occurs, the material loses any resistance to strain and can adhere to another surface or detach and be removed from a surface. Thus, the material is displaced and is characterized as wear once a final measurement of the slipper is performed. Hale hypothesized that the percentage of measured wear due to melt in this scenario is approximately 20% [3].

1.4 Previous Wear Research

1.4.1 Overview.

Throughout the years, previous research has been conducted in the area of wear. In particular, high speed sliding wear has been investigated for many years with a mechanical as well as a thermal focus. Research has occurred at AFIT and elsewhere in these areas. This section summarizes attempts to characterize and model wear associated with unlubricated wear of metals due to sliding. It shows the incremental improvements that have occurred and that relate to the current research. What follows is work that has attempted to use numerical modeling to predict wear as experienced by the slipper traveling down the rail at high speeds. Several models were developed that characterized material behavior under differing wear scenarios. These numerical models have matched experiments with varying success. At AFIT, the hydrocode Three-dimensional shock hydrodynamics code (CTH) was initially used since it is designed to model high velocity impact. That effort was focused primarily on gouging where impact happens at a macro scale. For further details on CTH specifics, see Laird [38]. Recently, the commercial finite element software package ABAQUS [27] incorporated the Mie-Gruneisen equation of state and the Johnson-Cook plasticity and failure models into its code. This coupled with its robust contact algorithm makes it an ideal candidate to model the high velocity wear event of interest.

The mechanical interaction between an asperity and the slipper has been modeled in ABAQUS [27] as plane strain and as a three-dimensional model. Unfortunately, the coupled thermal environment has proven more problematic. To date the thermal analysis has been done in an uncoupled manner where a one-dimensional heat transfer analysis has been accomplished in the commercial software package MATLAB [39]. This has been improved upon over several years and was used and improved in this research as well.

The scenario at the HHSTT is different than many other wear scenarios that have been studied in the past. This is due to several factors. As stated, most previous work has been done with pin on disk experiments. This will be discussed in the next section but it bears pointing out how different the slipper and rail scenario is from that situation. The pin on disk research has made great strides including the use of finite elements to simulate those experiments [40]. However, the velocities studied in those experiments are far below the 1.5 km/s velocities achieved by the slipper and the temperatures are usually below melt. These factors necessitate a different approach to modeling and to wear calculation as discussed in the next sections.

1.4.2 Review of Wear Research.

In 2002 Laird studied gouging phenomenon that occurred at the HHSTT. Laird utilized the hydrocode CTH to investigate gouging as high-speed impact. Temperature effects were included and an effort was made to model the shock wave due to the impact. The models developed were based on previous work at Sandia National Labs by Barker[41] and Tachau[42], and they attempted to account for gouging under differing conditions at the micro scale. Laird's model was used to simulate several types of impact event outcomes including an asperity collision. The model considered imparted vertical velocity on the slipper model without an asperity, and several different slipper leading edge angles. In addition, temperatures were varied for the slipper model. This was done by imposing an initial temperature on the slipper model. The temperature rise due to friction was calculated using work done by Krupovage and Rassmussen [43] while aerodynamic heating was calculated with work done by Korkegi and Briggs[44][5].

In 1969, Korkegi and Briggs developed a model for the flow field between the slipper and the rail. Figure 1.5 depicts how the flow enters the gap and how it is affected by the shock from the front of the slipper.

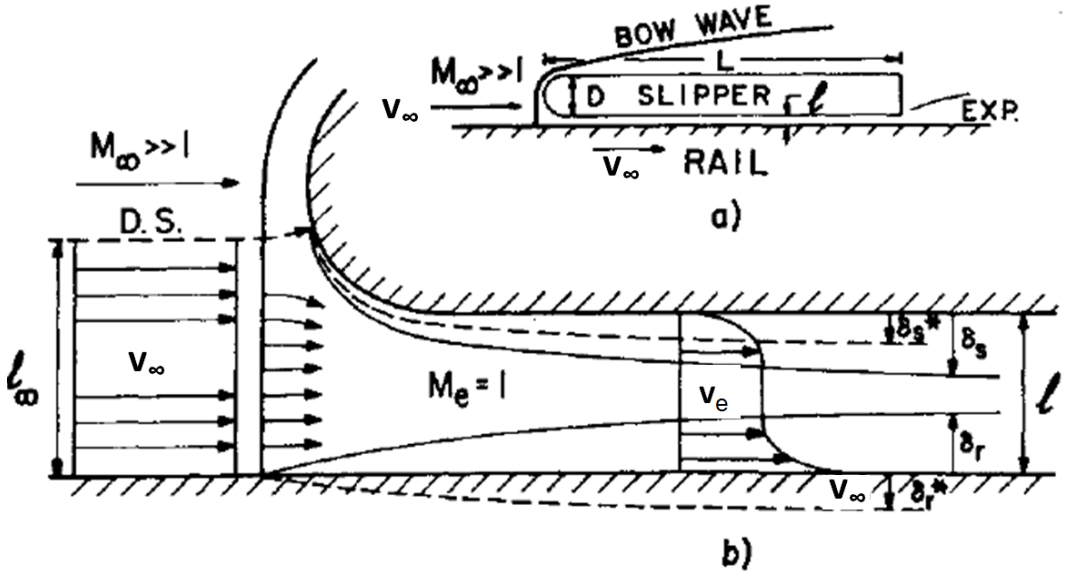

Figure 1.5: Slipper cross section and boundary-layer growth in gap.[5]

The flow transitions from boundary layer flow in the front of the slipper to Couette flow at the rear as shown in Figure 1.6.

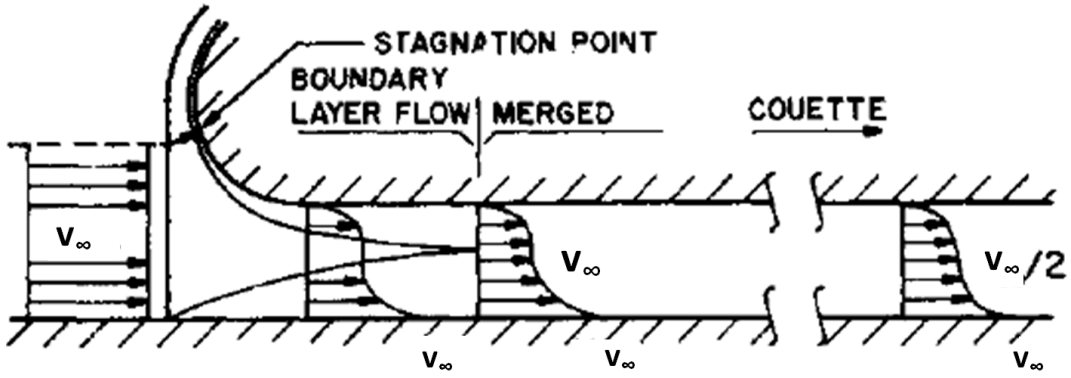

Figure 1.6: Flow model with characteristic velocity profiles.[5]

M∞ - Mach (freestream)

M_e - Mach in the gap

v_∞ - velocity (freestream)

v_e - velocity in the gap

l - gap between slipper and rail

l_∞ - freestream tube

Laird estimated that the slipper experienced temperatures on the order of 2500K during a test run. The material was modeled with an equation of state, the constitutive relations, and failure. The equation of state was required due to the level of deformation and strain rates producing a stress wave of high enough magnitude to result in changing density. Laird used the tabular Equation of State (EOS), SESAME, to model the high speed impact. The SESAME EOS can account for four solid phases (alpha, gamma, epsilon, delta), melting, and vaporization. The constitutive relations were handled by Johnson-Cook and Steinberg-Guinan-Lund models. The models used were based on available coefficients for the material of interest. To model material failure, material pressure was monitored and when the pressure was determined to be below a predetermined amount, fracture was assumed and the material replaced with a void.

Laird concluded that vertical forces were sufficient to model gouging. In addition, it was noted how temperature played a large role in increasing gouge damage[45].

To gain a better understanding of the aerodynamic heating as well as the aerodynamic loads in general, in 2002 Lofthouse developed a Computational Fluid Dynamics (CFD) model to investigate the airflow around the sled. The model can be seen in Figure 1.7. It depicts a model of the sled with attached slippers over a rail model with a calculated aerodynamic flowfield. The CFD model considered a simplified inviscid flow and did not consider the friction of the slipper as it slides down the rail. It was focused on the aerodynamic heating that occurs due to the high-speed airflow that occurs around the sled to include the slippers. The model includes aerodynamic shielding that is used on the forebody sled.

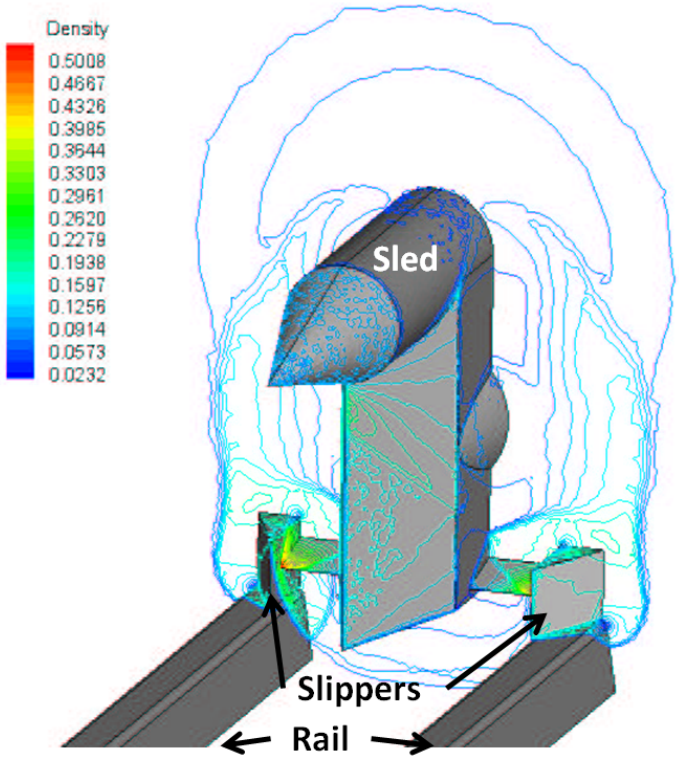

Figure 1.7: CFD Model[6]

Lofthouse also investigated the airflow between the sled and the rail. The simplified model used is shown in Figure 1.8. The figure is an expanded view of one of the model slippers, depicted as a three-dimensional triangle, in contact with the rail and connected to the sled.

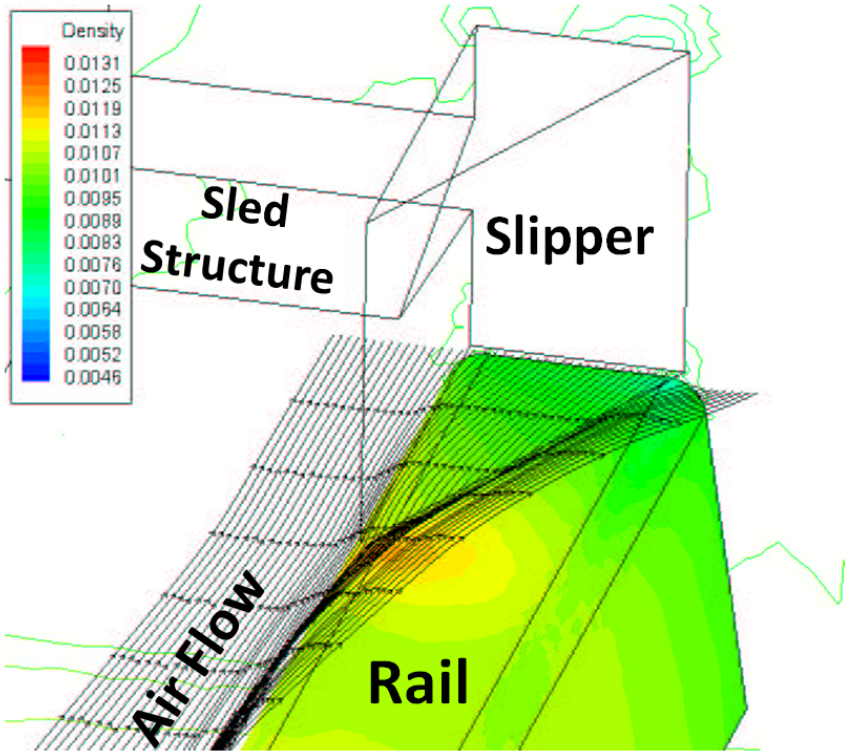

Figure 1.8: CFD Slipper Model[6]

Lofthouse examined the flow of both air and helium and plotted the temperatures at several locations along the length of the slipper. The model is in the shape of a triangle that is different from the wraparound slipper actually used. Lofthouse did not model the gap between the slipper and the rail. However, the temperature in the gap can be estimated by measuring the temperature just inboard of the slipper. This was just behind the shock that occurs at the front end of the slipper shield. This was assumed analogous to the region in the gap at half the length of the slipper.

Lofthouse concluded that the aerodynamic heating was dependent on accurately modeling the shocks that impinged on the structural components of the sled. To model shocks accurately, viscous effects would need to be included.

Szmerekovsky followed Laird's investigation of gouging[46], of the high speed event at the HHSTT, in 2004. During the investigation, multiple codes were compared. Lagrangian based Finite Element Analysis (FEA) codes were deemed unsuitable due to the

large deformations that take place during the event. Gouging was deemed a problematic event to model with Lagrangian based codes due to the material 'mixing' that occurs [35]. An Eulerian based code, CTH was similarly investigated and found to require a finer mesh than the Lagrangian based codes to capture necessary characteristics of the simulations.

Szmerekovsky found that the initial coefficient of friction did not have an effect on the solution. Also, the study found that at high speeds, the effective coefficient of friction could be manually estimated by integrating normal stress and shear stress solutions at points along the bottom of the slipper[35].

Another area of research undertaken was a dimensional analysis. This is of particular importance as the models used to study gouging and asperity collision are at the microscale, while the actual system under study ie the slipper-rail are at the macroscale [47].

Szmerekovsky concluded that a plane strain model was adequate to study gouging phenomenon. Also, in regards to dimensional analysis, that further study was required as *'the complexity of the problem makes it extremely difficult to consider every dimensioned quantity for the dimensional analysis'* [**?**].

In 2006, Cinnamon did further investigation into gouging at the HHSTT. The research involved material testing and evaluating the Johnson-Cook plasticity[48] and fracture coefficients[49] for 1080 steel and Vascomax 300. In addition, the coefficients for the Zerilli-Armstrong model were determined as that model is a better fit for high-strain rates[50]. The appropriate coefficients were then used in a CTH hydrocode model to simulate a microscale portion of the slipper traveling down a microscale portion of the rail. The model was two-dimensional and rail discontinuities were approximated by having the rail surface angled as shown in Figure 1.9. Cinnamon included a coating on the rail that was used for portions of the rail to reduce wear. This research also incorporated the idea of asperity collision albeit in a crude form as one of the possible explanations for gouging [51].

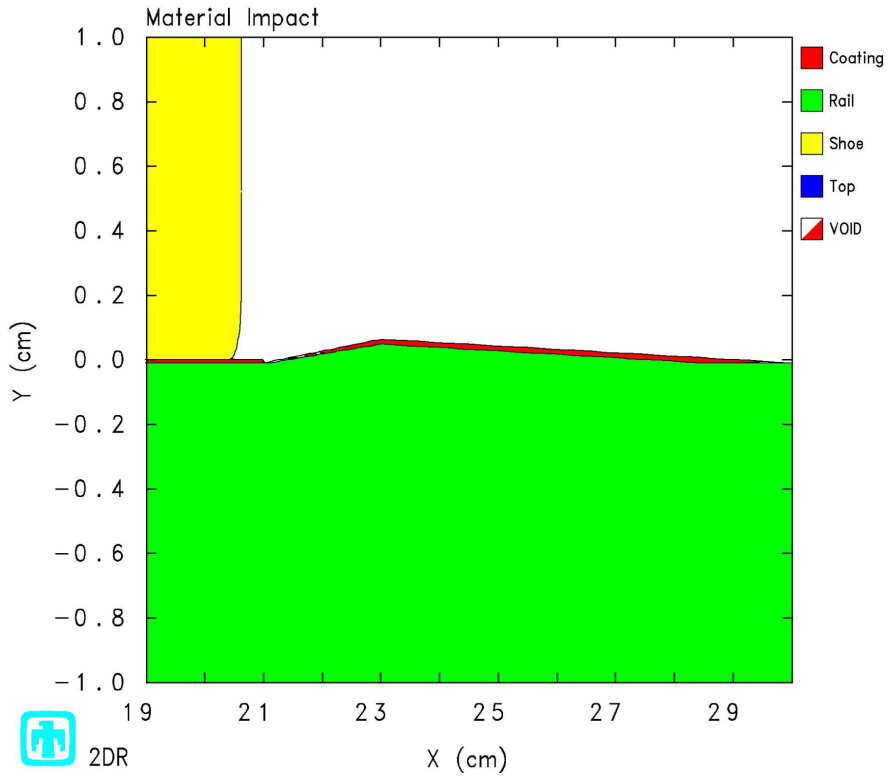

Figure 1.9: CTH Model with angled discontinuity[7]

Cinnamon concluded that the rail discontinuities were the cause of the gouging seen during test events at the HHSTT. The coefficients obtained for 1080 steel and Vascomax 300 were used in subsequent research including the current one.

In 2007, Cameron used the hydrocode, CTH to simulate the slipper traveling down the rail at the micromechanical scale. Cameron also used the Dynamic Analysis and Design System (DADS) data to predict wear based on Lim and Ashby, Montgomery, and Archard research[52][53][54][55]. DADS is commercial software that is a set of general purpose computer programs that can be used to model and predict the motion of a variety of real world mechanical systems. Using a set of data that describes the mechanism to be modeled, DADS builds a mathematical model of the real system that calculates positions, velocities, and accelerations of the various parts of the mechanism, as well as resultant forces that act on the system [56]. This data is simulated data. It approximates actual loads seen by the sled during a test run based on test parameters, test article particulars, and rocket

propulsion capabilities. This data is used as a substitute for real data as it is not possible to instrument a sled to collect this type and quality of data during a real-time test. This can increase the difficulty in estimating wear since the actual test variables are not available. The DADS output was validated against three instrumented test runs to provide confidence in the model [57].

Lim and Ashby reviewed previous work in wear research and from the numerous findings constructed wear maps for different materials. Figure 1.10 shows the wear map constructed for steel. What it shows is the type of wear that is expected to dominate under different loading conditions. The wear map was developed to summarize the findings of numerous studies. It is useful to understand the type of wear to expect given the magnitude of loads and velocities experienced. The wear experienced by the slipper in the scenario under study can be summarized by examining the wear map presented. The wear map, and its applicability to the current research, will be discussed in further detail in Chapter 3.

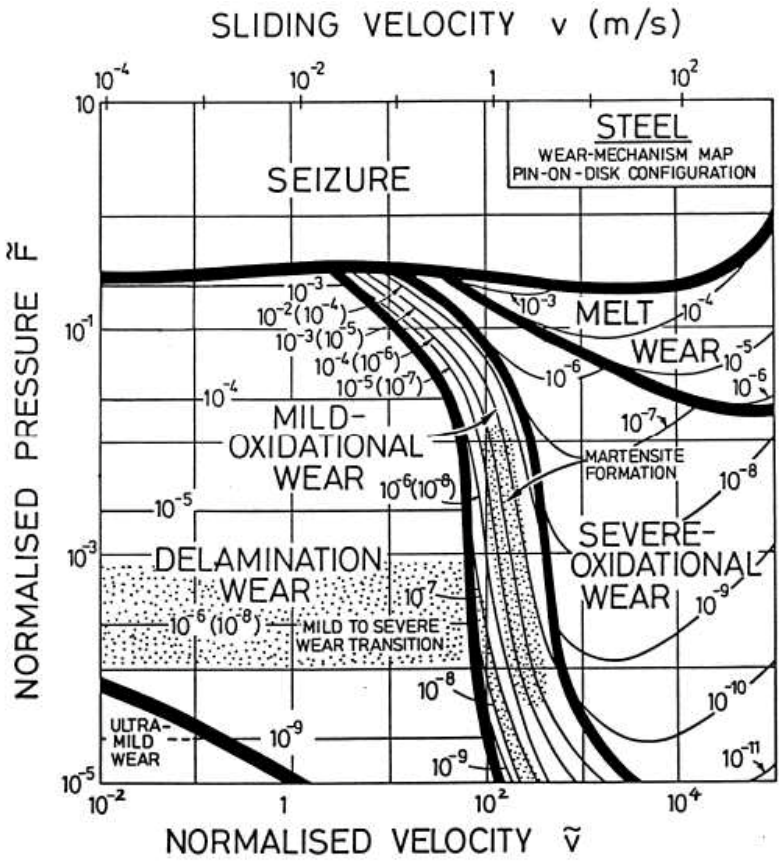

Figure 1.10: Wear Map for Steel[8]

Cameron used Lim and Ashby's calculation for melt wear and applied it to the HHSTT scenario. Lim and Ashby used work by Montgomery to validate their melt wear model. Montgomery performed pin-on-disk experiments in an attempt to simulate the wear experienced by artillery cannon barrels. The original work was performed in the 40's and 50's and only published later due to classification issues. The experiments showed that once the material melts it contributes to lowering the coefficient for friction by acting as a lubricant. Montgomery used pressure velocity (Pv) as an axis in his results. Montgomery multiplied bearing pressure by sliding velocity to arrive at the parameter Pv. Some of his results are shown in Figure 1.11.

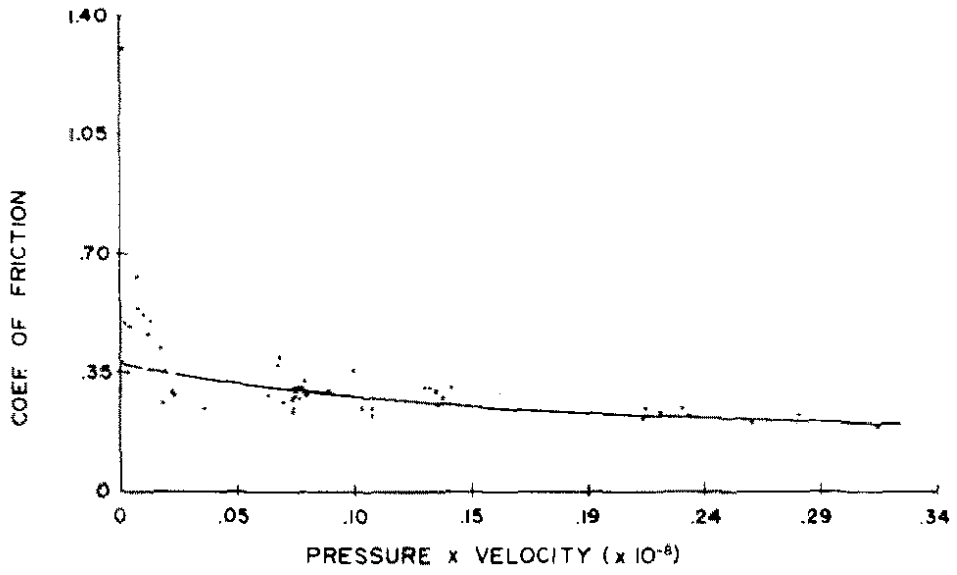

Figure 1.11: Coeff of friction of projectile steel as a function of press x vel (lb in^{-2} ft s^{-1})[9]

To account for mechanical wear, which Lim and Ashby termed 'plastic wear', they used Archard's law and then suggested that *voids nucleating around material inclusions beneath the surface generate wear particles as plastic shear strain accumulates*[52]. Archard and Hirst studied unlubricated metal sliding past each other at low speed under various loading conditions in 1956 [54]. They utilized pin on disk experiments with the disk rotating at 180 cm/s. A flat-ended pin was pressed against the pin under different loadings ranging from 50 grams to 10 kilograms. They found that once past a certain "running-in" period, the wear tended to be constant and independent of contact area. From these investigations, the concept of wear due to asperity collisions is the basis of the micromechanical models developed as plane strain, three-dimensional FEMs, and also utilized in this research. Cameron developed a one-dimensional finite difference heat transfer [39] code to calculate melt wear and mechanical wear as well as temperature through the thickness of the slipper. The temperature was used in the CTH model. The investigation examined several different cases to include with and without coatings applied to the rails as well as to include asperities in a limited fashion. The two-dimensional

model did not show melt. Cameron stated that this was due to thermal softening causing a reduction in thermal flux due to reduced plasticity. Figure 1.12 shows the CTH model including an asperity and coating.

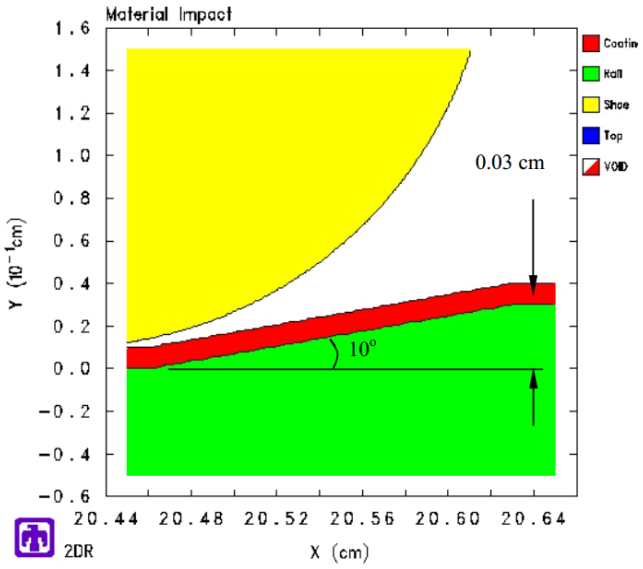

Figure 1.12: Cameron's CTH Model with Asperity[10]

Cameron's calculation based on Lim and Ashby work to determine melt and mechanical wear rates was deemed unrealistic.

In 2008, Chmiel investigated the HHSTT wear scenario with two different FEMs utilizing ABAQUS [27]. One was a macro model that incrementally simulated a pin on disk scenario at low speeds. Every time step completed by the FEA solver was checked for wear using the Archard Equation [54]. Friction was estimated by using an equation developed by Cameron to approximate the friction coefficient based on Montgomery work [10]. This effort matched Archard's equation at speeds in the 1 m/s range. The second method consisted of a global and local model. The local model attempted to simulate the roughness of the rail and have the slipper model come into contact with asperity models. It was a plane strain model and only tested at low velocities. Figure 1.13 shows the microscale FEM that Chmiel developed.

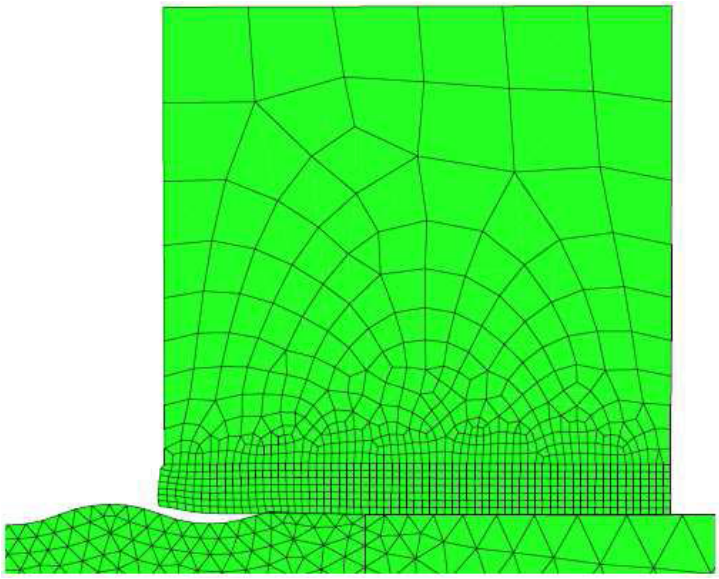

Figure 1.13: Chmiel's Plane Strain Model[11]

Chmiel's work showed the viability of using ABAQUS to model wear for the HHSTT scenario. The model used Johnson-Cook plasticity model and Montgomery based friction coefficient calculation, but used a ductile failure criteria which failed to predict any wear. The model was also only used at low speeds without temperature considerations included. In 2009, Hale obtained a worn slipper from a 2008 test at the HHSTT. The DADS data for the same test was also acquired. Hale measured the slipper down the centerline to estimate the amount of material worn away as shown in Figure 1.14.

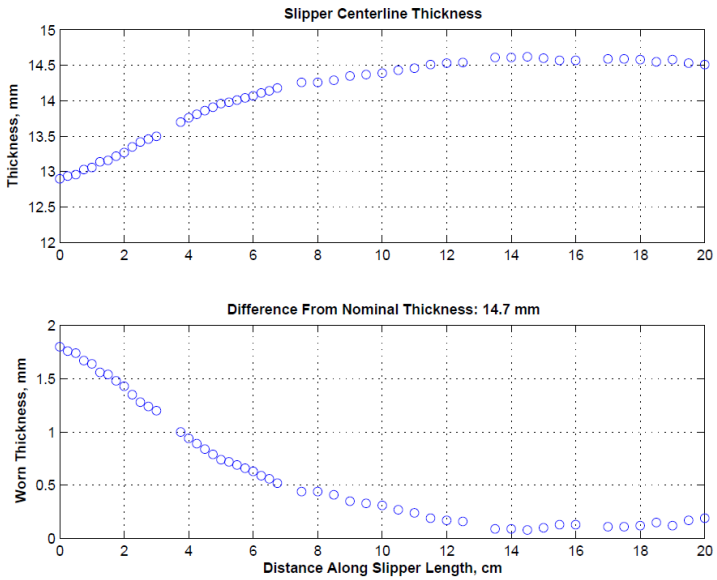

Figure 1.14: Worn slipper thickness measurements (centerline).[3]

Hale plotted the contact forces experienced by the slipper from the DADS data. This showed the magnitude and timing of the slipper bounce as it traveled down the rail. The contact forces are shown in Figure 1.15

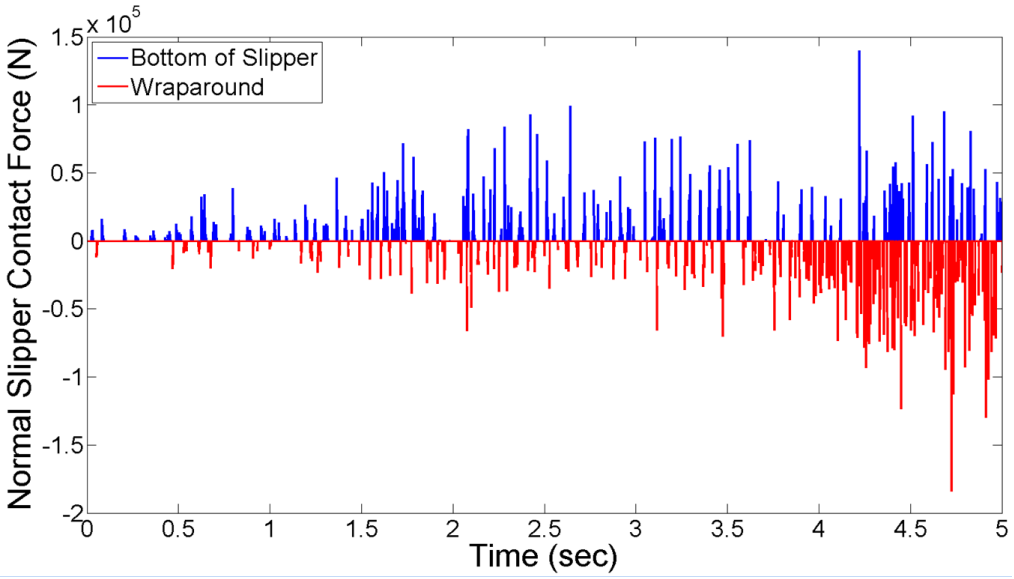

Figure 1.15: Contact forces experienced by the slipper.[3]

The DADS data was used extensively in Hale's research to estimate loads and bouncing of the slipper as it traveled down the rail. As the slipper bounces on the rail during the test

run, either the top portion of the slipper is in contact with the rail or the wraparound bottom portion of the slipper is in contact with the underside of the rail, preventing the slipper from departing the rail. This wrap around design is shown in Figure 1.16.

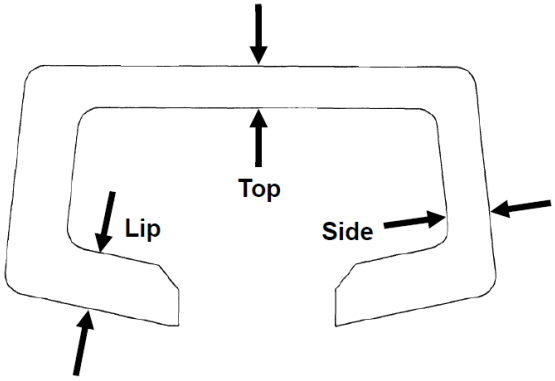

Figure 1.16: Slipper wrap around design.

Hale continued Chmiel's methodology of developing both a local model and a global plane strain model in ABAQUS to predict wear. The local model was sized at the micro scale (10^{-6} m). Figure 1.17 shows the plane strain local FEM used by Hale. There was no gap between the rail and the slipper.

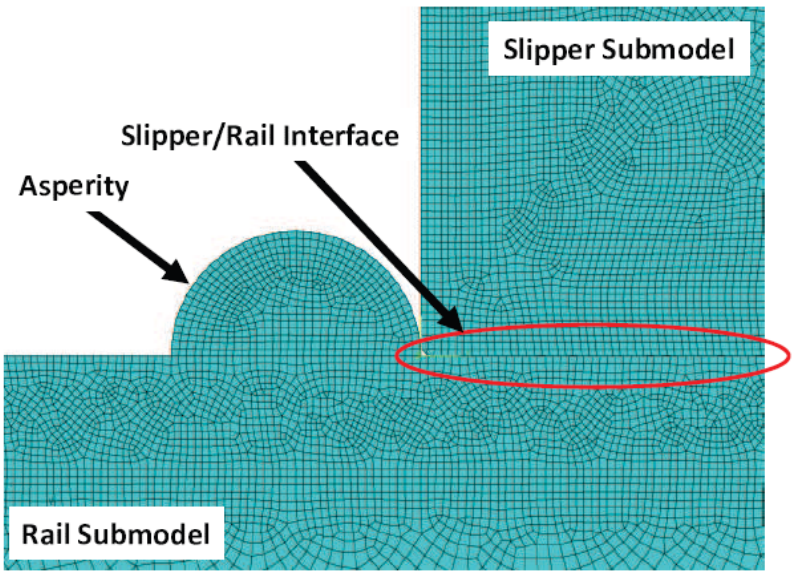

Figure 1.17: Plane Strain FEM sub-model.[12]

By taking the curve from Montgomery's work shown in Figure 1.11 and the DADS data one can arrive at the frictional heating based on work by Krupovage and Rassmussen[43]. They found that the power developed by friction is directly proportional to the material friction coefficient, bearing pressure, and relative velocity. Hale used a curve fit to Montgomery's results, as shown in Figure 1.18 to estimate the material coefficient of friction based on Krupovage and Rassmussen's work. Given the pressure and velocity provided by DADS data, one can calculate the friction coefficients as was done in Hale's research.

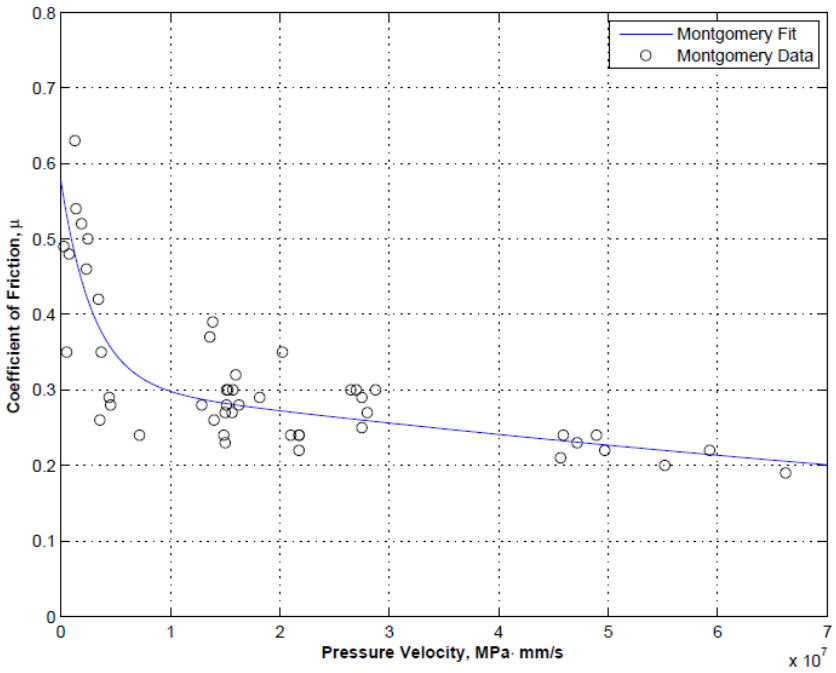

Figure 1.18: Friction coefficient per pressure-velocity.[12]

Figure 1.19 shows how the plane strain model accounts for different asperity sizes. Although the model only used a 6 μm asperity in the analysis.

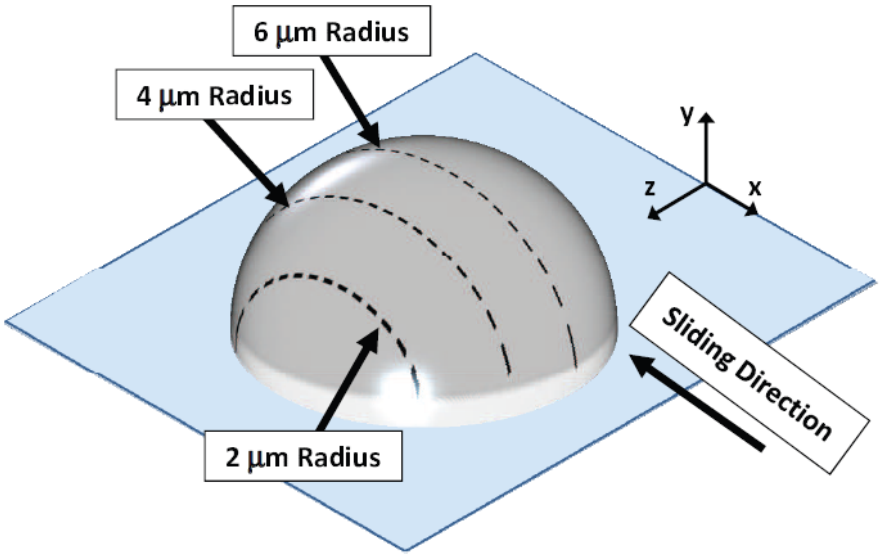

Figure 1.19: Asperity Model.[3]

Figure 1.20 shows the boundary conditions used in Hale's model. They are very similar to the boundary conditions used in Buentello's three-dimensional model [58]. The slipper model top surface has an initial velocity imposed on it. The rear surface also has the same initial velocity imposed on it. This is to ensure that the slipper model has the correct momentum as it impacts the asperity model. The bottom surface of the slipper model does not have an imposed velocity. This is to ensure that it reacts realistically to the asperity model. Otherwise, the slipper would continue through the asperity at the constant imposed velocity. There would be no momentum transfer into the slipper elements.

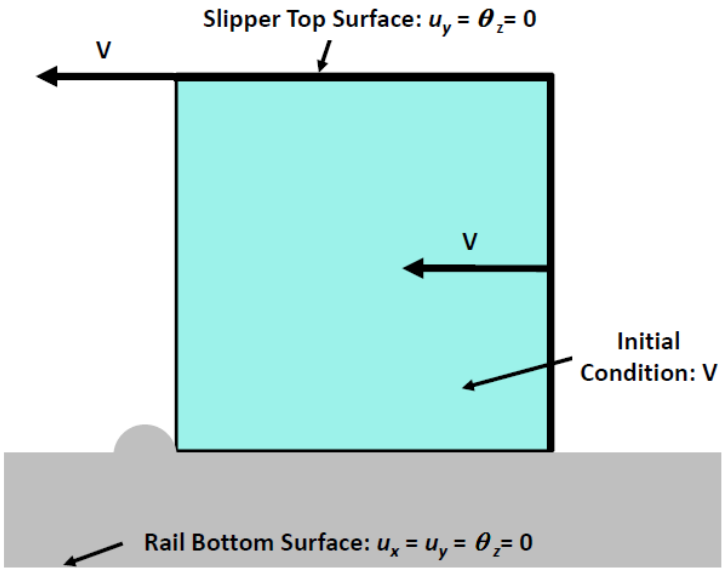

Figure 1.20: Local sub-model boundary and initial conditions[3]

Hale also used a MATLAB[39] script to solve a one-dimensional finite difference scheme to conduct heat transfer analysis to account for initial temperatures of the sub-model. Hale assumed a partition function of 50/50. A partition function is used to estimate the thermal energy imparted to the surfaces in contact. The partition function in this case is complicated by the dynamic nature of the slipper-rail contact due to bouncing. When in contact conduction occurs and the thermal energy flows unevenly to the heated slipper and the cooler rail. The partition function is an area of ongoing study and will be discussed further as part of this research. Figure 1.21 depicts the one-dimensional finite difference scheme developed by Hale.

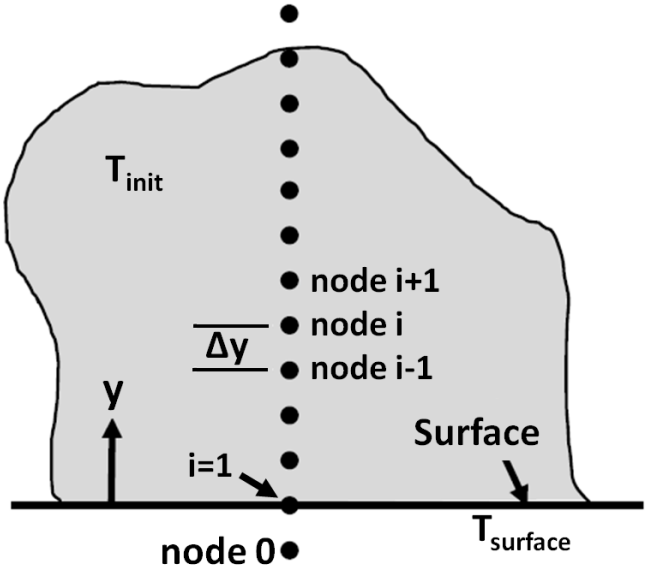

Figure 1.21: One-dimensional heat transfer model[3]

Hale concluded that a global model was unnecessary as the stresses transferred to the sub-model were negligible compared to the stresses experienced due to high velocity impact with the asperity. Hale's work accounted for approximately 35.7% of the measured wear. A plane strain ABAQUS [27] model with asperities was used in Burton's research in 2009. Surface roughness measurements were used to create the geometry of the model. These measurements were used to model an accurate representation of the rail surface. This model was used to explore the correlation between surface roughness and the Montgomery coefficient of friction [9]. The study showed that micro scale asperities could be modeled to account for measured friction at the macro scale. This finding was used as justification for removing friction from asperity collision modeling as well as the continuum mechanic scaled FEM used in this research.

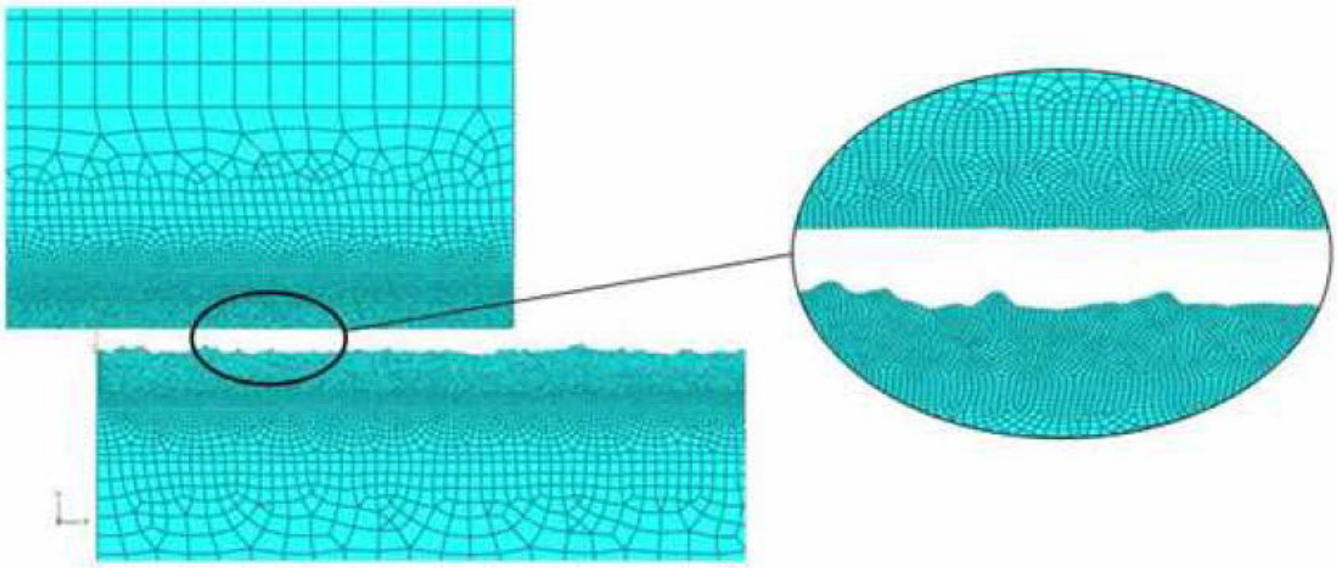

Figure 1.22: Plane Strain FEM derived from measured and filtered surface profile.[13]

Figure 1.23 is a depiction of the CTH micromechanical model used by Meador in this work. By analyzing the DADS data, Meador hypothesized that the vertical velocity was of minor consequence compared to the horizontal velocity. Meador also improved the one-dimensional heat transfer model by refining the partition function from the 50% assumed by Hale. This was done by calculating the frictional heating based on total melt wear, assumed to be 20%, in the worn slipper from the 2008 test. The heat transfer model did not account for bounce nor did it include latent heat due to material removal. This resulted in a melt wear estimation that was based on the worn slipper results as opposed to being predictive [59].

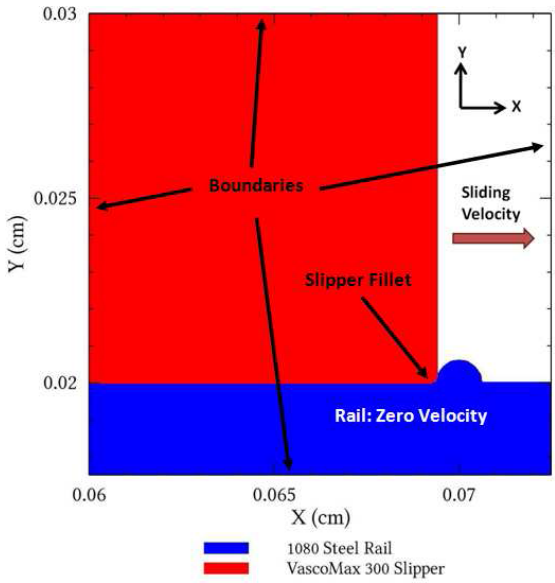

Figure 1.23: CTH Materials Illustration[14]

Meador was able to show that the flash heating calculated by Hale was insignificant when compared to the frictional heating and did not include it in his analysis. Frictional heating is the basis for the conduction boundary condition in the heat transfer model that was further developed in the current research.

Meador's model predicted a total wear that accounted for approximately 46% of the total wear measured on the recovered slipper from the 2008 test.

Huber returned to a CTH microscale model to estimate the wear of the HHSTT 2008 event. Huber used DADS [56] to incorporate the effect of bouncing into the total mechanical wear calculation. By using a MATLAB [39] script to post process the CTH output, two failure criteria were evaluated: critical von Mises stress and strain at max stress [60]. Two boundary conditions at the slipper-rail interface were also considered. One boundary condition, simulated a frictionless surface, the second boundary condition, no slide, simulates a surface with a semi-infinite coefficient of friction. This was Huber's attempt to model the two contact extremes as opposed to estimating the friction coefficient. Also, Huber derived a plane strain calculation for the Hugoniot Elastic Limit (HEL) from the uni-axial representation. The result was used in the current research. Finally, Huber

concluded that a microscale model could not accurately model the vertical forces but a larger scale model could, as was done in the current research. Huber's work accounted for between 40.9% and 80.9% of the measured wear.

In 2013, Paek-Spidell further refined the one-dimensional heat transfer model by performing an investigation into the analytic underpinnings of the partition function. The function, α, partitions the heat flux into the rail and slipper as shown in Figure 1.24. Paek-Spidell developed a representation of α as shown in Equation 1.1.

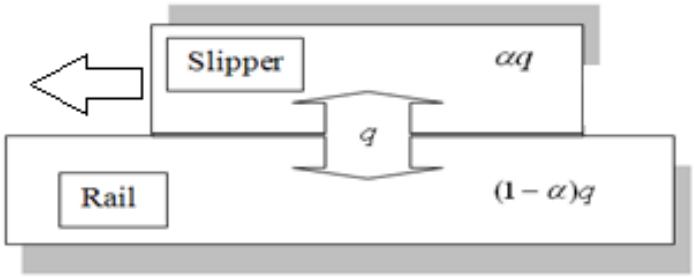

Figure 1.24: Frictional Heat Distribution of Slipper and Rail with Heat Partition Fraction[15]

$$\alpha(t) = 0.4e^{-5t^2} + 0.1 \tag{1.1}$$

Paek-Spidell further developed and implemented slipper bounce into the model and updated the MATLAB[39] script. It was also improved to enable tracking of melt depth into the slipper. Paek-Spidell assumed that the material properties were constant and that the contact area consisted of the entire underside of the slipper. Paek-Spidell's model showed no material melt for the acceleration portion of the test run. In addition, during bounce the temperature was assumed to be ambient. During an actual test, aerodynamic forces would increase the air temperature in the gap between the slipper and rail.

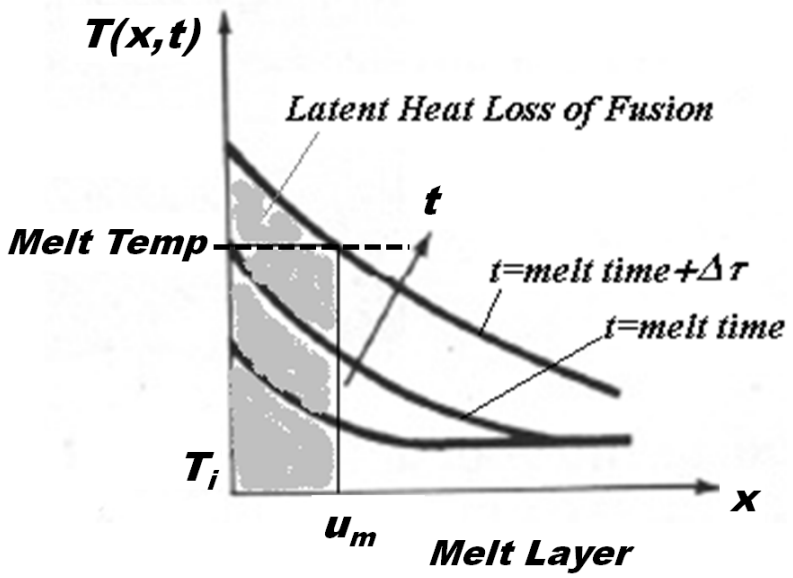

Figure 1.25: Dynamics of Melt Layer Removed Due to Latent Heat of Fusion[15]

Figure 1.25 is a representation of how the latent heat of fusion is used to account for material removal. It depicts the heat transfer solution for three time steps. At each time step the surface temperature, the left of the graph, is tested for exceeding melt. If it does a melt layer is measured, u_m. The material removed is accounted for with the Latent heat of fusion and the heat transfer is performed again to ensure that enough material was removed to ensure that the surface temperature is below melt temperature. The method will be further discussed in Section 3.3.7.2.

In 2013, Le revisited the partition function used in the one-dimensional heat transfer model. As discussed above, the partition function divides the heat flow into the slipper and the rail.

Figure 1.27 shows the steps taken during Le's research. Le used Wolfson data to compare the results of the heat transfer analysis using several different partition functions. In the 1960's, Wolfson[16] conducted experiments to investigate wear rates of various metals. Figure 1.26 depicts the apparatus used in the experiments. The apparatus shown was mounted on a test sled. Once the predetermined velocity was reached, a pneumatic piston forced the slider into contact with the rail. Various metals were tested and Wolfson

concluded that metals with high melt points were most resistant to wear during HHSTT sled runs. Le[17] used this research while investigating the partition function. By attempting to match temperatures and the percentage of slipper melt present at different velocities, the partition function was inferred to be exponential in nature.

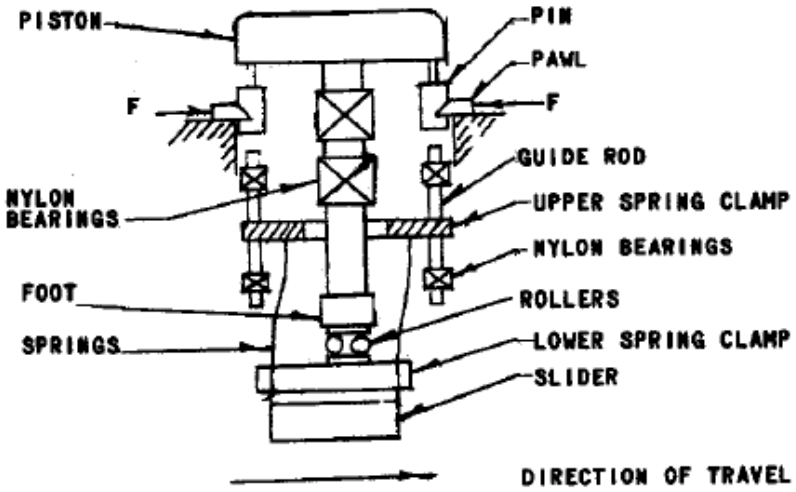

Figure 1.26: Frictional Energy Between Rail and Slipper[16]

The exponential function developed by Paek-Spidell provided the closest match to Wolfson's work and was consistent with Hale's findings. More details on the partition function can be found in Section 3.3.5.1.

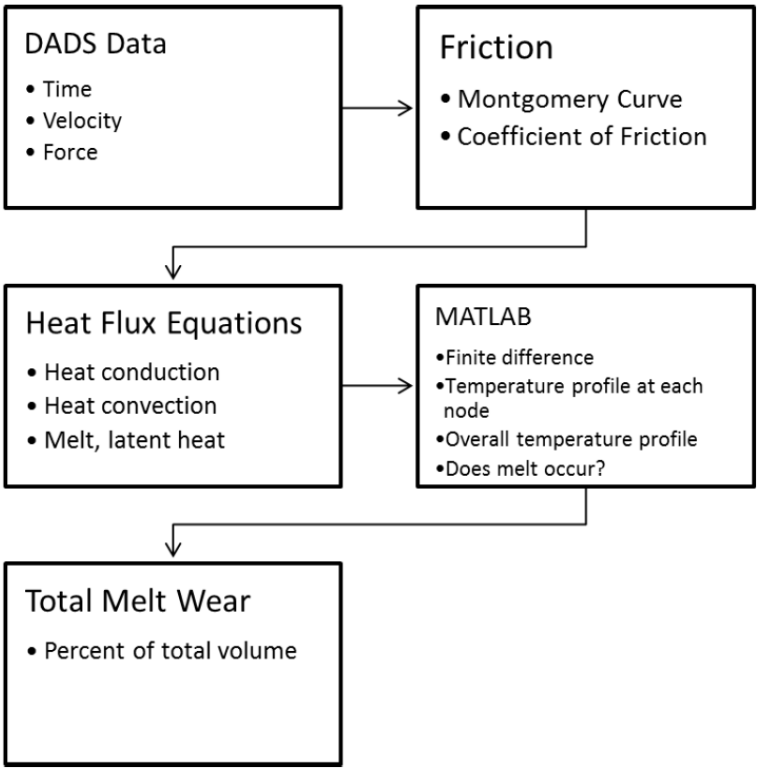

Figure 1.27: Analysis Flow Chart[17]

Le's melt wear results are shown in Figure 1.28. Consistent with Paek-Spidell's findings, no melt was measured during the acceleration phase i.e. < 5 seconds. Also consistent with Paek-Spidell, Le assumed constant material properties and a contact area equal to the entire underside of the slipper. The air temperature between the slipper and rail was also assumed to be ambient.

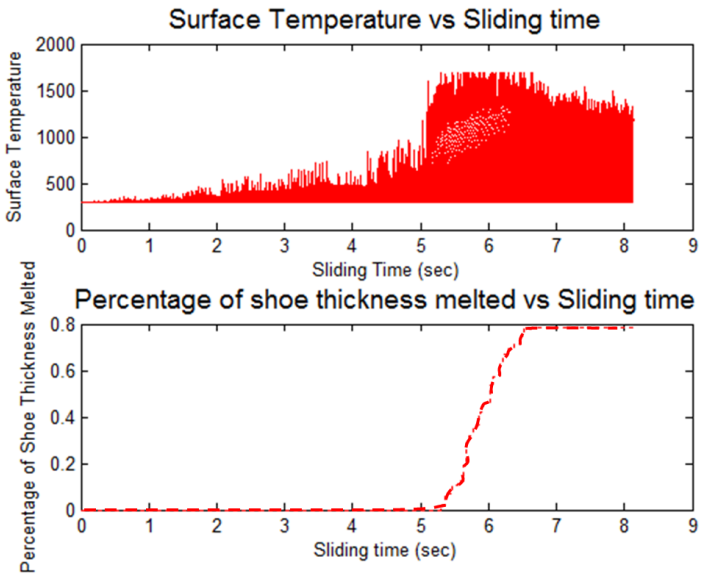

Figure 1.28: Surface Temperature and Melt Wear Percentage vs. Sliding Time Using Exponential Partition Function[17]

Buentello extended Hale's work to three dimensions. The ABAQUS micromechanical scale model is shown in Figure 1.29. The model consists of five asperities sized 1 μm to 5 μm on the surface of the rail. The slipper has five corresponding sections with finer mesh than the majority of the slipper model.

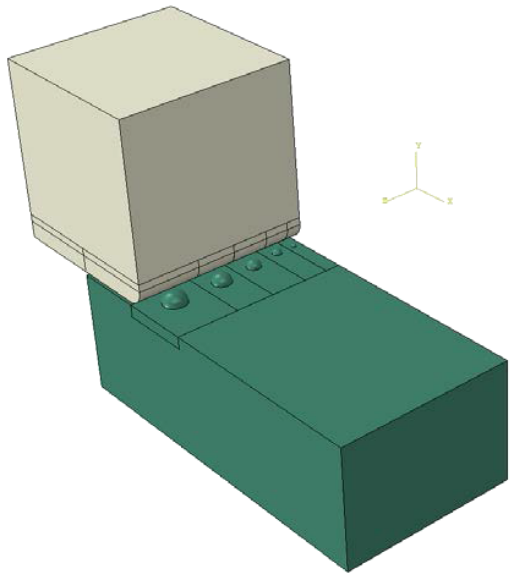

Figure 1.29: Three-dimensional FEM[18]

Buentello's model included a gap between the slipper and the rail as shown in Figure 1.30 for the first time. This assumption was based on Voyiadjis [20] work on surface roughness.

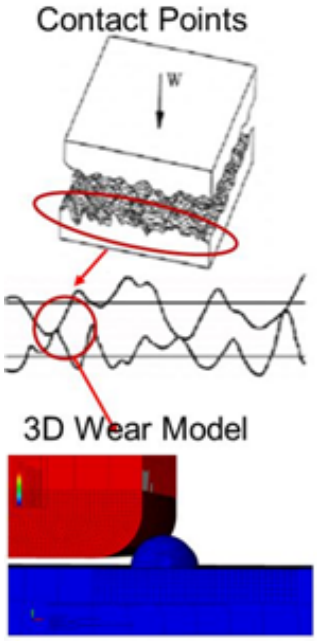

Figure 1.30: Slipper-Rail gap[18]

In 2010, Voyiadjis worked at the National Engineering School of Metz to create two and three-dimensional scanning electron microscope measurements of the surface of 1080 steel and Vascomax 300. This was done in order to characterize the surface roughness of these materials in order to increase the measurement[19] accuracy of the dry sliding coefficient. The surface of 1080 steel is shown in Figure 1.31. The Vascomax 300 surface was very similar. In previous research at AFIT, the asperities on the rail were of most interest so the Vascomax results were neglected. One of the three-dimensional FEMs used in the current research follows this reasoning as well.

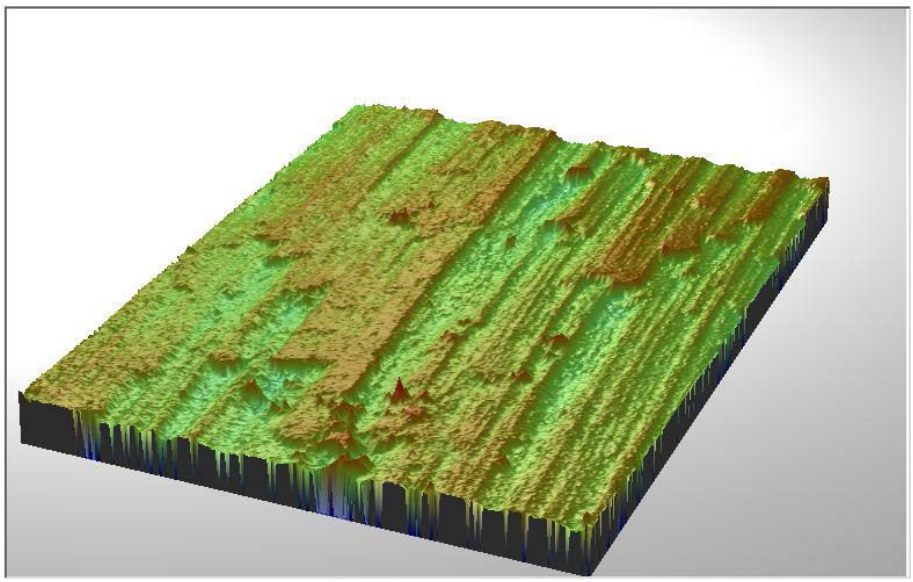

Figure 1.31: 3D View of AISI-1080 steel[19]

From Figure 1.31, the average asperity size, range of sizes and percentage of each size can be calculated as shown in Figure 1.32.

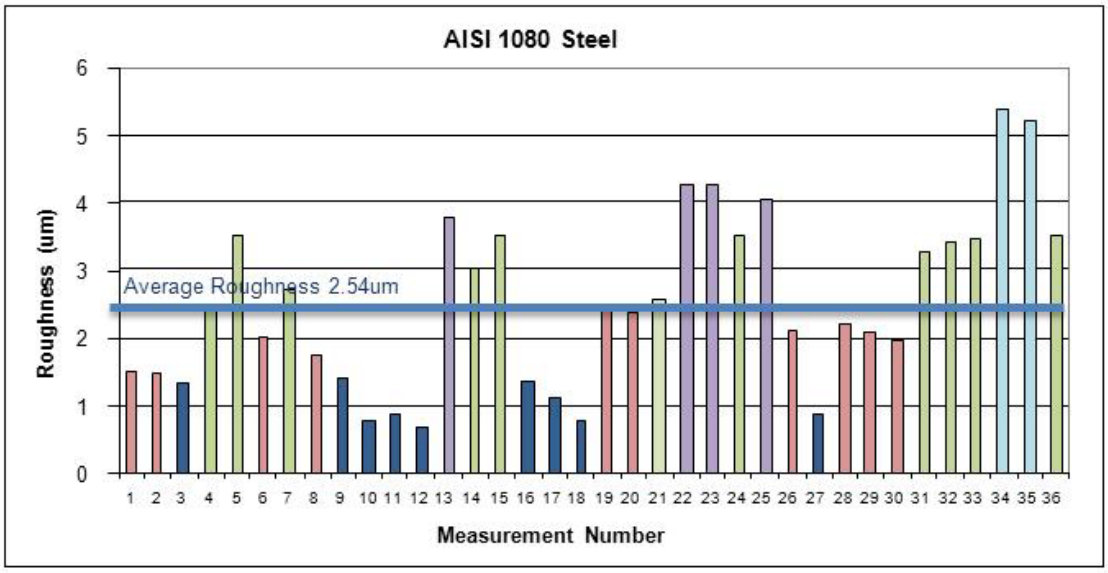

Figure 1.32: Surface Roughness of AISI-1080 Steel[20]

Buentello followed previous work by Cinnamon[7] and Polyzois [61] in using the Johnson-Cook plasticity model in a three-dimensional finite element model (FEM) undergoing high strain rates and large strains. The Mie-Gruneisen equation of state was chosen due to its

incorporation into ABAQUS and the high-velocity impact modeled. Following work done by ElTobgy [62] and Dean[63], the Johnson-Cook failure model was included. In 2005, M. S. El-Tobgy created a FEM to simulate erosion that occurs when a particle impacts a surface. Erosion can be used to erode material into a specified shape and is used in machining. An accurate model can be used as a substitute for actual tests of various materials reducing time and costs. In this case, a commercially available finite element solver was used.

ABAQUS/EXPLICIT[27] is the same program used for the micromechanical model in Buentello's research. In addition, this effort required the use of the Johnson-Cook plasticity model as well as the Johnson-Cook failure model. Failed elements could be deleted and then an eroded volume could be calculated.

> *The impacting-particle material simulated was a steel ball with a density of 7870 kg/m^3. In the finite element model, the impacting-particle material was modeled as a rigid body (stresses and strains are assumed to be zero in the impacting particle material.)*[62]

The results reportedly matched experimental results as well as analytical models. The particles that impacted the surface had relatively low momentum and thus caused relatively light damage. In contrast, the asperity in Buentello's research was attached to the rail model. This leads to relatively higher damage. Research done by Dean showed an ABAQUS model that also successfully modeled high-strain rates utilizing Johnson-Cook plasticity and failure models. The model showed elements departing from the model due to failure of surrounding elements. This occurs in the three-dimensional models used in other research. The failed and separated elements are tabulated as lost volume. In the current research, volume loss is considered wear. Buentello's model was the first to estimate the wear rate during the HHSTT scenario by measuring the volume of deleted elements from a high-speed impact and comparing the damage to the asperities sized from Voyiadjis work.

The initial temperature of the slipper model was imported from Le's work[17]. It was the calculated surface temperature of the slipper and it was selected at the various velocities of interest. This resulted in realistic looking damage to the slipper model as shown in Figure 1.33. In the same figure, it is shown how the number and size of the asperities as measured by Voyiadjis are used to calculate total wear. Buentello was conservative on many of his assumptions. The wear rate is dependent on the gap size, area of the slipper in contact with the rail, as well as the geometry of the asperity.

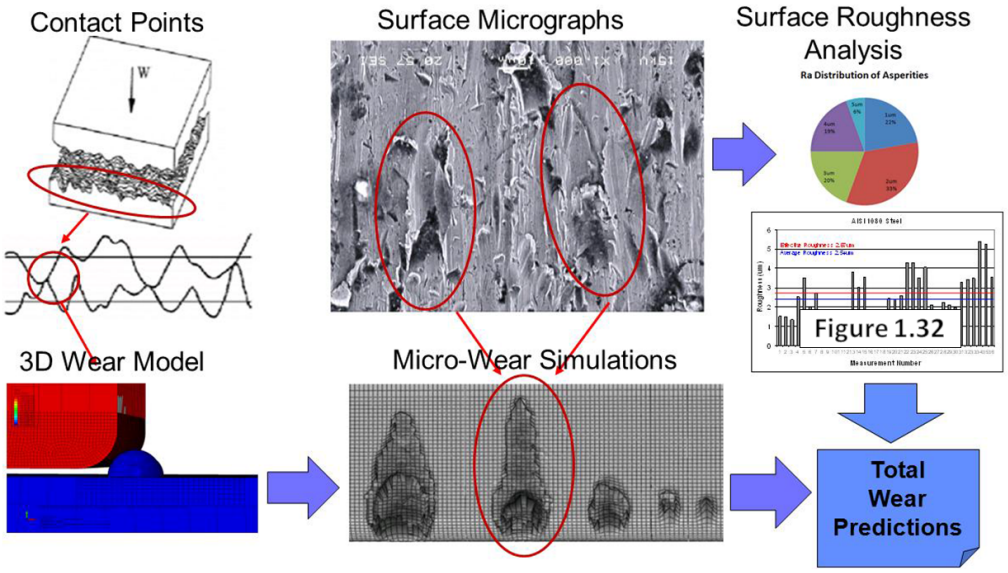

Figure 1.33: Modeling Wear[18]

Figure 1.33 shows the basic outline of how Buentello estimated wear for the sled run of 2008. The upper left portion of the figure purports to show the surface roughness of the slipper and the rail as shown by Voyiadjis [64]. This leads to the FEM with a gap and asperities as shown in the lower left. The FEM models the damage that occurs when the slipper impacts the asperities at 25 different velocities. By using a statistical distribution of asperities that occur on the surface of the rail, the total wear can be estimated. The wear calculation is shown in more detail in Section 3.2.2.4.

As part of the wear calculation, Buentello hypothesized that the slipper rotated during the test event. This was based on the wear pattern from the worn slipper as measured by

Hale. Figure 1.34 depicts several different slopes correlated to the measurements. Since the slipper experienced three rocket stages, it is reasonable to assume that the slipper rotated at each stage through accelerations.

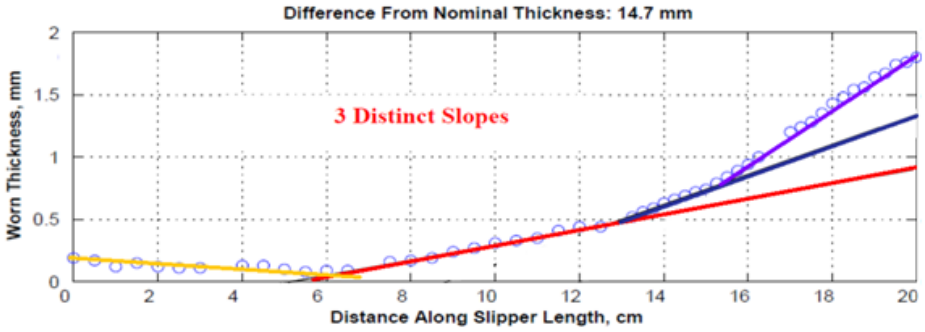

Figure 1.34: Slipper wear pattern[18]

Buentello stated that the accelerations caused the slipper to rotate changing the area of slipper contact with the rail. This hypothesis leads directly to the mechanical and melt wear estimations used in the present research. Buentello's model predicted approximately 30% more wear than measured.

In 2014, Cavallaro investigated asperity collisions at low speeds. Using a similar approach to Buentello's work, Cavallaro utilized a micromechanical scale model to obtain wear estimates based on damage from asperities colliding with a slipper model. Damage, due to asperity and slipper model collisions, was compared when varying gap spacing, mesh density, specific heat, and vertical velocity for two horizontal speeds 20 m/s and 40 m/s. The mesh densities are shown in Figure 1.35.

Part Instance	Coarse Mesh	Medium Mesh	Fine Mesh
Wedges	0.6 μm	0.5 μm	0.4 μm
Asperities	0.3 μm	0.3 μm	0.3 μm

Figure 1.35: Mesh Densities[21]

Figure 1.36 shows how Cavallaro remeshed the slipper model in an effort to keep the computation time at the same magnitude as utilized by Buentello. The figure on the left is of the slipper model as originally meshed by Buentello and the figure on the right is the slipper model as meshed by Cavallaro [21]. This was done as the slipper damage occurred over an extended slipper length at lower velocities, due to the asperity not being obliterated as quickly, as occurs at higher velocities investigated by Buentello.

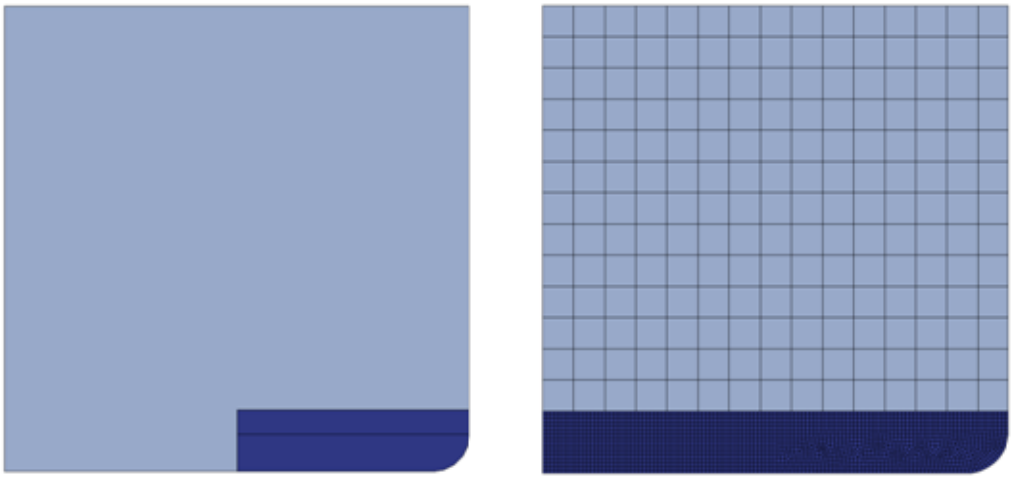

Figure 1.36: Remeshed Slipper model[21]

Research done by Cavallaro showed that the FEM was sensitive to the different aspects examined. The wear measured was dependent on vertical velocity as well as varying the specific heat versus keeping it constant as Buentello used [65]. Cavallaro also attempted to correlate the slipper rail wear scenario with the Lim and Ashby wear map. Figure 1.37 shows the result of the calculations. The calculations utilized the full underside of the slipper as the contact area. Chapter 3 will reexamine the Lim and Ashby wear map with respect to the 2008 test run.

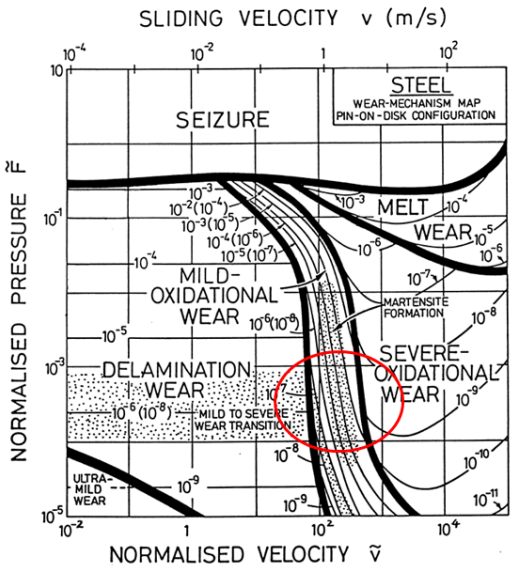

Figure 1.37: Lim Ashby Wear Map[21]

Alban considered aerodynamic forces acting on the slipper in 2014. When the slipper is in contact with the rail, conduction occurs. The shock at the front of the slipper affects the airflow across the top of the slipper as well. Alban's simplified model is shown in Figure 1.38. The aerodynamic loads affect the temperatures in the slipper. Previous research had neglected this effect.

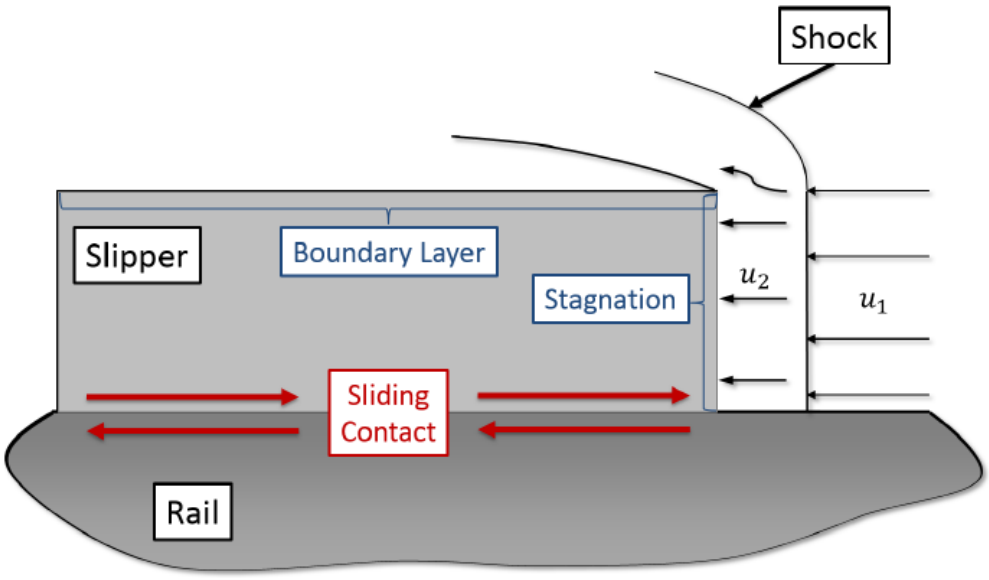

Figure 1.38: Contact[22]

By re-examining work done by Korkegi and Briggs[44] as well as Lofthouse[6], Alban was able to incorporate a boundary layer calculation to the gap between the bottom of the slipper and the rail. Figure 1.39 shows how the airflow in the gap transitions from a boundary layer to Couette flow. Alban's calculated convective heat flux was different from other work due to this more accurate simulation of what occurs as the slipper travels down the rail.

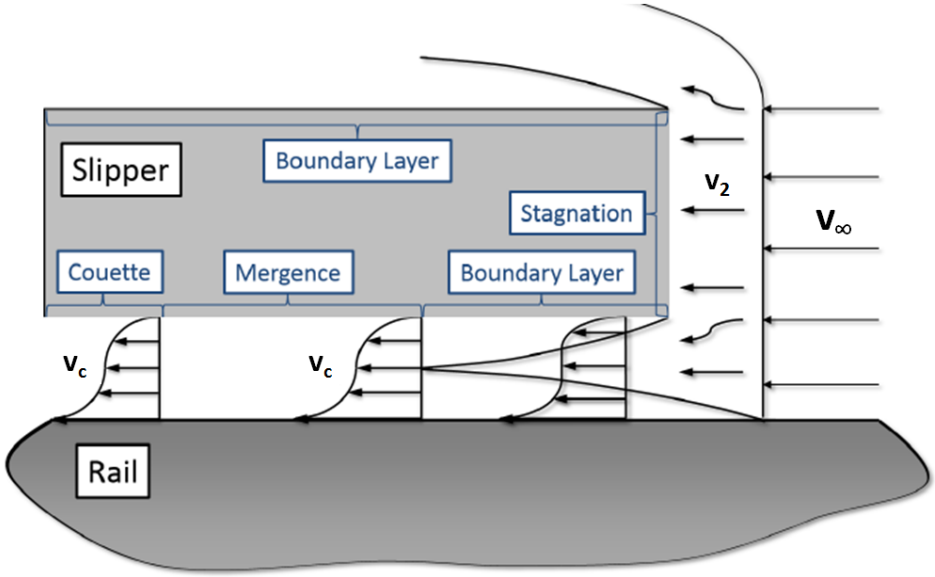

Figure 1.39: Bounce[22]

Alban took the results from the one-dimensional heat transfer analysis and applied the heat flux as boundary conditions of a two-dimensional FEM. Figure 1.40 shows the boundary conditions that reflect the slipper in contact with the slipper while Figure 1.41 shows the boundary conditions of a slipper bouncing above the rail.

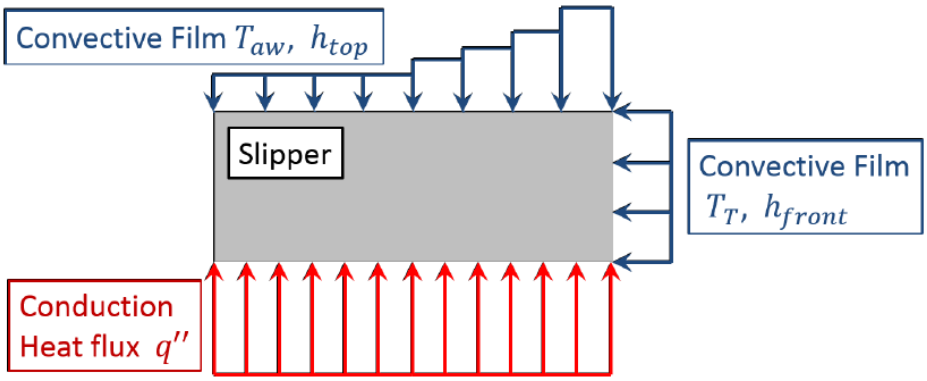

Figure 1.40: Contact Heat Flux and Boundary Condition Distribution.[22]

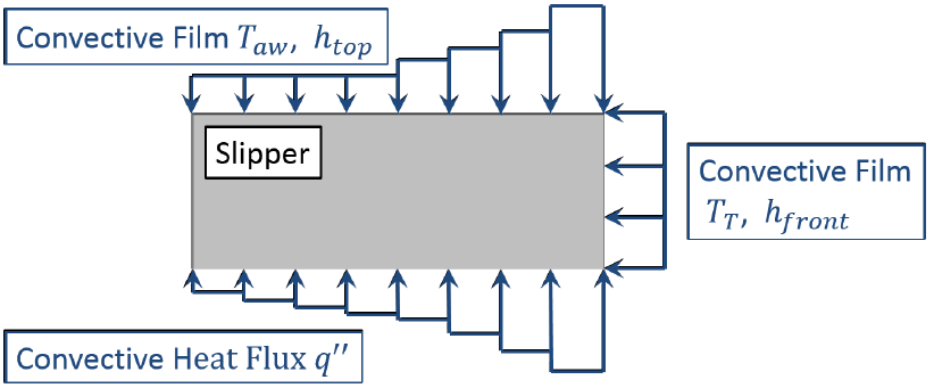

Figure 1.41: Bounce Heat Flux and Boundary Condition Distribution.[22]

Figure 1.42 shows the results of the two-dimensional FEM heat transfer analysis. This model shows through the thickness temperature distribution of the slipper at a previously unseen scale.

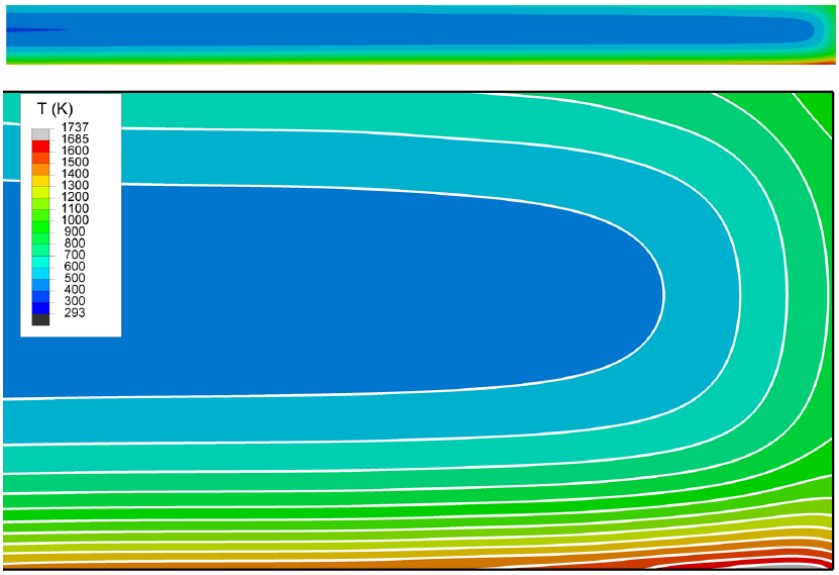

Figure 1.42: Top - Total Slipper Model Bottom - Slipper Leading Edge Temperature Distribution, t = 5.38 s.[23]

The temperatures calculate by the CFD analysis done by Lofthouse[6] are comparable to what Alban[22] calculates, ~ 860°F to ~ 840°F respectively. This lends confidence to Alban's aerodynamic estimates used in the heat transfer model as discussed in Section 2.4.4.

In 2016, Wuertemberger investigated a test at the HHSTT in 2014. That test was on a single rail as shown in Figure 1.43.

Figure 1.43: 2014 HHSTT monorail test setup.

Wuertemberger, tested the material that the slipper was constructed of (4130 steel). Following previous work by Cinnamon, Kennan and Borvik, Wuertemberger obtained Johnson-Cook parameters for both plasticity and failure [7][66][67][68]. Wuertemberger also investigated the micro-structure of the tested material in an attempt to correlate material grain structure changes with Johnson-Cook parameters [69].

1.4.3 Key Concepts from Previous Wear Research.

As shown, there has been a lot of previous work in high-speed impact and wear modeling. Both micromechancial and continuum mechanics scales have been investigated. This work increased the understanding in the phenomenon that occurs as two solid objects travel past each other at high speeds at elevated temperatures. The slipper wear, that occurs during a test at the HHSTT, is due to mechanical, thermal, and chemical changes. This research focused on the mechanical and thermal aspects that have been studied in recent research using different modeling scales and techniques. The microscale model used in this study was derived from Laird's microscale model developed to investigate gouging. It models material based on Johnson-Cook plasticity and failure models using coefficients developed by Cinnamon and Kennan. It uses an EOS to model high-speed impact as most previous research in this area has done to account for material shocks. The boundary conditions are based on previous work by Hale, Chmiel, Buentello, and others to incorporate DADS data into the model. The initial temperature was required and lead to the development of a one-dimensional heat transfer model developed and used previously by Hale, Paek-Spidell, Le, and Alban. They improved the model over time by incorporating DADS data, to estimate the frictional coefficient based on Montgomery's work, accounting for bounce and applying conduction or convection as appropriate, incorporating a melt depth estimate, validating the partition function, and providing a more accurate estimate for the aerodynamic heating between the slipper and the rail. All of these items were used

for this research. The theory behind the heat transfer model is discussed in Chapter 2 and the model details are discussed in Chapter 3.

In addition, the other FEM used was newly developed for this research at the millimeter scale and uses inputs from DADS as proposed by Huber to better correlate the mechanical wear with the 2008 test results in that they share approximate scales. It incorporates slipper measurement by Hale and Buentello's research to approximate slipper length in contact to better simulate the slipper and rail while in contact. This leads to further understanding of the wear environment at the slipper-rail interface. The FEM at the millimeter scale is discussed in Chapter 3.4. A comparison is made of the results in Chapter 4.

1.4.3.1 Considerations.

There are numerous factors that impact the slipper wear. Several of them are listed below. This list is not meant to be exhaustive but rather informative. The items marked red were investigated in this research.

Table 1.1: Considerations when modeling high speed wear.

∗ variable thermal properties	∗ acceleration	• deceleration
• vertical impact from bouncing	• rail coatings	∗ bouncing
• variable material properties	∗ shock waves	∗ asperity distribution
• hypersonic aerodynamics	• grain size	∗ rocket stages
• high temperature gas dynamics	∗ material model	• material dislocations
• mechanical and thermal coupling	• strain hardening	∗ contact modeling
∗ slipper length in contact	∗ heat partition	∗ material melt
∗ aerodynamic heating between slipper & rail	∗ scaling	• chemical (oxidation)
• aerodynamic heating at front of slipper	∗ diffusivity time	∗ diffusivity length
∗ equation of state requirement	∗ friction	∗ material failure model

1.5 Methodology Preview

Chapter 2 covers some of the more applicable development required for this research. This includes the Johnson-Cook plasticity model, Johnson-Cook failure model, Mie-Gruneison equation of state, shock wave considerations, contact formulation, inelastic heat fraction, as well as the one-dimensional heat transfer model development.

Chapter 3 discusses the three numerical models developed and utilized in this research. Section 3.2 discusses the three-dimensional FEM that simulates a slipper model colliding with an asperity at various velocities. The model is used to examine the equation of state as well as the contact algorithm used by the modeling software ABAQUS [27]. The FEM also explores different boundary conditions and initial conditions than previous research. Section 4.1 discusses the heat transfer model in depth. It discusses the MATLAB[39] code used for the finite difference scheme. It also includes the assumptions, inputs, initial conditions, boundary conditions, discretization, coding and outputs. Section 3.4 describes the three-dimensional FEM which uses friction as opposed to asperities as the interaction condition between the slipper and the rail. The mechanical wear is also approximated for the studied time increments.

Chapter 5 reviews the wear predictions from the three models used in this research. Conclusions are drawn from the methods incorporated and the results. Recommendations are made for further research in the area.

II. Background Theory

2.1 Chapter Overview

This research consisted of estimating the mechanical and melt wear experienced by a slipper during a test run at the HHSTT. In order to accomplish this, three models were developed with consideration given to the underlying physics of the problem. The theories that describe the phenomena, that was modeled, are contained in this chapter.

The research discussions on background theory are broken into three major sections. The upper right of Figure 2.1 shows the microscale FEM used to study contact, the equation of state, and the wear rate estimate. The material modeling that will be discussed is also displayed. The upper left, depicts the heat transfer model and the various considerations that were taken into account and that are discussed in the appropriate section. The bottom middle portion of the figure is a representation of the macroscale FEM that incorporates concepts from the other models shown.

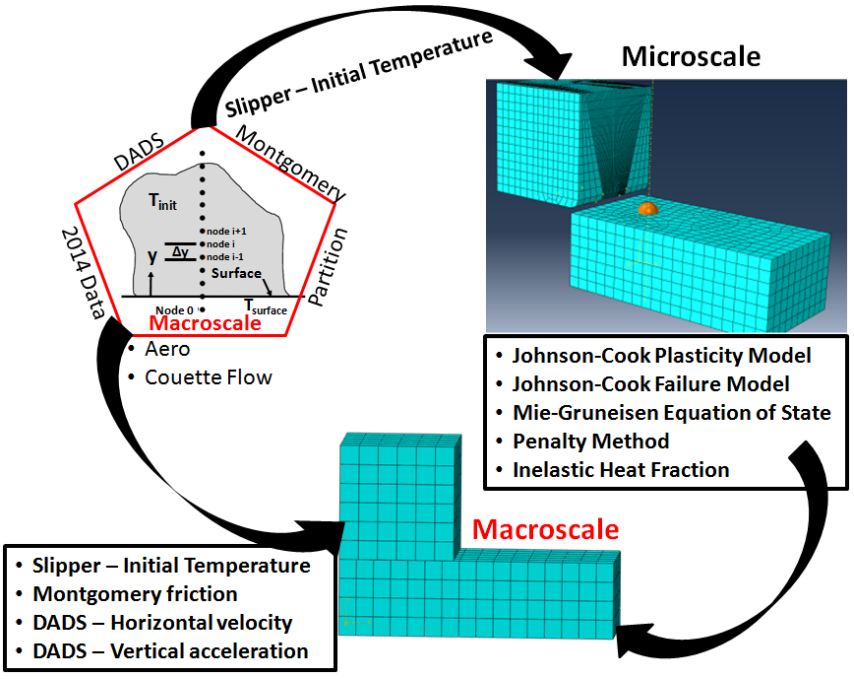

Figure 2.1: Three main sections of discussion

In the first section, the theories behind the microscale FEM are discussed. Modeling the HHSTT scenario at this scale entails a portion of the slipper impacting an asperity model at high velocity. Consideration is given to ensure that the resulting shock wave was properly understood, and its results taken into consideration. The requirement for an EOS arises out of those consequences as the conservation of energy equation must be further developed to account for the discontinuity that a shock wave represents. In addition, the nature of the impact also required a constitutive model that could model the large strain and high strain rates that occurred. A material failure model was also included as failed elements were the method of estimating wear, a central focus of this research. The plastic deformation leads to heat generation in the model so that is also addressed. The two objects collide and a method is presented that ensured that the models interpenetration was at a minimum.

The next section discusses the heat transfer model, which used a finite difference scheme to solve the heat equation in one-dimension through the thickness of the slipper. The heat equation was derived as the specific heat and thermal conductivity contained therein were taken as variables dependent on temperature in this research. The required boundary conditions and initial condition required to solve the heat equation are discussed as well. The Runge-Kutta based solver used to solve the heat equation is also described. As mentioned, the specific heat and thermal conductivity, for the material under study (Vascomax 300), are dependent on temperature. The dependence is shown along with a discussion on the reasons for the material's thermal behavior. The energy input to this model was in the form of conduction and convection. The background on their estimation is discussed to include friction. Finally, the heat flux was partitioned into the slipper and the rail. The function used to accomplish this is also discussed.

The final section concerns the summation of the previous sections. It describes a three-dimensional FEM at a larger scale than the previous microscale FEM described. The spatial scale was on the order of millimeters to meters and temporal scale was on the order of 10^{-2}

seconds. This model incorporated the material modeling from the previously discussed FEM. However, it did not model impact. The model incorporated the coefficient of friction method from the heat transfer model. This included the variable slipper geometry.

As stated, this study is one of high temperatures, high strain rates, and continuously varying loads. The models were used to estimate the amount of mechanical and melt wear that occurred due to the slipper-rail interaction.

2.2 Microscale Modeling

2.2.1 Introduction.

The microscale model was developed to investigate the deformation that occurs due to high speed impact. The spatial scale was on the order of μm and the temporal scale was on the order of 10^{-6} seconds. The resulting deformation is viscoplastic in nature and includes shock wave phenomenon. This necessitates the use of an appropriate constitutive model and an equation of state. The equation of state is useful as a shock creates a major discontinuity and this phenomenon occurs as asperity collisions at high strain rates are modeled. A simple one-dimensional set of equations are presented that include the equation of state, and the Hugoniot expression based on the development by Meyer [25]. A plane strain representation was developed by Huber [60] and is described as well.

It is recognized that large displacement is required in this work and this will be handled using the explicit numerics in ABAQUS [27], and that the equations utilized will be associated with incrementation. In addition, material modeling will include the Johnson and Cook plasticity model [48] as well as the Johnson and Cook Failure model [49]. Also, since the FEM of the slipper and asperity models the interaction during impact, the contact algorithm was investigated and is included. Finally, the material undergoes deformation due to the high velocity impact leading to energy transfer. A portion of this energy becomes heat and this is also discussed.

2.2.2 Finite Element Model.

In this section, the relevant theory used in the microscale model is discussed. Several equations are required, to model the slipper-asperity impact, to include the conservation equations, the equation of state, and the constitutive equations. In addition, when modeling high speed impacts, the results can have large deformations. Lagrangian based codes can have trouble converging due to severe mesh distortion. That is not a concern in this research as element failure, damage evolution, and element deletion was used. This necessitated the use of a material failure model. An additional item considered was the slipper and asperity interaction during contact. This FEM makes use of the penalty method which results in a realistic material response. Finally, material deformation led to temperature increase. The model incorporated an inelastic heat fraction as the method of converting a portion of the plastic deformation into heat.

2.2.3 Material Modeling.

2.2.3.1 Shock Wave Considerations.

For completeness, discussion of the shock development is presented based on the simplified 1-D relations given by Myers [25]. When modeling high-speed collisions such as an asperity model colliding with the slipper model, a shock wave occurs. A shock wave dissipates energy when the material transport velocities exceed respective acoustic wave propagation velocities [24]. The FEM used in this research was based on Lagrangian mesh. Thus, the mesh deforms with the material. This limits the degree of deformation that can occur. Shock waves have rapidly changing properties with possibly large deformations making Lagrangian methods less than ideal in accurately describing them. Eulerian based hydrocodes have been used to a much greater extent while studying shock wave phenomenon [38][4][7][25]. Shock wave profiles describe the temporal history of the mechanical and thermal state at a material point [70]. Work done with flyer plates by Cinnamon [71] will be discussed in further detail in Chapter 3. Also of note, shock waves

have been successfully modeled in metals using three-dimensional Arbitrary-Lagrange-Eulerian (ALE3D) [72]. ALE3D is a finite element formulation that can move to account for large deformation but still track boundaries [73]. Hydrocodes with experimentally validated constitutive models have also been successful in modeling shock wave behavior [74]. These methods were not utilized for this research due to the ease of calculating wear using ABAQUS element deletion feature, incorporation of Johnson-Cook models and EOS, as well as its robust contact feature.

2.2.3.2 Rankine-Hugoniot Equations.

A 1-D shock wave is representative of plane waves. Davis derived the Rankine-Hugoniot equations from a simplified example that accounts for the mass, momentum, and energy balances in front of and behind the shock wave [75]. Figure 2.2 is a schematic representation of the shock wave as it moves through a material.

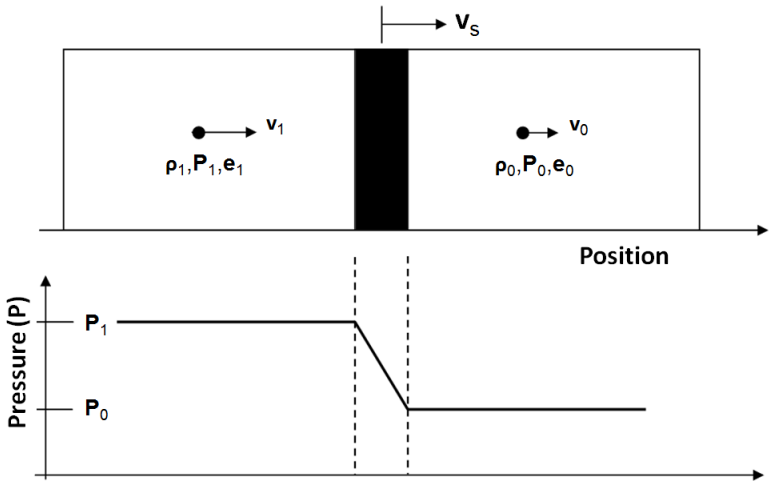

Figure 2.2: Shock wave propagation schematic representation).[24]

v_s - shock wave velocity

ρ_0 - density behind shock wave

ρ_1 - density in front of shock wave

P_0 - pressure in front of shock wave

P_1 - pressure behind shock wave

e_0 - specific internal energy in front of shock wave

e_1 - specific internal energy behind shock wave

v_0 - particle velocity in front of shock wave

v_1 - particle velocity behind shock wave

A - Area

dt - increment of time

The indices indicate the states in front and behind the shock wave which propagates at a velocity designated v_s. Balancing the mass flow into and out of the shock front provides the following representation. The density, ρ, represents the material mass per volume. The difference between the shock front velocity, v_s, and the particle velocity v_1 and v_0 are not the same leading to a change in density.

$$\rho_1(v_s - v_1) = \rho_0(v_s - v_0) \tag{2.1}$$

Now, accounting for the momentum flow into and out of the shock results in the following equation. This equation shows that the pressure difference in front of and behind the shock must equal the momentum change from the shock wave.

$$P_1 - P_0 = \rho_0(v_s - v_0)(v_1 - v_0) \tag{2.2}$$

The work done by P_1 minus the work done by P_0 is shown in Equation 2.3.

$$\Delta W = \underbrace{(P_1 A)}_{\text{force}} \underbrace{(v_1 dt)}_{\text{distance}} - \underbrace{(P_0 A)}_{\text{force}} \underbrace{(v_0 dt)}_{\text{distance}} \tag{2.3}$$

The difference in total energy is the kinetic energy and internal energy (per unit mass) equal to the final energy minus the initial energy [25] as shown in Equation 2.4.

$$\Delta e = \frac{1}{2}[\rho A(v_s - v_1)dt]v_1^2 + e_1 A\rho(v_s - v_1)dt - \left(\frac{1}{2}[\rho_0 A(v_s - v_0)dt]v_0^2 + e_0 A\rho_0(v_s - v_0)dt\right) \tag{2.4}$$

The balancing of energy in the system means that the external work must equal the change in internal energy plus the change in kinetic energy as shown in Equation 2.5 with $v_0 = 0$.

$$P_1 v_1 = \frac{1}{2}\rho(v_s - v_1)v_1^2 - e_0\rho_0 v_s + e_1\rho(v_s - v_1) \tag{2.5}$$

Meyers [25] substituted Equations 2.1 and 2.2 into Equation 2.5 and the result is below.

$$e_1 - e_0 = \frac{1}{2}(P_1 + P_0)\left(\frac{1}{\rho_0} - \frac{1}{\rho_1}\right) \tag{2.6}$$

These three equations are not sufficient to account for the four variables that describe the material state. An equation of state is the additional equation required. The EOS describes the dependency between the pressure, density, and internal energy of a material. The EOS used in this research is further discussed in Section 2.2.3.4.

2.2.3.3 Rankine-Hugoniot Curves.

A strong shock is defined by Myers as an event in which the pressure exceeds 10 GPa [25]. Equation 2.6 provides a pressure-density relationship that can be shown in graphical form. The inverse of density $\frac{1}{\rho}$ is designated as the specific volume v.

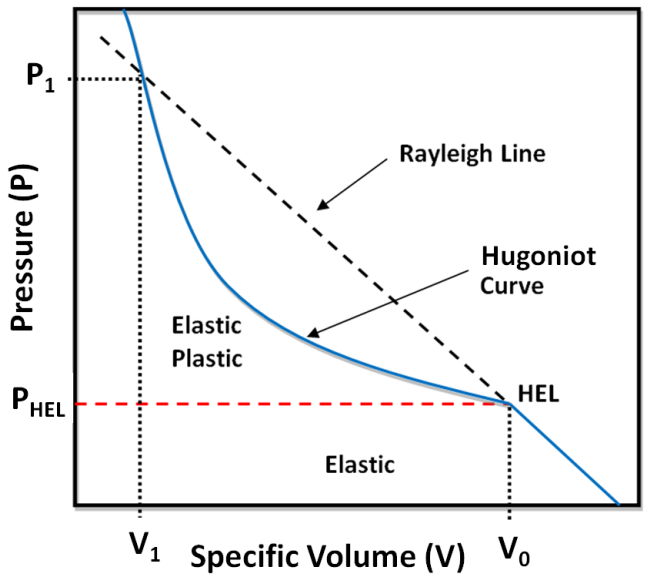

Figure 2.3: Characteristic Hugoniot (P-V) curve.[25]

Figure 2.3 displays the P-V curve. The Hugoniot is defined as the locus of all the shocked states of the material. It defines all states that can be reached from a specific starting state. The Rayleigh line refers to the shock state at P_1. There is a discontinuity in pressure and density when a shock is present [25].

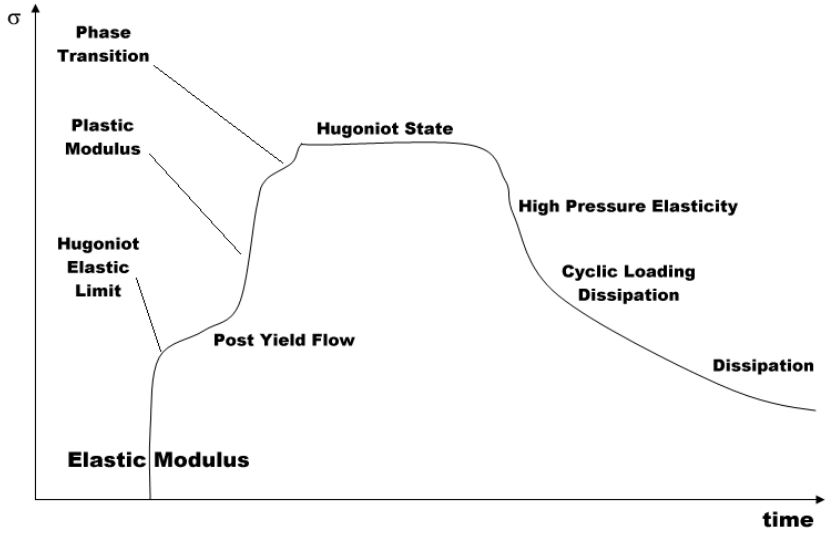

Figure 2.4: Realistic shock wave profile.[26]

Figure 2.4 shows a realistic shock profile that includes the Hugoniot Elastic Limit. The HEL for the uniaxial stress case was estimated by Meyer to be equal to $\frac{4}{3}$ times the yield stress in shear added to the pressure [25].

$$\sigma_y = P + \frac{4}{3}\tau_y \tag{2.7}$$

Huber developed the equivalent HEL for the plane strain case [60]. The equation is shown below.

$$\sigma_{HEL} = \sigma_Y \left[\frac{3}{8 - 16\nu} + \frac{1}{2} \right] \tag{2.8}$$

σ_Y - yield stress for a uniaxial elastic - perfectly plastic material.

Cinnamon's work investigated the HEL for Vascomax 300 and 1080 steel. This will be discussed further in Chapter 4.

2.2.3.4 Equation of State.

In this research, the microscale model used was focused on asperity collisions at speeds on the order of 1000 m/s. As such, it is important to establish the actual equation of state used. A shock wave is defined by Myers "as a discontinuity in pressure, temperature, and density" [25]. As previously discussed the three conservation equations, as presented, are not sufficient to describe the state of a material experiencing a shock wave propagation. An EOS is also required. This equation is usually obtained through experiments to provide the relationship of pressure, density, and temperature.

As the thermal environment interacts with the mechanical relations in which a major discontinuity of each of the previous relations occurs, it becomes necessary that state variables become associated with each other. The state variables characterize the system at the macroscopic level. This leads to a relationship tying the mass and temperature together in a formation that associates itself with the stress field. The equation that does this is referred to as the EOS. The next series of equations attempts to do this for a simple one-dimensional formulation.

One of the more commonly used equations of state for ballistic impact problems is the Mie-Gruneison equation of state. It utilizes statistical mechanics to account for the energy at the atomic level and arrives at expressions suitable for thermodynamic analysis. The conservation of energy is made of two parts, the first is the 1st Law of Thermodynamics while the 2nd Law of Thermodynamics considers entropy. Equation 2.9 is the mathematical definition of Helmholtz free energy, per unit volume. The Helmholtz free energy is a measure of the amount of energy put in, to create a system once the spontaneous energy transfer to the system from the environment is accounted for.

$$A_H \equiv e - TS \tag{2.9}$$

where,

A_H - Helmholtz free energy

e - internal energy of the system

T - absolute temperature (kelvins) of the surroundings

S - entropy of the system

By taking the differential of the Helmholtz free energy with respect to volume while holding the temperature constant (adiabatic), pressure is obtained as shown in Equation 2.10.

$$P = \left(\frac{\partial A_H}{\partial \mathrm{V}}\right)_T \tag{2.10}$$

This provides an appropriate thermodynamic relationship between pressure and volume. A 1-D development is shown as an example and follows Meyers [25]. The Mie-Gruneisen equation of state 2.11 is shown below.

$$P - P_H = \Gamma\rho(e - e_H) \tag{2.11}$$

P - pressure

P_H - Hugoniot pressure

Γ - Gruneisen ratio

ρ - density

e - internal energy

e_H - Hugoniot specific energy, is the internal energy per unit mass on the Hugoniot

The Gruneisen ratio is defined by:

$$\Gamma = \Gamma_0 \frac{\rho_r}{\rho} \tag{2.12}$$

Γ_0 - material property

ρ_r reference density

The Hugoniot specific energy is defined by:

$$e_H = P_H \frac{\eta}{2\rho_r} \tag{2.13}$$

η - nominal compressive strain

The nominal compressive strain is given as:

$$\eta = 1 - \frac{\rho_r}{\rho} \tag{2.14}$$

The Hugoniot pressure is:

$$P_H = \frac{\rho_r c_0^2 \eta}{(1 - s_H \eta)^2} \tag{2.15}$$

c_0 - reference speed of sound in the material

s_H - $\frac{d\mathrm{v}_s}{d\mathrm{v}_P}$ linear Hugoniot slope coefficient

$$\mathrm{v}_s = c_0 + s_H \mathrm{v}_P \tag{2.16}$$

Equation 2.16 shows a linear relationship between the shock velocity to the particle velocity. They are related by the c_0 and s_H which are material properties.

As stated the connection between statistical mechanics and thermodynamics relies on the Helmholtz free energy and an adiabatic assumption. This is discussed in Section 2.2.3.8.

The Mie-Gruneisen EOS has shown good results with respect to the slipper asperity collision scenario. Vanderhyde did show that it was not as reliable as other EOS when phase changes were involved [76]. The very short time scales modeled may reduce the errors involved though.

Part of this study includes analyzing the behavior of a shock wave as it passes through the microscale slipper model upon impact with an asperity sized collider. At the high velocities investigated the model approximates a plane strain scenario.

2.2.3.5 ViscoPlasticity.

The slipper-rail interaction is complex and modeling the material requires an understanding of the underlying behavior. Viscoplasticity describes the rate-dependent inelastic behavior of the material. In the determination of mechanical wear, through the microscale model (μm and 10^{-6} sec), the strains and strain rates are of importance and hence the need to model this behavior as accurately as possible is necessary while keeping in mind that the focus is on wear. This means that the material response is important until failure is reached after which the state of the material becomes irrelevant to the simulation. The material modeled undergoes elastic deformation leading up to plastic deformation dependent on varying rates of loading. The temperature plays an important role as well. The temperatures associated with the slipper-rail interaction reach melt temperatures and thus material softening does occur.

The material model requires a relation between the stress and strains to reflect the behavior as it undergoes these variable loads. The constitutive equation must reflect experimental facts that are pertinent to the system being modeled and also be simple enough to enable prediction of certain behavior that can be confirmed [77].

2.2.3.6 Johnson-Cook Model.

Since this work deals with a dynamic problem with large strains, high strain rates, and high temperatures, it requires a constitutive model that can deal with rate-dependent plasticity. The deviatoric stress state drives plastic flow as opposed to the hydrostatic stress state which strongly influences damage prediction. There is a phenomenological viscoplasticity model that was used that accounts for the strain hardening seen in the material of interest, mainly high strength metals. It is the true stress-strain curve incorporated in the σ_{ij} vs.ε_{ij} constitutive equations. The Johnson-Cook plasticity model, developed in 1983 [48], assumed decoupling of strain hardening, strain rate, and temperature effects. In reality, these influences are coupled which limits the area of

applicability [78]. The equation incorporates the Von Mises yield criterion into the plastic relation. It is popular due to the relative ease that the coefficients can be determined. This model can be used for various materials. It is suitable for high-strain rate deformation and adiabatic transient dynamic simulations [27].

$$\overline{\sigma}_y = \left[A_y + B(\overline{\varepsilon}_p)^n\right]\left[1 + Cln\left(\frac{\dot{\overline{\varepsilon}}_p}{\dot{\overline{\varepsilon}}_0}\right)\right]\left[1 - \left(\frac{T - T_0}{T_m - T_0}\right)^{m_{JC}}\right] \tag{2.17}$$

$\overline{\sigma}_y$ - static yield stress

$\overline{\varepsilon}_p$ - equivalent plastic strain

$\dot{\overline{\varepsilon}}_p$ - equivalent plastic strain rate

$\dot{\overline{\varepsilon}}_0$ - reference strain rate

T - current temperature

T_m - melt temperature

T_0 - transition temperature

A_y - initial yield stress

B - hardening modulus

C - strain rate dependent coefficient

n - work hardening exponent

m_{JC} - thermal softening coefficient

The first bracket captures the accumulated plastic strain behavior, termed strain hardening. The second bracket describes the effect of the strain rate. The last bracket includes the non-dimensional temperature i.e. homologous temperature, and its softening effect on the yield stress. These three behaviors are quantified by using Split-Hopkinson bar tests at various temperatures and strain rates, then curve fitting the data points to determine the coefficients. Previously, both Cinnamon[7] and Keenan[66] obtained coefficients for the material commonly used to construct slipper, Vascomax 300. The worn slipper recovered after the test in 2008 was constructed of this same material.

2.2.3.7 Material Failure.

Since this work is primarily interested in measuring wear, a way must be used to account for it in the three dimensional FEM. As developed by Buentello [18] and discussed in 3.2.2.4, the method used, measures the volume of failed elements after the slipper collides with an asperity. As the slipper impacts the asperity, the stresses in both bodies rapidly exceed the materials yield strength and enter the plastic zone of deformation. As discussed, the Johnson-Cook plasticity model accounts for the strain hardening that occurs in ductile materials. However, the material fails or fractures at a certain point. Various fracture models attempt to model material behavior at failure. In previous work, it has been shown that the Johnson-Cook failure model can be used to model progressive failure of material [79] and to model erosive wear by ElTobgy [62].

The Johnson-Cook failure model was developed in 1985[49]. It is based on the assumption that failure occurs due to the initiation, growth, and coalescence of micro-cracks/voids at the center of a specimen[49]. Once all the internal failures have been accumulated the damage evolution begins. The failure point i.e. damage initiation is shown as C in Figure 2.5.

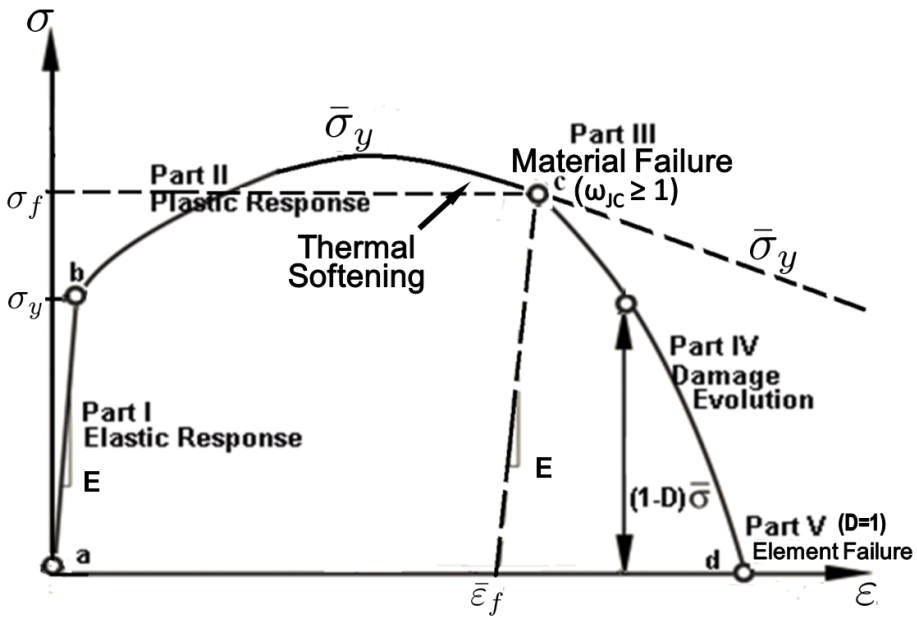

Figure 2.5: Stress-Strain Curve for typical metals

$$\overline{\varepsilon}_f = \left[d_1 + d_2 exp\left(d_3 \frac{P_{hyd}}{q_{vm}}\right)\right]\left[1 + d_4 ln\left(\frac{\dot{\overline{\varepsilon}}_p}{\dot{\overline{\varepsilon}}_0}\right)\right]\left[1 + d_5\left(\frac{T - T_0}{T_m - T_0}\right)\right] \tag{2.18}$$

σ - stress

ε - strain

σ_f - stress at failure

$\overline{\varepsilon}_f$ - strain at failure

$\dot{\overline{\varepsilon}}_p$ - plastic strain rate

$\dot{\overline{\varepsilon}}_0$ - reference strain rate

T - current temperature

T_m - melt temperature

T_0 - transition temperature

P_{hyd} - hydrostatic pressure

q_{vm} - Von Mises stress

d_1 - d_5 - fracture constants

The first set of brackets weighs the fracture strain as a function of the triaxiality. It reflects the observation that strain to fracture decreases as hydrostatic tension increases. The triaxiality term, P_{hyd}/q_{vm}, is the hydrostatic tensile stress based on the true Cauchy stress. It is the hydrostatic pressure divided by the Von Mises stress. The second set of brackets changes the material ductility based on the strain rate. The last bracket is the effects of a scaled temperature, termed homologous temperature, on the material softening. In the past, a FEM was constructed of a specimen to simulate the tensile test since there is no physical means to measure these values internal to the specimen during a test. Recently there have been attempts to calculate these values by using quasi-static tests with seemingly good results as seen in [67] and [68]. This model was used in the Buentello model [18]

and was used in this research. The model predicts that failure occurs when the damage parameter $\omega_{JC} \geq 1$. Johnson-Cook defined ω_{JC} in terms of the equivalent plastic strain as:

$$\omega_{JC} = \sum \frac{\Delta \bar{\varepsilon}_p}{\bar{\varepsilon}_f} \tag{2.19}$$

Where $\Delta \varepsilon_p$ is the increment of the equivalent plastic strain evaluated at each time step. Once this occurs the damage evolution process begins as mentioned. The effective plastic displacement is used instead of plastic strain. The softening response after damage initiation is characterized by a stress-displacement response rather than a stress-strain response to reduce mesh dependency. This is based on work by Hillerborg [80]. The ABAQUS implementation is as follows.

Before $\omega_{JC} \leq 1$

$$\dot{\bar{u}}_p = 0 \tag{2.20}$$

after $\omega = 1$

$$\dot{\bar{u}}_p = \mathrm{L}\dot{\bar{\varepsilon}}_p \tag{2.21}$$

L - characteristic length, dependent on element type and size

This is used in the linear damage evolution by using equation:

$$\dot{D} = \frac{\mathrm{L}\dot{\bar{\varepsilon}}_p}{\bar{u}_p^f} = \frac{\dot{\bar{u}}_p}{\bar{u}_p^f} \tag{2.22}$$

$\bar{u}_p^f$ - user specified effective plastic displacement

The resistance to stress decreases over time as an instant reduction i.e. $\bar{u}_p^f = 0$, would cause numerical instabilities [27]. The deletion criteria used in this study was based on associating the strain magnitude with the deformed element size [81].

2.2.3.8 Heat Generation.

The FEMs used in this research have internal energy sources. However, there is an adiabatic assumption that was used. This assumption ensures that there is no heat transfer

into or out of the system. The internal energy, U, of the system is then defined as the adiabatic work. This is the work done on the system, using an adiabatic process, which takes the system to a different state [82].

In the previous sections, it was shown that the material behavior is temperature dependent. The modeling of the temperature rise in the FEMs was an important component of this research. As two metallic surfaces slide past each other at high velocities, friction results in high temperatures. This process was captured in the heat transfer model and the combined model discussed further below. The temperature rise was captured in the asperity collision model based on material deformation. The inelastic strain energy due to the material deformation was converted into thermal energy [81]. This assumed an adiabatic process. This type of analysis is typically used when large amounts of inelastic strain are involved and where the heating of the material caused by its deformation is an important effect on the material model [27]. The adiabatic assumption was reasonable based on the time the model simulates slipper asperity collision (10^{-7} seconds) versus the time required for heat conduction to take place. The heat flux per unit volume, r^{pl}, is calculated by ABAQUS using the following formulation [27]:

$$r^{pl} = \eta_{hf}\sigma_{VM} : \dot{\bar{\varepsilon}}_p \tag{2.23}$$

η_{hf} - user-specified inelastic heat fraction

$\dot{\bar{\varepsilon}}_p$ - plastic strain rate

σ_{VM} - Mises stress

The change in temperature is dependent on the material density ρ and specific heat C_p as shown below [27]:

$$\Delta T \rho C_p(T) = r^{pl} \tag{2.24}$$

The equations are solved at each integration step. The calculated temperature is an input into the material modeling as thermal softening does occur as shown in Figure 2.5.

2.2.4 Contact.

2.2.4.1 Background.

In this study, the slipper model impacted the asperity model as a method to estimate wear. Thus, the interaction between the two was important to understand. ABAQUS [27] contains a robust contact algorithm that has proven to give realistic results over a wide variety of interaction scenarios. In multi-body problems, the modeled bodies must not interpenetrate. As stated, this FEM simulates a high velocity impact between the slipper and an asperity. The surface interpenetration was kept to as minimal as practical. This lead to the rise in stress and strain that was central to modeling mechanical wear.

There are two different methods of contact constraint enforcement used in ABAQUS Explicit [27]. The kinematic contact algorithm and the penalty method. The penalty method was the constraint enforcement method used in this research. It was better suited for the scenario modeled as described below.

2.2.4.2 Penalty Method.

The general contact algorithm includes the penalty method to enforce contact constraints. The penalty contact algorithm has a weaker enforcement of contact constraints but allows for treatment of more general types of contact [27]. The penalty method does impact the stable time step size. ABAQUS/Explicit does adjust the time step size as necessary to ensure numerical stability. Figure 2.6 illustrates the basic concept. As in the kinematic contact constrain enforcement, there is a pure master-slave version as well as the balanced master-slave version.

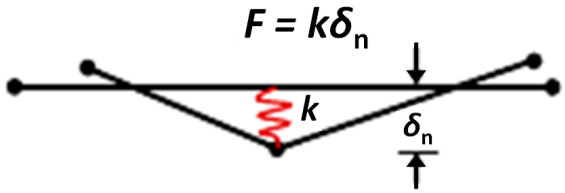

Figure 2.6: Schematic of the Penalty Method.[18]

F - force

k - spring stiffness

δ_n - nodal encroachment distance

When the penalty contact algorithm encounters slave node penetrations, forces calculated based on the penetration distance are applied to the slave nodes in opposition to the penetration. Equal and opposite forces are imposed on the master surface at the penetration point. The master surface contact forces are distributed to the nodes of the master surfaces being penetrated. For the pure master-slave penalty algorithm, there is no resistance to master surface nodes penetrating slave surface. Refining the mesh of the slave surface reduces this issue [27].

The second penalty method formulation is the balanced master-slave contact. This computes the average of the contact forces calculated as described above for the master and the slave. ABAQUS/Explicit then applies a weight to the two values. The weighting used with each set of forces depends on the weighting factor specified but defaults to an equal weight for each surface.

The 'spring' shown in Figure 2.6 has a stiffness which can be scaled. This reduces the penetration distance that the nodes can travel. However it will significantly impact the computational time as the time step size is significantly reduced as shown in Figure 2.7

Penalty scale factor	Lower bound to ratio of the time increment with contact divided by the time increment without contact
1.0	0.96
10.0	0.34
100.0	0.13
1000.0	0.04
10000.0	0.013

Figure 2.7: Effect of time scale on time increment.[27]

ABAQUS balances CPU time vs penetration. Increasing the Penalty Stiffness affects accuracy. Increasing Mesh density reduces surface crossing while increasing cpu time.

2.2.4.3 Contact Summary.

In addition to previous concern regarding energy and external work, another factor that indicates the use of the penalty method in this work is that element based rigid surface can only act as master surfaces within the kinematic algorithm. This work includes the slipper model and the asperity model both of which are element based rigid surfaces. The penalty method also includes numerical 'softening' which acts to eliminate the energy loss from collision seen in the kinematic algorithm. These differences resulted in the penalty method being used in this research.

In the impact scenario that this research is based on, the penalty enforcement of contact conditions provides the loadings on the respective surfaces that act as inputs into the material modeling as described previously. These loads lead to possible element failure. In this case, the eroded surface gives way to a new topology as seen in Figure 2.8.

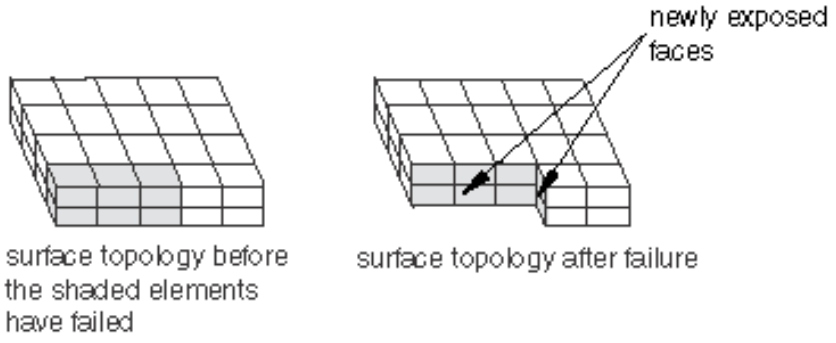

Figure 2.8: Topology of an eroding contact surface.[27]

The newly exposed surfaces interact with other surfaces using the same penalty enforcement technique without the need to re-designate master-slave surfaces. This is ideal as the mechanical wear estimate is based on elements deleted during the entire simulation and not just the elements at the surface.

2.3 Scaling Discussion

The first model considered a collision between a slipper and an asperity. This model has certain limitations as will be pointed out in the subsequent chapter on results and discussion. A consideration is now going to be presented in which it is assumed that wear is only a by-product of material melt due primarily to the sliding of the slipper with respect to the rail. This event is represented by the Heat Transfer model, at the continuum mechanics scale as described in Figure 2.9. The figure is used by material researchers to ensure that appropriate considerations are taken into account for the scale modeled. Grain structure and dislocations become very important at length scales of 10^{-7} and less and time scales on the order of 10^{-9} and less.

Unit	Length scale	Timescale	Mechanics
Complex structure	10^{3} m	10^{6} s	Structural mechanics
Simple structure	10^{1} m	10^{3} s	Fracture mechanics
Component	10^{-1} m	10^{0} s	Continuum mechanics
Grain microstructure	10^{-3} m	10^{-3} s	Crystal plasticity
Dislocation microstructure	10^{-5} m	10^{-6} s	Micromechanics
Single dislocation	10^{-7} m	10^{-9} s	Dislocation dynamics
Atomic	10^{-9} m	10^{-12} s	Molecular dynamics
Electron orbitals	10^{-11} m	10^{-15} s	Quantum mechanics

Figure 2.9: Length and Time scales in materials [28][29]

2.4 Macroscale Modeling

2.4.1 One-Dimensional Heat Transfer Model.

2.4.1.1 Background.

As previously discussed, the slipper-rail interaction occurs in an elevated thermal environment. The temperature rises due to the heat flux arising from friction, as the slipper slides across the rail, and/or aerodynamic heating, as the air flows into the gap between the slipper and rail during bouncing. Both the FEMs utilized in this study require an initial

temperature to properly account for the slipper history as these models can only simulate fractions of the test run. The 2008 test had an acceleration phase that lasted approximately 5 seconds. This would require enormous computational resources to model using only a FEM.

In order to estimate the slipper surface temperature as it evolves during acceleration, a simulation of the entire test run was required. Past researchers in this area have recognized this problem and have turned to heat transfer models in an attempt to account for the slipper history from a thermal perspective. A one-dimensional model was used to estimate the surface temperature of the slipper for the entire test run. The model simulated the test using heat transfer and the reduced complexity allowed a solution in a relatively short amount of time. Previously, Paek [15] derived the one-dimensional heat equation and the algorithm to obtain the solution for each time step of interest. However, one of the major contributions of this study was to account for varying material properties. It is with that in mind that the derivation follows in the next sections.

It is important to note that this work included estimating the aerodynamics between the slipper and the rail. This did not include taking hypersonic aerodynamics or high temperature gas dynamics into account. A higher fidelity accounting of the aerodynamics could have a significant impact on the model results especially at higher velocities.

2.4.1.2 Objective.

This research takes a one-dimensional heat transfer model and improves on several of the assumptions previously utilized. This model was used to estimate the amount of melt wear that occurred during the 2008 test event. What follows in the next several sections is the derivation of the heat equation and the development and application of the boundary conditions and initial condition required to carryout its solution. Considerations are made to ensure that the melt wear is tracked as the melt temperature is exceeded. A MATLAB[39] script was utilized in this research to solve the equations at time steps incorporated in a

finite difference approach considering through the thickness of the slipper. In Chapter 3, the script is developed and additional considerations, pertaining to the HHSTT setup, are investigated and taken into account.

2.4.1.3 One-Dimensional Heat Equation Derivation.

In this section, the one-dimensional heat diffusion equation is derived. This provides further insight into the thermal considerations involved in this research by following the underlying assumptions and coefficient relationships. This derivation follows from Reference [83].

By examining energy within a control volume, as shown in Figure 2.10, one can develop an initial relationship since the energy must be balanced. Equation 2.25 shows the relationship described.

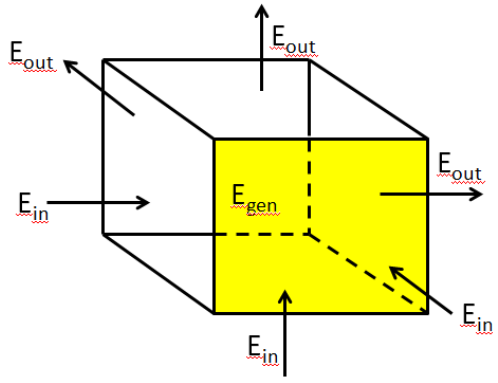

Figure 2.10: Control volume

$$E_{in} - E_{out} + E_{gen} = E_{st} \tag{2.25}$$

with:

E_{in} - Energy entering control volume

E_{out}- Energy leaving control volume

E_{gen} - Energy generated within control volume

E_{st} - Energy stored within control volume

The energy entering the control volume can enter from any direction. Let Q be the energy entering the control volume through the coordinate direction indicated by the subscript.

$$E_{in} = Q_x + Q_y + Q_z \tag{2.26}$$

Since the energy can also leave the control volume, as shown in Figure 2.10, through any direction, let Q be the energy exiting the control volume through the direction indicated by the subscript.

$$E_{out} = Q_{x+dx} + Q_{y+dy} + Q_{z+dz} \tag{2.27}$$

Eventually the solution is obtained through a finite difference scheme and thus a finite expression is needed. Taylor expansion of Q_{x+dx} provided:

$$Q_{x+dx} = Q_x + \frac{\partial Q_x}{\partial x} \cdot dx \tag{2.28}$$

Similarly,

$$Q_{y+dy} = Q_y + \frac{\partial Q_y}{\partial y} \cdot dy \tag{2.29}$$

$$Q_{z+dz} = Q_z + \frac{\partial Q_z}{\partial z} \cdot dz \tag{2.30}$$

Since the system under study consists of two parts sliding past each other, an assumption can be made of a uniform heat generation throughout. That heat generation rate was designated q_g and it can be expressed as:

$$E_{gen} = q_g \, dx \, dy \, dz \tag{2.31}$$

All of the energy entering into the volume plus the heat generation causes an increase in temperature. This is also a function of the density of the material ρ as well as the specific heat C_p. Specific heat is defined as

the amount of heat per unit mass required to raise the temperature by 1°C.

The specific heat for the steels used in the wear scenario studied is dependent on the temperature of the material as discussed further in Section 2.4.2.

$$E_{st} = \rho\, dx\, dy\, dz \cdot C_p(T)\frac{\partial T}{\partial t} \tag{2.32}$$

With:

T - temperature

t - time

If we substitute these terms into Equation 2.25, we have the following.

$$(Q_x + Q_y + Q_z) - \left(Q_x + \frac{\partial Q_x}{\partial x} \cdot dx + Q_y + \frac{\partial Q_y}{\partial y} \cdot dy + Q_z + \frac{\partial Q_z}{\partial z} \cdot dz\right) \tag{2.33}$$

$$+q_g\, dx\, dy\, dz = \rho\, dx\, dy\, dz \cdot C_p(T)\frac{\partial T}{\partial t} \tag{2.34}$$

As the objective of the model was heat transfer, temperature was the variable of interest. Fourier's Law gives the relation between the rate of heat flow and the temperature gradient. This arises out of experiments and is related to the property of thermal conductivity and thermal resistance. Utilizing Fourier's Law for Q_x, Q_y, and Q_z gives the following:

$$Q_x = -k_x^{TC} A_x \frac{\partial T}{\partial x} = -k_x^{TC}\, dy\, dz\, \frac{\partial T}{\partial x} \tag{2.35}$$

$$Q_y = -k_y^{TC} A_y \frac{\partial T}{\partial y} = -k_y^{TC}\, dx\, dz\, \frac{\partial T}{\partial y} \tag{2.36}$$

$$Q_z = -k_z^{TC} A_z \frac{\partial T}{\partial z} = -k_z^{TC}\, dx\, dy\, \frac{\partial T}{\partial z} \tag{2.37}$$

Substituting these expressions back into Equations 2.33 and 2.34 and dividing by $dx\, dy\, dz$ one obtains the following:

$$\frac{\partial}{\partial x}\left(k_x^{TC}\frac{\partial T}{\partial x}\right) + \frac{\partial}{\partial y}\left(k_y^{TC}\frac{\partial T}{\partial y}\right) + \frac{\partial}{\partial z}\left(k_z^{TC}\frac{\partial T}{\partial z}\right) + q_g = \rho C_p \frac{\partial T}{\partial t} \tag{2.38}$$

This is the heat diffusion equation in Cartesian coordinates for time dependent conduction when thermal conductivity (k^{TC}) varies with temperature and with uniform heat generation

within the body.

Also, since the material of the actual slipper was assumed to be isotropic, k^{TC} is the same in all directions.

This allows the removal of the subscripts (x, y, z) from k^{TC} in the equation above.

$$\frac{\partial}{\partial x}\left(k^{TC}\frac{\partial T}{\partial x}\right)+\frac{\partial}{\partial y}\left(k^{TC}\frac{\partial T}{\partial y}\right)+\frac{\partial}{\partial z}\left(k^{TC}\frac{\partial T}{\partial z}\right)+q_g=\rho C_p(T)\frac{\partial T}{\partial t} \tag{2.39}$$

Previous research in this area assumed k^{TC} was constant and thus not varying with temperature. However, in this work k^{TC} is dependent on T as discussed in Section 2.4.2. Thus, k^{TC} remains within the differential.

If we restrict ourselves to the one-dimensional case, then only the temperature in the y-direction is considered i.e. through the thickness of the slipper.

$$\frac{\partial}{\partial y}\left(k^{TC}(T)\frac{\partial T}{\partial y}\right)+q_g=\rho C_p(T)\frac{\partial T}{\partial t} \tag{2.40}$$

Heat flux $\left(q_g\right)$ is present at the slipper-rail interface due to friction, but to simplify the current derivation it is temporarily removed leaving the following equation.

$$\frac{\partial}{\partial y}\left(k^{TC}(T)\frac{\partial T}{\partial y}\right)=\rho C_p(T)\frac{\partial T}{\partial t} \tag{2.41}$$

This equation requires further refinement before it can be solved. The next section delves into the boundary conditions, initial condition, scaling, and discretization required prior to using a MATLAB [39] script to solve for the acceleration phase of a HHSTT slipper-rail interaction scenario.

Of particular note in this research was that the material properties were not taken as constants. This was due to the wide range of temperatures that the material experienced during the test event. The temperatures rose from ambient up to and including melt temperatures.

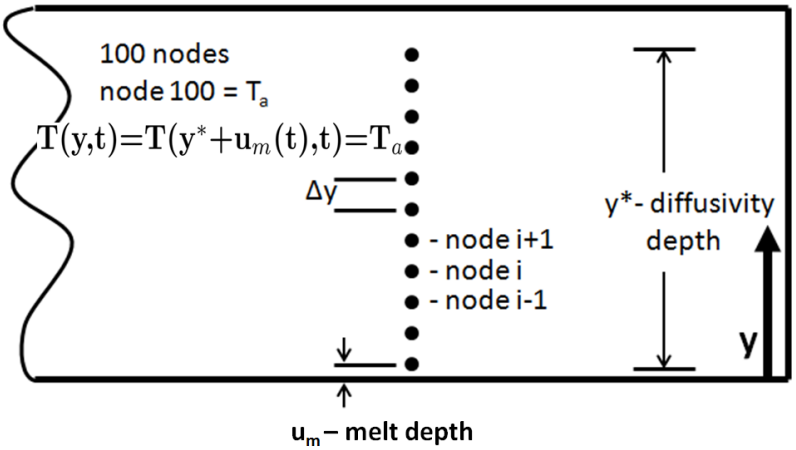

Figure 2.11: Diffusion Length

As the solution was based on a finite difference scheme, a distance must be used to attach the boundary conditions. Distance was not set at infinity for T_a because it had to be computed numerically (truncated domain). It was based on the thermal conductivity, density, and specific heat of the material used. Thermal diffusivity is defined as:

$$\kappa = \frac{k^{TC}}{\rho C_p} \tag{2.42}$$

It measures the rate of transfer of heat of a material from the higher temperature side to the relatively cooler side. For this study, the length of diffusivity is needed to set the distance for the span of 100 nodes. Since the specific heat and the thermal conductivity are treated as variables with respect to temperature, the max diffusion length, y^* was calculated using Equation 2.43 and shown in Figure 2.11.

$$y^* = \max_{T_a<T<T_m} \sqrt{\frac{k^{TC}(T)}{\rho C_p(T)} t^*} \tag{2.43}$$

This equation finds the maximum value for the diffusivity length over the time, t^*, of the entire test scenario with regard to temperature. This was the value used to set the boundary condition farthest away from the rail as described in Equation 2.46.

2.4.1.4 Boundary conditions.

In order to solve Equation 2.41, boundary conditions are required. The two boundary conditions were carefully chosen based on the physics of the problem. A portion of the slipper was modeled with 100 evenly spaced nodes as depicted in Figure 2.11. The distance from the front of the slipper is set far enough away to avoid the effects of aerodynamic heating, as depicted in Alban's work [32]. In addition, it was assumed that the heat traveled through the depth of the slipper but only in the direction away from the surface. Thus the model behaves as an insulated wire. At the bottom of the slipper, is the interaction of the slipper with the rail. That interaction consisted of a intermittent contact. As the slipper contacted the rail at high velocity, friction caused a heat flux condition.

For this heat flux condition, the following holds:

$$-k^{TC}(T)\frac{dT}{dy}\bigg|_{y=u_m(t)} = q''(t) - \rho l_h \frac{du_m}{dt} \tag{2.44}$$

$T(u_m, t) = T_m, \qquad t > 0 \text{ when } \dot{u}_m > 0$

$T(y, t) = T_a, \quad \text{as } y \to \infty, \;\; t > 0$

Equation 2.44 says that at the slipper surface in contact with the rail, the temperature is determined by the frictional heat, q'' (as discussed in Section 2.4.3) and the thermal conductivity $k^{TC}(T)$. Figure 2.11 displays u_m, the melt depth. The latent heat l_h, density ρ, and $\dot{u}_m$ remove energy from the equation. This occurs if u_m is > 0 which only occurs if the nodal temperature exceeds melt. This moving boundary due to phase change is known as the "Stefan condition" [84]. A gap, generated by non-contact, produces high speed airflow. This results in convection at the slipper surface following Newton's Law of Cooling [85].

$$-k^{TC}(T)\frac{dT}{dy}\bigg|_{y=u_m(t)} = \mathrm{h}(T_{aw} - T_{surf}) \tag{2.45}$$

Equation 2.45 shows how the temperature is dependent on the convective heat transfer coefficient, h, the temperature at the surface of the slipper, T_{surf}, and the freestream temperature T_{aw}. These are discussed further in Section 2.4.4. One should recall that

the objective of this model was to estimate melt wear. Figure 2.11 shows the melt depth as u_m. Thus, as the temperature exceeded melt, the melt depth increased and energy was removed via the latent heat of fusion. This accounted for the phase change from solid to liquid when the melt temperature was exceeded. When the actual slipper traveled down the rail at high velocity, the material is assumed to be removed, as it melts, from the scenario.

The node numbering begins at Node 1 which is at the bottom of the slipper and Node 100 is in the direction toward the top of the slipper. Node 100 is set at ambient temperature for the duration of the slipper acceleration phase of the test run. Node 100 begins at t_0 at the diffusivity length y^* as calculated in Equation 2.43. As $t > 0$ the maximum distance from the flux location is taken to be:

$$y_{max} = y^* + u_m(t)$$

with u_m increasing as the temperature exceeds melt temperature. The Boundary Condition at y_{max} is:

$$T(y^* + u_m(t), t) = T_a \tag{2.46}$$

The nodes are evenly spaced and their positions change as the melt depth changes. Due to this, the positions of the boundaries constantly change. This nonlinear behavior mirrored the wear that occurred as the slipper traveled down the rail.

2.4.1.5 Initial conditions.

The initial condition is the initial temperature distribution as described by:

$$T_{t=0}(y, 0) = T_0(y) \tag{2.47}$$

This is the representation of the temperature distribution through the slipper in the y-direction (thickness) at time zero. The initial temperature is assumed to be ambient throughout the thickness at the beginning of a test run.

In addition, as the temperature exceeds melt the melt depth increases. Equation 2.48 shows

that the temperature in the melt depth exceeds melt.

$$T(u_m(t), t) = T_m \text{ when } u_m(t) > 0 \tag{2.48}$$

2.4.1.6 Solver.

The heat equation, boundary conditions, and initial condition were scaled and discretized as shown in Appendix A. The ODE was solved at each time step with a method that is a member of the RungeKutta family of solvers. The solver, designated ODE45[39], is based on the Dormond-Prince method [86]. This method improves on the 4th order Runge-Kutta solver in a few important aspects. First it improves on the accuracy of the solution by utilizing seven function evaluations to calculate seven different slopes as opposed to four. The four are the ones that make up the next step solution of the 4th order Runge-Kutta algorithm as seen in Equation 2.49. The slopes are used in two different linear combinations to approximate the error.

$$RK_{n+1} = RK_n + \frac{1}{6}(k_1 + 2k_2 + 2k_3 + k_4) \tag{2.49}$$

The second improvement is using this approximate error to modify the step size to obtain the desired accuracy. This adaptive step size scheme ensures a more efficient use of processing time as larger step sizes can be utilized when appropriate and smaller step sizes used only when needed to ensure the accuracy desired. For further details please see reference [86].

2.4.2 Material Modeling.

2.4.2.1 Background.

In this section, the material properties are discussed. The slippers used in the 2008 test were composed of Vascomax 300. Developed in the 1950s, this material is known as a 'maraging' steel. It is so named due to the martensitic microstructure obtained through the concept of substituting other elements into the material matrix. This resulted in an extra low carbon steel with an iron base and an 18% nickel composition which significantly increased

strength as well as fracture toughness [87]. The following discussion is based on material properties obtained from Vascomax 250 as data for 300 was not readily available. The main difference between the two maraging steels is that Vascomax 250 has an approximate yield strength of 250 ksi while Vascomax 300 has an approximate yield strength of 300 ksi. This can be attributed to small changes in the ratio of other elements that make up each steel respectably [88].

2.4.2.2 Thermal Properties.

Thermal Conductivity

As stated, the thermal conductivity k^{TC} and the specific heat C_p are temperature dependent for the slipper material. Figure 2.13 shows the thermal conductivity of the material with respect to temperature.

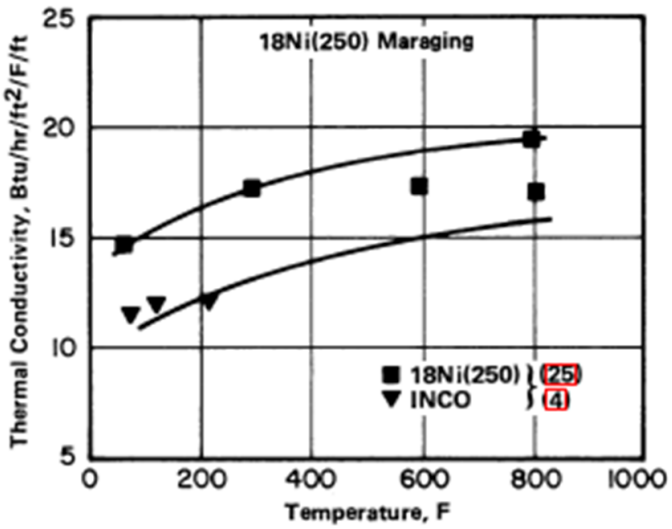

Figure 2.12: Thermal Conductivity Vascomax 250[30]

This dependence adds a challenge to the wear prediction for several reasons that will be discussed in further detail in Chapter 3. In addition, the data for Vascomax 250 only extends to approximately 800K, well short of melt temperature, 1685K. The thermal conductivity was assumed to continue this behavior shown as slowly increasing. Figure 2.13 is a curve

fit of the data in metric units due to their use in this study. The method of implementation of the equation is discussed in Chapter 3.

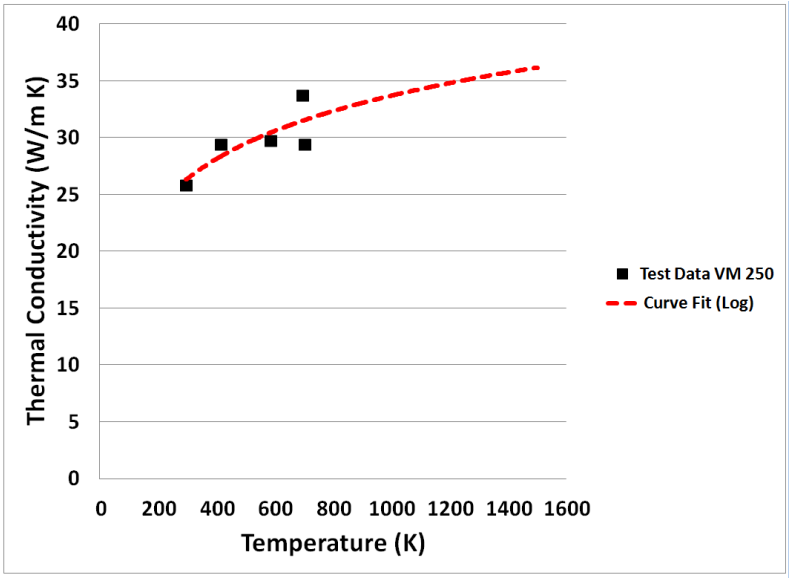

Figure 2.13: Thermal Conductivity Vascomax 300[30]

Specific Heat

The specific heat dependence on temperature is shown in Figure 2.14. The data shows an increase in specific heat as the temperature increases past 800°F is due to a solid-solid phase transition. The material transforms from martensite to austenite crystalline structure [88]. Unfortunately, the data available is not near melt temperature necessitating an inference on the behavior at high temperatures.

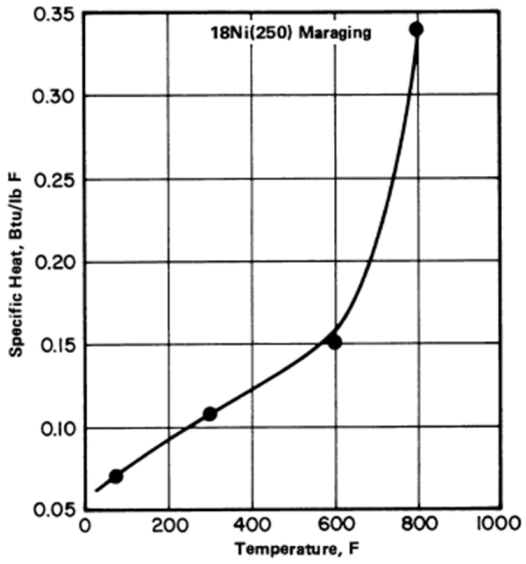

Figure 2.14: Specific Heat Vascomax 250 [30]

A reasonable assumption is based on Figure 2.15 which shows data for AISI 4130 [30] at higher temperatures. In these types of materials, the specific heat value rises then falls as the austenite phase transformation occurs.

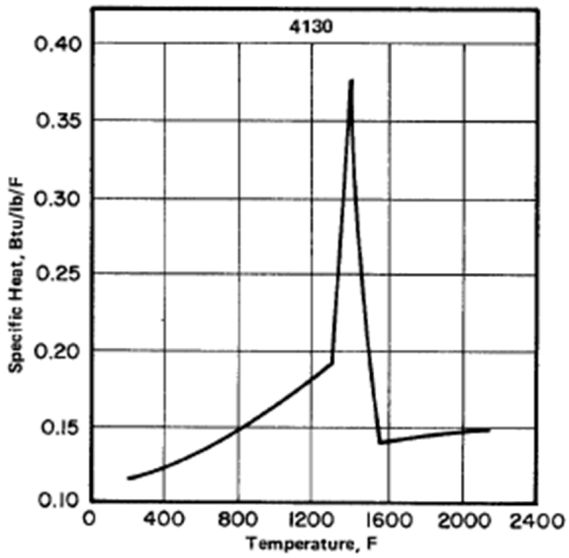

Figure 2.15: Specific Heat AISI 4130 [30]

A curve fit, in metric units due to their use in this study and shown in Figure 2.16, was done to approximate the specific heat behavior for Vascomax 300. Its implementation is discussed in Chapter 3.

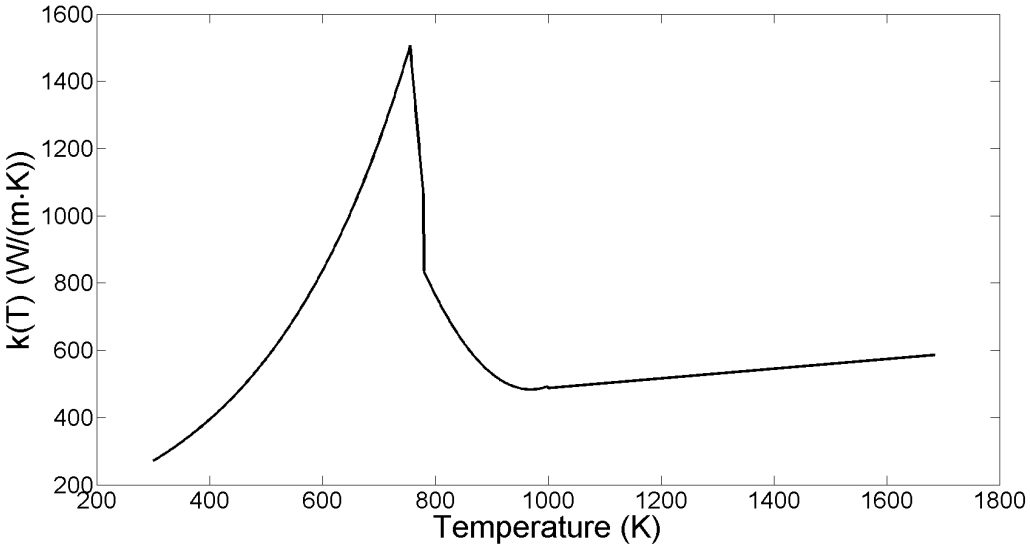

Figure 2.16: Specific Heat Vascomax 300 (hypothesized)

2.4.3 Conduction.

Of primary importance to the one-dimensional model is frictional heat as it is the energy source that drives the heat transfer. As the slippers contact the rail, conduction occurs as mentioned in Section 2.4.1.4. The frictional heat q'' accounts for the energy driving the heat transfer. It is calculated below:

$$q''(t) = \frac{\mu(t)F(t)v(t)}{A(t)} \tag{2.50}$$

q"(t) - frictional heat

μ(t) - coefficient for friction

F(t) - Force

v(t) - velocity

$A_c(t)$ - Contact Area

Friction between the slipper and rail was modeled by the Coulomb law with a friction coefficient μ. As discussed in the previous chapter, the coefficient of friction used in this study is approximated based on work done by Montgomery [89], Krupovage and Rasmussen [43], as well as Hale [3].

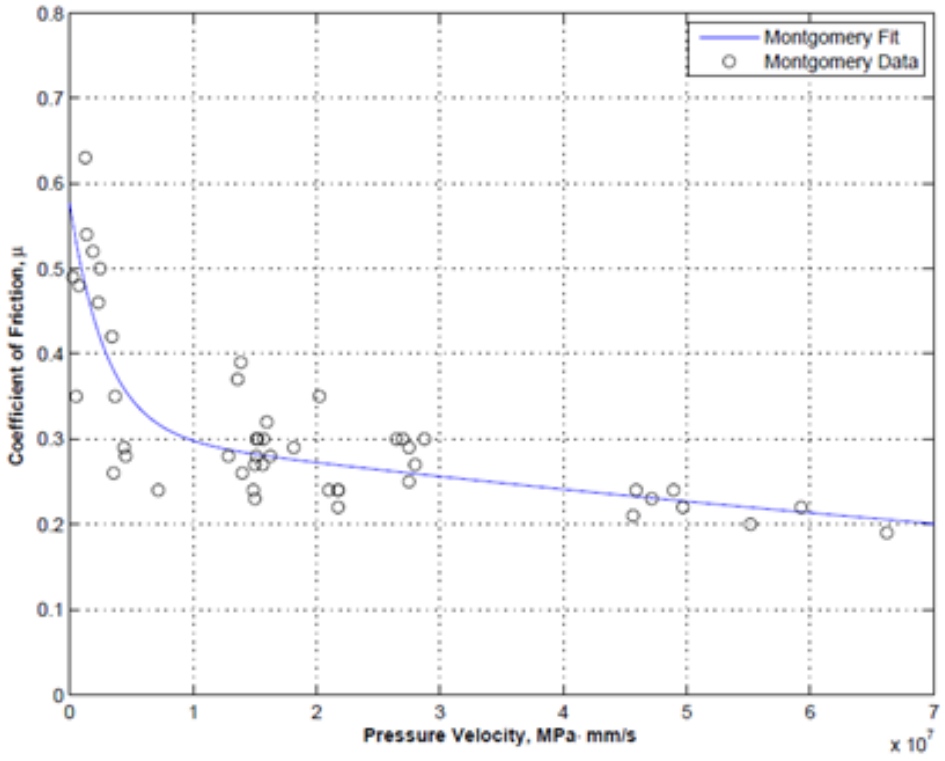

Figure 2.17: Montgomery data with Hale curve fit [3]

Figure 2.17 is Hale's plot of Montgomery's data with a curve fit. The equation developed by Hale is below:

$$\mu = \begin{cases} 0.2696e^{-3.409x10^{-7}Pv} + 0.3074e^{-6.08x10^{-9}} & \text{for } 0 < Pv < 4.45x10^8 \\ 0.02 & \text{for } Pv \geq 4.45x10^8 \end{cases} \tag{2.51}$$

The pressure P is estimated from the force and the slipper area in contact with the slipper. The slipper does not fully contact the slipper but rather rotates per work done by Buentello[18] and shown in Figure 2.18.

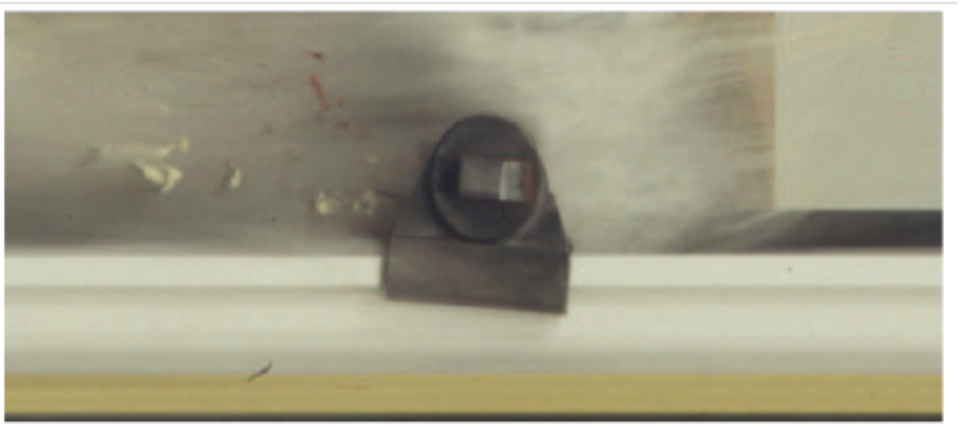

(a) 80X-G1 Test Mission, April 2003, V = 2,853 m/s.

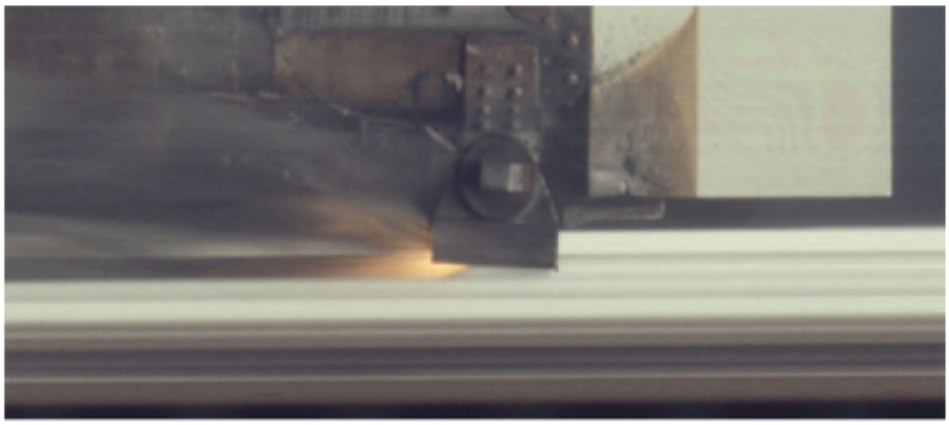

(b) 80X-G1 Test Mission, April 2003, V = 2,861 m/s.

Figure 2.18: Slipper rotation[3]

Buentello hypothesized that the slipper rotation changed the slipper length in contact per Figure 2.19. This leads to a contact area that changes as the slipper travels down the rail. This impacts the coefficient of friction calculation as well as the frictional heat estimation, as discussed in Section 3.3.5.2.

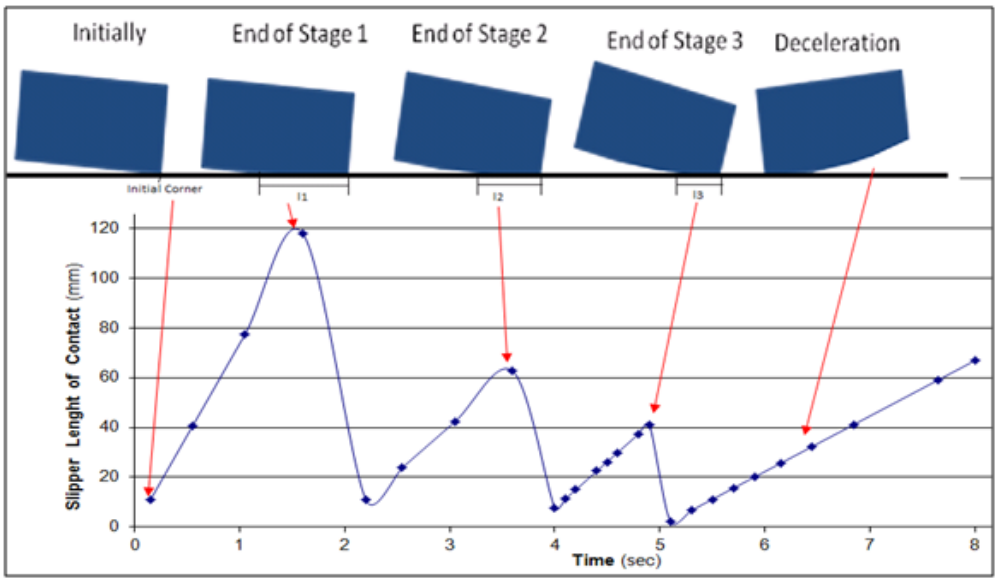

Figure 2.19: Length in contact[18]

The force, F and velocity, v are known variables in Equation 2.50. They are discussed in further detail in Chapter 3.

2.4.4 Convection.

As discussed in Section 2.4.1.4, when the slipper is not in contact with the rail, air flow occurs between the slipper and the rail. Figure 2.20 depicts the gap and the air flow as it develops between the slipper and the rail. Convection occurs due to the difference in temperatures between the air and the surfaces. The slipper surface was the surface of interest and Equation 2.45 was used to calculate the convection present.

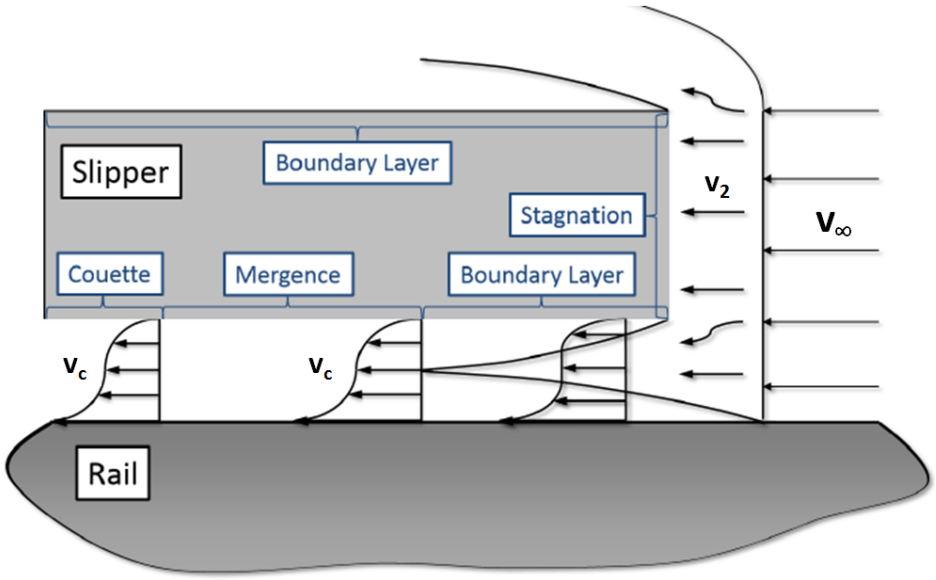

Figure 2.20: Bounce[22]

v_∞ - freestream velocity of airflow

v_2 - airflow velocity post shock wave

v_c - couette flow velocity profile

Alban used the local Nusselt number, Nu, which provides a relationship between the convective to conductive heat transfer across a boundary [85]. In the simple case it is defined as Equation 2.52.

$$Nu = \frac{hx}{k_f} \tag{2.52}$$

h - convective heat transfer coefficient

x - distance from the surface boundary to the local point of interest

k_f - thermal conductivity of the fluid

To determine the heat transfer coefficient, the bottom surface of the slipper was assumed to be a flat plate in high speed flow. The local Nusselt number for flow over a plate is given by,

$$Nu = 0.0296 Re_x^{4/5} Pr^{1/3} \tag{2.53}$$

Re_x - Reynold's number

Pr - Prandtl number for air

$$Pr = \frac{\nu}{\kappa} \tag{2.54}$$

The Prandtl number, Pr, is a dimensionless parameter defined as the ratio of a material's kinematic viscosity ν and its thermal diffusivity κ. For this study the Prandtl number was taken as constant and for air it is equal to approximately 0.7. By combining these equations, the heat transfer coefficient can be calculated as shown in Equation 2.55.

$$h = \frac{0.0296 k_f Re_x^{4/5} Pr^{1/3}}{x} \tag{2.55}$$

$$q'' = h_(T_{aw} - T_{surf}) \tag{2.56}$$

q'' - heat flux

T_{surf} - temperature at bottom surface of slipper

T_{aw} - adiabatic wall temperature

Viscous heating generates a thermal boundary layer. The film temperature under these conditions is the adiabatic wall temperature. For high-speed, turbulent flow, the adiabatic wall temperature T_{aw} was calculated using Equation 2.57[90].

$$T_{aw} = T_{1|2}\left(1 + \frac{\gamma - 1}{2} Pr^{1/3} M_{1|2}^2\right) \tag{2.57}$$

λ - ratio of specific heats

$\mathrm{T}_{1|2}$ - temperature ratio

$\mathrm{M}_{1|2}$ - Mach ratio

The specific heat for air was calculated at the reference temperature 293K and at the elevated temperature with λ as the ratio of the two that varies as the temperature changes over the duration of a test run. The temperatures in front of and behind the shock are also in a ratio designated as $\mathrm{T}_{1|2}$. The same is true for the Mach number, $\mathrm{M}_{1|2}$.

2.4.5 Partition Function.

A partition function was required to estimate the percentage of generated thermal flux that was applied to the bottom of the slipper versus the percentage applied to the rail during conduction. This was important because the frictional heat on the slipper surface drove the melt wear rate. This partition function apportions the total frictional heat, q'', entering the slipper and the rail respectively, during contact as shown in Figure 2.21. The relative amounts are not known and have previously been estimated.

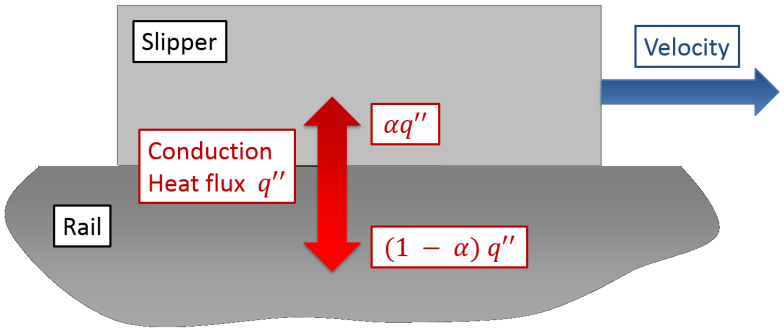

Figure 2.21: Frictional Energy Between Rail and Slipper and the Partition Function, α[17]

Previously, Paek developed a hypothetical partition function [15]. This equation was based on modeling the HHSTT scenario with a one-dimensional heat transfer model and varying the partition function to approximate expected melt wear. The partition function that best estimated this assumed melt wear is below.

$$\alpha(t) = 0.4e^{-5t^2} + 0.1 \tag{2.58}$$

This partition function begins at 0.5 (50%) at $t = 0$ and exponentially decays from there to near 0.1 or 10%

Le used Wolfson data [16] to compare the results of the heat transfer analysis using different partition functions. The exponential function, developed by Paek[15], provided the closest match to Wolfson's work and was also consistent with Hale's findings [17] and

was thus used in Alban's work as well as Buentellos's work [65]. Le [17] calculated melt wear using four separate partition functions. Figure 2.22 shows the four partition functions analyzed by Le. They all begin with Hale's 50% assumption and end when 10% of the heat flux is transferred to the underside of the slipper.

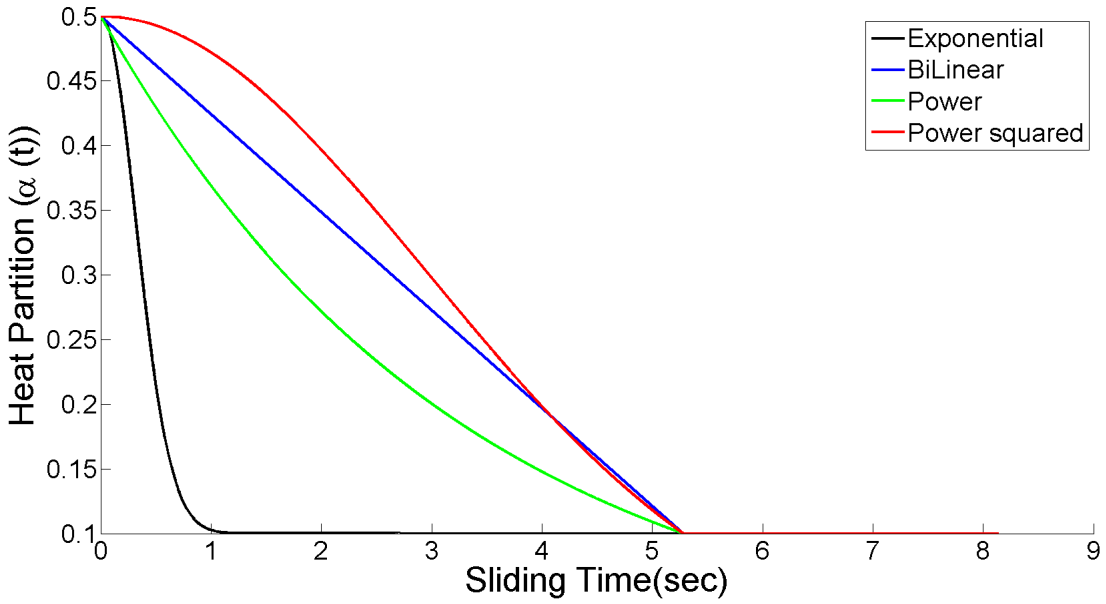

Figure 2.22: Partition Functions.[17]

The black line represents the exponential decay partition expressed as:

$$\alpha(t) = 0.4e^{-5t^2} + 0.1 \tag{2.59}$$

The green line represents the power partition function represented by:

$$\alpha(t) = \begin{cases} \alpha_0 \left(\frac{\alpha_m}{\alpha_0}\right)^{\frac{t}{\delta \cdot t_m}} & \text{for } t < \delta \cdot t_m \\ \alpha_m & \text{for } t > \delta \cdot t_m \end{cases} \tag{2.60}$$

The blue line represents the bilinear decay partition function expressed as:

$$\alpha(t) = \begin{cases} \alpha_0 + (\alpha_m - \alpha_0)\frac{t}{\delta \cdot t_m} & \text{for } t < \delta \cdot t_m \\ \alpha_m & \text{for } t > \delta \cdot t_m \end{cases} \tag{2.61}$$

Finally, the red line represents the power squared partition function that is based on a decaying function that fits the Gaussian distribution. It is expressed as:

$$\alpha(t) = \begin{cases} \alpha_0 \left(\frac{\alpha_m}{\alpha_0}\right)^{\left(\frac{t}{\delta \cdot t_m}\right)^2} & \text{for } t < \delta \cdot t_m \\ \alpha_m & \text{for } t > \delta \cdot t_m \end{cases} \tag{2.62}$$

t - time

t_m - time to melt

α_0 - initial value at time zero, assumed to be 0.5

α_m - value at time of melt, assumed to be 0.1

δ - constant, based on percent time in contact

Le's results are shown in Figure 2.23 which showed ~ 0.8% of the slipper thickness melting during the investigated test run. This seemed comparable to the ~ 20% melt wear described by Hale [3].

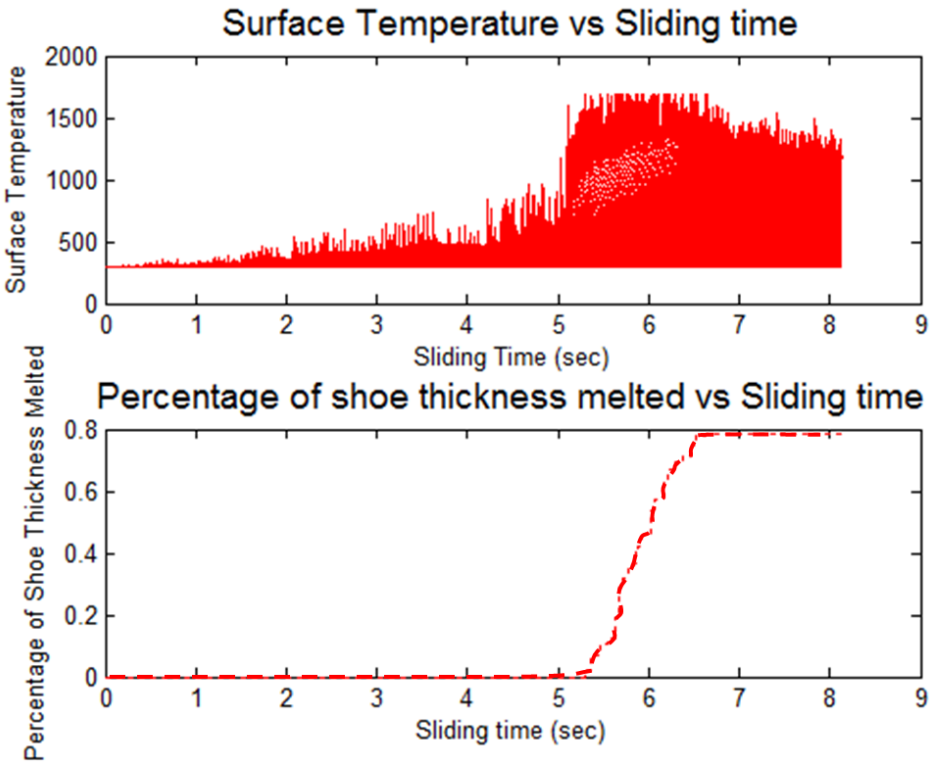

Figure 2.23: Surface Temperature and Melt Wear Percentage vs. Sliding Time Using Exponential Partition Function[17]

2.5 Combined Model

The second FEM used in this work is at the continuum scale with the slipper model interacting with a model of the rail. This model was an attempt in bringing together the first two models. The material modeling includes the Johnson and Cook plasticity model [48] as described in Section 2.2.3.6 and the Johnson and Cook Failure model [49] as described in Section 2.2.3.7. In addition, since this FEM models the slipper and rail interaction, the contact algorithm based on the penalty method was used as discussed in Section 2.2.4. Friction is a primary consideration for the larger scaled model as it is the mechanism for energy entry into the model. The coefficient of friction was calculated as described in Section 2.4.3. Material modeling used in both previous models was used in this model to include mechanical as well as thermal properties. This model is described in further detail to include boundary conditions, initial condition, as well as their development and application in Section 3.4.

2.6 Chapter Summary

This Chapter covered a wide range of theory relevant to this research. The micromechanic scale FEM required considerations for the material modeling including temperature, deformations due to impact, and shock waves. These were discussed and their relevance to this study were mentioned. The underlying principles of the heat transfer model were also developed and discussed. The heat equation was derived to reflect the variable material properties used along with the boundary conditions and initial condition of interest. Those same material properties were shown and their temperature dependence was discussed. Friction was a large input to the model and the equation to obtain the coefficient was shown. The aerodynamics used to calculate the airflow through

the slipper-rail gap was also described. Recall that the aerodynamics discussed did not include hypersonic considerations to include high temperature gas dynamics. Finally, the combined FEM model was outlined. It combines many of the features already described in the previous models. That section contained a descriptive summary of those features as appropriate.

III. Numerical Models

3.1 Chapter Overview

Several different models were developed to approximate the wear scenario as experienced by the slipper sliding down a rail at the high velocities typical of HHSTT tests. In this research the thermal and mechanical wear rates were investigated using different models. In this Chapter, the models are described in detail. This includes the intent of the model, assumptions that they are based on, required inputs, material modeling, boundary conditions imposed, simulation times, and the wear calculations used.

The micromechanical model was a FEM that simulated impact between the slipper model and an asperity. This model was sized at the micron, μm, scale and the simulation time is on the order of a microsecond, μs. The model was used to investigate shock wave phenomenon, the contact algorithm employed by ABAQUS [27], and to calculate the mechanical wear through material failure and element deletion establishing a wear rate. Note that the model used to study the shock wave phenomenon as well as the contact algorithm used different material than the wear model. This was due to the fact that the material used for those studies was immaterial to the underlying phenomenon and that additional data was available for the material used (AISI 1045). The second model was related to thermal heat analysis calculated by utilizing a one-dimensional finite difference scheme. The MATLAB [39] code used for this purpose calculated the conduction developed through friction and partitioned to the slipper and rail as well as the convection brought about by the airflow through the gap between the slipper and the rail. It also accounts for this intermittent contact between the slipper and rail. This model was used to estimate the temperature of the slipper surface for use as an initial condition required by the FEMs. It was also used to estimate melt wear for an entire HHSTT test run based on a 2008 test there. The final model discussed was developed from concepts from the previous

models described. The three-dimensional FEM models a slipper model traveling down a rail model during a fixed contact time. The interaction between the two was the friction calculated by the MATLAB [39]. It also utilized material modeling from both models. This model was used to estimate the wear rate for specific times when the slipper contacted the rail.

The following sections will go into further depth on the different models.

3.2 Micromechanics Modeling

3.2.1 Contact Model.

3.2.1.1 Concept.

This research was focused on estimating wear rate of the 2008 HHSTT test run. One of the methods was utilizing the commercial finite element modeling software package, ABAQUS [27]. This provided an opportunity to use a robust contact algorithm to assist in simulating asperity collision. By modeling the material with Johnson-Cook plasticity and failure modeling, damage could be estimated by summing the volume of elements deleted through failure. Thus, it was a priority to account for the contact algorithm employed by ABAQUS. The contact penalty method was discussed in Chapter 2. This section of the chapter describes a model that used these concepts.

Figure 3.1 shows the meshed model incorporated in this study showing a portion of the slipper in contact with a rail model. The mesh density was coarse as the intent was to examine the element behavior as opposed to accurate material behavior. The element used is shown in the same figure. The element chosen is due to the fact that it was used throughout this research. The particular details of this element is discussed in the microscale model wear model discussed in the Section 3.2.2. The material modeled was 1045 steel. AISI 1045 steel was chosen due to the availability of coefficients for the Johnson-Cook Plasticity and Failure models as well as equation of state variables. Note that this material was not used in the construction of either the actual slipper or the actual

rail used at the HHSTT. This was carried out to investigate certain portions within the overall analysis.

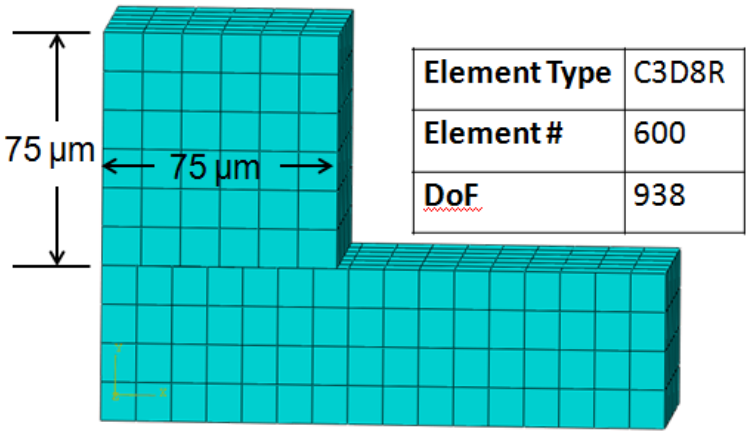

Material	AISI 1045 Steel
E(kPa)	2.03E+08
Poisson's Ratio	0.291
Shear Modulus	7.984E+07
Density(kg/mm^3)	7.861E-06
Melting Temp(K)	1733
A(kPa)	5.53E+05
B(kPa)	6.00E+05
n	0.23
C	0.013
m	1.00
d1	0.06
d2	3.31
d3	1.96
d4	0.0018
d5	0.58
Gruneisen Coeff	1.63

Figure 3.1: FEM used in contact simulation

Figure 3.2 displays the boundary conditions imposed on the FEM. The horizontal velocity of 20 m/s was relatively low as compared to the HHSTT scenario as high velocities would impart large energy inputs into the model possibly interfering with the contact response. The vertical velocities of 1, 2, and 5 m/s were used to ensure that the separate parts were forced into each other. This tested the contact algorithm as nodes could interpenetrate the bodies and showed trends as the velocities were increased. The initial temperature imposed was 300°K. The temperature was not a primary focus of this study. Symmetry was imposed to reduce any edge effects.

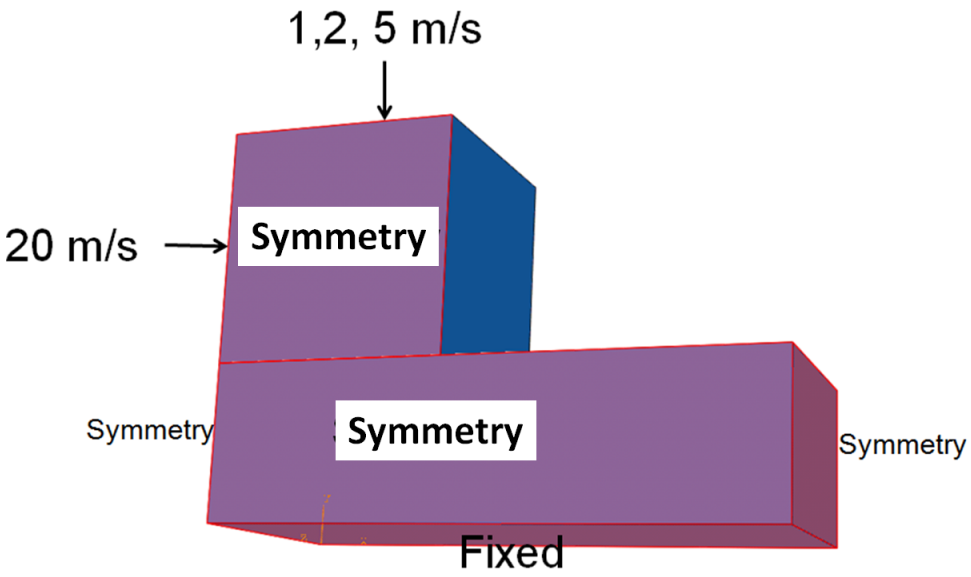

Figure 3.2: Boundary conditions - contact simulation

The model allowed a study of the stresses and forces as experienced by elements in the slipper and the rail on the surface that interact with each other. In addition, the penalty algorithm as implemented by ABAQUS includes a scaling factor [27]. The impact of this scaling factor was also investigated. The results of this model are discussed in Chapter 4.

3.2.2 Wear Model.

3.2.2.1 Concept.

As part of this research, a microscale FEM was used to investigate the high speed collision between a slipper model and an asperity. At the scale of interest, 10^{-6} m, it is observed that surfaces that appear smooth at the macro scale are actually rough, consisting of peaks and valleys. This was modeled as asperities. The damage caused on the slipper model, as the result of these collisions, was assumed to be a representative of the wear measured on a worn slipper. The initial temperature was taken from the one-dimensional heat transfer model discussed in Section 3.3.1.

This three-dimensional FEM was used to model a portion of the slipper and different sized asperities similar to work done previously by Buentello [18]. The model allowed a

study of several assumptions previously made. Comparative studies were done to examine the effects of utilizing an equation of state, different boundary conditions and the contact algorithm used by ABAQUS [27]. Wear was also approximated by using a failure model that removed elements from the model in a proscribed manner. The method of taking the volumes of these deleted elements then calculating the wear rates is also discussed.

3.2.2.2 Assumptions/Limitations.

There are several assumptions that accompany this model. One was that at the velocities of interest, previous stress history was irrelevant. The model was associated with a collision of the slipper with an asperity, this impact overrides any previous materials history accumulated in the slipper's run. The strain rates are so large at these velocities that damage due to previous collisions was obliterated as shown by Hale [3].

Next, was that the uncoupled solution was approximating reality. During an actual test run, a mechanical-thermal coupling occurs. The heat flux inputs are history oriented, leading to changing temperatures, which lead to changing material properties, which also change due to plastic deformation, which causes a rise in temperature, which changes the material properties. This non-linear behavior was difficult to reproduce using the current three-dimensional FEM. It was also assumed that the mechanical collision was an adiabatic process that has the temperature rising due only to plasticity effects, a "safe" assumption due to the time scale involved.

All the material modeled was assumed homogeneous and isotropic. At the scales modeled, it was realized that these assumptions were not accurate since at smaller scales dislocations and impurities were present. In addition, the heat treatments were not perfectly applied to the material in every direction.

It was also assumed, due to previous work, that the asperity collision was friction-less. Contact modeling of asperity interaction is commonly used to model friction on the microscale. Thus, this assumption was deemed reasonable.

Element deletion was the method used to account for wear in this model. This is problematic in that the forces applied to the element are not accounted for when the element deletes. This is a recognized issue that was assumed to be reasonable to the overall results.

The overall wear estimate for the model was assumed to be scaled from the volume of the deleted elements from asperity collision. There are orders of magnitude difference between the micromechanical model and measured wear from a worn slipper. Scaling factors, that were used, assumed that previous statistical sampling held for the full sized slipper, damage only occurred upon slipper-rail contact, and the wear was due to physical removal only.

3.2.2.3 Model Details.

The wear model used to model asperity collision, consisted of a slipper model and a rail model to include an asperity. It is displayed with dimensions in Figure 3.3.

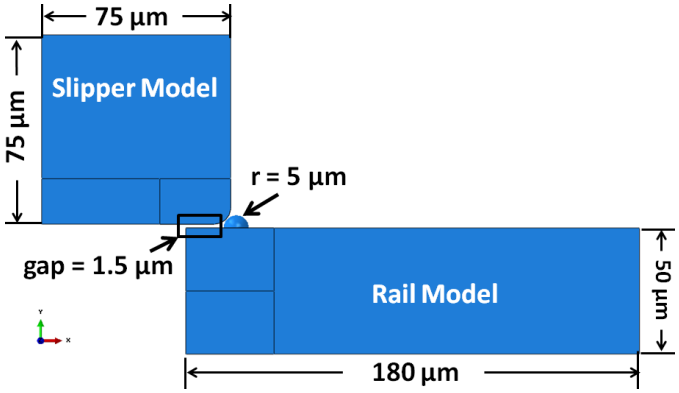

Figure 3.3: Microscale FEM dimensions

The previous two figures represent the contact model that consisted of a slipper model in contact with the rail model without any asperities modeled. The contact model also used the material properties of 1045 steel for both models as previously stated. In contrast are the material property coefficients used for this study and shown in Figure 3.4. For the wear estimate, the slipper model consisted of Vascomax 300 while the rail model consisted of 1080 steel. Of note is that the coefficients listed are the same ones used in previous research by Buentello [18]. This was done for to ensure that the model was providing reasonable

results. Although the materials listed were the ones used to construct the rail and slipper respectfully, several coefficients were taken from similar materials due to a dearth of high strain rate data required to obtain the needed coefficients for the Johnson-Cook models for plasticity and failure as well as the coefficients for the Mie-Gruneisen equation of state. The material modeling and equation of state background was discussed in Chapter 2.

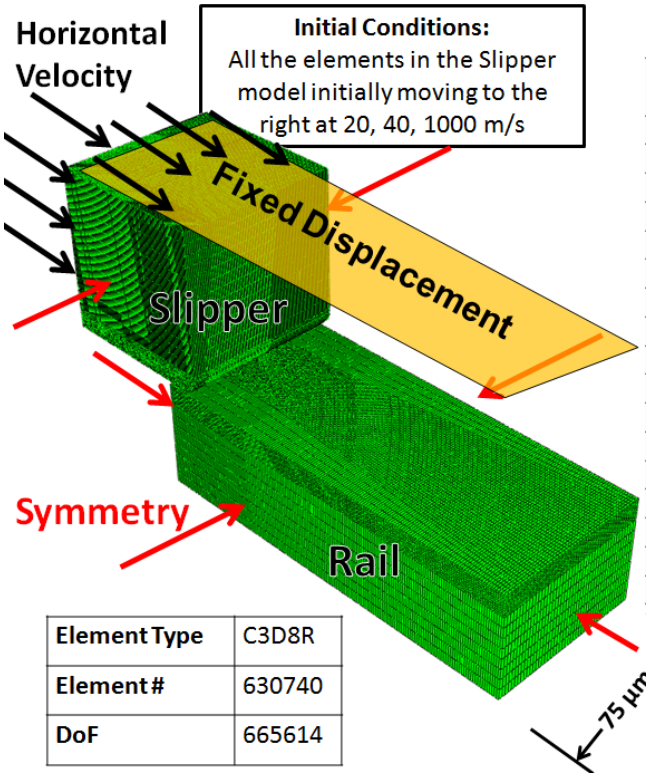

Material	AISI 1080 Steel	VascoMax 300
E(kPa)	2.02E+08	1.807E+08
Poisson's Ratio	0.27	0.283
Density(kg/mm^3)	7.8-06	8.0-06
Melting Temp(K)	1670	1685
A(kPa)	7.0E+05	2.1E+06
B(kPa)	3.6E+06	1.24E+05
n	0.3737	0.6
C	0.17	0.03
m	0.25	0.8
d1	3.6	0.124
d2	0.17	0.03
d3	0.25	0.8
d4	0.6	0.3737
d5	1670	1685
C_0 (kn/s)	3.980	4.605
s	1.580	1.456
Gruneisen Coeff	1.6	1.65

Element Type	C3D8R
Element #	630740
DoF	665614

Figure 3.4: Microscale FEM used in wear estimate

The initial temperature for the rail was 300°K. This was based on the assumption that the rail was at ambient temperature prior to any contact with the slipper. This presupposes that the slippers ahead of the slipper studied did not heat the rail. In addition, studies done on the partition function verify that the temperature in the rail was not raised to a significant amount as the partition function is based on the assumption that the energy would flow in an uneven manner toward the rail as it would be cooler than the slipper at the time of contact. The initial temperature for the slipper was taken from the one-dimensional heat transfer

model for the velocity of interest. That model provided the temperature at the underside of the slipper which was used for the temperature of the entire slipper model. Due to the scale of the model (75 μm), it was assumed the temperature would vary only slightly throughout the slipper model as utilized.

As shown in Figure 3.4, the boundary conditions on the rail were that the rail was fixed at the bottom. The actual rail is many miles in length and secured in a robust manner to prevent premature departure of the test sled. On the other dimensions symmetry was imposed to reduce and stress wave interference and to better model the actual rail which is orders of magnitude larger. The top surface was free as it consisted of a single asperity that collided with the slipper model.

Continuing the description shown in Figure 3.4, the slipper had an initial velocity imposed on it to prevent unrealistic accelerations at the beginning of the simulations. The horizontal velocity of interest was placed on the rear and top surface of the slipper model. The top surface of the slipper was also constrained to only move in the horizontal direction. This was done to more accurately reflect the vertical motion of the actual slipper over the time modeled which was on the order of $10e^{-}8$ seconds. The bottom and front of the slipper were free to interact with the asperity on the rail model. The other two dimensions had symmetry imposed to reduce stress wave interactions and to account for the actual slipper dimensions which were orders of magnitude larger. Finally, there was a gap between the slipper and rail of 1.5 μm. This dimension was used in previous work [65] and was based on surface roughness work done by Voyiadjis [20].

The model was meshed using elements designated as C3D8R in ABAQUS [27]. The element is a three-dimensional eight noded linear brick as shown in Figure 3.5.

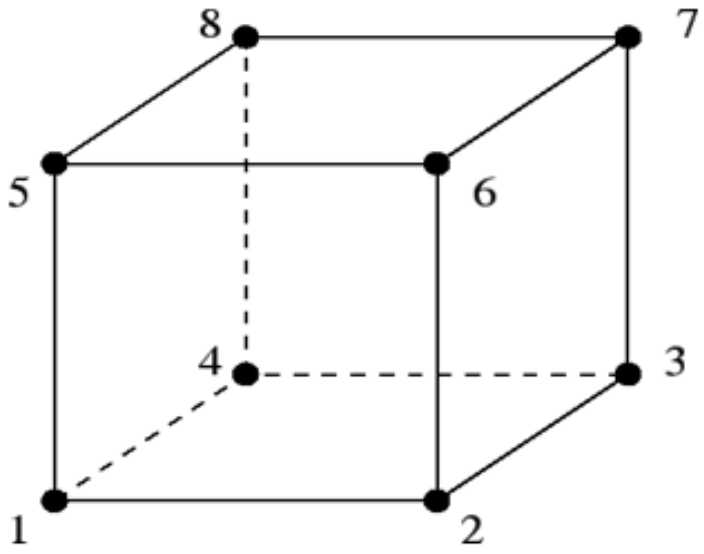

Figure 3.5: Eight noded brick element

The element used utilized a reduced integration formulation. This formulation obtains the strains not at the first-order Gauss point but are obtained as the average strain over the element [91]. This reduces the integration points and the computation time. It also reduces the possibility of an element 'lock' in that the stiffness would be orders of magnitude too large if the element was fully integrated. In addition, hourglass control was selected to control the zero-energy modes.

> **Since the elements have only one integration point, it is possible for them to distort in such a way that the strains calculated at the integration point are all zero, which, in turn, leads to uncontrolled distortion of the mesh** [27].

The element discussed was used for the rail as well as the slipper models. It has also been successfully used in prior work simulating high-speed impacts and high strain rates with finite elements [63][62][18].

The mesh was limited by computational realities. As a result the finer mesh was used at the bottom of the slipper and the top of the rail with coarser meshing throughout the rest of the model. The total number of elements is shown in Figure 3.4.

3.2.2.4 Wear Rate Calculation.

The three dimensional FEM is used to calculate a wear rate for the slipper during a test event. The overall method is shown in Figure 3.6 and will be described in more detail in the following section.

The first step in this method is determining the asperity sizes that are present in the rail. Voyiadjis carried out work in 2009 [20]. By using a scanning electron microscope, the surface roughness of the 1080 steel rail was resolved to view peaks or asperities. These were compiled by size and distribution as shown in Figure 3.7. From this, it is shown that there are five asperity sizes ranging from 1 μm to 5μm. These asperities are modeled as shown in Figure 3.8.

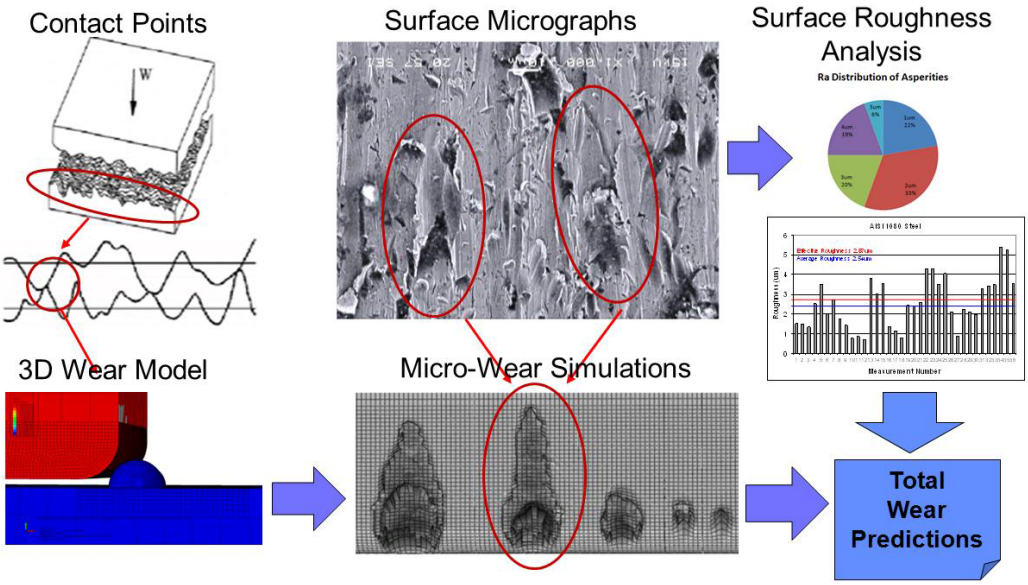

Figure 3.6: Wear calculation method.[18]

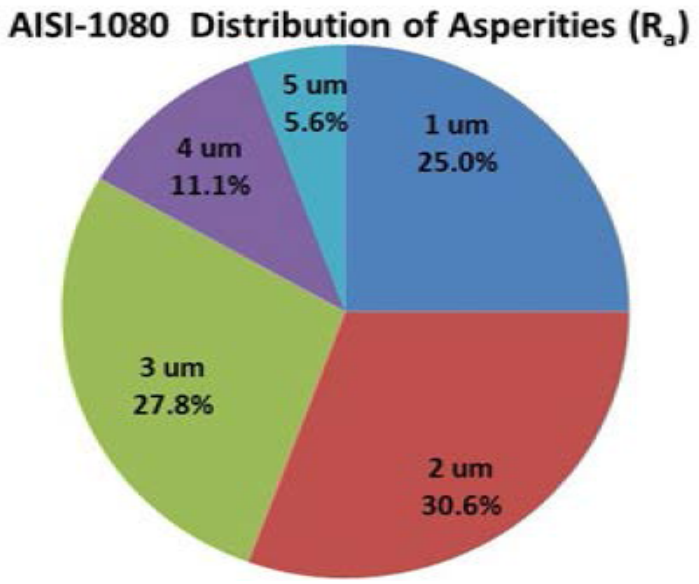

Figure 3.7: AISI-1080 Steel Distribution of Asperities.[18]

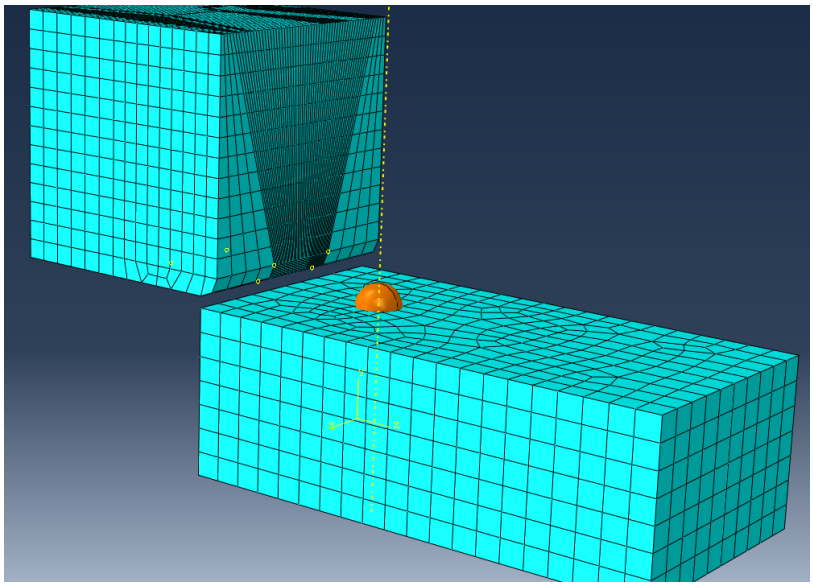

Figure 3.8: 3D FEM with 5μm asperity.[18]

The three dimensional FEM provides damage simulations as shown in Figure 3.6. There are three additional steps required to obtain the total wear rate.

1. Normalized Wear Volume

2. Normalized Wear Rate

3. Total Wear Rate

The normalized wear volume is required to account for different size asperities causing damage to the slipper. By obtaining normalized wear, the result can then be used to estimate wear based on area versus per asperity. The FEM is used to simulate the slipper contacting an asperity of a certain size at a certain velocity. This results in damage to the slipper in the form of removed elements, which can be used to calculate the volume of material removed and thus eventually the wear rate. This is expressed in the equation below as $Vol_{I,na}$. There are four asperities and thus four values of $Vol_{I,na}$ per velocity interval. The asperity sized at 1 μm would never interact with the slipper model due to the gap sized at 4.5 μm. The resulting value for $Vol_{I,na}$ is multiplied by the percentage of each asperity size found on the surface of the rail per Figure 3.7. The product is added to the other products due to the different asperity sizes. This result is multiplied by the number of asperities per unit area to find the volumetric wear per unit area Vol_I.

$$Vol_I = \#Asp \sum_{na=2}^{5} \%Asp_{na} Vol_{I,na} \tag{3.1}$$

Vol_I - Volumetric wear per unit area at velocity increment, I

I - selected velocity interval, this study modeled 4

$\#Asp$ - # of asperities per unit area, Buentello determined 601 from Scanning Electron Microscope (SEM) image in Figure 3.6

na - size of the asperities, this study modeled 4 sizes

$\%Asp_{na}$ - % of asperities of size n (from Figure 3.7)

$Vol_{I,na}$ - simulated wear (volumetric) due to an asperity of size n at velocity increment I

All of these values are known except for $\#Asp$. To estimate this value, Buentello [18] hypothesized that damage observed under SEM was due to asperities of sizes 3μm, 4μm, and 5μm. The size of the SEM sample ($0.09mm \times 0.125mm$) is used to estimate $\#Asp$.

The normalized wear rate is then calculated. The normalized wear rate, W_I is defined as the volume of material removed per unit of sliding distance [92]. It is calculated by dividing the volumetric wear per unit area at each velocity interval, Vol_I by the sliding distance D_s. The sliding distance is taken to be a unit value (1 mm). This results in a FEM estimate for wear rate that can now be applied to the slipper wear from a sled test.

$$W_I = \frac{Vol_I}{D_s} \tag{3.2}$$

Once the normalized wear rate is calculated, the total wear rate can be estimated. Due to the various velocities experienced by the sled, the entire test must be divided into intervals. This is due to the fact that wear is dependent on velocity. The FEM simulates material damage at different velocities. This translates into several different normalized wear rates, W_I. This in turn is used to calculate the total wear rate for that portion of the test using the equation:

$$Vol_{I,Tot} = W_I \times l_{c_I} \times w_c \times D_{sl_I} \times \%Cont_I \tag{3.3}$$

Finally, this total wear for the interval is added to the total wear at the rest of the intervals to arrive at the total wear for the entire sled test (acceleration only).

$$Vol_{Tot} = \sum_{I=1}^{4} W_I \times l_{c_I} \times w_c \times D_{sl_I} \times \%Cont_I \tag{3.4}$$

where:

l_{c_I} - slipper length per velocity interval

w_c - slipper width, fixed 90mm per Buentello estimate [18]

D_{sl_I} - sliding distance per velocity interval, this study used 4

%Cont - percentage of time slipper in contact with rail, determined from DADS

W_I - normalized wear rate per velocity interval

3.2.3 Shock Wave Model.

3.2.3.1 Concept.

As part of this phase of modeling a shock wave due to the high velocity asperity impact modeled was a consideration. As such, the wave propagation and behavior were studied. Figure 3.9 is a graphical representation of the model used in the study. It was identical to the microscale wear model discussed on Section 3.2.2.

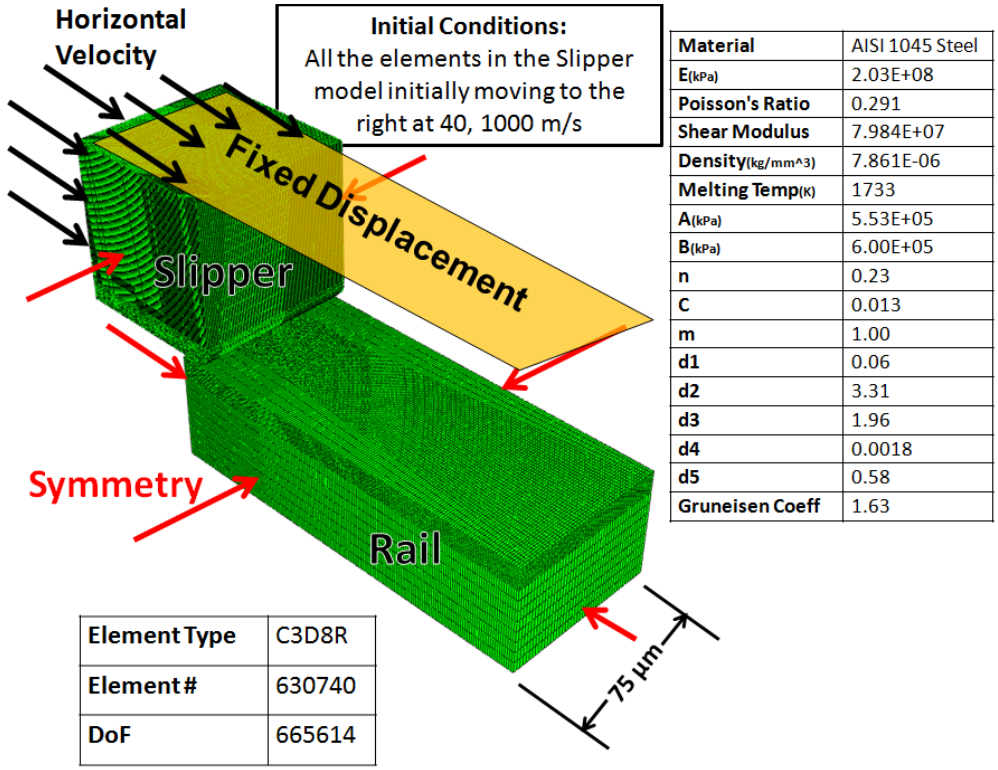

Material	AISI 1045 Steel
E(kPa)	2.03E+08
Poisson's Ratio	0.291
Shear Modulus	7.984E+07
Density(kg/mm^3)	7.861E-06
Melting Temp(K)	1733
A(kPa)	5.53E+05
B(kPa)	6.00E+05
n	0.23
C	0.013
m	1.00
d1	0.06
d2	3.31
d3	1.96
d4	0.0018
d5	0.58
Gruneisen Coeff	1.63

Element Type	C3D8R
Element #	630740
DoF	665614

Figure 3.9: Microscale FEM used in shock wave analysis

The major difference in the models is the material modeled. As opposed to the materials that were used in the construction of the slipper and rail i.e. Vascomax 300 and 1080 steel respectably, AISI 1045 steel[30] was modeled for both the slipper and rail models. This was done due to the fact that the model response was not the primary focus of this study. To model the shock wave with minimal interference from other factors, variables were reduced. As previously mentioned, there is a dearth of data for 1080 steel and Vascomax 300 in regards to Johnson-Cook failure model parameters and Mie-Gruneisen equation of

state coefficients. These were all available for 1045 steel. In addition, both the slipper and rail models utilized the same material model to reduce effects of differing material behavior impacting the results.

The boundary conditions, initial conditions, meshing and element type are all the same as used for the microscale wear model.

3.3 Heat Transfer Model

3.3.1 Overview.

Of the three modes of heat transfer, conduction, convection, and radiation, this model attempts to approximate two of them. Conduction is the heat transfer between two materials at different temperature. In this case, the temperature differences are due to frictional heating. Convection is the heat transfer due to the movement of mass within a fluid. As the sled moves down the track, the air interacts with it providing lift as well as cooling to some extent.

This model incorporates a one-dimensional finite difference scheme to estimate the heat transfer through the thickness of the slipper. The slipper used in the 2008 test was constructed of Vascomax 300. This model used material properties closely associated with that metal as discussed in Section 2.4.2.2.

The HHSTT scenario has several features that need to be accounted for in the one dimensional thermal model. These features include inputs of velocity, acceleration, and intermittent contact. The inputs are used to calculate thermal energy, aerodynamic forces and contact/no contact. Several other considerations must also be accounted for including partitioning the thermal energy between the slipper and the rail, material properties of the slipper, and slipper geometry as it travels down the rail. Figure 3.10 graphically represents the heat transfer model inputs and algorithm. The inputs on the left are updated at each time step. The check for bouncing determines whether the heat flux due to either conduction or convection was utilized. If the slipper and rail are in contact, the partition function was

utilized to determine the amount of energy that enters the slipper whereby the rest goes into the rail. In addition, the material properties are used to fill the matrices that represent the finite difference heat equation which utilized 100 nodes through the slipper's thickness. At each time step the temperatures are checked to ensure that melt was not exceeded. If it does, a melt depth is calculated with linear interpolation and the heat equation solved repeatedly until the energy removed through the latent heat of fusion was enough to reduce the temperature below melt. Once this occurred the algorithm advanced to the next time step. Each of these items will be discussed in detail below.

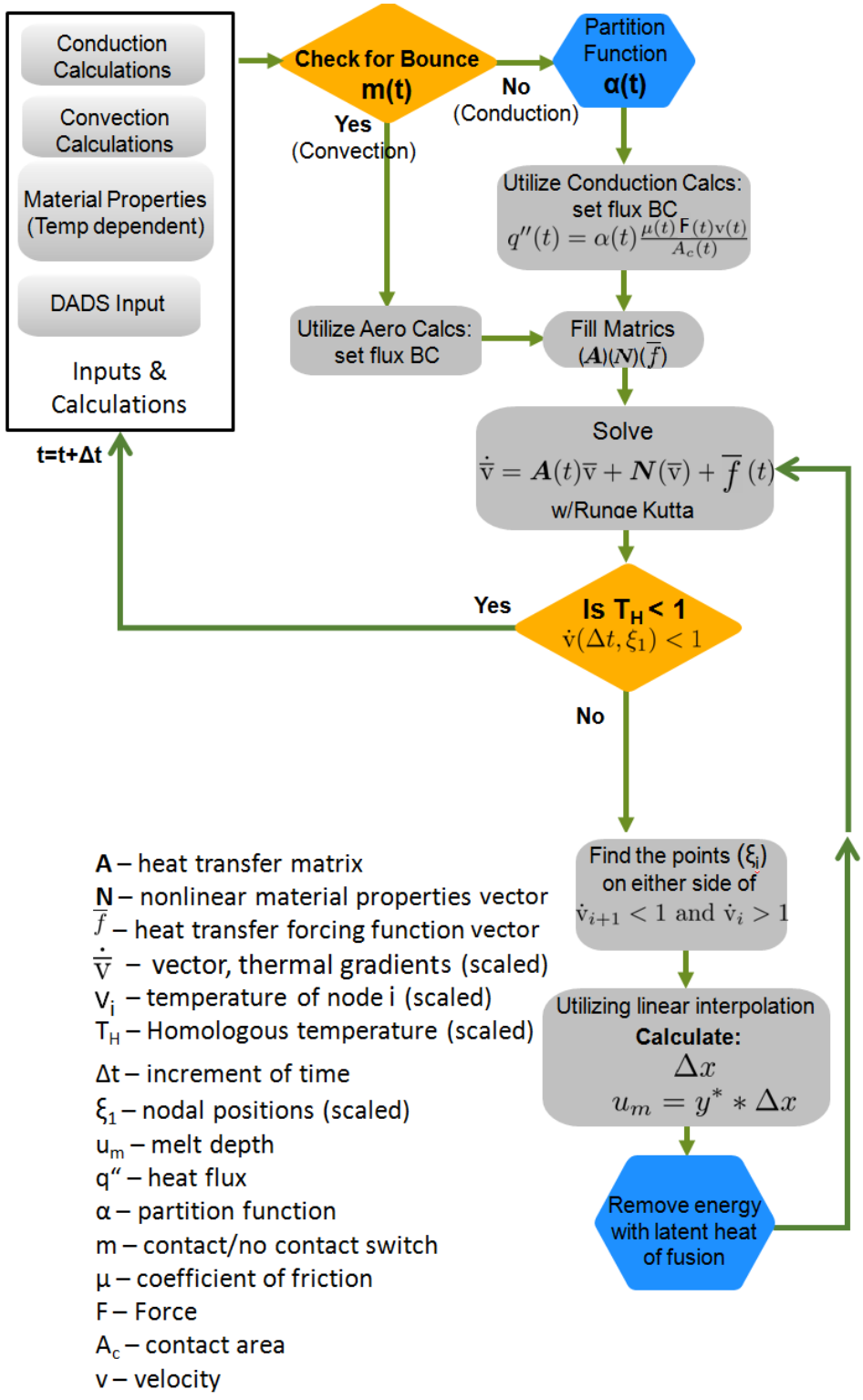

Figure 3.10: Melt Wear Estimation Flowchart

3.3.2 Assumptions/Limitations.

This model incorporated input parameters from DADS and used material properties (specific heat and thermal conductivity) that were temperature dependent. In addition, the friction was based on varying pressure by changing the contact area of the slipper per previous work done by Buentello [18]. The one dimensional heat transfer solution assumes insulation along the length(depth) as seen in Figure 3.11.

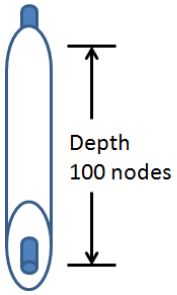

Figure 3.11: Insulated wire representation

The one-dimensional heat transfer analysis is limited to a single position on the slipper. In addition, to calculate the conduction and convection that occurs on the underside of the slipper a partition function is required. This function α, divides the thermal flow to the slipper and to the rail. This function has not been matched to actual test data but is an approximation based on previous models. Figure 3.12 shows the partition function as portions of the total frictional energy (q") entering the slipper and the rail respectively. The relative amounts are not known and in the past have been estimated. The partition function is discussed in further detail in Section 3.3.5.1.

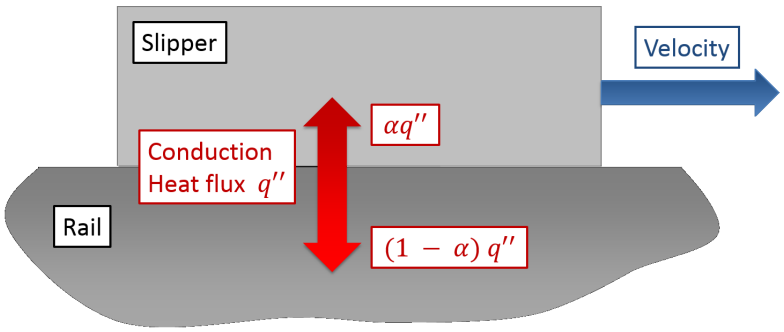

Figure 3.12: Partition function [17]

During the test run, the sled also bounces due to aerodynamic forces as pointed out. This results in the slipper bouncing on the rail as seen in Figure 3.13. This means that the distance between the slipper and the rail changes as a function of time. The one-dimensional heat transfer analysis utilizes a binary definition of bounce. Either the slipper is in contact or it is not. When it is not in contact, it is assumed that the distance between the slipper and the rail is 3.175mm. This is the maximum clearance between the slipper and the rail not the average. In addition, this is the measurement from the 2008 sled test.

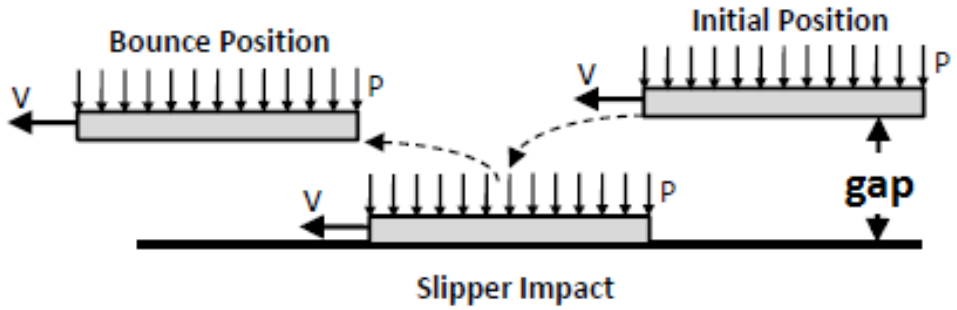

Figure 3.13: Slipper bounce [3]

While the sled is lifted, there is a gap between the slipper and the rail as described above. Air flows through this gap and contributes to the heat flux as shown in Figure 3.14. This flow is modeled as two-dimensional flow when in reality the airflow is three-dimensional and complex due to the wraparound nature of the slipper and the slipper bouncing resulting in constantly changing gap dimensions. The slipper also rolls with respect to the rail further changing the geometry and hence the airflow in the gap [18]. Any yaw that the slipper experiences would likewise change the airflow. The slipper position on the sled also contributes to the airflow complexity. A slipper at the front of the sled will see very different conditions than the slippers in the middle and the rear of the sled respectively. The airflow is also assumed to maintain its velocity for the entire length of the slipper. In

reality the temperatures, friction, and different geometries would change the velocity and properties over the slipper length. As previously mentioned, the airflow is not modeled with hypersonic considerations such as high temperature gas dynamics. This could affect the model results, however the shock due to structure impingement may lower the velocity of the airflow thereby reducing the error of the approximation used.

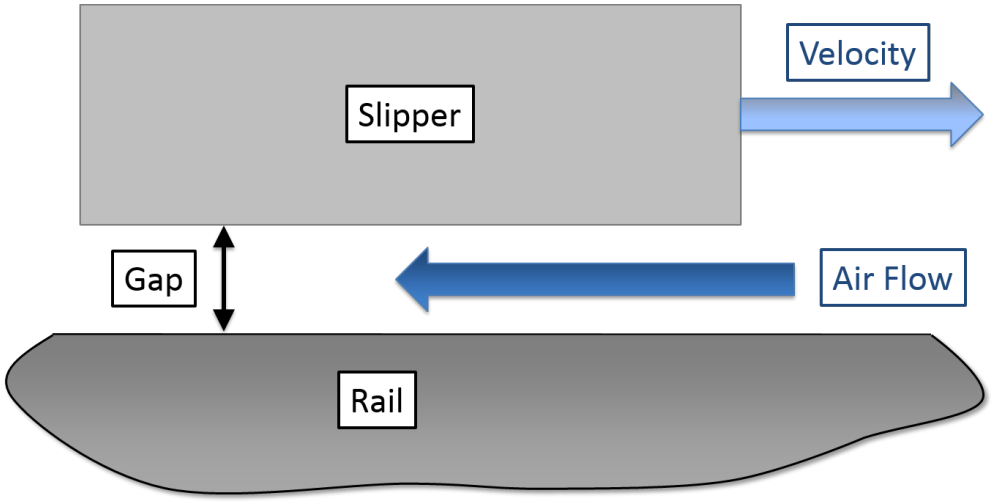

Figure 3.14: Slipper-Rail Gap [22]

3.3.3 Material Properties.

One of the contributions made in this research was taking into account the fact that the specific heat and thermal conductivity for the materials under study are not constants over the temperature range of interest. As the slipper experiences temperatures ranging from ambient to above melt, these properties change significantly.

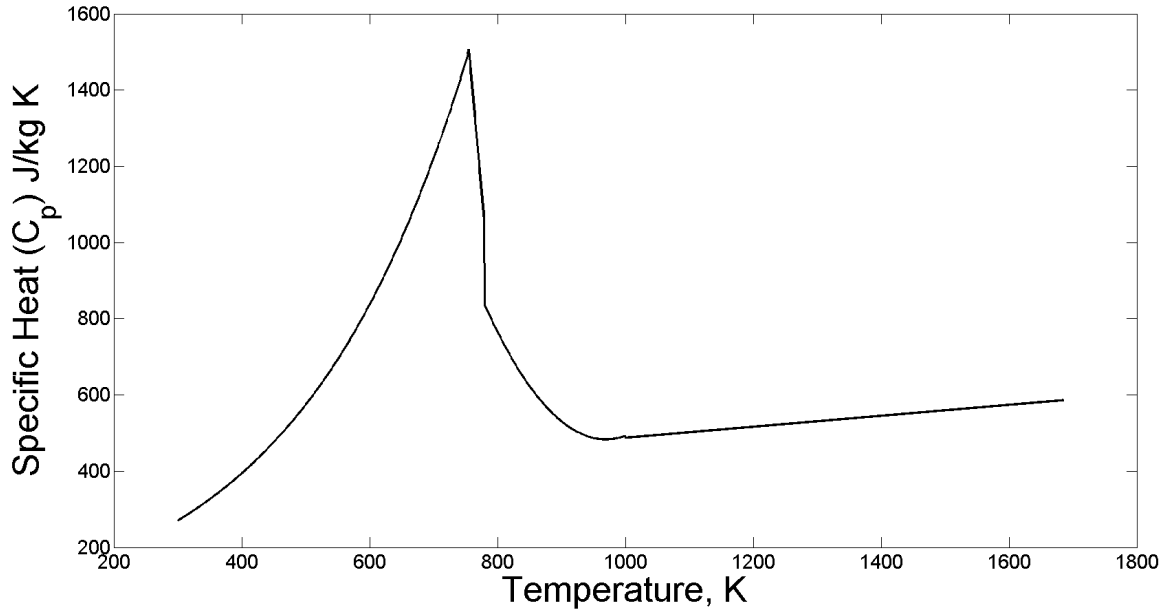

Figure 3.15: Specific Heat (estimated)[30]

Figure 3.15 shows the specific heat as estimated by curve fitting data and extrapolating as discussed in Section 2.4.2. At each node for each time step as the temperature is calculated the specific heat was selected as appropriate based on this curve. The same held true for the thermal conductivity as shown in Figure 3.16. This coupled behavior between the temperature calculation and material property dependence led to a nonlinear solution. This required the coefficients for each node to be calculated at every time step. This is reflected in the matrix equation developed in Section 3.3.7.1 and shown in Equation 3.25.

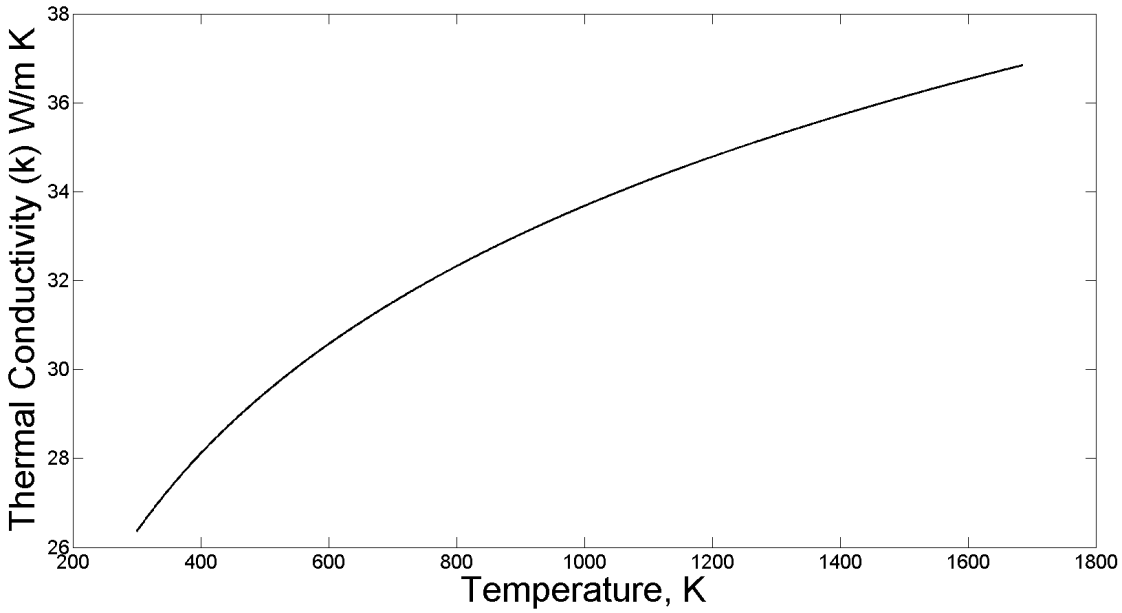

Figure 3.16: Thermal Conductivity (estimated)[30]

3.3.4 Slipper Geometry.

As shown in Section 3.3.5.2, the melt estimation is dependent on friction as an input to calculate the heat flux at the interface between the slipper and the rail. The friction is dependent on the pressure and velocity. The velocity is input directly from DADS but the pressure must be calculated. This was done by taking the DADS input as described in Section 3.3.4.1 and dividing it by the contact area at each time step. The contact area varies over time as described below.

As previously stated, this research compared a calculated melt wear estimation with thickness measurements from a worn slipper as shown in Figure 3.17. Previous research from Buentello[18] has indicated that the slipper rotated, during the 2008 test, due to momentum shifts as the different stages of rockets were fired. This was based on measurements taken from a worn slipper by Hale [3]. Figure 3.18 depicts the slipper rotation during a test run at the HHSTT in 2003 [31]. This rotation caused the slipper to have less than full contact, lengthwise, with the rail. Figure 3.17 is based on the wear measurements of the 2008 slip-

per overlaid with the hypothesized slopes due to the different rocket stages.

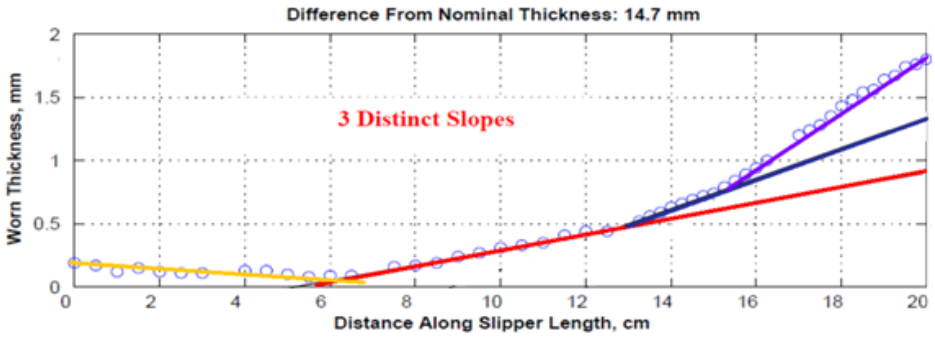

Figure 3.17: Wear due to slipper rotation[18]

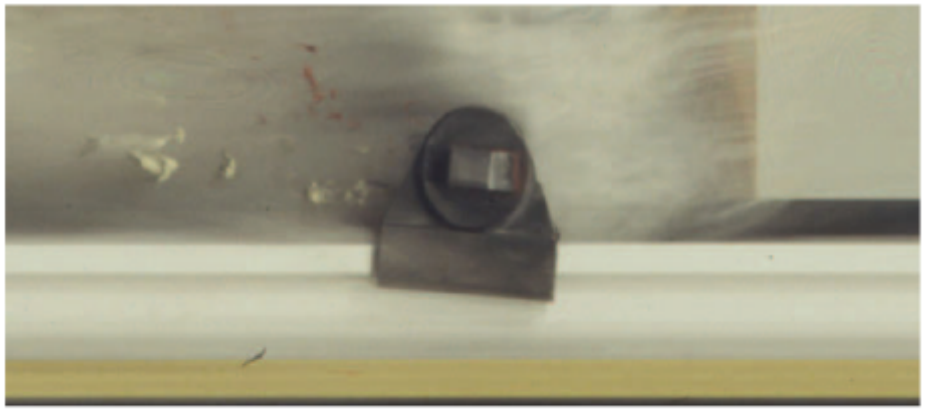

(a) 80X-G1 Test Mission, April 2003, V = 2,853 m/s.

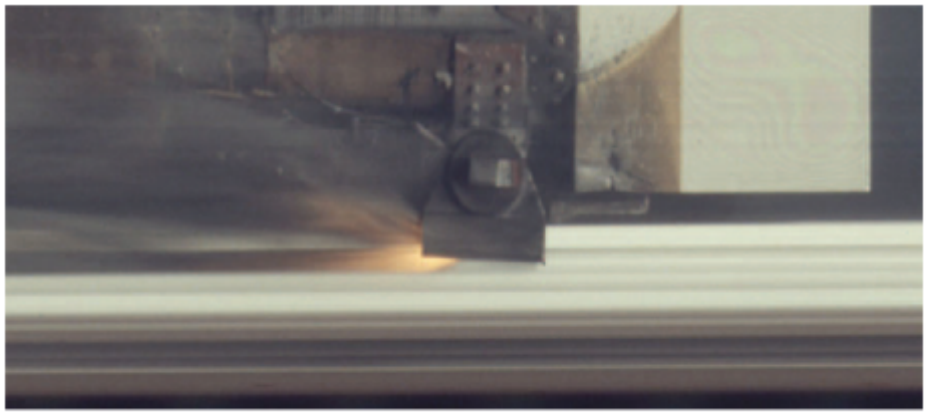

(b) 80X-G1 Test Mission, April 2003, V = 2,861 m/s.

Figure 3.18: Slipper rotation[31]

The slipper width was taken to be a constant in this research. Buentello showed in Figure 3.19, the width in contact is less than the full width of the actual slipper [18]. Previous research used the full width of the slipper to calculate the area in contact. It is actually the width of the rail that needs to be considered. As the pressure is of interest in calculating friction, the area in contact is used and 90 mm was taken to be the constant width in this research.

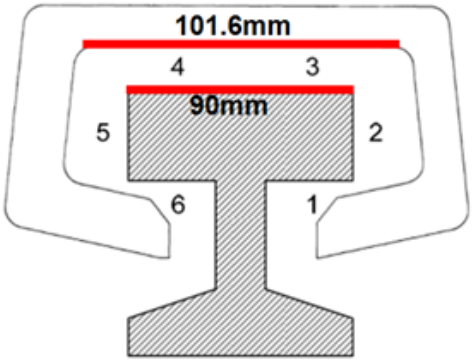

Figure 3.19: Slipper - width in contact[18]

Thus the area in contact constantly changes as shown in Figure 3.17. Figure 3.20 relates the length n contact from Figure 3.17 to the contact area. In the same figure, the slipper rotation is shown as a rectangle that initially contacts the rail on a corner. As that contact length grows, due to wear, the contact area grows. L1 is the contact area during the first rocket stage. The length grows to its final distance of approximately 140 mm. The corresponding final contact area is shown as approximately 12000 mm^2. As the second stage fires, the slipper rotates and the corresponding contact area is reduced to near zero. This area again grows due to wear and is labeled L2 in Figure 3.20. L2 has a final length of near 70 mm. The corresponding contact area grows to approximately 6000 mm^2. The final stage experienced by this particular slipper reduces the contact area to near zero once again. The length labeled L3 grows due to wear with a final length of near 45 mm. As shown, the final

contact area is approximately 4000 mm^2.

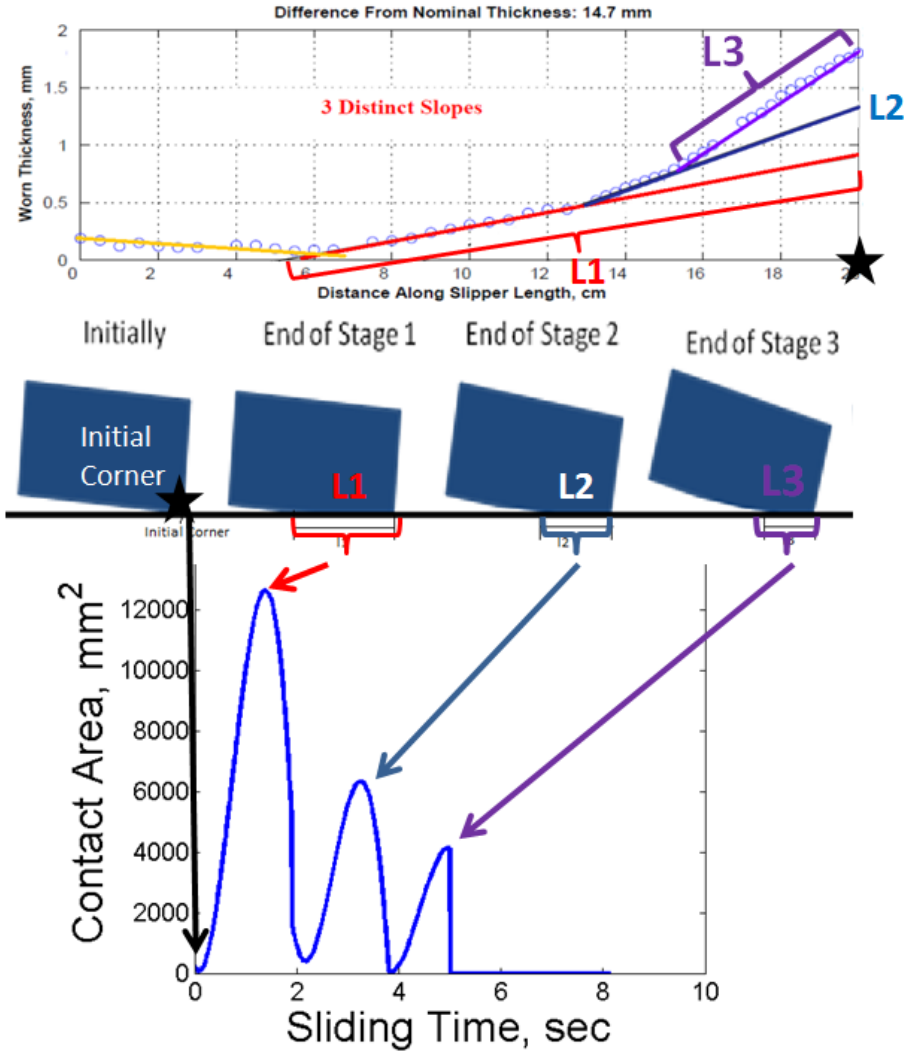

Figure 3.20: Slipper area in Contact

The slipper length in contact was never reduced to zero. Figure 3.21 displays the physical reason for this. The wraparound design of the slipper limits the amount of rotation for the slipper. The largest gap between the slipper and the rail is 3.175 mm. The minimum length in contact was set at 0.2 mm.

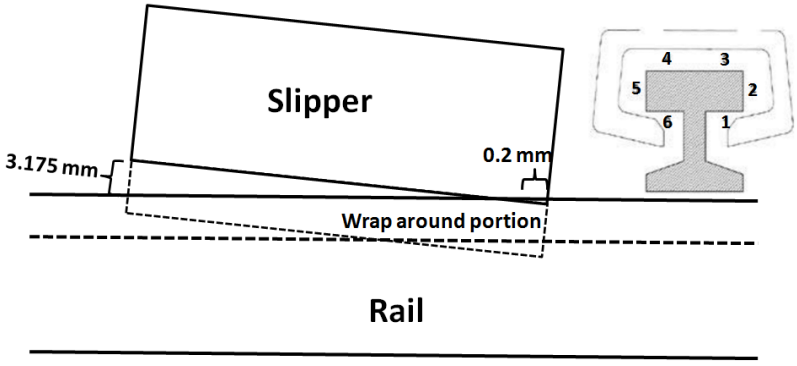

Figure 3.21: Length in contact - Limit

At every time step, the model checks to ensure that the surface temperature does not exceed the melt temperature. The one-dimensional model estimates the melt depth at each time step when the temperature exceeds melt. This resulted in varying pressure, leading to increased friction inputting more heat energy into the slipper driving the higher temperature. The higher temperature eventually reached a melt temperature leading to material removal. This fact is important as it was not taken into account in previous research leading to far lower melt estimations. It must be noted that the contact area is dependent on number of rocket stages and structural design and differs from test to test. The method of melt estimation is described in further depth in Section 3.3.7.2.

3.3.4.1 DADS.

For this research the force data is supplied by the Dynamic Analysis and Design System (DADS)[56]. DADS is commercial software that is a set of general purpose computer programs that can be used to model and predict the motion of a variety of real world mechanical systems. Using a set of data that describes the mechanism to be modeled, DADS builds a mathematical model of the real system that calculates positions, velocities, and accelerations of the various parts of the mechanism, as well as resultant forces that act on the system [56]. The DADS was used extensively in this research to estimate loads and bouncing of the slipper as it travels down the rail. This data is simulated data. It approximates actual loads seen by the sled during a test run based on test parameters, test

article particulars, and rocket propulsion capabilities. This data is used as a substitute for real data as it is not possible to instrument a sled to collect this type and quality of data during a real-time test. This can increase the difficulty in estimating wear since the actual test variables are not available. Figure 3.22 is the DADS output as related to the slipper bounce of the 2008 test.

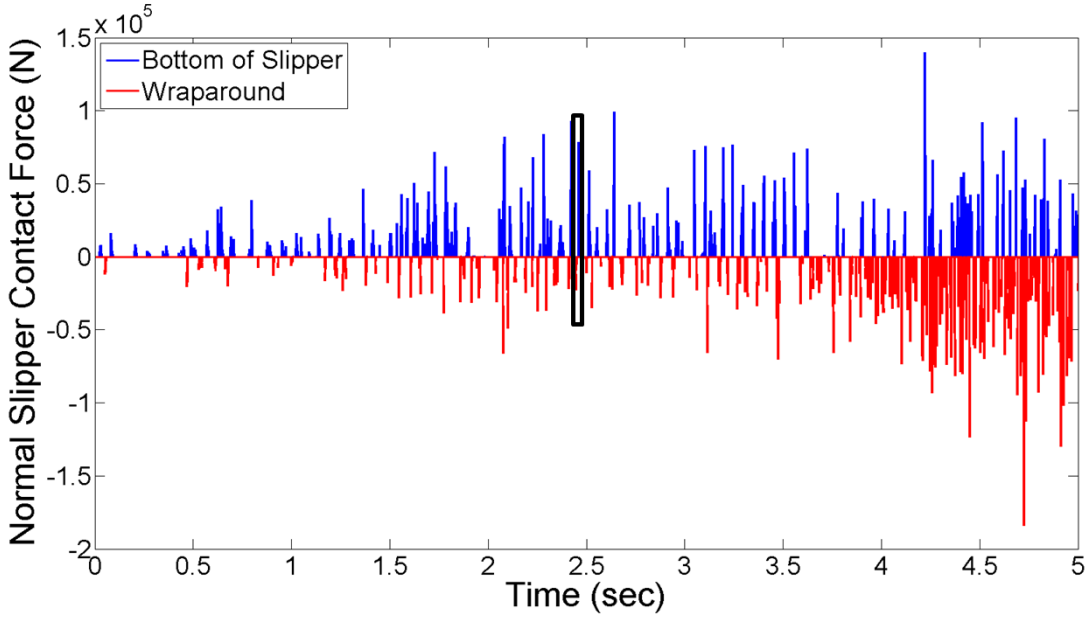

Figure 3.22: DADS Output (Force)[3]

As the slipper bounces on the rail during the test run, either the top portion of the slipper is in contact with the rail or the wraparound bottom portion of the slipper is in contact with the underside of the rail, preventing the slipper from departing the rail. The blue lines are the combined force predicted at the locations marked as 3&4 in Figure 3.23 while the red lines are the combined forces predicted at locations 1&6 in Figure 3.23.

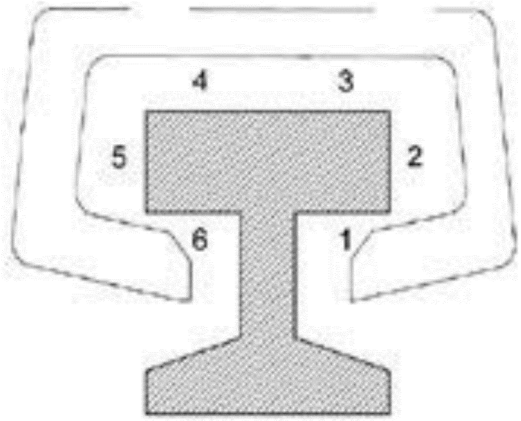

Figure 3.23: Wraparound Slipper

Figure 3.24 plots the portion of Figure 3.22 as delineated by the rectangular box at approximately 2.4 seconds. It first shows contact between the wraparound portion of the slipper (locations 1&6 in Figure 3.23) and the underside of the rail. There is intermittent contact followed by no contact. This is when the slipper is fully supported by aerodynamic forces but not to the point of having the slipper wraparound in contact. The blue line shows the underside of the slipper in contact with the top of the rail. In this particular instance the contact force is much greater than the wraparound contact (in red). Over the acceleration phase the underside of the slipper is in contact with the top of the rail approximately 11% of the time. The wraparound portion of the slipper is in contact with the underside of the rail approximately 7.5% of the acceleration time. Thus, leaving approximately 89% of the time when aerodynamic heating (cooling) occurred as discussed in Section 3.3.6.

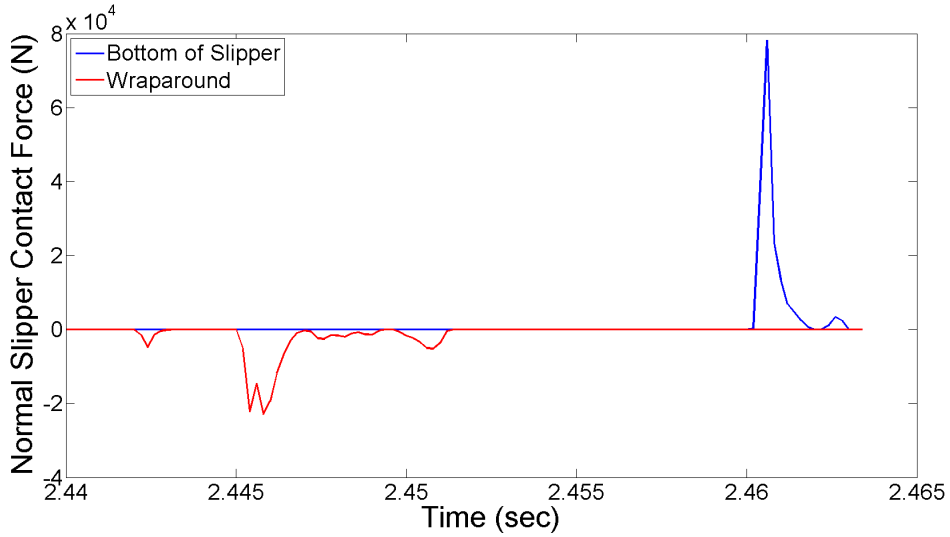

Figure 3.24: DADS Output (Force)[3]

Each high speed experiment at the HHSTT is first evaluated with DADS before being carried out to ensure its success. The DADS output was validated against three instrumented test runs to provide confidence in the model [57]. The data rate developed by DADS was used by the heat transfer model to simulate the acceleration portion of the 2008 test with $25,000+$ time steps. Within those steps a finite difference scheme was then used to solve the heat equation at each time step.

3.3.5 Conduction.

As the slipper travels down the rail, it constantly bounces as depicted in Figure 3.25. This is due to the aerodynamic forces that occur at high velocity. The sleds used for testing are designed to create lift in order to reduce contact pressures on the slippers thus reducing wear. As the sled is lifted above the rail, the wraparound slipper prevents the sled from departing the rail as shown in Figure 3.23. The combinations of these different forces cause the bouncing. As the slipper remains in contact with the rail, heat is conducted from one surface to the other. As shown, there is a heat flux condition that occurred when the slipper contacted the rail.

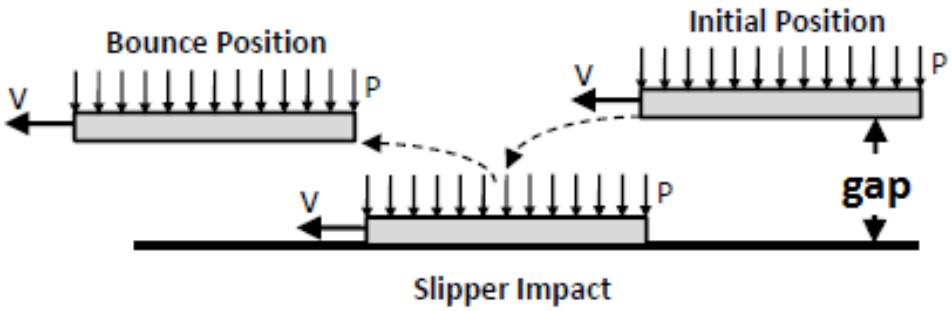

Figure 3.25: Slipper bounce[17]

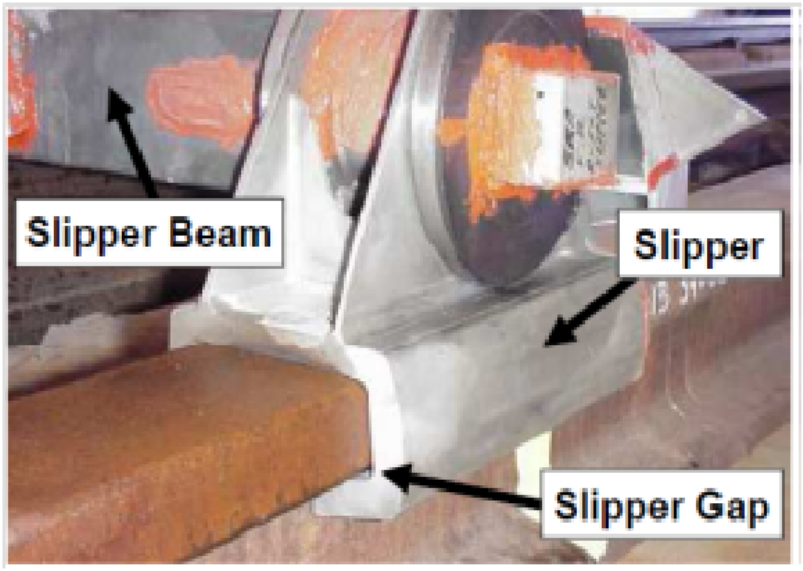

Figure 3.26: Wrap Around Slipper [3]

The actual distance between the slipper and the rail changed as a function of time. As a simplification, the one-dimensional heat transfer model utilized a binary definition of bounce. Either the slipper is in contact or it is not. When it is not in contact, it is assumed that the distance between the slipper and the rail is the slipper gap, shown in Figure 3.26. This is the maximum clearance between the slipper and the rail not the average. When the slipper is in contact, conduction occurs as shown in Figure 3.27 and the heat flux is calculated using Equation 3.3.6.

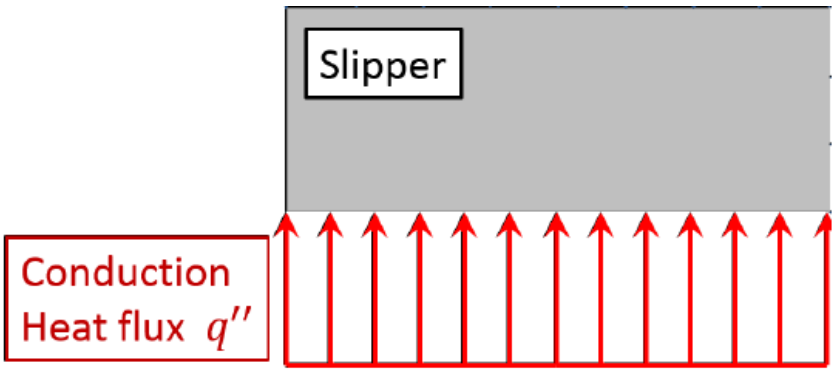

Figure 3.27: Conduction Heat Flux.[22]

$$q''(t) = \frac{\delta(t)\mu(t)F(t)v(t)}{A(t)} \tag{3.5}$$

$\delta(t)$ - partition function

$\mu(t)$ - coefficient of friction

F(t) - Force input from DADS

v(t) - velocity input from DADS

A(t) - Area in contact (discussed in previous section)

3.3.5.1 Partition Function.

The partition function background was discussed in Section 2.4.5. The exponential function described in Equation 3.6 was used throughout this study.

$$\delta(t) = 0.4e^{-5t^2} + 0.1 \tag{3.6}$$

As part of this research, data from a HHSTT test in 2014 was used to partially validate the partition function. Figure 3.28 shows the locations and depths where thermocouples were placed in a slipper during a 2014 test. Figure 3.29 displays the temperatures recorded by the two thermocouples embedded in the slipper that provided usable data. The

thermocouples were designed for temperatures up to 500^0 Fahrenheit. The temperatures experienced during the 2014 test exceeded those limits. However, the data that was recorded still allowed a partial characterization of the partition function.

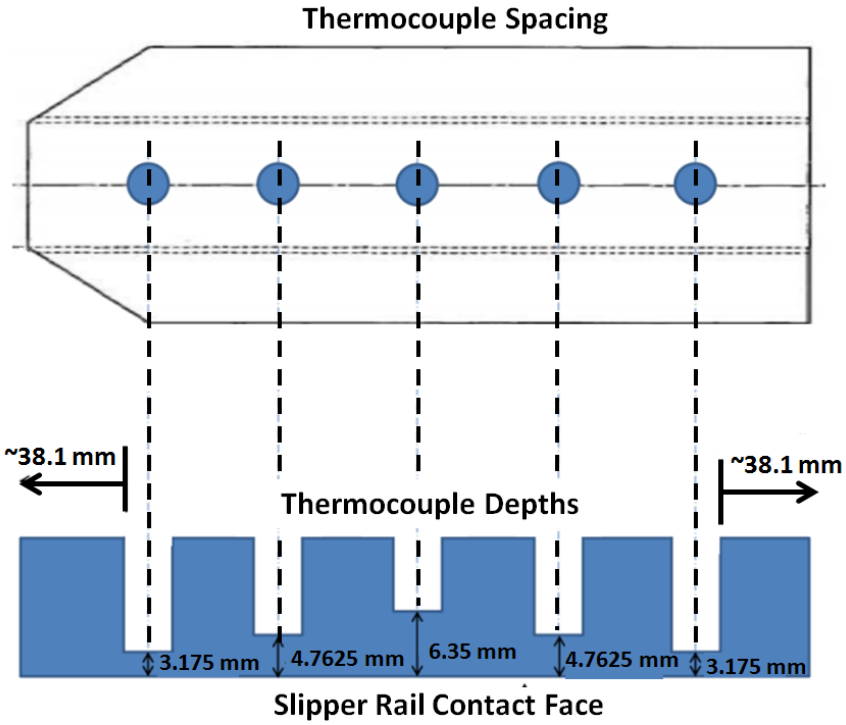

Figure 3.28: Thermocouple locations.

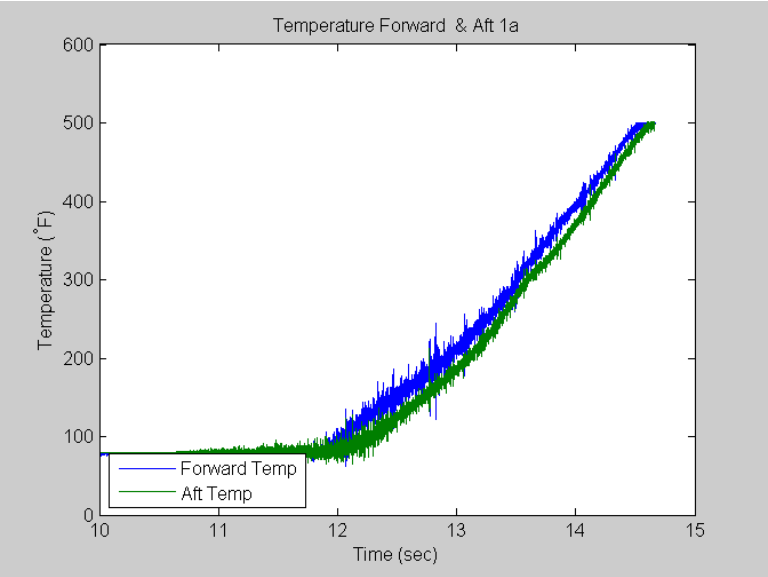

Figure 3.29: Recorded temperatures at front and rear of slipper.

The results are discussed in Chapter 4 Discussion and Results.

3.3.5.2 Friction.

Friction is defined as the force resisting the relative motion of solid surfaces, fluid layers, and/or material elements sliding against each other [93]. Charles-Augustine de Coulomb developed a model to calculate the force of dry friction using the following governing equation:

$$F_k = \mu_k N \tag{3.7}$$

where F_k is the frictional force exerted by each surface on the other, μ_k is an empirical coefficient of kinetic friction, and N is the normal force exerted by each surface on the other.

With the DADS providing the force and velocity, the frictional coefficient can be calculated from previous work by Hale[3]. By using a curve fit of data from research done by Montgomery[89], Figure 3.30 was plotted by Hale[3] with use of the equation:

$$\mu_k = \begin{cases} 0.2696e^{-3.409x10^{-7}Pv} + 0.3074e^{-6.08x10^{-9}Pv} & \text{for } 0 < Pv < 4.45x10^8 \\ 0.02 & \text{for } Pv \geq 4.45x10^8 \end{cases} \tag{3.8}$$

The values from this curve and the DADS data leads to the frictional heating based on work by Krupovage and Rassmussen[43]. They found that the power developed by friction is directly proportional to the material friction coefficient, bearing pressure, and relative velocity. The first is found with the function above while the latter two are provided by DADS data for Force and velocity and the model providing an estimate for slipper area in contact. Since, P(t)=F(t)/A(t) all the variable are knowns. In Figure 3.30, the units for pressure and velocity are MPa and mm/s, respectively.

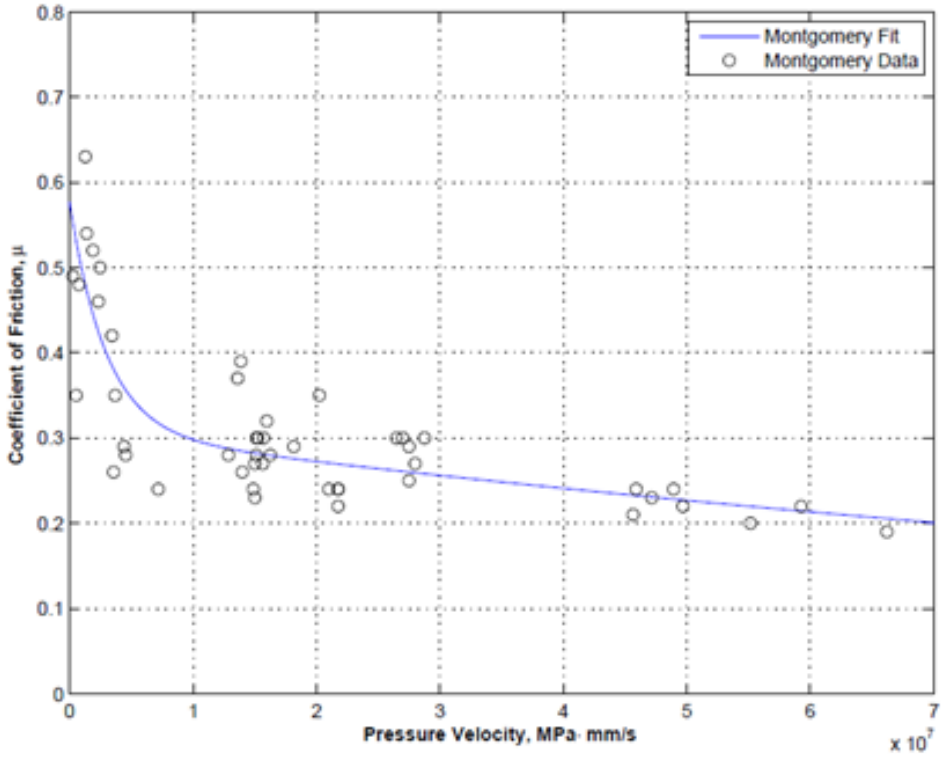

Figure 3.30: Montgomery Curve fit[3]

This is crucial to the heat transfer analysis as we now have pressure and velocity, which was shown to be related to the coefficient of friction. Based on Equation 3.8 and the inputs described, the coefficient of friction, which varies as the slipper travels down the rail, is shown in Figure 3.31. Figure 3.32 shows more detail on a smaller time scale. The coefficient of friction is zero when the slipper is not in contact with the rail. This figure shows the values varying while the slipper is in contact with the rail. This is due to the imposed slipper geometry varying, as previously described, as well as the varying vertical force as calculated by DADS. These values are used in Equation 3.5 to determine the heat flux at the slipper-rail interface.

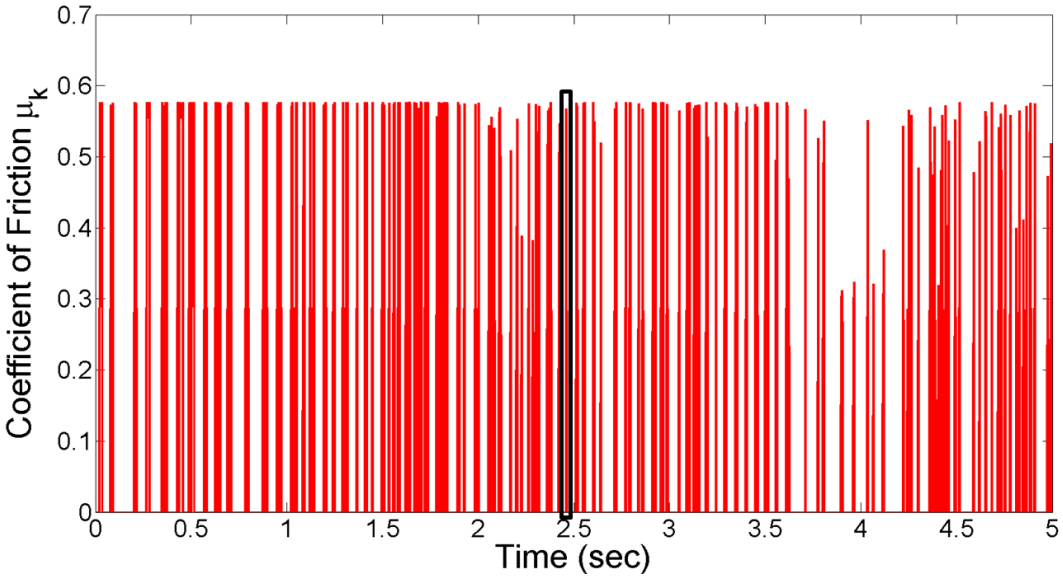

Figure 3.31: Calculated Friction Coefficient.

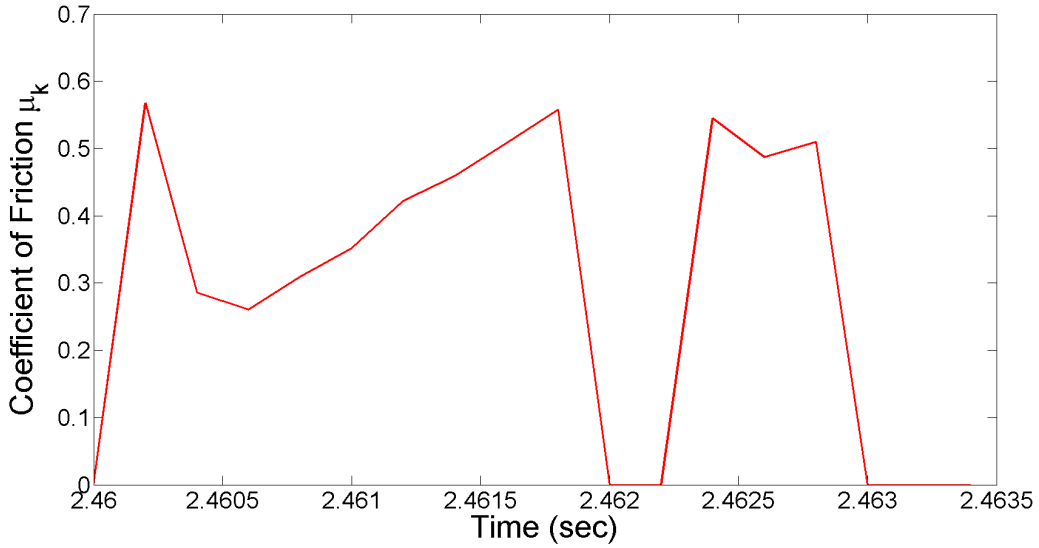

Figure 3.32: Calculated Friction Coefficient.

3.3.5.3 Heat Flux.

The previous sections discussed the slipper geometry and the Dynamic Analysis and Design System (DADS)output. Incorporating those, along with the sections on the partition function and calculating friction, provides sufficient information to calculate the heat flux

due to conduction per Equation 3.5. Recall that this calculation occurs at each time step with the Δt taken from the DADS output frequency. The times when the slipper is not in contact with the rail, the heat flux due to conduction is set to zero.

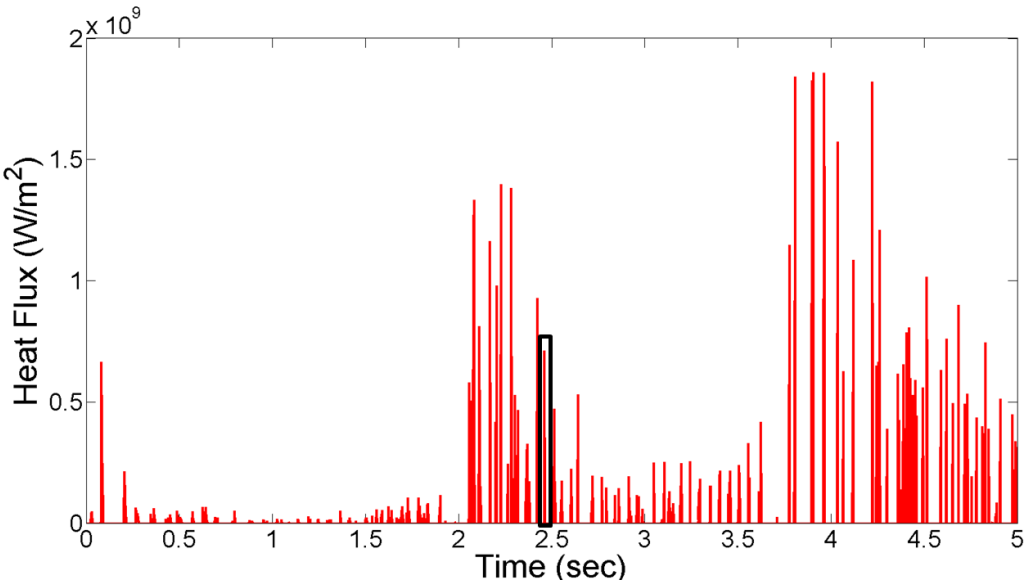

Figure 3.33: Heat Flux - Conduction.

Figure 3.33 is a plot of $q''(t)$. The rapid changes are due to the contact/no contact boundary condition due to bounce. At the beginning of the acceleration phase there is a spike that occurs. This is due to the initial contact area, which begins on the order of 50mm^2. As the contact area grows per Figure 3.20, the heat flux is reduced. It grows quickly at just after the 2 second mark due to the second stage firing. Per the slipper rotation hypothesis, the area in contact is reduced and the heat flux is increased due to its dependence on contact area per Equation 3.5. As the contact area grows the heat flux is again reduced. Stage 3 occurs at approximately 3.8 seconds when the contact area is once again reduced. In addition, the heat flux is also dependent on velocity and those effects are seen in the figure as well.

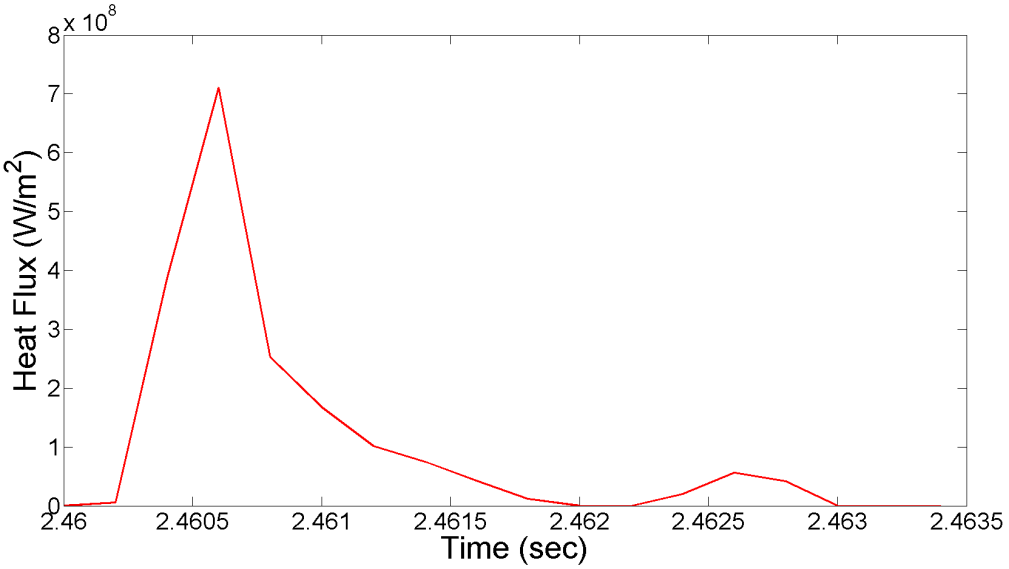

Figure 3.34: Heat Flux - Conduction.

Figure 3.34 presents a detailed view of the time indicated in Figure 3.33 by the black rectangular box at approximately 2.4 seconds. It begins at zero indicating that the slipper is not in contact with the rail. It rapidly grows due to the effects previously mentioned. It begins to decay

3.3.6 Convection.

As the sled travels down the rail at hypersonic speeds, numerous shocks develop at various locations on the sleds and their interactions are difficult to predict. As the gap develops, a boundary layer forms and convection occurs. This leads to heat transfer due to convection and will be discussed in this section. As the slipper travels down the rail and bounces, there is the gap between the slipper and the rail. Air passes between the slipper and rail, and through convection, tends to cool the material previously heated due to conduction. As the velocity increases, the air temperature rises but never reaches melt temperature. Thus, when the slipper is not in contact, convection occurs as shown in

Figure 3.35 and the heat flux is calculated using

$$q''(t) = h(T_{awb} - T_s) \tag{3.9}$$

The values of h and T_{awb} were calculated by Alban[22]. These values are calculated with equations derived from aerodynamics as discussed in Section 2.4.4. The dynamic nature of the flow-field necessitates the location, along the length of the slipper, where the calculations could be completed. Figure **??** includes the approximate location where the results of the calculations hold. Several items need to be considered when choosing a location. First is the wear pattern that occurs on the underside of the worn slipper from the 2008 test. Hale noted that the most occurred toward the front of the slipper with the highest loss at the very front [3]. However, recall that the contact area has a large influence on the wear due to its relationship to the coefficient of friction through pressure. The contact area grows over time but the one-dimensional finite difference scheme should be as near to the center of that as possible. Note that the nodes do not move lengthwise during the simulation and are thus notionally placed through aerodynamic and contact area considerations. T_s is the surface temperature of the underside of the slipper as calculated at each time step.

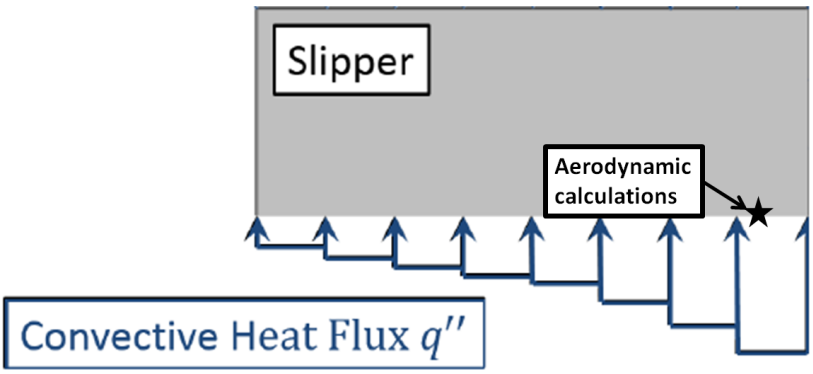

Figure 3.35: Convection Heat Flux.[22]

Figure 3.36 shows the results of the aerodynamic calculations previously discussed. Since the calculations are highly dependent on velocity it is logical that the heat flux grows over the acceleration phase. The different stages are reflected in the slopes of the flux growth.

The first stage ends at approximately 1.9 seconds. This correlates with approximately 340 m/s which is equivalent to Mach 1 at sea level. The next stage occurs at approximately 3.8 seconds where the flux begins an even steeper climb. It is noted that the predominate flux imposed on the underside of the slipper is the convective heat flux. As discussed the slipper is in contact with the top of the rail only 11% of the time. The rest of the time there is a gap between the slipper and the rail where air flows, cooling the slipper.

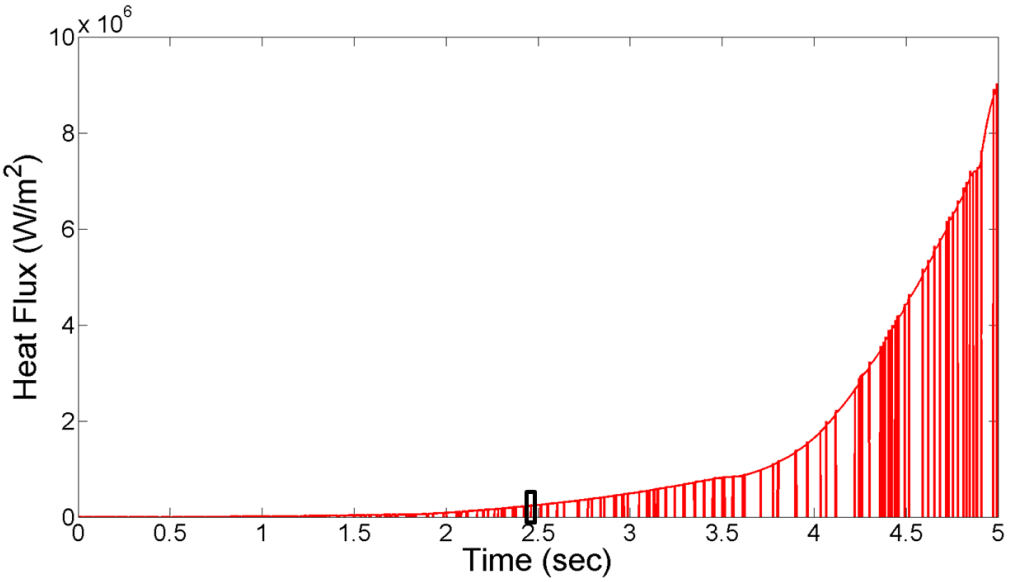

Figure 3.36: Heat Flux - Convection

Thus, Figure 3.37 is in contrast to Figure 3.34 in that it shows a relatively long period of time that the convective heat flux is imposed on the underside of the slipper. The times when the value drops to zero correlates with the times that the slipper contacts the top of the rail and conduction occurs.

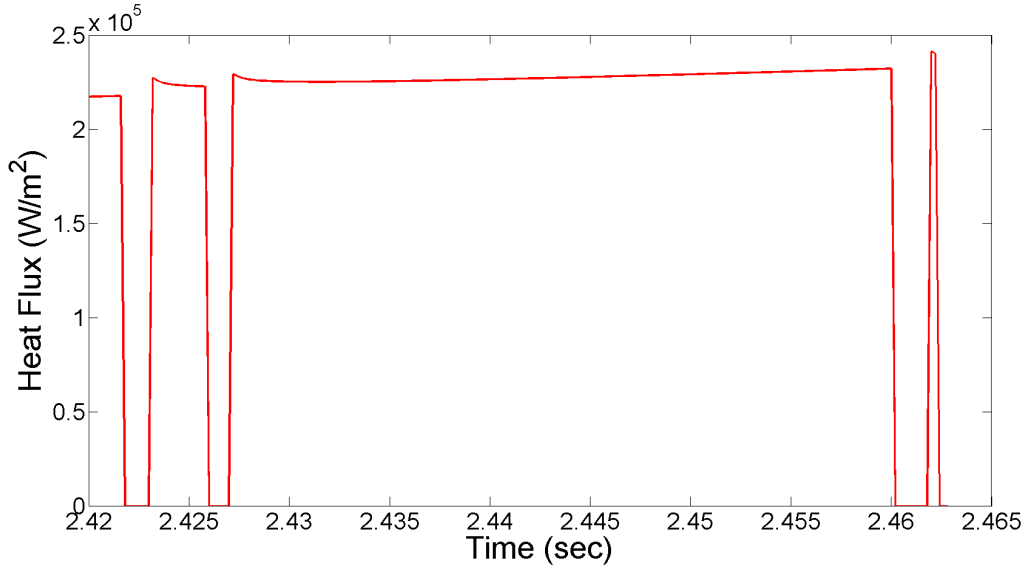

Figure 3.37: Heat Flux - Convection

Figure 3.38 plots the temperatures calculated due to aerodynamic effects. Of note is that the temperatures are all at or above 300°K. This is a more accurate representation of the temperature between the slipper and the rail as the slipper accelerates. The temperature never approaches the melt temperature of 1685°K. The aerodynamics heat the air but it acts to cool the slipper due to the relative temperatures.

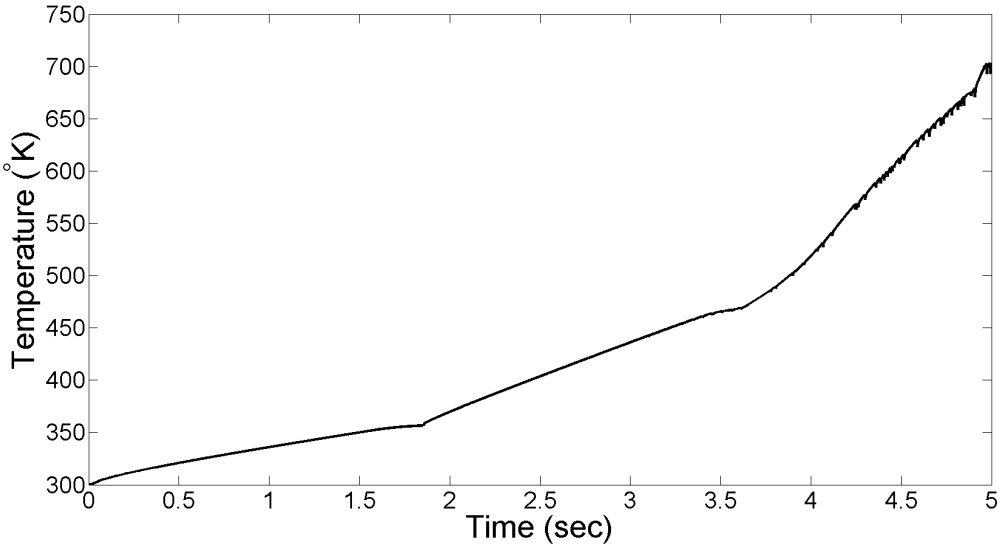

Figure 3.38: Temperature due to aerodynamics [32]

3.3.7 Heat Equation.

3.3.7.1 Finite Difference.

The heat transfer calculation was performed every 0.0002 seconds for the duration of the run. This was based on the data from DADS. This results in approximately 40000 increments for the eight second test run of the 2008 test. At each of these increments, the MATLAB code calculates a heat transfer solution using the finite difference scheme. This accounts for the conduction that occurs at the slipper-rail interface during those times that they are in contact as depicted in Figure 3.27. It also calculates the convection that occurs during the times of bouncing when a gap occurs between the slipper and the rail as shown in Figure 3.35.

The heat transfer equation for the slipper rail scenario must be discretized. The spatial derivatives are discretized using a central difference scheme. The equation is first scaled by temperature, hence ω, and spatially with ξ. The scaling and further development of the heat equation is contained in Appendix A.

$$\frac{\partial \omega}{\partial \xi}(\xi_i, t) = \frac{\omega(\xi_{i+1}, t) - \omega(\xi_{i-1}, t)}{2\Delta\xi} = \frac{\overline{v}_{i+1} - \overline{v}_{i-1}}{2\Delta\xi} \tag{3.10}$$

ω - scaled temperature

ξ - scaled distance

and

$$\frac{\partial^2 \omega}{\partial \xi^2}(\xi_i, t) = \frac{\overline{v}_{i+1} - 2\overline{v}_i + \overline{v}_{i-1}}{(\Delta\xi)^2} \tag{3.11}$$

N - number of nodes

for $2 \leq i \leq N$

and define $\overline{\mathrm{v}}_i(t) = \omega(\xi_i, t)$

Then

$$\dot{\overline{\mathrm{v}}}_i(t) = \frac{d}{dt}\overline{\mathrm{v}}_i(t) = \frac{\partial \omega}{\partial t}(\dot{\xi}_i, t) \tag{3.12}$$

$\overline{\mathrm{v}}$ - vector, nodal temperatures

$\dot{\overline{\mathrm{v}}}$ - vector, nodal temperature gradient

Thus the Partial Differential Equation (PDE), Equation 3.13 becomes Equation 3.14.

$$\frac{\partial}{\partial y}\left(k^{TC}(T)\frac{\partial T}{\partial y}\right) = \rho C_p(T)\frac{\partial T}{\partial t} \tag{3.13}$$

$$\begin{aligned}\dot{\overline{\mathrm{v}}}_i = a_i(t)\frac{\overline{\mathrm{v}}_{i+1} - 2\overline{\mathrm{v}}_i + \overline{\mathrm{v}}_{i-1}}{(\Delta\xi)^2} + \frac{a_i(t)G_i(t)}{4\Delta\xi^2}(\overline{\mathrm{v}}_{i+1} - \overline{\mathrm{v}}_{i-1})^2 \\ + \mathrm{s(t)}\left(\frac{\overline{\mathrm{v}}_{i+1} - \overline{\mathrm{v}}_{i-1}}{2\Delta\xi}\right)\end{aligned} \tag{3.14}$$

for $2 \le i \le N$

Substituting variables to simplify the expression. First define a variable a as:

$$a(T) = \frac{k^{TC}(T)}{\rho C_p(T)}\frac{1}{y^{*2}} \tag{3.15}$$

It defines a ratio of thermal conductivity, specific heat, density, and diffusivity length.

$$s(t) = \frac{\dot{\sigma}(t)}{y^*} \tag{3.16}$$

The variable s is a ratio of the the speed of the melt front and the diffusivity length.

$$G(T) = (T_m - T_a)\frac{\frac{\partial k(T)}{\partial T}}{k(T)} \tag{3.17}$$

Variable G encapsulates the change that thermal conductivity undergoes as the temperature changes. It is noted that if the thermal conductivity were a constant then $G = 0$.

Next, we need to examine the boundary conditions in terms of the discretization. At the slipper-rail interface $i = 1$ as shown in Figure 3.39.

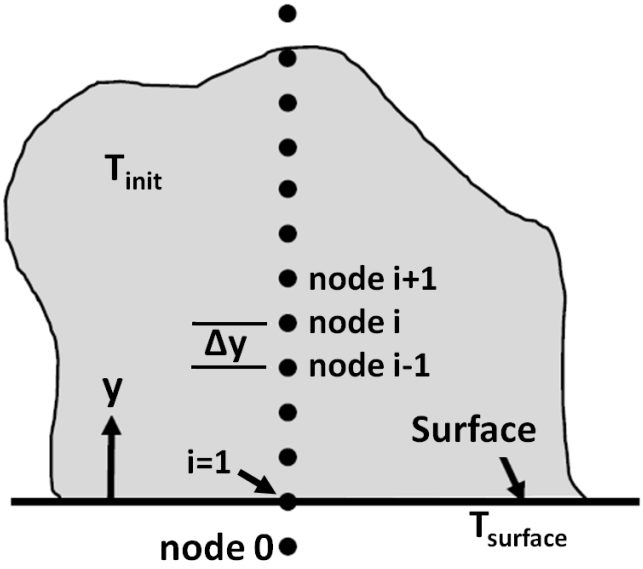

Figure 3.39: Finite Difference representation[3]

Boundary Conditions

$i = 1$

$$\dot{v}_1 = a_1 \frac{v_2 - 2v_1 + v_0}{(\Delta\xi)^2} + \frac{a_1 G_1}{4(\Delta\xi)^2}(v_2 - v_0)^2 + s(t)\frac{v_2 - v_0}{2\Delta\xi} \tag{3.18}$$

and v_0 is determined using Equation 3.10 as

$$-\left.\frac{\partial\omega}{\partial\xi}\right|_{\xi=0} \approx \frac{v_2 - v_0}{2\Delta\xi} = Q(t) \tag{3.19}$$

$$\text{or} \quad v_0 = v_2 - 2\Delta\xi Q(t) \tag{3.20}$$

Q(t) - energy entering system

At the diffusivity length away from the slipper-rail interface $i = N$. The temperature is set to ambient T=T_a that is $v_{N+1}(t) = 0$

$$\dot{v}_N = a_N \frac{(v_{N+1} - 2v_N + v_{N-1})}{(\Delta\xi)^2} + a_N G_N \frac{(v_{N+1} - v_{N-1})^2}{4(\Delta\xi)^2} + s(t)\frac{v_{N+1} - v_{N-1}}{2\Delta\xi} \tag{3.21}$$

leaving

$$\dot{v}_N = \frac{-2v_N + v_{N-1}}{(\Delta\xi)^2} + a_N G_N \frac{v_{N-1}^2}{4(\Delta\xi)^2} + s(t)\frac{-v_{N-1}}{2\Delta\xi} \tag{3.22}$$

In order to simplify coefficients, define the following variables. Several of the coefficients relate to particular thermal considerations. The heat flux terms are grouped

into the $Q(t)$ coefficient. The material properties dominate the $\alpha(T)$ term. The energy that was removed due to material removal through melt is reflected in the term $b(T)$. The variable $\beta(t)$ contains the melt depth term. Convection calculation results are collected in the variable $C_v(T)$, while the conduction calculation results are gathered in the term C_d.

$$\begin{aligned} Q(t) &= \frac{q''(t)y^*}{k^{TC}(T)(T_m - T_a)}, \quad b(T) = \frac{\rho l_h y^*}{k^{TC}(T)(T_m - T_a)}, \\ \alpha(T) &= \frac{k^{TC}(T)}{(y^*)^2 \rho C_p(T) \Delta\xi^2}, \quad \beta(t) = \frac{\dot{u}_m(t)}{2y^* \Delta\xi}, \\ a(T) &= \alpha(T)\Delta\xi^2, \\ C_v(T) &= (2\alpha\Delta\xi - s)\frac{y^* h(t)}{k^{TC}(T)(T_m - T_a)}, \quad C_d = q(t) - b(T)\dot{u}_m(t) \end{aligned} \tag{3.23}$$

C_v - scaled convective heat flux

C_d - scaled conductive heat flux, incorporates material removal

Utilizing these defined coefficients, allowed the PDE (Equation 3.14) to be expressed as a matrix system:

$$\dot{\overline{v}}(t) = \mathbf{A}(t, \overline{T})\overline{v}(t) + \mathbf{N}(\overline{v}(t)) + \overline{f}(t) \tag{3.24}$$

where

$$\mathbf{A}(t, \overline{T}) = \begin{bmatrix} -2\alpha - (1-m)C_v & 2\alpha & 0 & \dots & 0 \\ \alpha - \beta & -2\alpha & \alpha + \beta & \dots & 0 \\ \vdots & \ddots & \ddots & \ddots & \vdots \\ 0 & \dots & \alpha - \beta & -2\alpha & \alpha + \beta \\ 0 & \dots & 0 & \alpha - \beta & -2\alpha \end{bmatrix} \tag{3.25}$$

also

$$\begin{aligned} \overline{f}(t) =& m((a_1 G_1 C_d^2) + (2\alpha_1 \Delta\xi - s)C_d) + \\ & (1-m)((2\alpha_1 \Delta\xi - s)(C_v)\left(\frac{T_{awb} - T_0}{T_m - T_0}\right)\overline{e}_1 \end{aligned} \tag{3.26}$$

and

$$\mathbf{N}(\overline{v}) = \begin{bmatrix} (1-m)a_1 G_1 C_v^2 \frac{T_{awb}-T_0}{T_m-T_0} v_{i-1}^2 \\ \frac{a_i G_i}{4(\Delta\xi)^2}(v_{i+1}-v_{i-1})^2 \\ \vdots \\ 0 \end{bmatrix} \tag{3.27}$$

A - heat transfer matrix

N - nonlinear material properties vector

$\overline{f}$ - heat transfer forcing function

$\overline{e}_1$ is the unit vector $e_1^T = [1, 0, 0, \cdots 0]$

However, the matrix implicitly depends on $\overline{v}$ through the determination of $\overline{T}$. This nonlinear system utilizes a Runge-Kutta Order 4 type of solver solver, as discussed in Section 2.4.1.6, to ensure stability as it arrives at a solution for each time step.

NOTE: The switch, demarcating when the slipper is in contact versus no contact, is designated m. It has the value of 1 when in contact and 0 when not in contact. Further details with regard to the development of the discretized PDE can be found in Appendix A. It follows derivation work by Paek [15].

3.3.7.2 Melt Estimation.

The melt estimation consisted of monitoring the temperature calculated at Node 1 shown in Figure 3.39.

The surface temperature was checked at each time step. Once the melt temperature of the material modeled was surpassed as depicted in Figure 3.40, a second calculation was carried out.

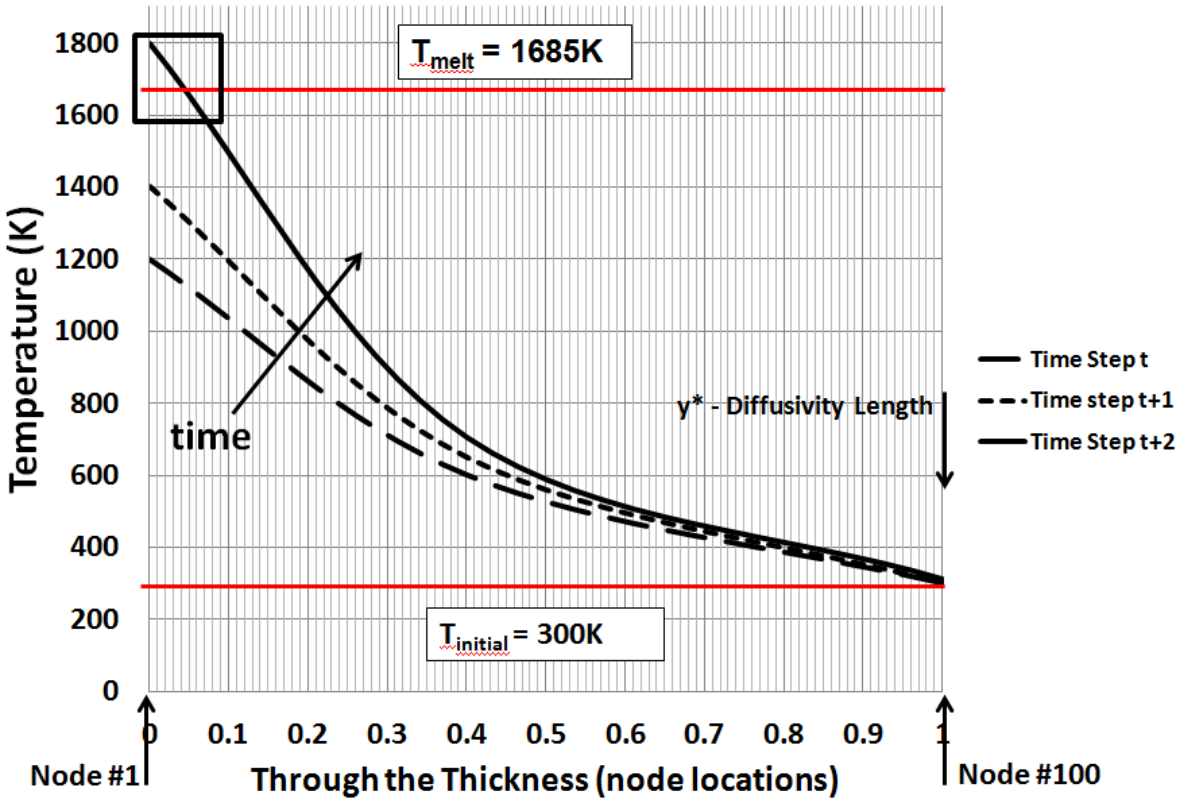

Figure 3.40: Melt temperature exceeded

A melt depth was assumed based on a linear interpolation of the temperature between Node 1 and Node 2 as graphically depicted in Figure 3.41.

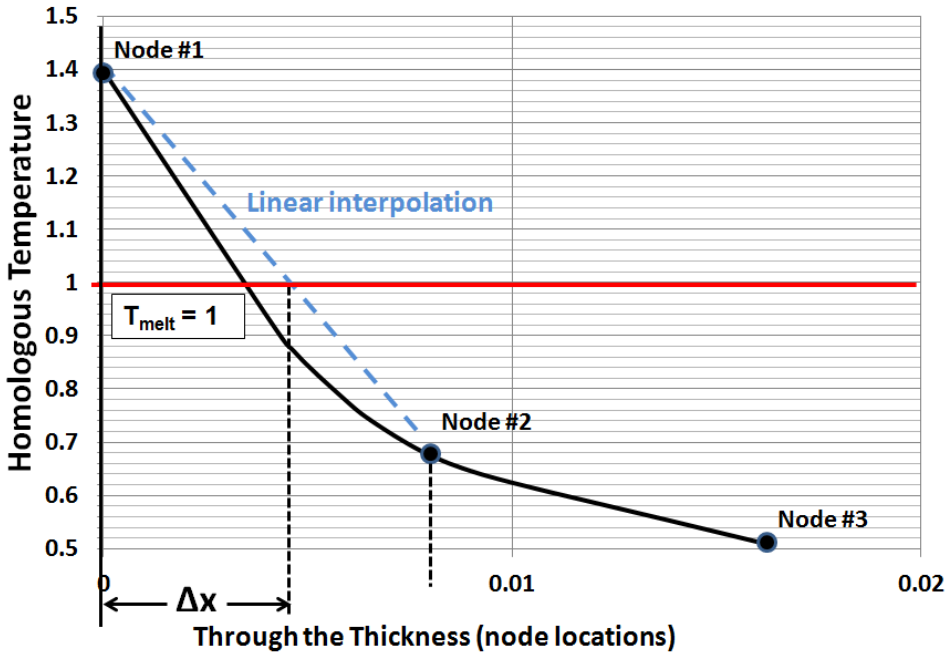

Figure 3.41: Melt depth estimated

This depth (Δx) equaled the amount of material that would be removed. Note that the melt depth is through the thickness of the slipper which is in the y-direction. This means that the Δx shown in Figure 3.41 is equivalent to u_m once it is scaled. In this model, the latent heat of fusion was used to estimate the energy lost due to the phase change of a material becoming a liquid (ie melting). This is shown in Equation 3.28 with the l designating the latent heat of fusion, ρ the density of the material, and $\frac{du_m}{dt}$ the rate of melt through the thickness.

$$-k^{TC}(T)\frac{dT}{dy}\bigg|_{y=u_m(t)} = q''(t) - \rho l_h \frac{du_m}{dt} \tag{3.28}$$

This time step was iterated on until the melt depth chosen resulted in a lowered temperature that did not exceed melt when the heat transfer was recalculated. This is shown in Figure 3.42.

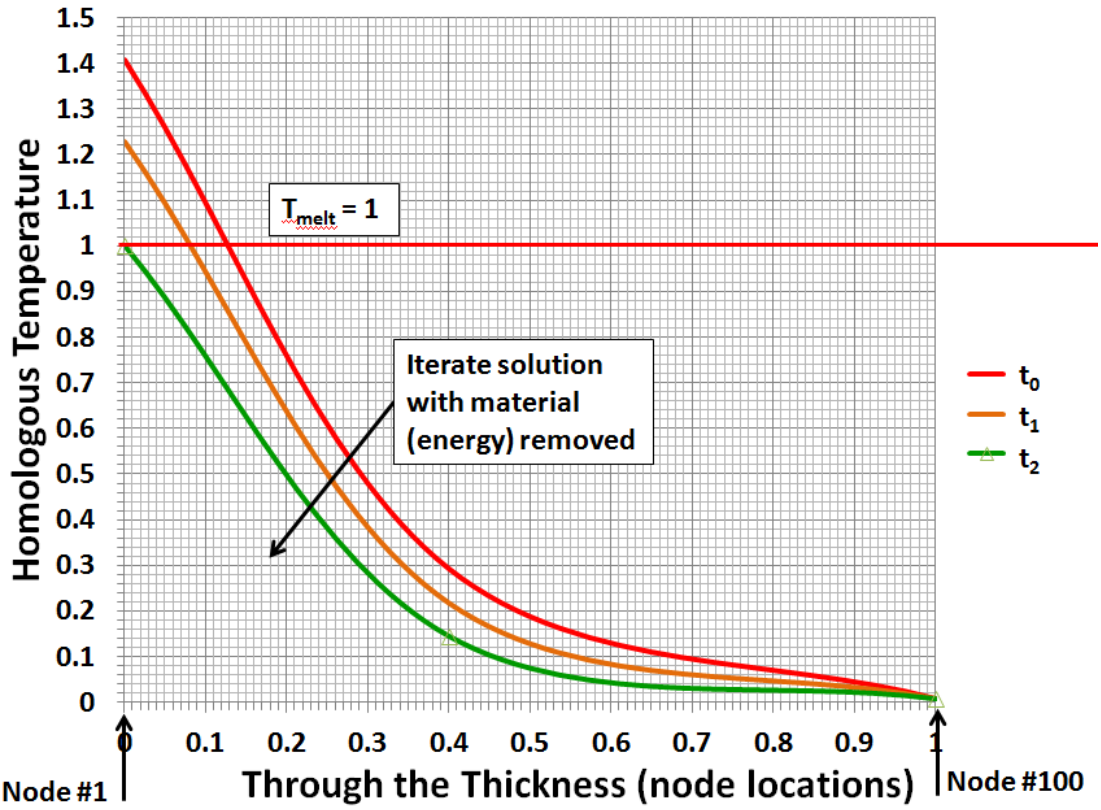

Figure 3.42: Melt depth estimated

This method assumed that the temperature at Node 2 had not exceeded the melt temperature as well. This assumption can be made due to the relatively small time increments taken (0.0002 sec). This distance (scaled melt depth) was then added to the location of Node 1 and the entire spatial grid was relocated by this distance in the y-direction at every time step as appropriate. This resulted in non-linearity as the boundary were constantly moving. The mesh always consisted of 100 nodes. Total melt depth is defined as the accumulated melt depth over the course of a run.

3.4 Combined Model

3.4.1 Concept.

The second FEM was sized at the millimeter scale. It incorporated concepts and inputs from the previous models to estimate a wear rate for the mechanical portion of the total

wear estimate. It is a three-dimensional FEM that modeled a portion of the slipper as it traveled down the rail. It simulated three distinct time intervals that the slipper was in contact with the rail as shown in Table 3.1. The DADS data was used to inform the time of the simulation as the slipper was only in contact for brief periods as it bounced down the track. The time increments when this occurred are listed in the second column of Table 3.1. The velocities per simulation are listed in the third column.

Table 3.1: Slipper-Rail contact times.

Simulation	**Contact times** (sec)	**Avg. Velocity** (m/s)
#1	0.2042 - 0.2132	42.75
#2	2.46 - 2.4628	502.5
#3	4.2996 - 4.301	1099.75

They were chosen as representative of the velocities reached during the 2008 test. The 40 m/s simulation was at relatively low velocity. The 500 m/s simulation was at mid level velocity and the last simulation was at a relatively high velocity of 1100 m/s. Figure 3.43 was based on data from DADS, it depicts the velocity profile experienced by the slipper in that 2008 test during the acceleration portion. The three velocities simulated in this research are marked in Figure 3.43 by vertical lines.

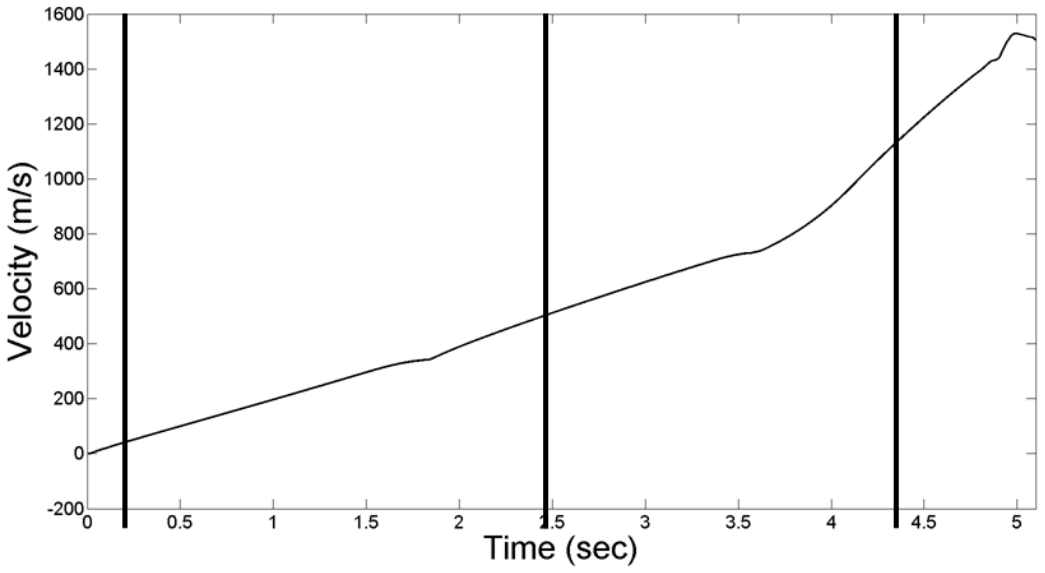

Figure 3.43: 2008 Velocity profile w/model segments3.3.4.1

The model utilized the same material properties as the microscale model, temperature outputs from the heat transfer model for required initial conditions, friction and specific heat estimates from the heat transfer model, and inputs from DADS for boundary conditions. Figure 3.44 represents these various tie-ins.

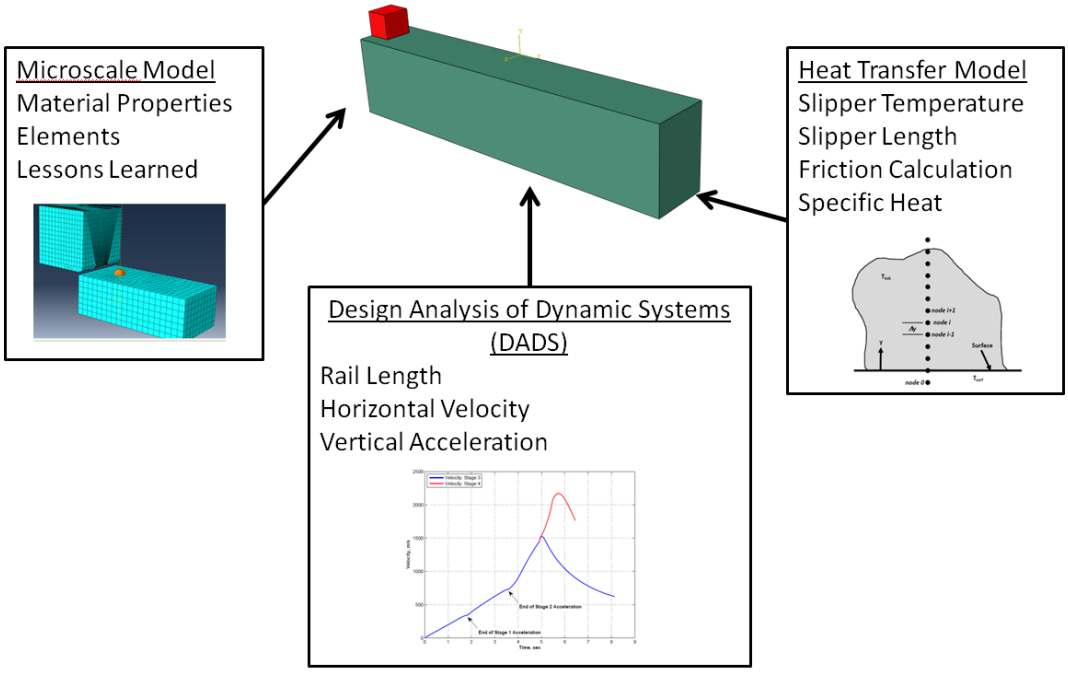

Figure 3.44: Macro scale model concept

In this section, the model used to simulate the three velocities will be described in further detail. The reasoning and assumptions used for the boundary conditions, initial condition, material modeling, meshing, and contact considerations are further discussed as appropriate.

3.4.2 Rail Model.

The rail model utilized in this research was based on several considerations discussed in this section. The slipper-rail contact times, edge effects, elastic wave propagation, mesh and element type as well as material modeling all played a role in the development of the rail model.

The length of the rail model was based on the time that the slipper was in contact with the rail during the 2008 test at the HHSTT. This information was gleaned from the DADS data. DADS lists the vertical forces that a slipper experiences during a test run. The data accounted for the bouncing as previously discussed. When the forces on the top of the slipper were nonzero, it indicated that the slipper was in contact with the rail. The slipper remained in contact with the rail for a finite amount of time before the next bounce occurred. Figure 3.45 displays the DADS output for the vertical forces during the acceleration phase of the 2008 test. The velocities that were simulated are indicated with boxes at the appropriate times. Figure 3.46 is a zoomed in view of the vertical forces, as calculated by DADS, at approximately 40 m/s.

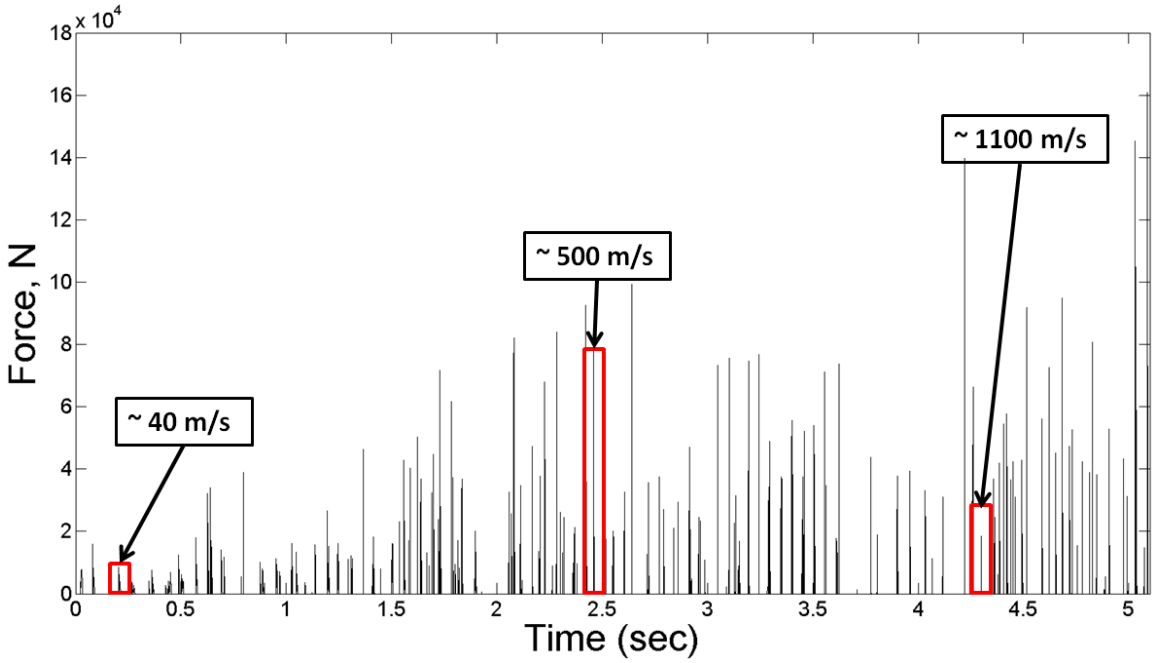

Figure 3.45: DADS - Vertical force

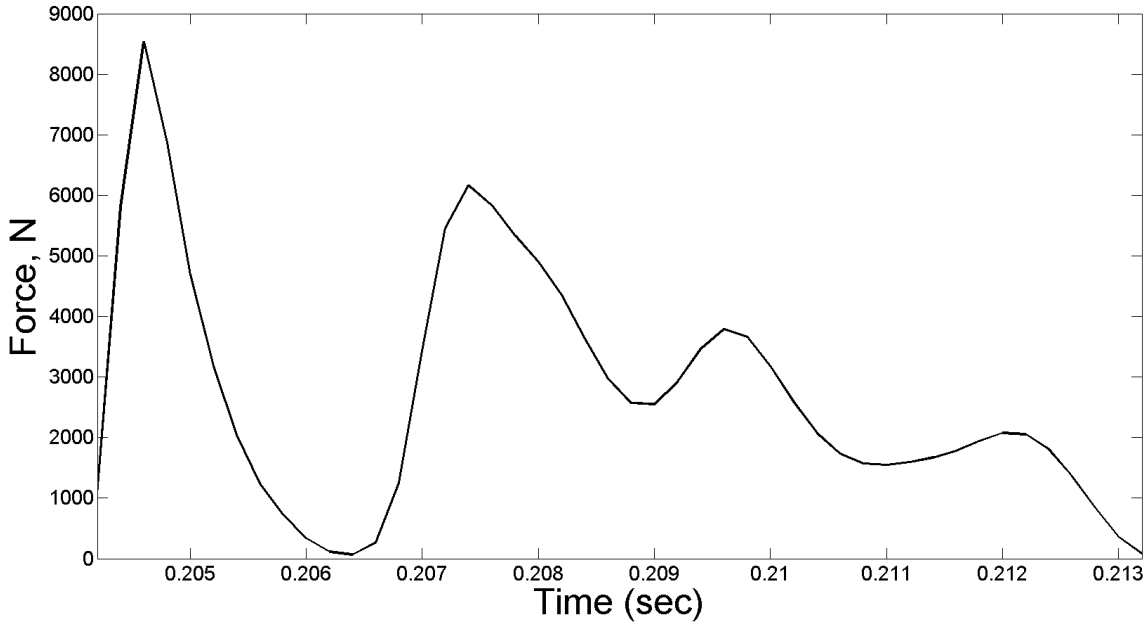

Figure 3.46: DADS - Vertical force (40 m/s)

Column 1 of Table 3.2 displays the time the slipper was in contact with the rail. DADS data was calculated at discrete time steps of 0.0002 seconds. The finite time in contact

occurred over several time steps. The second column of Table 3.2 displays the time steps per the selected velocities with the third column containing the velocities of interest.

Table 3.2: DADS Slipper-Rail contact times.

Δt (sec)	**time steps**	**Avg. Velocity** (m/s)	**Rail Length** (m)
0.009	46	42.75	0.40
0.0028	14	502.5	1.31
0.0014	8	1099.75	1.54

Thus, from the time in contact and the velocity of interest, a rail length was determined. The fourth column displays the resultant rail length for the three velocities listed.

Figure 3.47 shows the rail model. The rail length determination was discussed above. Next the width determination is discussed. The rail width is twice that of the slipper model. This dimension was selected to minimize edge effects while reducing the overall number of elements required in the mesh. With a finer mesh, this width could be reduced but the overall model would result in an increased number of elements. The compromise solution was to select a greater width with a more coarse mesh. Figure 3.48 displays the mesh used. It shows that the mesh is coarser the further it is from the top surface. The surface interacts with the slipper model and thus is of most interest. Increasing accuracy in the area while keeping the overall number of elements to a manageable level was the goal.

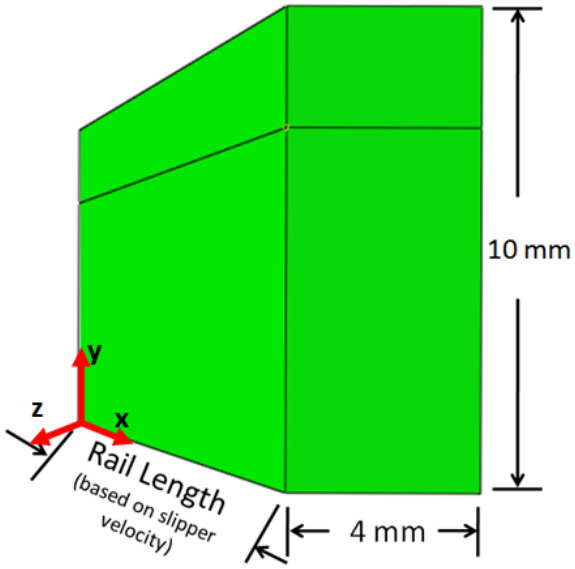

Figure 3.47: Rail model

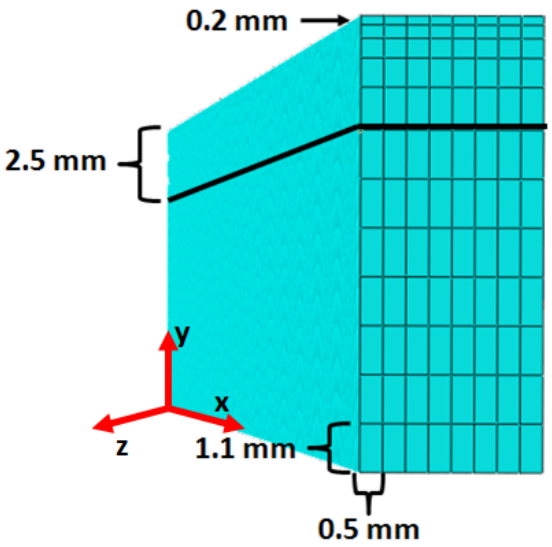

Figure 3.48: Rail mesh

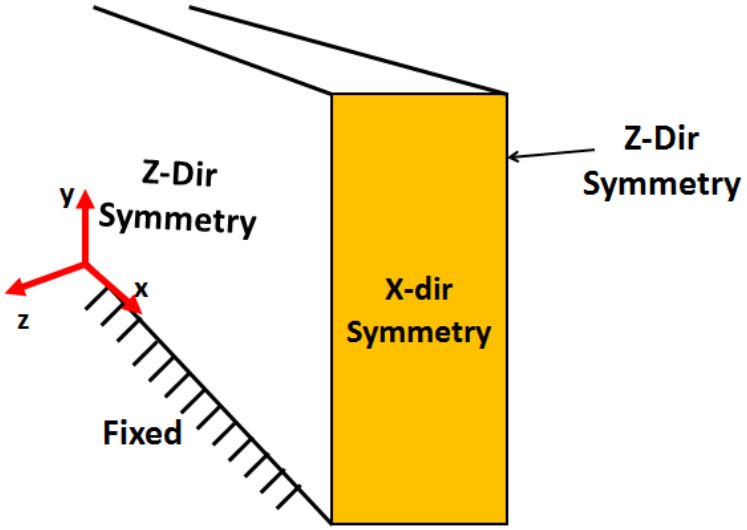

Figure 3.49: Rail Boundary conditions

The depth of the rail model was determined in part by the need to ensure that the slipper motion did not displace the rail model in an unrealistic manner. The elastic wave speed for this material is calculated with Equation 3.29 [25].

$$C_s = \sqrt{\frac{E}{\rho}} \tag{3.29}$$

Table 3.3: Elastic coefficients.

Materials	**E** (GPa)	**Poisson's ratio** ν	**density** ρ (kg/m^3)	**Elastic wave velocity** C_s (m/s)
AISI-1080 Steel	203	0.27	7800	~5000

The rail model had the properties of 1080 steel, the elastic wave speed calculation, based on the values in Table 3.3, resulted in a velocity of approximately 5000 m/s. This result ensured that the wave would reflect and return during the simulation as in the y-direction the rail was fixed at the bottom as shown in Figure 3.49. During this time, the elastic wave also dissipated. Previous work with the microscale model showed that the elastic wave dissipated quickly relative to the model run time (see Chapter 4). The other consideration with respect to the height of the rail was the total number of elements in the model. In order to reduce the number of elements, the mesh was coarse toward the bottom of the model as shown in Figure 3.48.

Also, shown in Figure 3.49, is that the rail model had symmetry imposed in the x-direction and the z-direction. This ensured that the elastic wave propagated in those directions, without reflecting, for the duration of the simulation.

The model was meshed using elements designated as C3D8R in ABAQUS [27]. The element discussed previously was used for the rail as well as the slipper models.

Since this model was interested in representing wear through material deformation, the material was modeled in the same way as the microscale model. The same coefficient were used for the Johnson-Cook Plasticity model as well as the Johnson-Cook Failure model as described in that section.

3.4.3 Slipper Model.

The slipper model has different considerations than the rail model. These are discussed in this section.

The slipper length was based on the varying slipper geometry as previously discussed and shown in Figure 3.50. The figure shows three vertical lines corresponding with the velocities of interest. Figure 3.43 was used to correlate those velocities with distinct test time. Those same times are correlated with slipper areas in contact as shown in Figure 3.50.

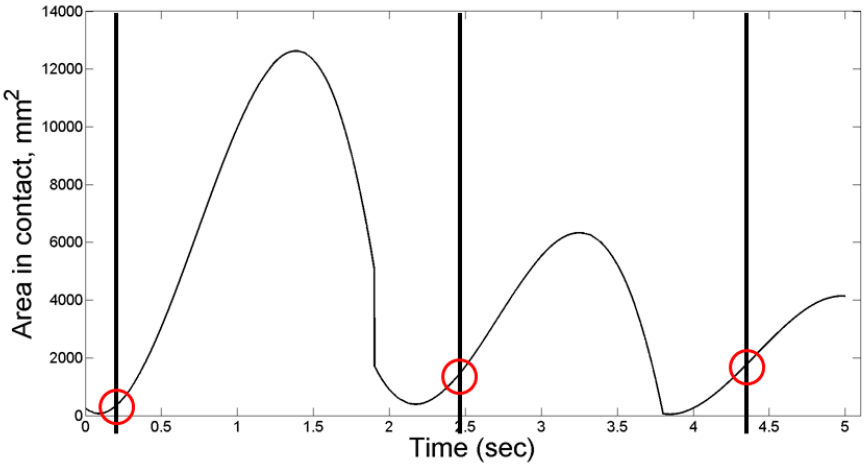

Figure 3.50: Slipper Contact Area

The slipper area in contact is made up of the slipper width and slipper length. As stated, the area in contact is shown in Figure 3.50. The width of the slipper was taken to be fixed at 90 mm based on work by Buentello [18]. This results in the slipper lengths in contact as listed in Table 3.4.

Table 3.4: Slipper Contact Area.

Area in contact (mm^2)	**Slipper Width** (mm)	**Slipper Length** (mm)
372.6	90	4.14
909	90	10.1
1503	90	16.7

In this manner, the slipper lengths were determined for each velocity of interest. This is shown in Table 3.5.

Table 3.5: Slipper length vs Velocity.

Avg. Velocity (m/s)	**Slipper Length** (mm)
42.75	4.14
502.5	10.1
1099.75	16.7

Figure 3.51 represents the dimensionality of the slipper. The width and height of the model were based on attempting to minimize any edge effects while ensuring a reasonable computational time. Figure 3.52 shows that there is symmetry imposed in the z-direction. Any stress waves will propagate in this drection for the duration of the simulation and thus would not interfere with the results. The other directions have imposed boundary conditions that ensure reflections. From the wave speed calculation, there was enough time during the simulation for the wave to propogate through the slipper model and interact with the surfaces. However, previous work with the microscale model showed that the wave rapidly dissipates and thus reduces the possibility of interference. This is discussed further in Chapter 4.

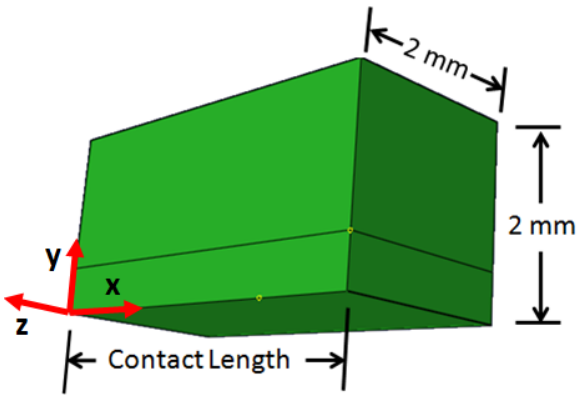

Figure 3.51: Slipper model

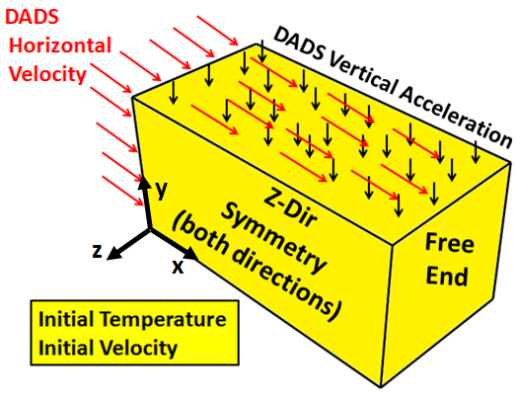

Figure 3.52: Slipper Boundary and Initial conditions

Figure 3.52 also displays the imposed boundary conditions and the initial condition of the slipper model. The horizontal velocity was the average velocity calculated from the time in contact as shown in Table 3.2. This velocity was imposed on the back surface and top

surface of the slipper model. It was kept constant. The actual slipper velocity was variable over the time that was simulated. However, the differences were assumed to be negligible.

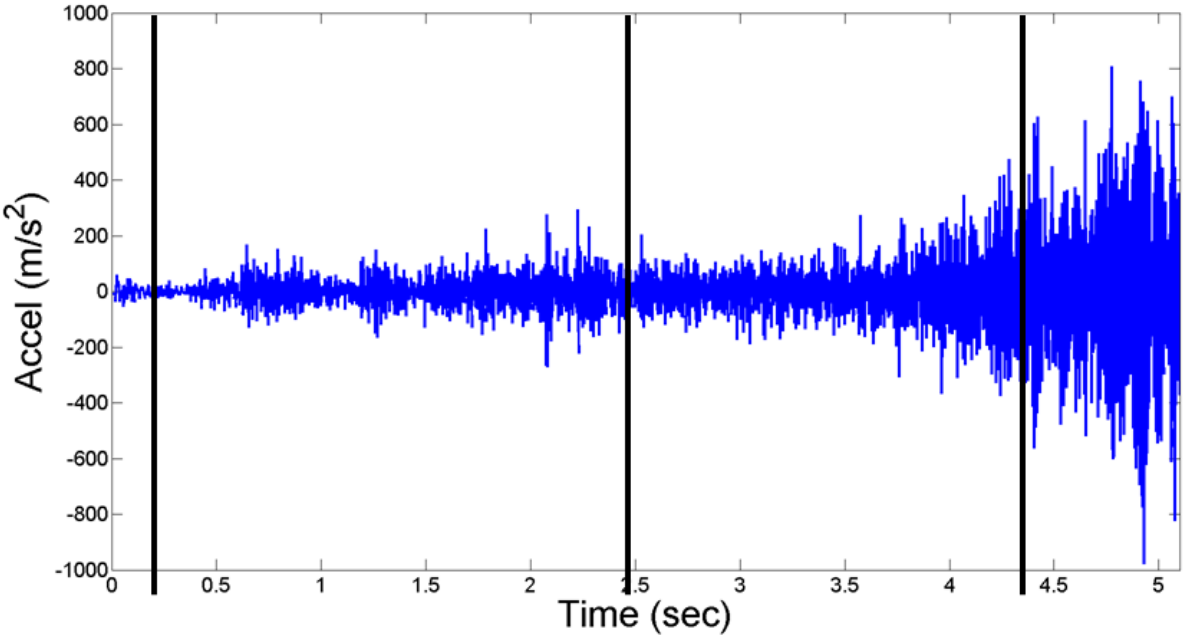

Figure 3.53: Vertical Acceleration (DADS)

Also displayed in Figure 3.52 is the vertical acceleration imposed on the top surface of the slipper model. These values were obtained from DADS data for the duration of the time in contact. Figure 3.53 is a graphical representation of the DADS estimation for the vertical acceleration experienced by the actual slipper during the 2008 test. The vertical lines represent the times corresponding to the velocities of interest. Figure 3.54 provides more detail on the first velocity of interest (40 m/s). It shows a greater acceleration change at the beginning as the slipper comes into contact with the rail followed by lesser magnitudes as the slipper is in contact. The other velocities modeled show a similar pattern. However, the longer time in contact experienced at this particular velocity has more detail and is thus more illuminating as to the physics.

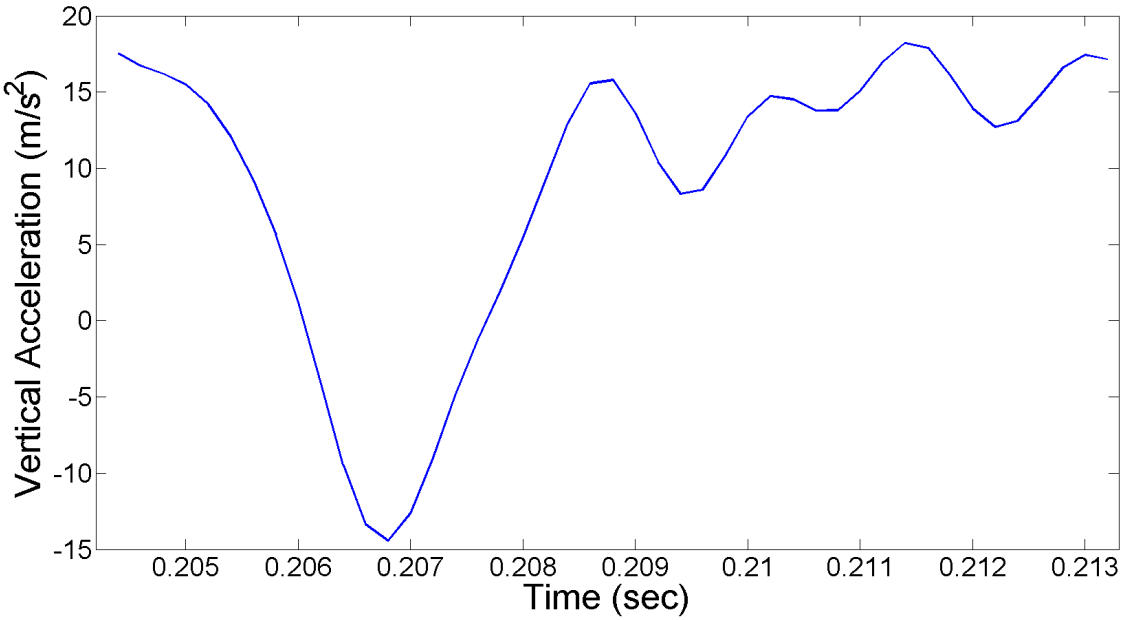

Figure 3.54: Vertical Acceleration (DADS)

The initial condition imposed on the slipper model is an initial temperature as output form the previously discussed one-dimensional Heat Transfer model. The temperature was taken as the temperature calculated at the bottom surface of the slipper by the one-dimensional Heat Transfer model. The initial temperatures are listed in Table 3.6.

Table 3.6: Slipper - Initial Temperatures.

Avg. Velocity (m/s)	**Initial Temperature** (°K)
42.75	831.2
502.5	1236.2
1099.75	1107.6

A wear rate estimation for the slipper was the focus of this model. The mesh reflected this by having the greatest number of elements at the bottom portion of the slipper. The mesh used for the slipper model is shown in Figure 3.55. The elements used were the the same C3D8R formulation as previously discussed.

Since this model was interested in modeling wear through material deformation, the material (Vascomax 300) was modeled in the same manner as the microscale model. The same coefficients were used for the Johnson-Cook Plasticity model as well as the Johnson-Cook Failure model. For further description, see Section 3.2.2.3 and Figure 3.4.

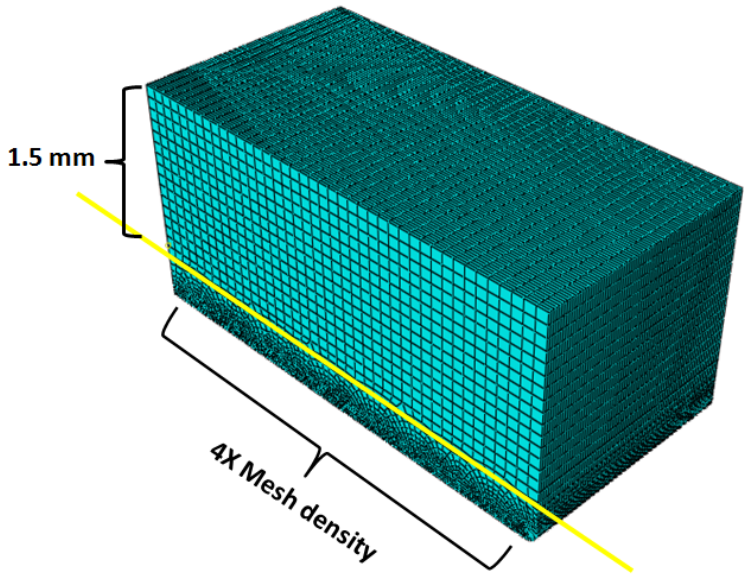

Figure 3.55: Slipper mesh

As part of the material modeling, an equation of state was considered. However, there was no impact modeled and the stress estimated did not exceed the HEL. The results that show this are discussed further in Chapter 4.

3.4.4 Contact.

The slipper model travels down the rail model for a fixed time determined by the DADS data. During this entire time the slipper model was in contact with the rail model. The actual slipper there is possibly a contact/no contact of the underside portion of the slipper with the rail. This interaction drives the wear estimate as this was the only connection between the two models. Figure 3.56 depicts the options available in ABAQUS concerning contact [27]. The background of the penalty method was discussed in Section 2.2.4.2.

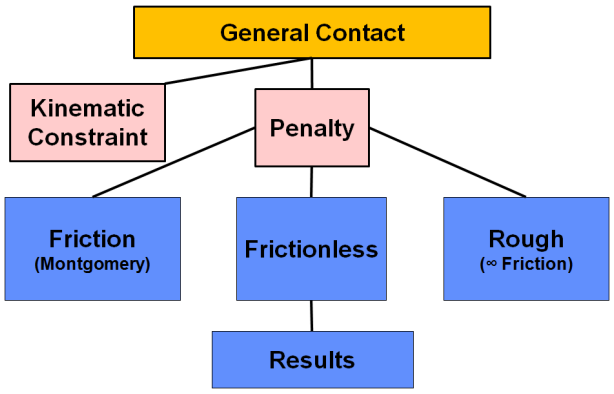

Figure 3.56: ABAQUS Contact options [27]

3.4.4.1 Friction.

As previously discussed, the coefficient of friction was calculated using estimates from a curve fitting equation developed by Hale [3] and based on data from Montgomery [53]. This calculation was completed as part of the Heat Transfer model study. The output is shown in Figure 3.57. The three vertical lines designate the three velocities that were simulated with this model. The coefficient of friction for the first velocity of interest is shown in Figure 3.58. It clearly shows that when not in contact the value is zero and when in contact the coefficient varies. This is due to the time dependent nature of the variables that determine the coefficient of friction as previously discussed. DADS provided data for the time steps per time in contact as tabulated in Table 3.2. The coefficient of friction was calculated at each of those time steps and input into the ABAQUS[27] FEM in tabulated form.

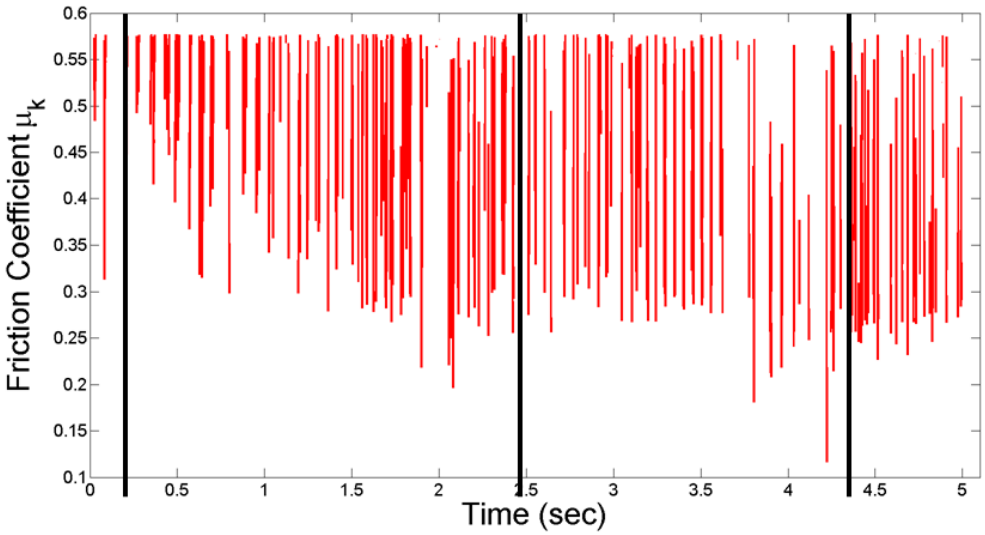

Figure 3.57: Coefficient of Friction at specific times

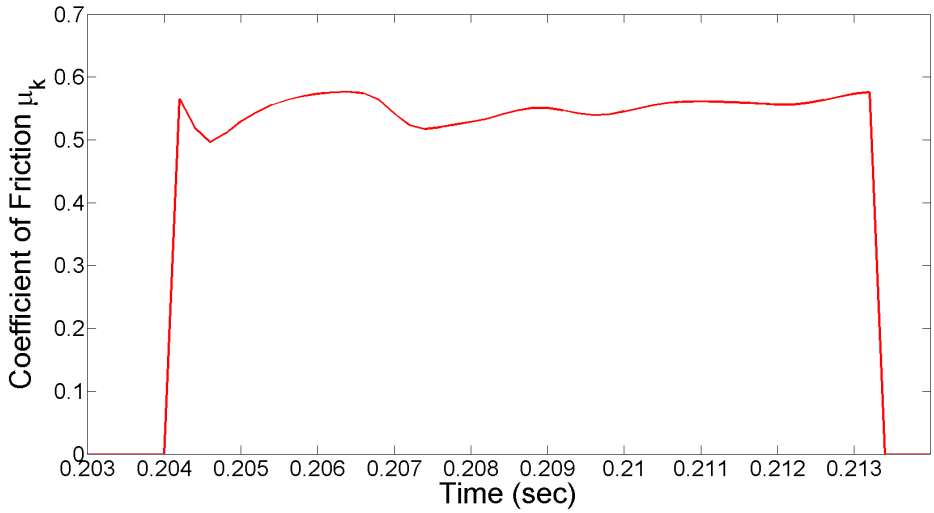

Figure 3.58: Calculated Friction Coefficient.

3.4.5 Wear Calculations.

This section discusses the method used to estimate the wear rate from this FEM. The actual results will be discussed in Chapter 4. There were three simulations run comprising a 40 m/s, 500 m/s, and 1100 m/s slipper-rail interaction. The depth eroded, as indicated in Table 3.7, was based on deleted elements at the bottom of the slipper model. This depth was multiplied by the width, taken as a constant 90 mm, and the same length used for the slipper

model. This was taken as a constant wear rate for the simulation and was then divided over the number of time increments in each of these simulations, as listed in column 3 of Table 3.7.

Table 3.7: Slipper - Wear calculation Part I.

Deleted elements depth (mm)	**Wear Volume** (mm^3)	**time steps**	**Wear per time step**
Wear depth - 1st simulation (A)	Width*Length 1*A	46	(Wear Volume 1)/46
Wear depth - 2nd simulation (B)	Width*Length 2*B	14	(Wear Volume 2)/14
Wear depth - 3rd simulation (C)	Width*Length 3*C	8	(Wear Volume 3)/8

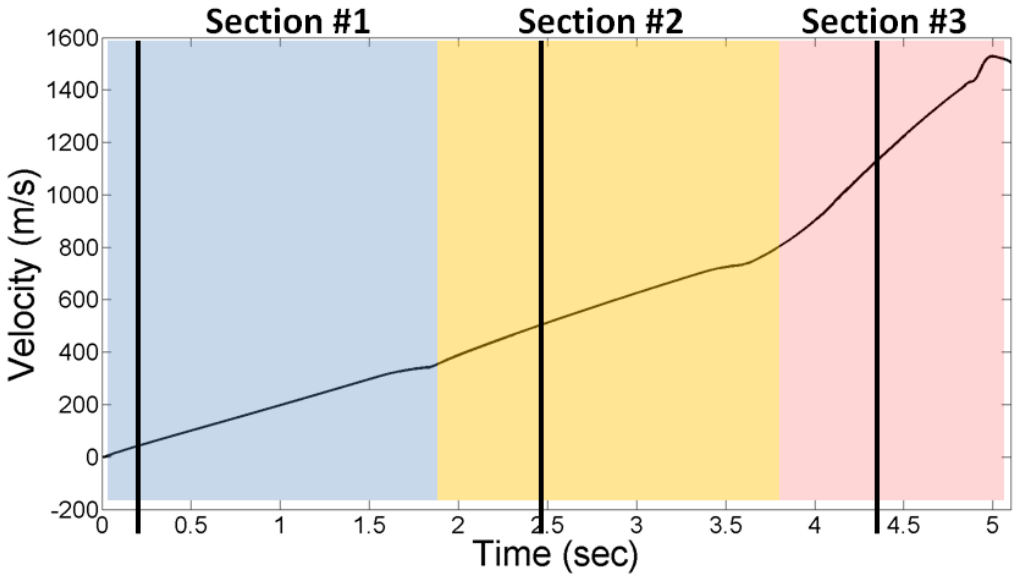

Figure 3.59: Wear rate estimate, applied per section

Figure 3.59 displays the three sections where the estimated wear rates were calculated. The sections correlate with the rocket stages from the 200 test. The slope changes of the velocity can be seen at the section boundaries. The wear rate increments are accumulated over the total number of time increments shown in column 3 of Table 3.8. Those time increments were derived from the DADS data per section as listed in Table 3.8. This was done for the three increments simulated to arrive at the overall wear rate.

Table 3.8: Slipper - Wear calculation Part II.

Section	**Wear rate section** (sec)	**Total # time steps in contact**	**Total wear per section**
#1	< 1.9	1299	Wear Rate 1 * 1299
#2	> 1.9 and < 3.8	684	Wear Rate 2 * 684
#3	> 3.8	277	Wear Rate 3 * 277

3.5 Chapter Summary

In this Chapter, the various numerical models used in this research were discussed. The utilization of the theories discussed in Chapter 2 were highlighted. Several assumptions that were made in the creation of the models were also discussed. As was shown, lessons learned were applied as appropriate to the different models. The FEMs were dependent on the one-dimensional heat transfer model for the initial temperatures of the respective simulations. In addition, other aspects of the one-dimensional heat transfer model were carried over to the final FEM shown, the combined model. Finally, the different techniques of estimating wear from the different models was discussed.

IV. Discussion and Results

4.1 Chapter Overview

This chapter presents the results of the research. It follows the same structure as the previous chapters. The results of the contact/penalty study are presented first. The shock wave and equation of state study results are then presented and discussed. This studies directly tie into the microscale wear model. As previously mentioned, this finite element model consists of a slipper model impacting an asperity model to estimate wear rate through element deletion. The results of that model, to include an estimated wear rate, follows. The next results discussed are from the heat transfer model. The one-dimensional model simulates the entire acceleration phase of the 2008 test run at the HHSTT. As such, several details concerning the thermal effects on the slipper are discussed. A wear estimate based on melt is also presented. Finally, the combined FEM is discussed. It is the same order of magnitude spatially as the heat transfer model. It used the same material properties as the FEM previously discussed. The results discussed include the measurements taken to estimate wear through element deletion. All of these models estimated the wear rate based on data from DADS and compared to measurements from a worn slipper used at a test in 2008. Figure 4.1 shows a typical multi stage test setup at the HHSTT.

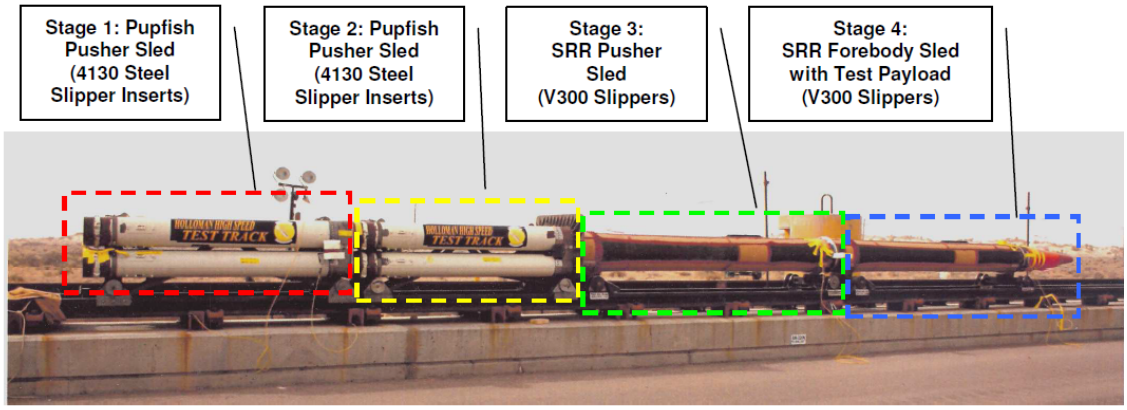

Figure 4.1: Typical HHSTT test

4.2 Micromechanical Model

This section concerns the FEM that modeled a slipper model impacting an asperity as part of the rail model. As part of this study, several items of interest were investigated regarding their influence on the results of the wear estimate. These items were the contact algorithm as utilized by the FEM software ABAQUS [27] to include the penalty method as formulated by the software. In addition, the shock wave was investigated due to concerns about its reflection from the boundaries of the slipper model. This also compared results of modeling the material by incorporating an Equation of State as opposed to not including one as part of the modeling. Finally, the section describes the model that was used for the wear estimate to include the various considerations that were included and how these items were estimated.

4.2.1 Studies.

4.2.1.1 Contact Results.

The contact model was described previously in Section 3.2.1. The objective was to study the penalty algorithm in ABAQUS. The contact interaction between the slipper model and the asperity model was of primary interest to the FEMs used in this research. The underpinnings of the implementation was previously discussed. First the contact implementation is investigated, then the penalty method is examined.

Figure 4.2 shows two elements of the model that were used to extract results from the model. Recall that the FEM is a slipper model in direct contact with a rail model. A vertical force was imposed at the top of the slipper in order to ensure slipper-rail model interaction. Three separate simulations were run to investigate contact. The imposed vertical velocities are shown in Table 4.1. The first two simulations listed are described in detail, the results of all three are also discussed.

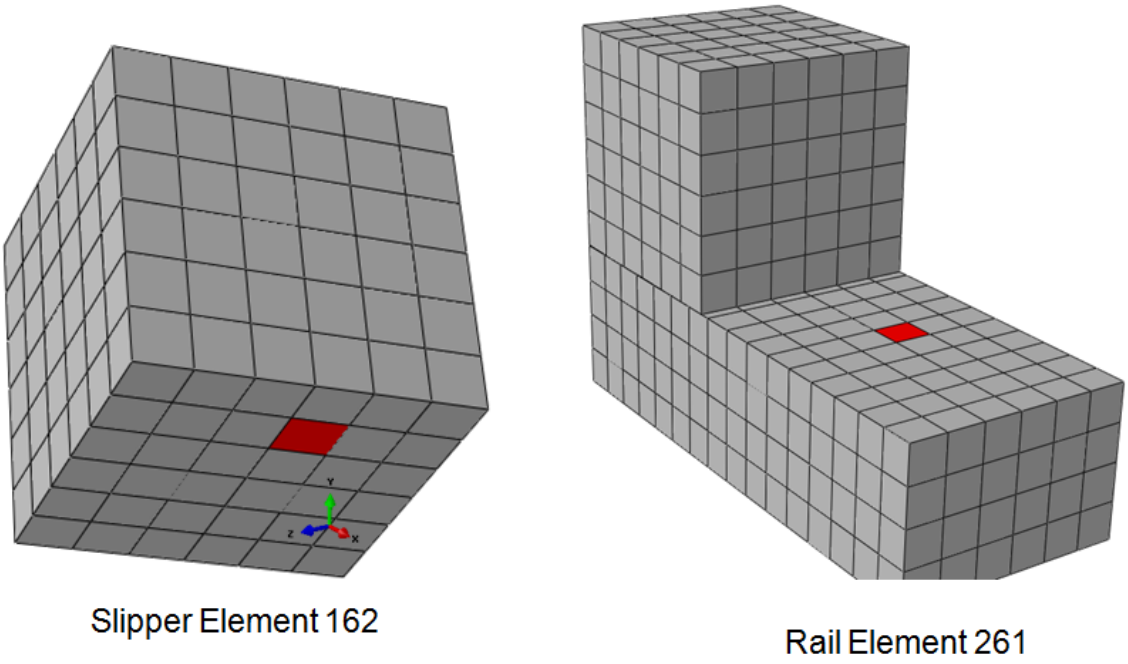

Figure 4.2: Examined elements

Figure 4.3 shows the results of the interaction between the slipper and rail models. The relative stresses are shown with the higher stress areas in red and the lower stress areas in blue. This snapshot of the slipper model shows it completely separated from the rail model. The simulation run time was approximately $10e^{-6}$ seconds. An imposed horizontal velocity of 20 m/s ensured that the slipper model traversed the entire length of the 180 μm rail model.

Table 4.1: Slipper Model - Boundary Conditions

Simulation	**Vertical Velocity** (m/s)	**Horizontal Velocity** (m/s)
#1	1	20
#2	2	20
#3	5	20

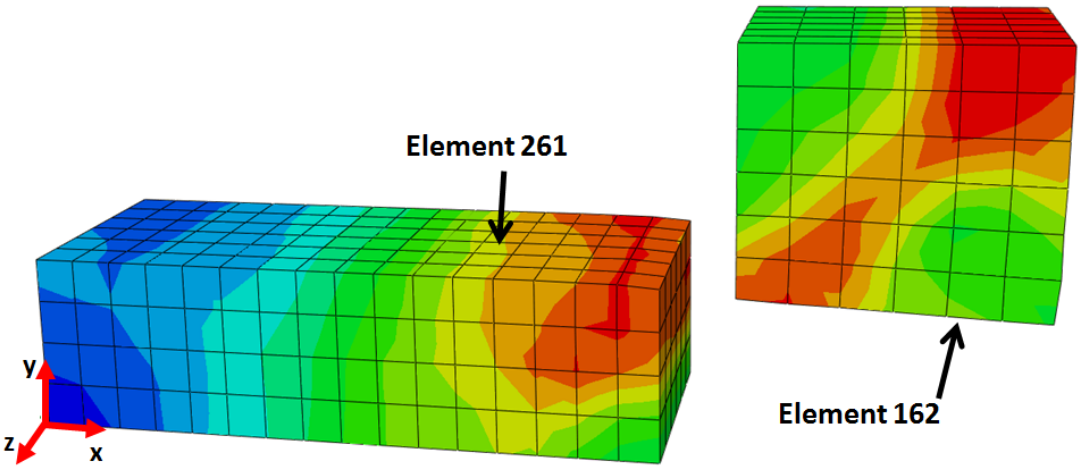

Figure 4.3: Vertical velocity - 1 m/s

Figure 4.4 displays the Mises stress as calculated at slipper element 162. As expected, it shows the rapid increase in Mises stress at the beginning of the simulations. This is due to the vertical velocity imposed on the upper surface of the slipper model. The slipper model travels the beyond the length of the rail model during the simulation. The Mises stress drops as the slipper element 162 loses contact with the rail model. The calculated Mises stress does not drop to zero due to residual stresses remaining. The yield stress for 1045 steel (material used for both slipper and rail models) is approximately 525 MPa. The stresses exceeded that reached a maximum of approximately 950 MegaPascal (MPa), thus plastic deformation occurred resulting in the residual stresses shown.

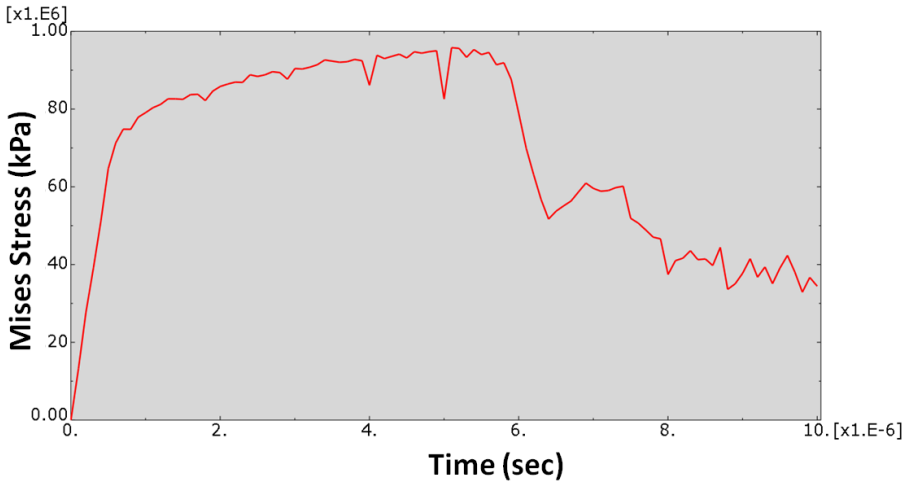

Figure 4.4: Slipper element 162 output - Mises Stress

Figure 4.5 represents the Mises stress calculated at rail element 261. It shows the Mises stress rising although in a delayed manner. This is due to the location of the rail element of interest. As the slipper model travels down the rail model, the Mises stress calculated at the rail element rises correspondingly. Once the slipper model crosses over rail element 261, the stress rises rapidly. Figure 4.5 does show a subsequent rise in the Mises stress once the slipper model loses contact with the rail. This is the elastic recovery in the rail model material. It also shows residual stresses that accompany the plastic deformation as a result of the slipper model interaction. The Mises stress exceeds the yield stress just as in the slipper model.

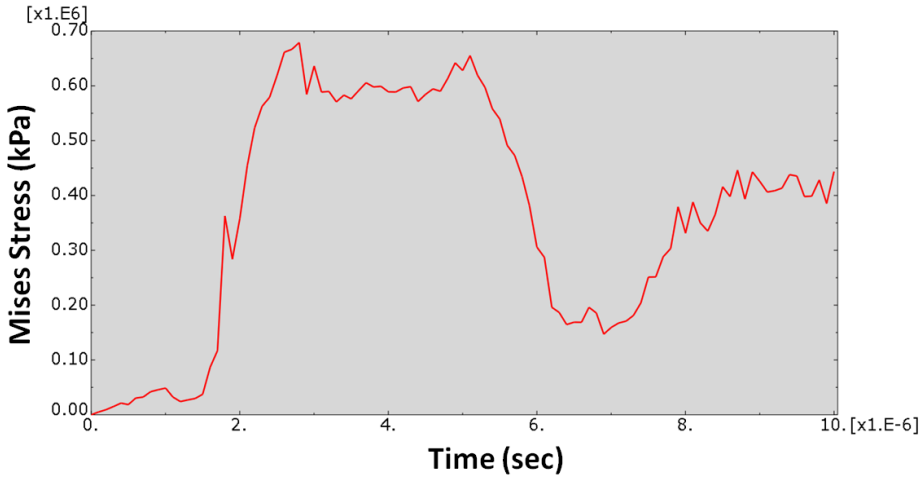

Figure 4.5: Rail element 261 output - Mises Stress

Figure 4.6 displays the forces as calculated at the slipper model element 162 and rail model element 261. These forces come about due to the imposed velocity causing the models to interact under loading. The plots of the forces reveal similar behavior as the plots of the Mises stress calculations. These plots were added for completeness to ensure that the model was behaving as expected. A check of that is that the forces at beginning and the end of the simulation are near zero. This is as expected since the two models are not in contact with one another after approximately the $6e^{-6}$ seconds mark.

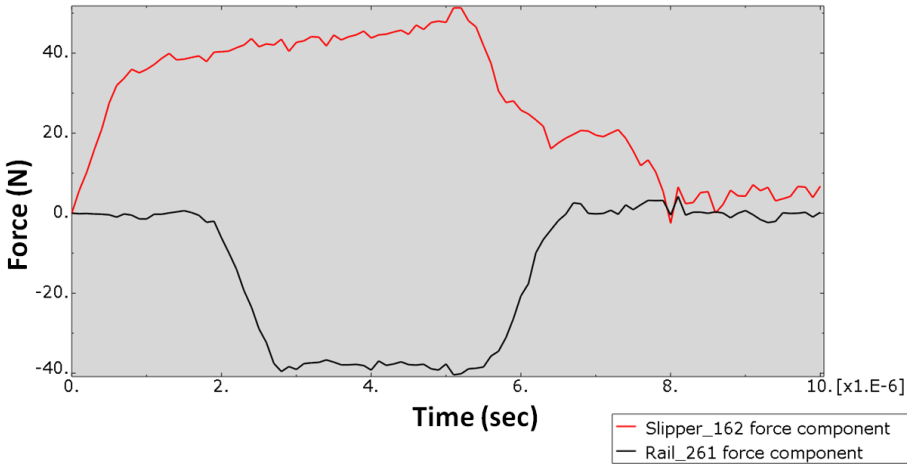

Figure 4.6: Calculated Force at Slipper-Rail Interface

The results of the second simulation are shown in Figure 4.7, Figure 4.8, Figure 4.9, and Figure 4.10. Similar patterns can be discerned in the results as compared to the previous simulation results. This simulation imposed a 2 m/s vertical velocity on the upper surface of the slipper model. Although double the previously imposed velocity, the results are consistent.

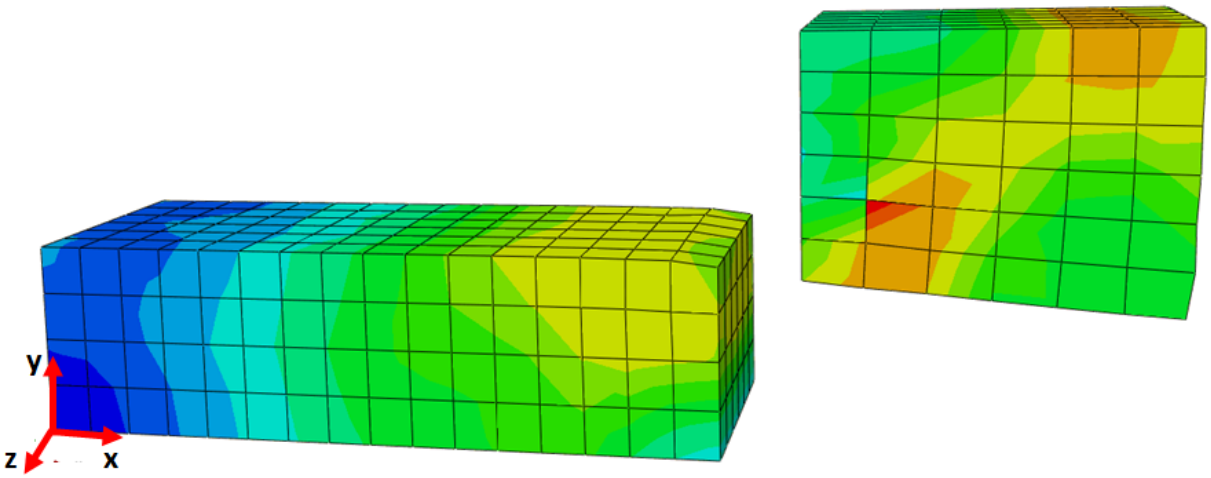

Figure 4.7: Vertical velocity - 2 m/s

The Mises stress calculated at both elements rise at expected times and fall as the slipper model loses contact with the rail model. At the Mises stresses calculated, plastic deformation occurs resulting in residual stresses as depicted in the appropriate figures.

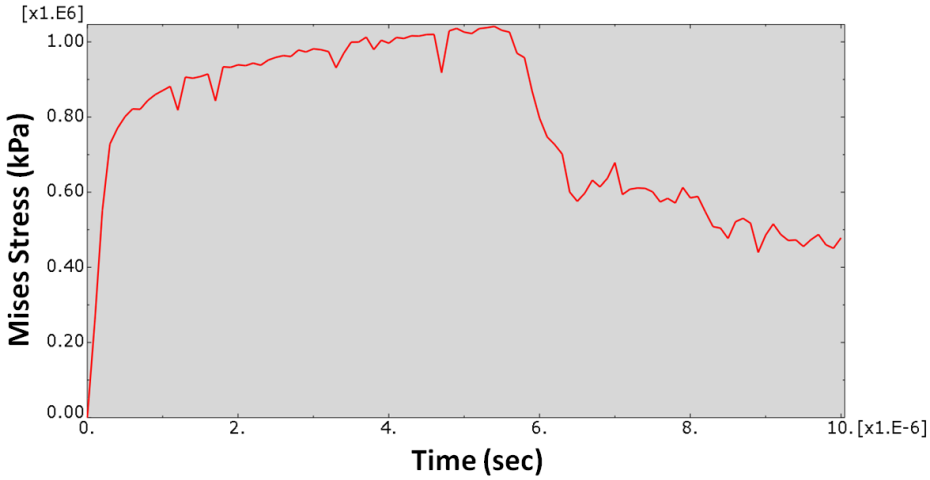

Figure 4.8: Slipper element - Mises Stress

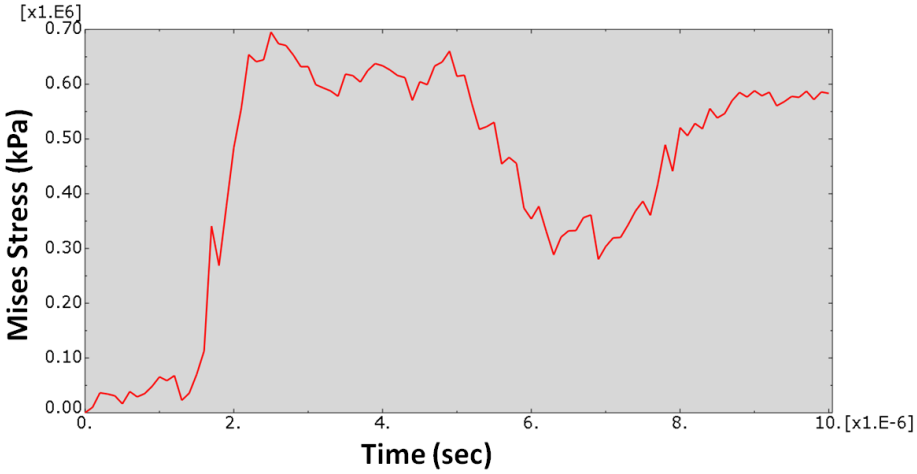

Figure 4.9: Rail element - Mises Stress

The forces follow a similar pattern as the previous simulation.

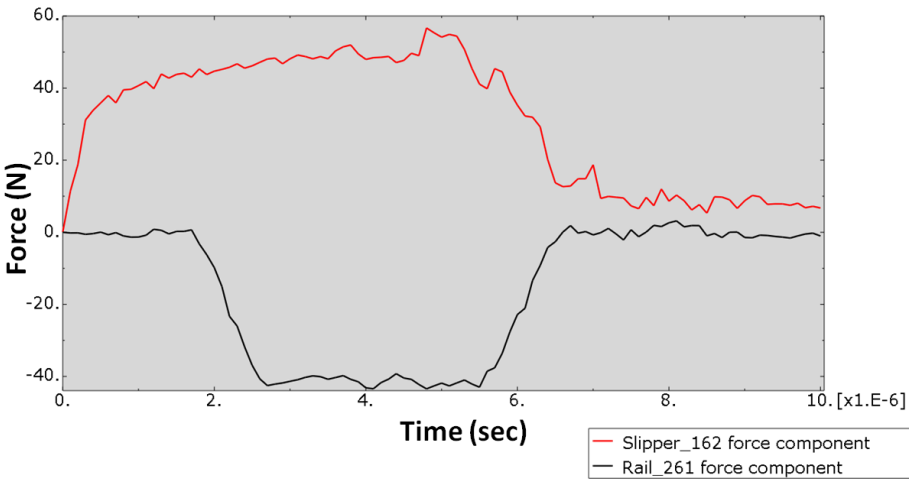

Figure 4.10: Calculated Force at Slipper-Rail Interface

The results from the three simulations are shown in Figure 4.11 and Figure 4.12. Figure 4.11 consists of the combined stresses of the two elements, of interest, from each simulation. The combined stresses are the result of subtracting the calculated stress at the rail element from the calculated stress at the slipper element. At the beginning of the simulation, the rail element does not calculate any stresses due to its location and hence at the beginning of Figure 4.11 the rise in the stress is strictly from the slipper element. As the slipper element and rail element converge, the calculated stresses are near identical. Thus, the middle of Figure 4.11 shows stress values of near zero. As the slipper element travels past the edge of the rail model, the stress calculated at the rail element is a higher magnitude than the stress calculated at the slipper element. This is reflected in the last portion of Figure 4.11 as the combined stresses for the final simulation are negative in value.

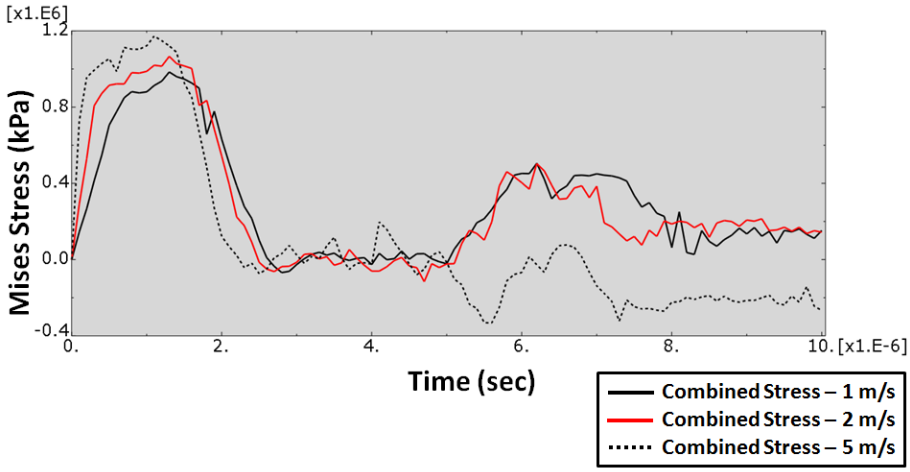

Figure 4.11: Combined Stresses of examined elements

Figure 4.12 follows a similar pattern. The forces calculated at the the rail element were subtracted from the forces calculated at the slipper element. The combined forces are near zero as the forces in the rail model oppose the forces in the slipper model. The small differences are the result of the imposed vertical velocity translating into forces which grow over time as the models are forced together. The forces quickly return to zero as the slipper model departs from the edge of the rail model.

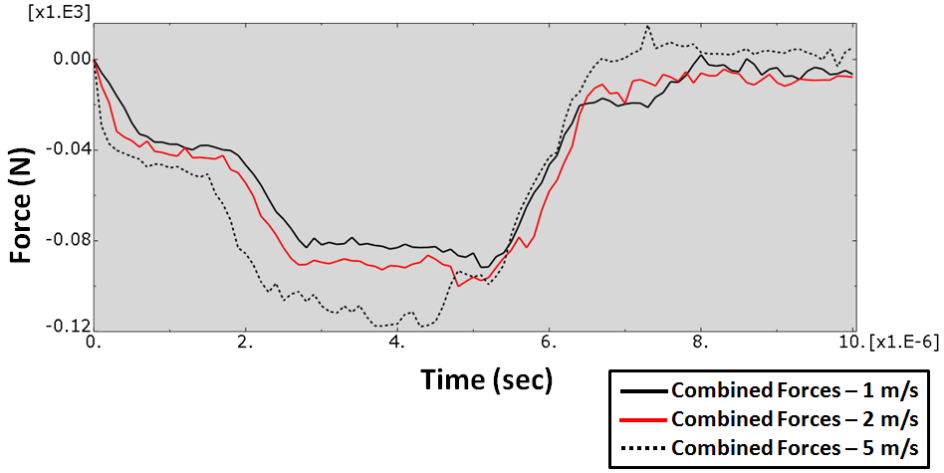

Figure 4.12: Combined Forces of examined elements

Contact Summary

These results indicate that the FEM model is reacting as expected to increased loading. The

importance of these results are that the software utilizes a method of enforcing boundaries. Without a method of boundary enforcement, the nodes that make up elements of one body would cross element boundaries of another. These results indicate that the algorithm is keeping the bodies separate and the method transmits the load to the slipper model and the rail model appropriately.

Penalty Method results

The FEMs used in this research modeled contact between bodies. The model utilized in this section modeled impact in particular. As the slipper model impacts with the asperity model the bodies are not allowed to mix. Hence, a method must be utilized to ensure that the nodes that form one body interpenetrate into the other body as minimal as possible. ABAQUS/Explicit [27] utilizes the penalty method as described in Section 2.2.4.2. This study was focused on the implementation as related to the slipper model and rail model interaction as previously described. As such the penalty scaling factor was changed by a factor of 10 and 100 and the results compared and examined to gain a deeper understanding of the implementation of the penalty method algorithm as implemented by ABAQUS.

The magnitude of the penalty within the algorithm can be controlled by the user. ABAQUS [27] refers to this as the *Penalty stiffness scaling factor* as shown in Figure 4.14.

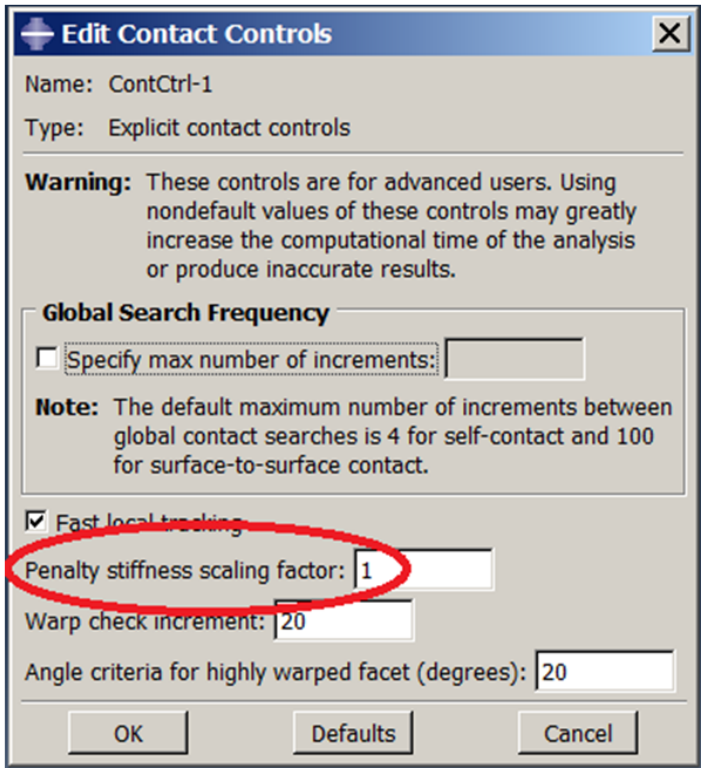

Figure 4.13: Penalty scaling factor controls

By default this value is set to ”1” and the penalty is determined by the algorithm based on a balance between speed/performance versus stability. Performance refers to the amount of nodal interpenetration that occurs. The models used were the same ones previously discussed. A vertical velocity of 5 m/s was imposed on the upper surface of the slipper model to ensure overclosure. Three simulations were performed with the penalty scaling factor increased for each one as shown in Table 4.2.

Table 4.2: Penalty Stiffness Scaling Factor.

Simulation	**Factor** (m/s)	**Slipper - Vertical Velocity** (m/s)
#1	1	5
#2	10	5
#3	100	5

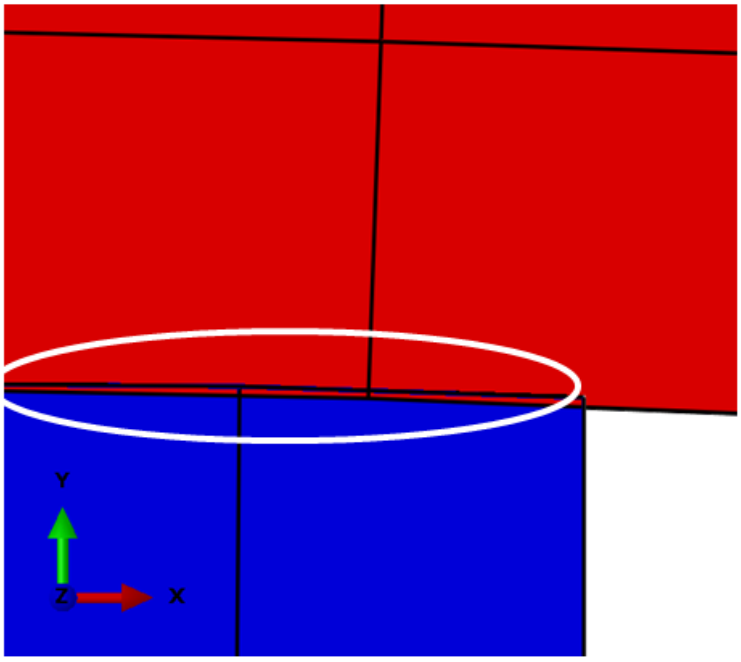

Figure 4.14: Interpenetration - Scaling Factor 1

Figure 4.14 is a graphical representation of a node, located at the bottom edge of the slipper model (red), interpenetrating into the rail model and a node, located at the upper edge of the rail model (blue), interpenetrating into the slipper model.

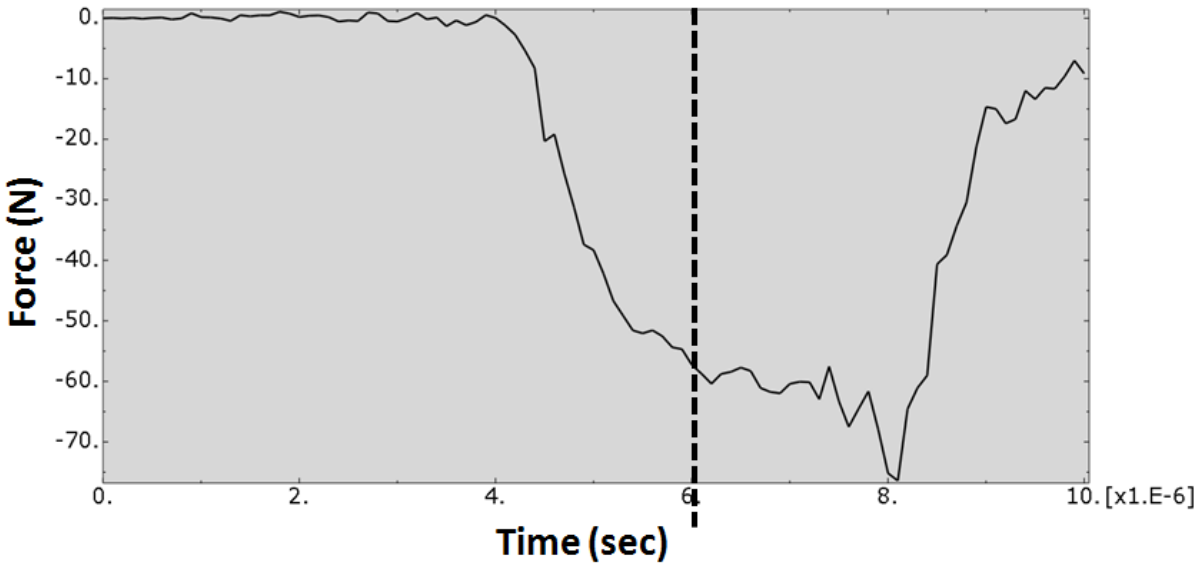

Figure 4.15: Nodal force vs time

Figure 4.15 depicts the penalty force imposed on the node as it crossed the surface of the rail model element. The dashed line corresponds to the time that Figure 4.14 depicts. The force grows as a result of the imposed vertical velocity increasing the magnitude of translation in the vertical direction over time. The force reduces rapidly after approximately $8 \times 10e^{-6}$ seconds as the node travels beyond the edge of the rail model.

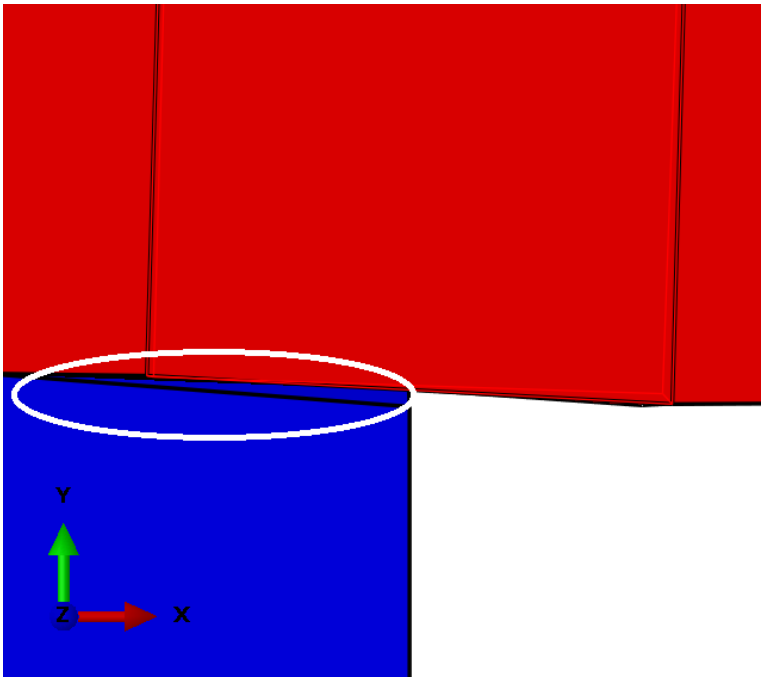

Figure 4.16: Interpenetration - Scaling Factor 10

Figure 4.16 shows the result of increasing the penalty scaling factor by 10. It shows that the node does not cross the rail model element boundary. Instead there is a gap between the slipper model and the rail model. This is a result of the penalty scaling factor being too large in magnitude at that instant in time.

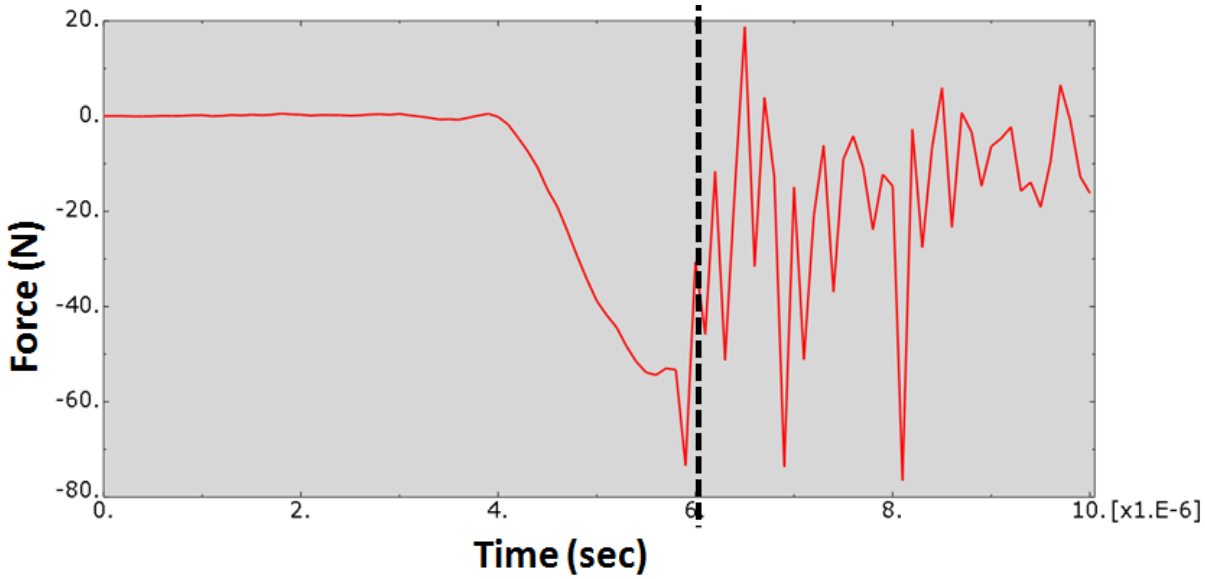

Figure 4.17: Nodal force vs time

This penalty force exerted on the slipper model node is plotted in Figure 4.17. At the instant in time, designated by the dashed line, the force is larger than the previous simulation at the same time in the simulation. In addition, the force magnitude becomes increasingly unstable as it attempts to compensate for the excessive force it imposed previously. The oscillations toward the end of Figure 4.17 reflect this observation.

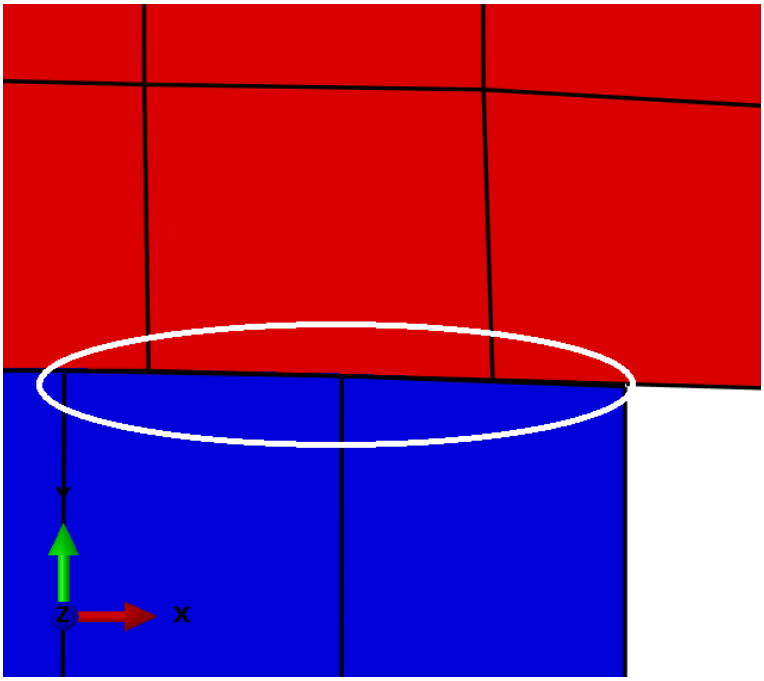

Figure 4.18: Interpenetration - Scaling Factor 100

Figure 4.18 is the result of the final simulation run. The penalty stiffness factor is increased to 100. It is apparent that any interpenetration by the nodes into either model was minimal.

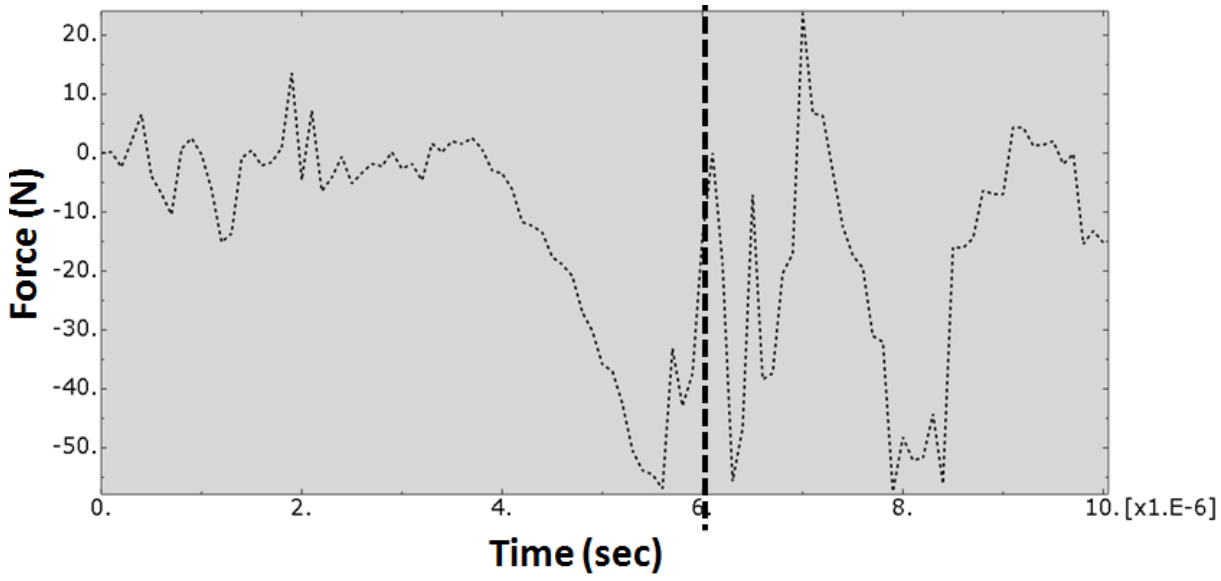

Figure 4.19: Nodal force vs time

The penalty force at the slipper model node is plotted in Figure 4.20. This plot shows increased instability for the duration of the simulation. Any imposed force is quickly reversed and this oscillation slowly damps out. At the time depicted in Figure 4.18, the force has been reduced to almost zero in a short amount of time only to grow again almost immediately. Although this results in very little interpenetration at the time examined, this instability could be problematic depending on the objective of the simulation.

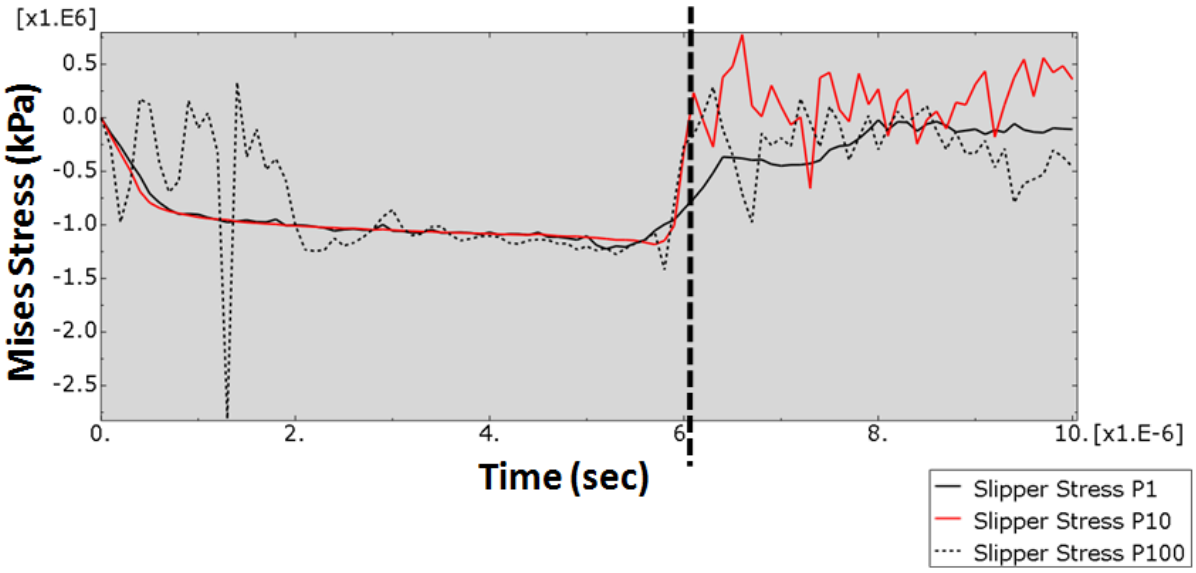

Figure 4.20: Superimposed Mises stress

Figure 4.20 traces the Mises stress at the slipper model element in contact with the rail model. Although the signs are reversed the behavior mirrors the behavior previously discussed above with respect to the contact scenario. The main difference is the instability shown in the second and third scenarios where the penalty stiffness factor was increased. This instability is due to the overcompensation of the algorithm as it attempts to adjust to nodal interpenetration. The third simulation show very large oscillations in the stress that would affect material behavior. This should be considered if the material behavior is important as it is in modeling wear through element failure and deletion.

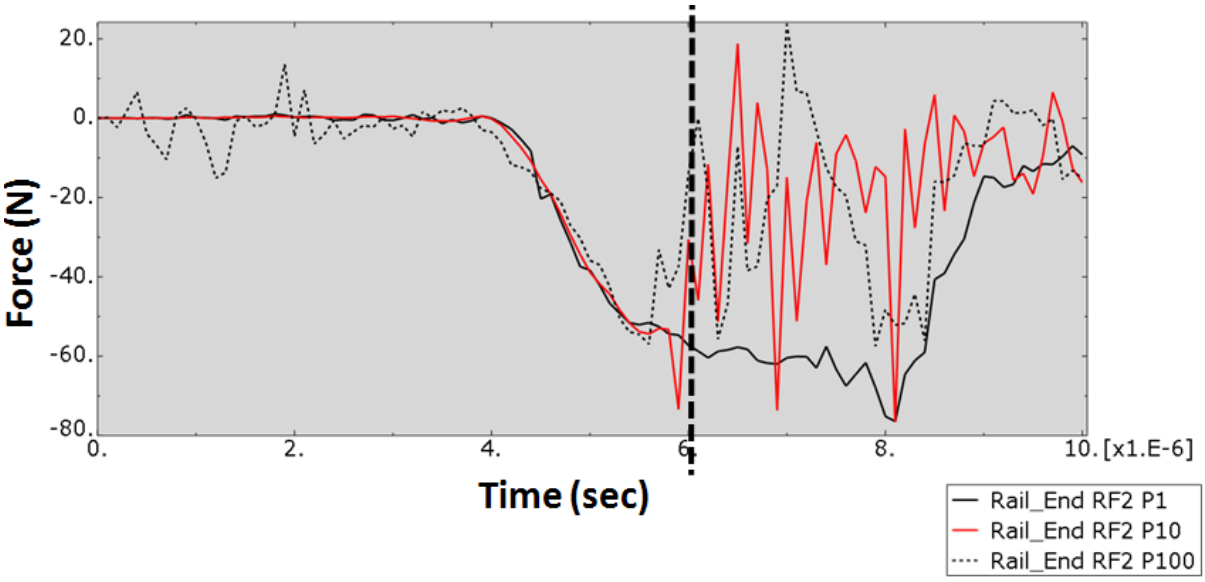

Figure 4.21: Superimposed - Force vs time

Figure 4.21 are the results shown in Figure 4.15, Figure 4.17, and Figure 4.19 to portray the dependence of instability on the increase in the penalty stiffness factor. There is a correlation between the iinstability and increasing the penalty stiffness factor. The alternative in reducing nodal interpenetration is to increase mesh density.

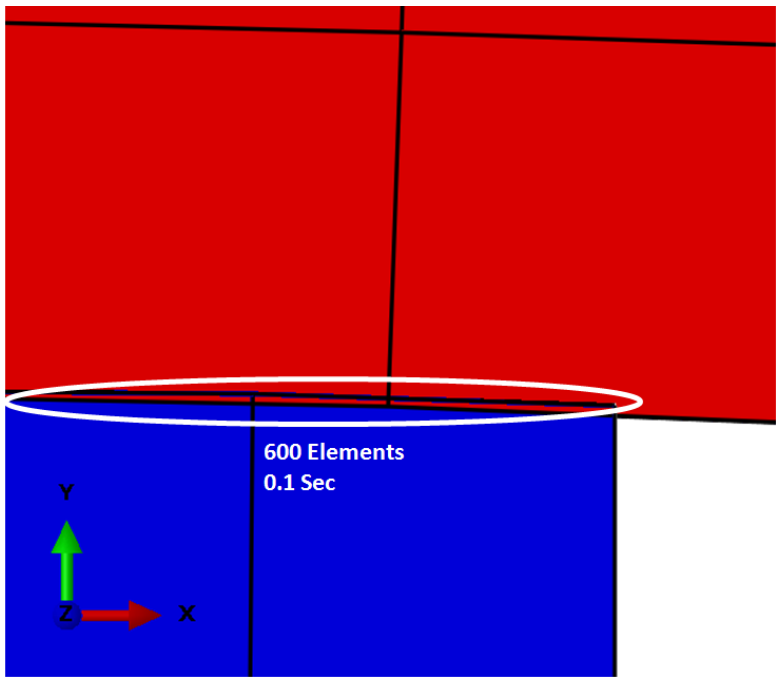

Figure 4.22: Penalty factor comparison (1x CPU time)

Figure 4.22 and Figure 4.23 show the relative difference in nodal interpenetration. The slipper model depicted in Figure 4.22 consists of 600 elements. The slipper model shown in Figure 4.23 consists of 20864 elements (34 times the number of elements). The nodal interpenetration is reduced however the CPU cost is 26 times greater.

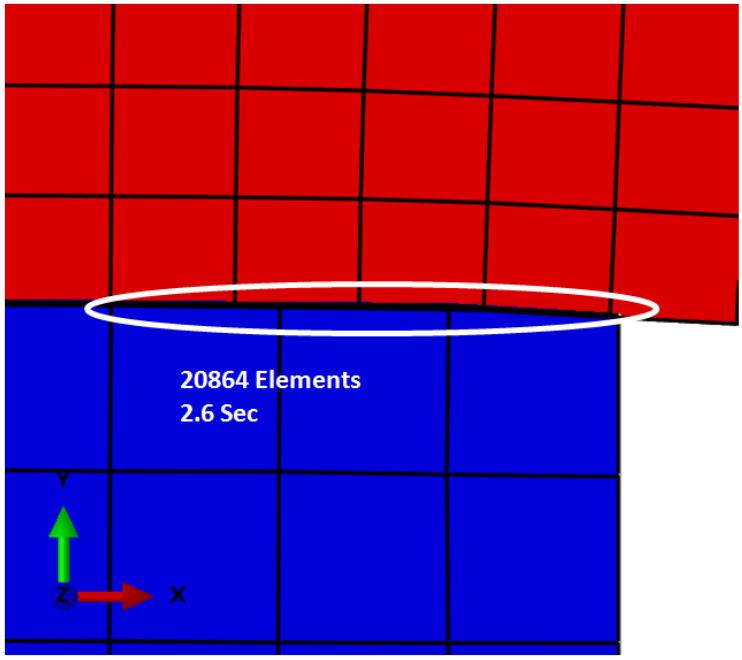

Figure 4.23: Penalty factor comparison (26x CPU time)

Penalty Method summary

Thus the decision to increase the penalty stiffness scaling factor must be done with caution. The possibility of instability must be weighed against the CPU costs of increasing the mesh density. Wear rate estimates, using FEM, are highly dependent on material behavior and hence it is best to remain conservative and accept the increase in CPU time to increase the mesh density.

4.2.1.2 Stress Wave Model.

In addition to contact, another item of particular interest in regards to modeling wear rate, through asperity collision, is the possibility of a shock wave and its impact on the

results. The possibility of a shock wave exists due to the high velocities modeled in this study. Thus there are two parts to this scenario. One is the propagation of the wave through the slipper model and two is the requirement for an equations of state, as discussed in Section 2.2.3.4.

Stress Wave Propagation

Figure 4.24 displays a slipper model traveling over a rail model that includes an asperity. As the slipper collides with an asperity, stress waves propagate through both. The waves in the asperity disperse through the rail and are of minimal concern since the wear of interest is in the slipper. The waves propagating through the slipper are thus the focus of this study. Any reflected waves could artificially increase the calculated strain on an element resulting in premature element failure and deletion increasing the wear estimate.

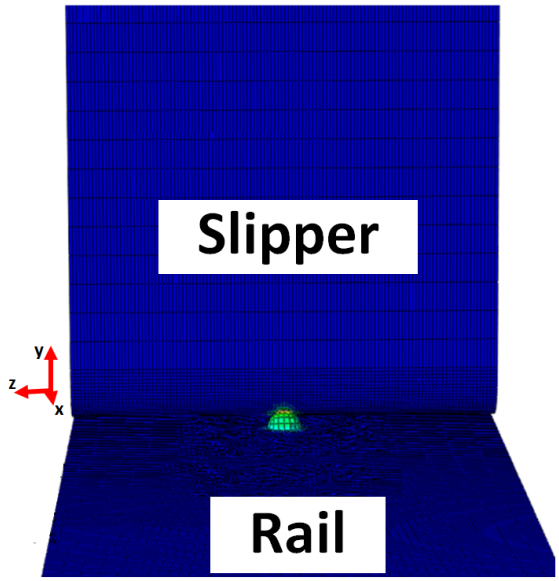

Figure 4.24: Asperity collision

The wave velocity is estimated with Equation 4.1 [25]. It calculated the wave speed using the assumption that the model approximated uniaxial strain.

$$V_l = \sqrt{\frac{(1-\nu)E}{(1+\nu)(1-2\nu)\rho}} \tag{4.1}$$

Substituting values that represent the material modeled (1045 steel) gives:

$$V_l = \sqrt{\frac{(1-0.291)\cdot 2.03e^{8}(\text{kPa})}{(1+0.291)(1-2\cdot .0291)\cdot 7.861e^{-6}(\text{kg/mm}^3)}} \approx 5824 \text{ m/s} \tag{4.2}$$

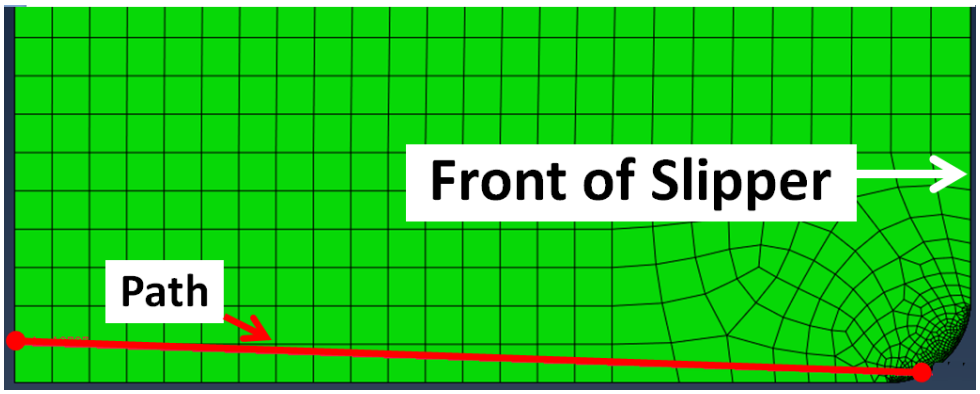

Figure 4.25: Stress measurement path

The slipper dimension is 75 μm while the simulation time is approximately 1 e^{-7} seconds. Utilizing Equation 4.3 provides the approximate time for the wave to encounter the slipper boundary.

$$t_w = \frac{\text{Slipper length}}{\text{Wave speed}} = \frac{75\ \mu\text{m}}{5824 \text{ m/s}} \approx 1.3\ e^{-8} \text{ seconds} \tag{4.3}$$

As shown in Section 3.2.3, symmetry was imposed on the boundaries in the z-direction of the slipper model. This allowed the the wave to propagate in this direction without the possibility of reflecting. The top boundary was fixed in the y-direction which did serve to reflect the wave as did the rear boundary due to the imposed horizontal velocity. Figure 4.25 graphically depicts the path of nodes that calculated the stress wave as it propagated from the front of the slipper model to the rear where the horizontal velocity was imposed.

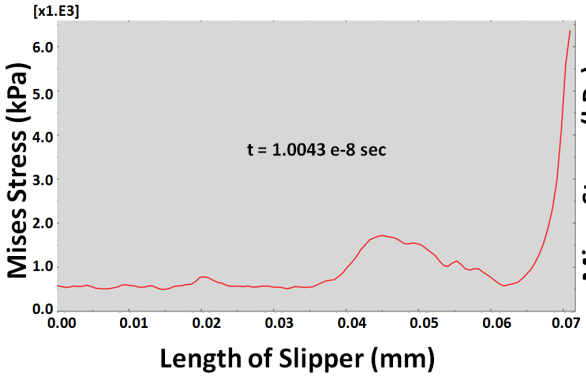

Figure 4.26: Wave - $1e^{-8}$ seconds

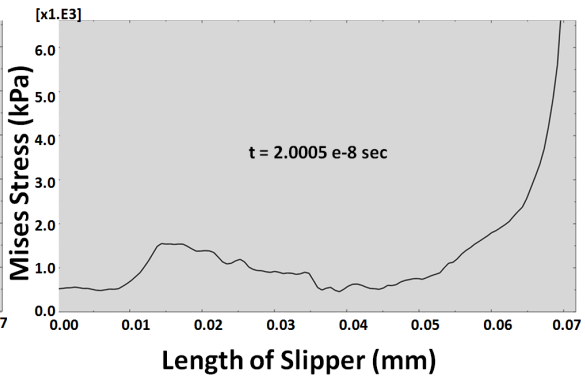

Figure 4.27: Wave - $2e^{-8}$ seconds

Figure 4.26 plots the stress wave (circled) after initial contact with the asperity. The plot also shows the horizontal velocity acting at the back of the slipper. Figure 4.27 shows the stress wave on its return journey to the front of the slipper. This matches the expected behavior and provides confidence that the model is tracing the stress wave.

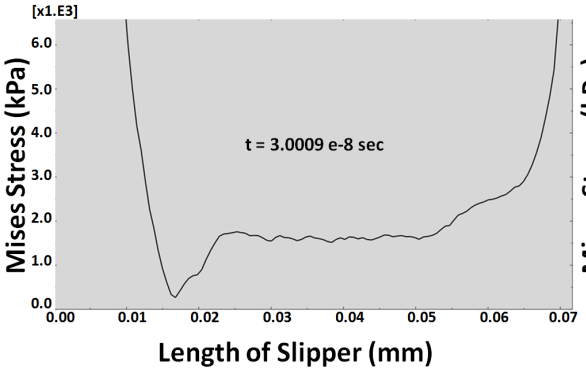

Figure 4.28: Wave - $3e^{-8}$ seconds

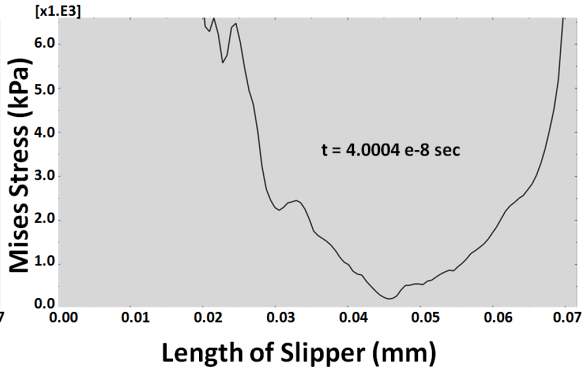

Figure 4.29: Wave - $4e^{-8}$ seconds

Figure 4.28 is the next snapshot taken of the stress along the path of nodes previously described The previous stress wave has been subsumed by the stress caused by the continuing collisions between the slipper elements and the asperity elements. Figure 4.29 shows the next time step, the stress waves continue to propagate. It also shows the stress due to the collision on the left as well as the stress due to the imposed horizontal velocity on the right. Note the scale of the Mises stress on the y-axis. The plot does not capture the behavior of the stresses at the front and the back of the slipper.

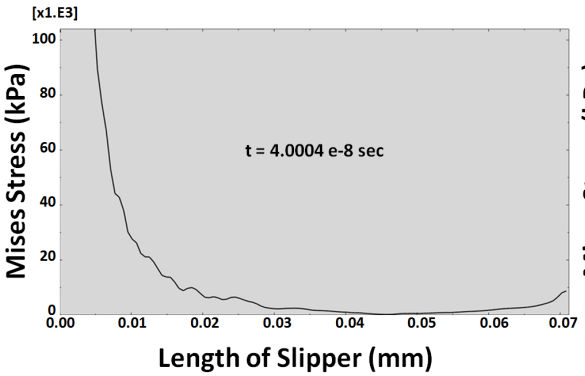

Figure 4.30: Wave - $4e^{-8}$ seconds

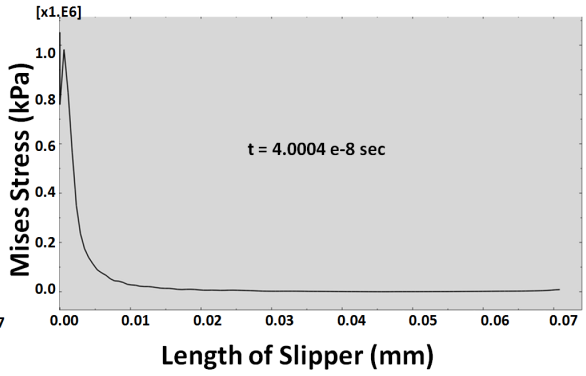

Figure 4.31: Wave - $4e^{-8}$ seconds

Figure 4.30 is a zoomed out view of the previous figure (Figure 4.29). This was done to show the relative scale of the stress induced from the asperity collision to the propagating stress waves under study. Figure 4.31 captures the entire stress magnitude due to the collision at the impact site.

Shock Wave Summary

These results make it clear that the waves do propagate through the slipper model and do reflect from the boundaries, returning to the area of interest within the time of the simulation runs. This should be taken into account when scaling collision models in the future. In this case the stress waves magnitudes are dissipated relatively quickly to the point that their impact can be assumed to be minimal as the stress from the actual collision dominates the material behavior. Note that this is particular to this model. Material modeling could change these conclusions. The dissipation of the stress waves may be far quicker in this model due to the plasticity model inherent in this study.

Equation of State

Figure 4.32 depicts the slipper element from which the results, discussed below, were obtained from. The asperity in the figure is directly in front of the slipper element. This was done to provide perspective of the slipper element's location in regards to the asperity prior to collision.

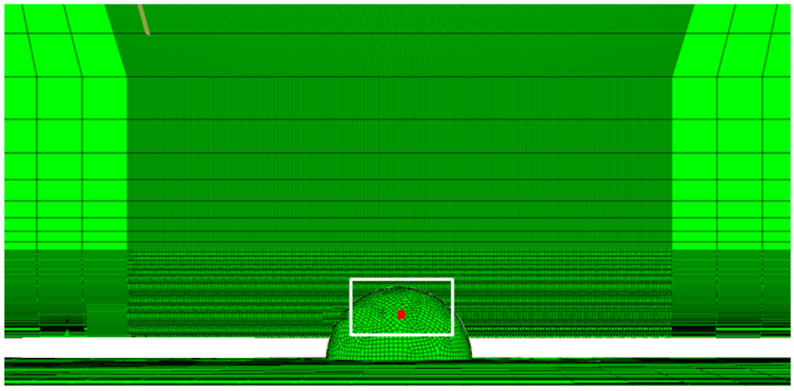

Figure 4.32: Slipper element - 308248

As discussed previously, due to the velocity of the impact between the slipper model and the asperity the possibility for a shock wave exists. Per Meyer's [25] a shock is typically generated when the stress levels exceed 10 GigaPascal in metals. Figure 4.33 portrays a typical shock wave profile. Figure 4.34 are the results from a 1500 m/s collision between the slipper model and a 5 μm asperity. The figure has 2 different curves they are from a model with the same boundary and initial conditions and dimensions. The only difference between the 2 is that one included the Mie-Gruneisen equation of state and the other model did not. The differences appear to be minor however the maximum pressure was between 15 and 17 GPa, thereby nominally exceeding the criteria for a shock wave.

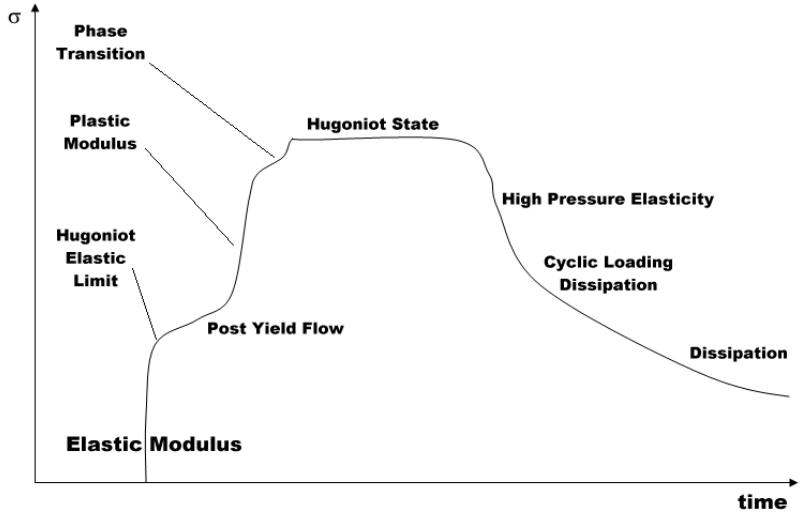

Figure 4.33: Low Pressure Shock wave - Nominal[26]

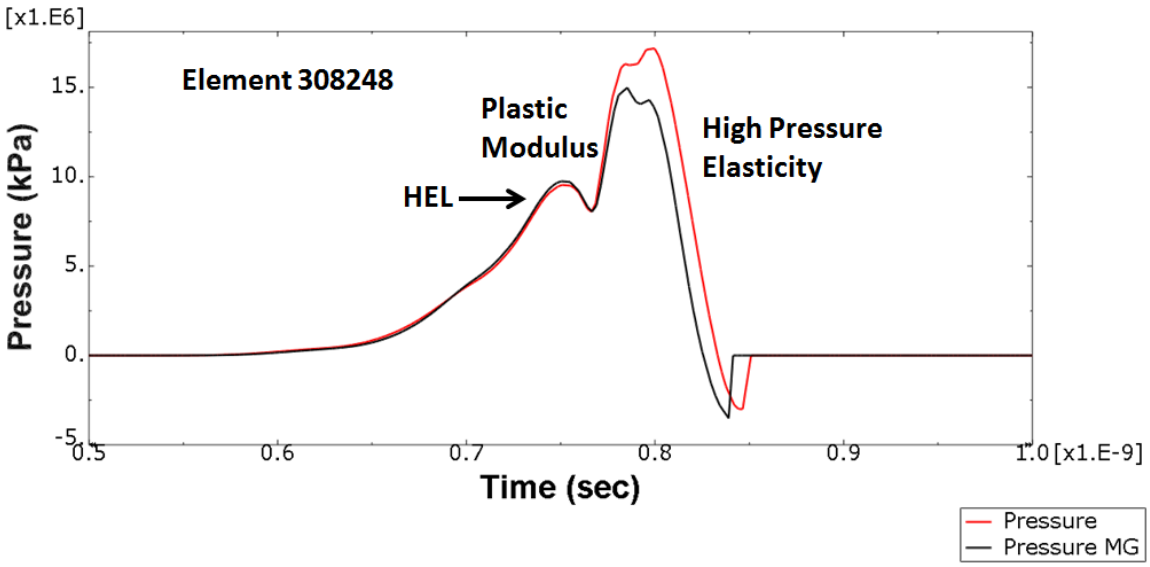

Figure 4.34: Low Pressure Shock wave - Results (element 308248

Since a shock is suspected, the effect on the model was of interest. In particular, the model sensitivity to wear rate was of primary importance since that was the purpose of the model. Figure 4.35 plots the 2 different results for the Johnson-Cook damage criterion. The two results are from the same model with the only difference being that one modeled material behavior to include the Mie-Gruneisen EOS (identified in the plot with 'MG') and the other did not. As discussed previously, the damage accumulates in an element until the damage criterion reaches 1 at which time the damage evolution begins. In this case, the results appear very closely matched. The criterion seems unaffected by whether or not a shock exists. It is interesting to note that the criterion is reached later than the results from the model that included an EOS.

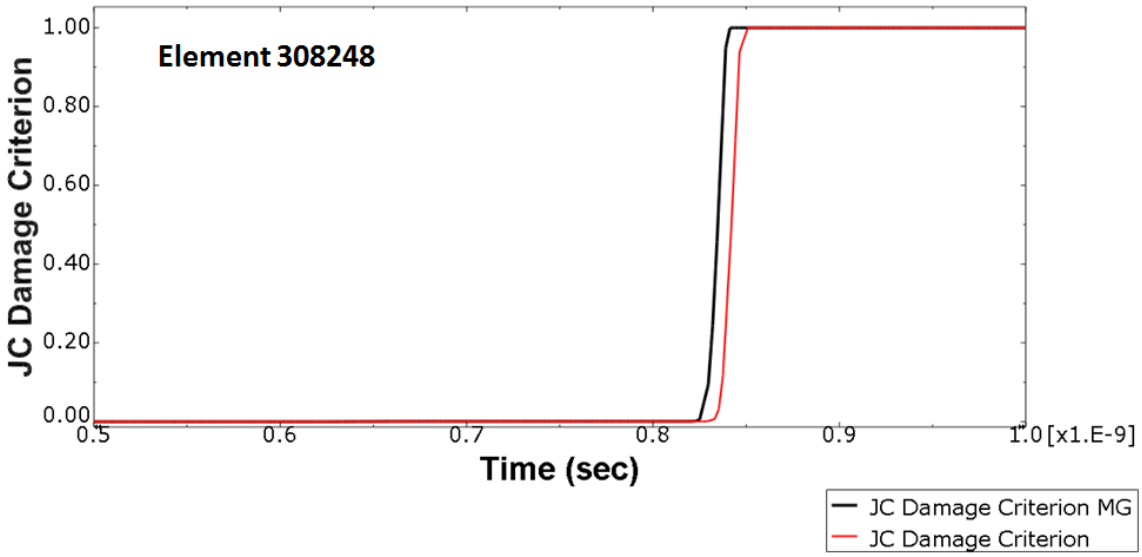

Figure 4.35: Johnson-Cook Damage criterion comparison

Figure 4.36 shows a similar comparison but this time of the Mises Stress. Again the results appear closely matched. However, closer inspection confirms what the previous figure showed. The stress drops off for the model with an EOS before the model without an EOS.

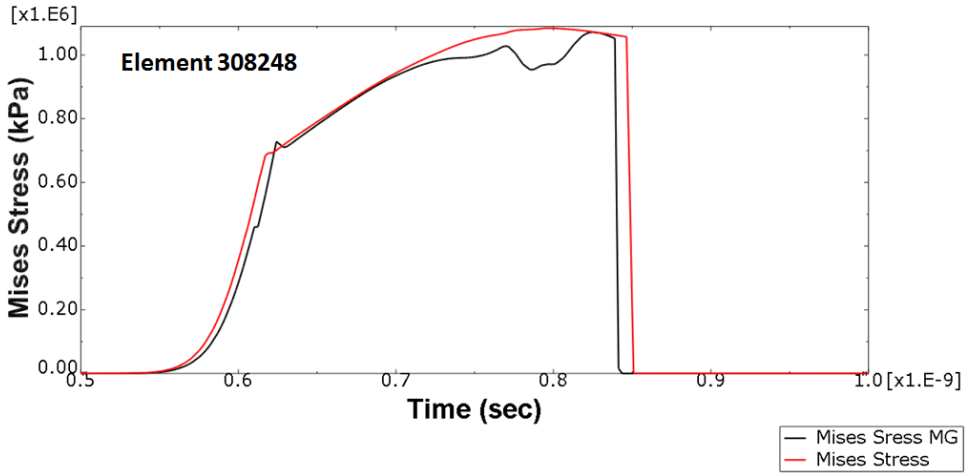

Figure 4.36: Mises Stress comparison - 1000 m/s

EOS Summary

Table 4.3 shows the end result of several simulations. The only difference between results is the lack or inclusion of an EOS as part of the material modeling. The results clearly show

an impact to not using an EOS. The difference of ~ 5% at 750 m/s and ~ 11% at 1500 m/s show the impact on the overall obtained wear results. Additional elements were deleted from the model without an EOS. The delayed element deletion in the model without an EOS has cumulative effects on other elements in the model. The greater the velocity the greater the impact in not using an Equation of state. This is logical as the shock wave would be expected to become stronger with an increase in impact velocity.

Table 4.3: Wear Damage comparison.

Velocity	Wear Damage - EOS	Wear Damage - No EOS	% Difference
750 m/s	9.57×10^{-9} mm^3	9.06×10^{-9} mm^3	5.44%
1500 m/s	3.60×10^{-8} mm^3	3.22×10^{-8} mm^3	11.25%

The question of accuracy arises with the 2 differing results. The pressure plotted in Figure 4.34 would lead one to conclude that there is a stress wave occurring due to the impact and that the EOS does reduce the wear results by less than 12%.

4.2.1.3 Summary of studies.

In this section, the results of several studies were analyzed that impact the FEM used to estimate wear through asperity collision. First, contact was studied and once the results were analyzed a deeper understanding was gained of how ABAQUS models contact [27]. The contact results provided the backdrop to the penalty method as employed by the software. The output supported that conclusion that ABAQUS strikes a satisfactory balance between computation time and encroachment by the nodes of the different models interacting during the simulation. Changing the penalty stiffness factor is a possibility that could affect the wear estimate results. However, other approximations that are necessary to obtain a wear estimate are of greater impact. One such example is the scaling of the FEM results. The shock wave results indicated that the wave does indeed reflect from the surface of the slipper model that do not have symmetry imposed on them. The wave does seem to attenuate as it travels through the model. Due to this, future high velocity impact modeling

should carefully consider the implications. Other elements should be utilized if they allow the wave to pass through a model surface without reflecting. Finally, the EOS results show evidence that with a shock suspected, it is necessary to incorporate an EOS to maximize accuracy.

4.2.2 Wear Model.

The FEM used in this portion of the research was described in Section 3.2.2.3. This section presents and analyzes the results from 16 simulations. The result of the asperity impact as simulated by the FEM is damage to the slipper models. This damage is shown in Figure 4.37, Figure 4.38, Figure 4.39, Figure 4.40, and Figure 4.40. These figures show that the elements that are not deleted are damaged in that they still show residual stresses. Hale's research showed that these stresses are dominated by the next asperity impact [3]. Thus, each simulation started with an undamaged slipper model.

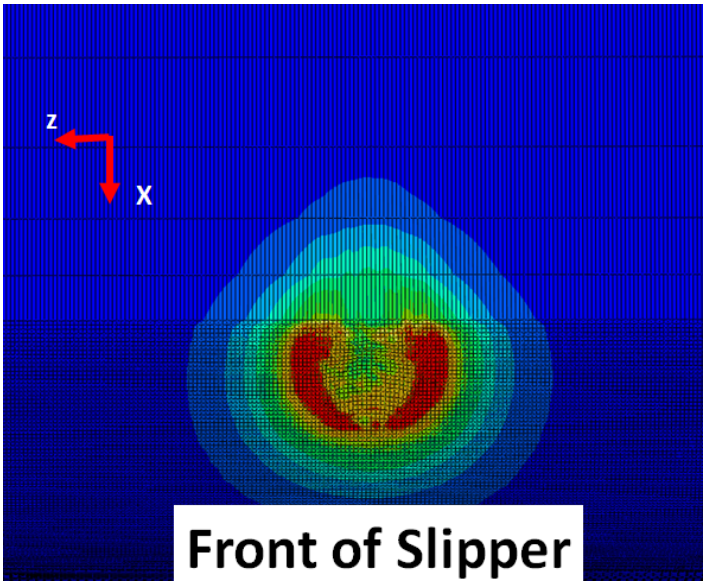

Figure 4.37: Mises stress, 800 m/s - 2 μm

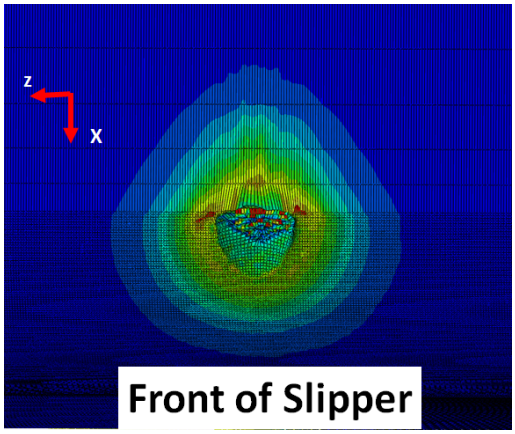

Figure 4.38: Mises stress, 1000 m/s - 2 μm

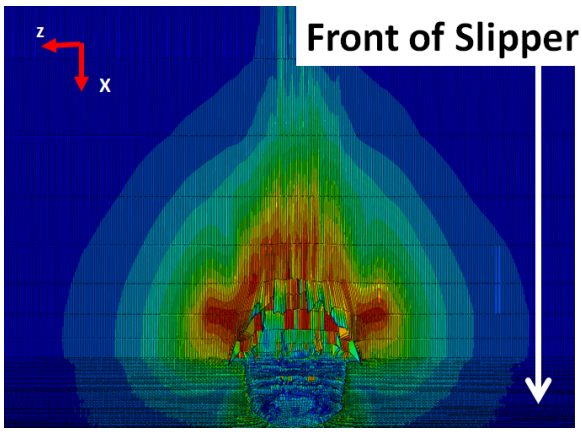

Figure 4.39: Mises stress, 1000 m/s - 3 μm

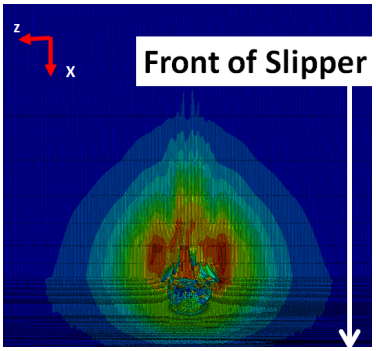

Figure 4.40: Mises stress, 1400 m/s - 2 μm

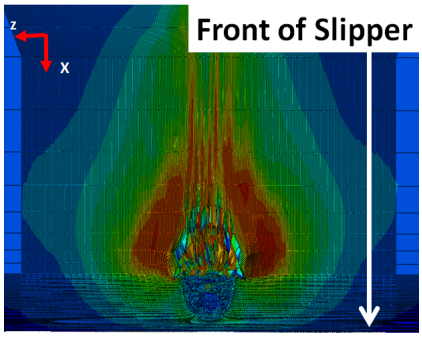

Figure 4.41: Mises stress, 1400 m/s - 3 μm

The FEM can trace the stress, strains, temperatures and other material behavior. These can only be compared to each other as these measurements cannot be taken in situ during a test run at the rates needed nor at the scale necessary to make a meaningful comparison. As such, these results are limited to hypothesis. Thus, the only comparison to data that can be made is total wear.

A method, developed by Buentello [18] and discussed in Section 3.2.2.4, estimates the total wear from the FEM results. This is presented below and compared to the wear measured from the worn slipper that was used in the 2008 test. The method to determine the slipper wear from the acceleration phase, to include 3 rocket stages, is now discussed. Recall that a worn slipper used in a 2008 test was provided to Hale [12]. Depth

measurements were taken along the center-line of the slipper lengthwise. The results are shown in Figure 4.42. This shows the acceleration effect on the front of the slipper as well as the wear due to deceleration at the rear of the slipper.

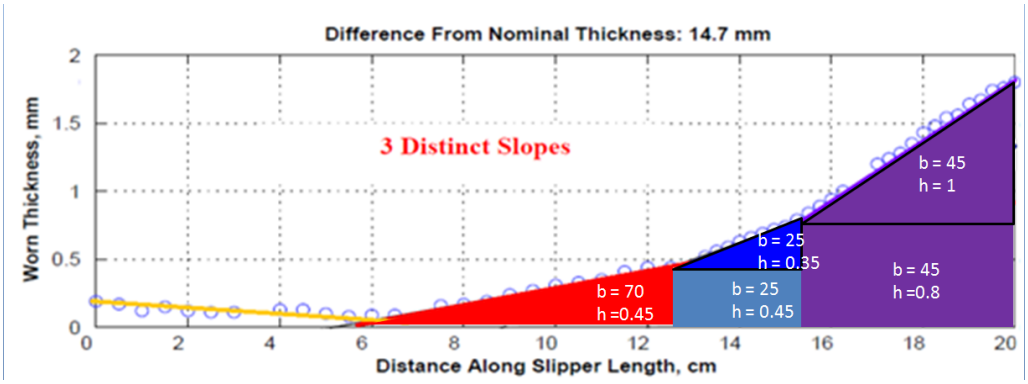

Figure 4.42: Wear Area, Worn Slipper

The slipper orientation is depicted in the figure as the length measurement from back to front. The rear of the slipper is at 0 cm and the front is approximately 20 cm. At the right of Figure 4.42, the overall depth of the removed material was measured as approximately 1.8 mm. Figure 4.42 is also a visual representation of the calculated wear area during the acceleration portion of the test run as experienced by the recovered slipper.

Table 4.4: Measured wear Area.

Color	Area calculation	Area (mm^2)
Red	$\frac{1}{2}$ b · h	15.75
Dark Blue	$\frac{1}{2}$ b·h	4.375
Light Blue	b x h	11.25
Purple Top	$\frac{1}{2}$ b x h	22.5
Purple Bottom	b x h	36
	Total	89.875

Table 4.5 lists the area calculation by colored area in Figure 4.42. Previous work by Buentello has assumed that the width of the slipper in contact was fixed at 90 mm [18].

By utilizing that assumption, a wear volume can be estimated. The total wear volume, during the acceleration phase (front portion), as measured from the worn slipper, was approximately 8100 mm^3.

Assuming a constant wear rate per rocket stage, the approximate wear volume per stage is shown in Figure 4.43. A constant wear rate is assumed due to the available data. The worn slipper provides the final wear and the previous hypothesis concerning slipper rotation provides an initial condition per stage. With only the final worn measurements available, only a final wear volume per stage can be calculated and is plotted against the time of the acceleration phase of the 2008 test.

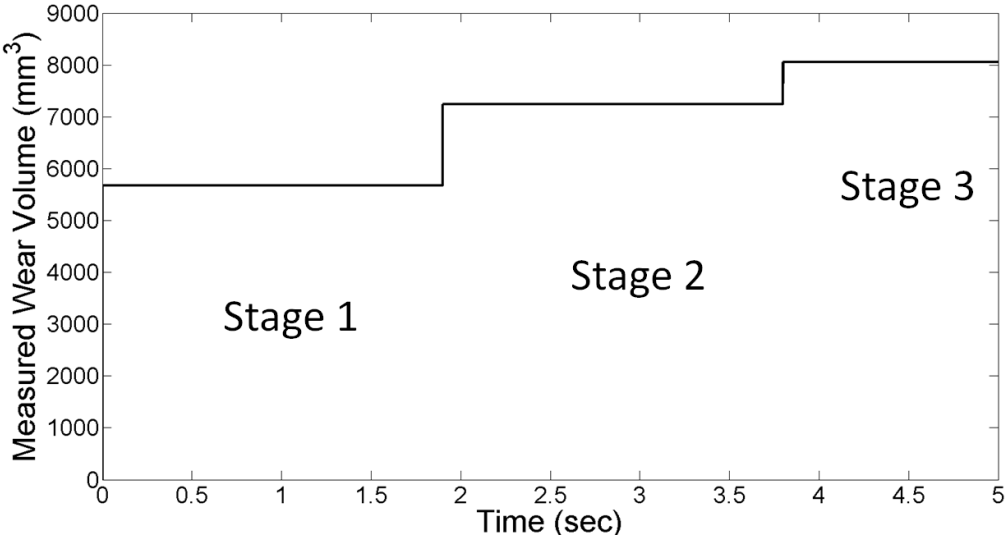

Figure 4.43: Wear Volume - measured

Figure 4.44 is the wear that occurs over the distance (versus the time) that the slipper travels. The accepted wear rate definition is based on wear volume removed per distance traveled. In this case the final distance per stage is taken as the distance traveled. This plot makes it apparent that the wear rate is higher at the beginning of the test run and is reduced at each rocket stage.

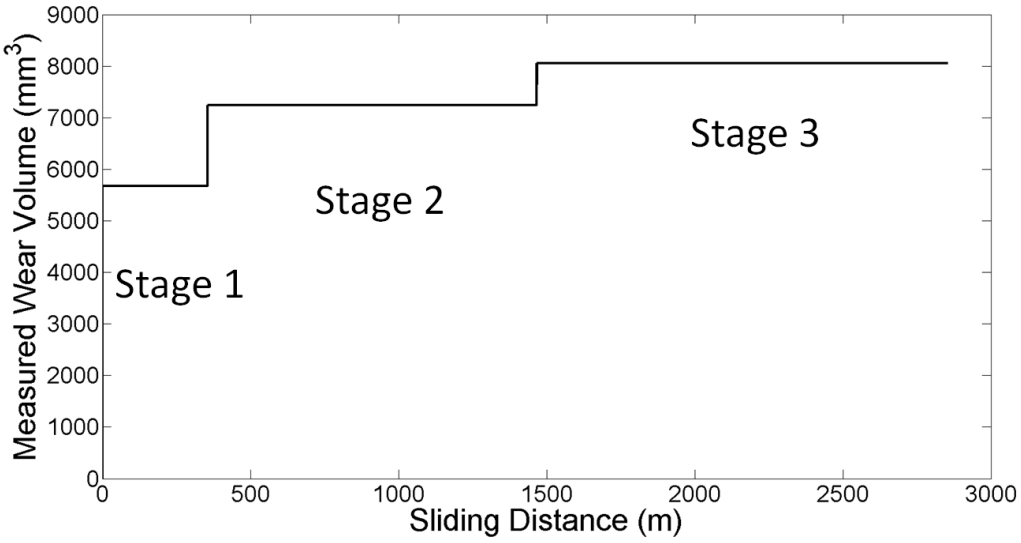

Figure 4.44: Wear Volume - measured

Table 4.5 lists the wear rates as estimated for each rocket stage. The wear rate is lower at each stage as shown in the previous figure. This is hypothesized to primarily be due to less contact. As the velocity increases, the aerodynamic lift increases, reducing the time in contact as shown in Table 4.5.

Table 4.5: Measured wear rates (worn slipper).

Stage	Wear Rate (mm^3/mm)	Percent in Contact
1	$1.6x10^{-2}$	13.7%
2	$1.4x10^{-3}$	7.2%
3	$5.8x10^{-4}$	4.6%

With the total wear of the acceleration phase of the worn slipper now estimated, the FEM results can be scaled with the method discussed in Section 3.2.2.4. Table 4.6 presents the results of the simulations. It lists the volumes of the deleted elements at the end of each of the simulation times. The volumes listed must be normalized before a wear rate can be calculated.

Table 4.6: Volume of deleted elements, $Vol_{I,n}$

Asperity sizes	300 m/s (mm^3)	800 m/s (mm^3)	1000 m/s (mm^3)	1400 m/s (mm^3)
2 μm	6.35×10^{-11}	0	6.35×10^{-10}	6.0×10^{-9}
3 μm	2.58×10^{-10}	2.16×10^{-8}	2.32×10^{-8}	9.24×10^{-8}
4 μm	3.08×10^{-10}	3.96×10^{-8}	4.89×10^{-8}	1.34×10^{-7}
5 μm	4.09×10^{-10}	3.76×10^{-8}	5.05×10^{-8}	2.36×10^{-7}

As discussed in Section 3.2.2.4, the normalized wear volume is computed using Equation 3.1 developed by Buentello [18]. Using the number of asperities per mm^2 to be 600 and the distribution of asperities from Voyiadjis work and shown in Figure 3.7, the results are listed in Table 4.7. Note that the values have units of mm^3/mm^3.

Table 4.7: Normalized Wear, W_I

	300 m/s	800 m/s	1000 m/s	1400 m/s
$\mathbf{W}_I$	1.4×10^{-7}	7.52×10^{-6}	8.96×10^{-6}	3.34×10^{-5}

The normalized wear rates are then used to calculate the wear for the four intervals that were simulated. The four velocities simulated created wear volumes as discussed. These are assumed valid over a velocity interval. The intervals are listed in Table 4.8.

Table 4.8: Velocity Intervals

Velocity	Velocity Interval
300 m/s	0-600 m/s
800 m/s	600-900 m/s
1000 m/s	900-1100 m/s
1400 m/s	1100-1520 m/s

Equation 3.4 (replicated below) is used to calculate the values shown in Table 4.9.

$$Vol_{Tot} = \sum_{I=1}^{4} W_I \times l_{c_I} \times w_c \times D_{sl_I} \times \%Cont_I$$

where:

l_{c_I} - slipper length per velocity interval

w_c - slipper width, fixed 90mm per Buentello estimate [18]

D_{sl_I} - sliding distance per velocity interval, this study used 4

%Cont - percentage of time slipper in contact with rail, determined from DADS

W_I - normalized wear rate per velocity interval

Table 4.9: Total Wear.

Velocity (m/s)	l_{c_I} (mm)	w_c (mm)	D_{sl_I} (mm)	Contact	Normalized Wear, W_I (mm^3/mm^3)	Total Wear, $Vol_{I,Tot}$ (mm^3)
300	58.7	90	86.6×10^4	11.57%	1.4×10^{-7}	74.4
800	45.2	90	88.6×10^4	6.32%	7.52×10^{-6}	1714
1000	9.0	90	30.3×10^4	3.17%	8.96×10^{-6}	69.7
1400	35	90	97.6×10^4	5.41%	3.34×10^{-5}	5543.9
					Vol_{Tot}	7402

In Table 4.9, each row corresponds with a velocity interval. The wear per interval is calculated by using the variables listed in the columns of the table. Each one is determined with the following method. The contact length is designated as l_c. It is based on the hypothesis that the slipper rotates and thus only a portion is in contact with the rail. This length grows due to wear and, as previously discussed, is reduced to near zero at the beginning of each stage. The values listed in Table 4.9 for the contact length are determined by correlating the velocity, that was simulated listed in the first column, with the time that the sled obtained said velocity. DADS provides this information. The time can then be used to determine the contact length based on the hypothesis just discussed. In this way a slipper contact length was determined for each interval as listed in the second column of

Table 4.9. The width of the slipper that was in contact with the rail was hypothesized by Buentello to be 90 mm based on Figure 3.19. This is listed in the third column of the table.

Column four of the table lists distances, D_{sl}. This is the average distance that the slipper traveled for the interval. Buentello used the average velocity of the interval multiplied times the entire time of the interval to calculate the sliding distance. Note that this is not the entire distance of the interval.

The next column lists the calculated percent in contact. This is the percentage of time that the slipper was in contact with the rail. Buentello used force differences between the contact points listed by DADS to estimate the percent in contact. However, the time when the slipper was not in contact with either was not accounted for. For this work, the percent in contact was derived from the times the slipper was in contact per DADS data estimating force at the top of the slipper. This method was used for all the work done in this research to remain consistent. This includes the pressure calculations, the coefficient of friction estimates, and the wear estimate used for the results from the subsequent FEM.

The total volume listed is slightly less than the measured wear of the worn slipper used in the 2008 test. As in the rest of this research, only the acceleration portion of the test run was modeled. Buentello's work used two different specific heat values to estimate two volumes for the total wear for the acceleration phase of the test run. Table 4.10 lists those two values as well as the measured volume.

Table 4.10: Wear Comparison.

Method	Total Volume (mm^3)
Current work	7402
Buentello (C_p = 4.5 $mm^2/s^2 \cdot °K$)	14318.0
Buentello (C_p = 7.0 $mm^2/s^2 \cdot °K$)	11608.1
Measured Test Slipper (2008)	8100

The total wear comparison is useful to validate the technique used. Comparing the wear rates is also important to validate the results from the model. Figure 4.45 and Figure 4.46 compare the wear per interval/stage. They plot the results from the worn slipper used in the 2008 test. The method of estimating the wear per stage is described above. The asperity collision results are obtained by utilizing the wear volume per interval shown in Table 4.9. The wear rate is assumed to be constant over the interval. This is due to the nature of the simulation. As it was accomplished by fixing conditions that actually vary with time, the results are dependent on that time. Thus the wear is constant over the interval as determined by the wear rate as described above. Since wear is cumulutive the results are presented as such. At each interval, the previous wear volume is added to that intervals total wear. This shows the wear ever increasing just as occurred on the test article.

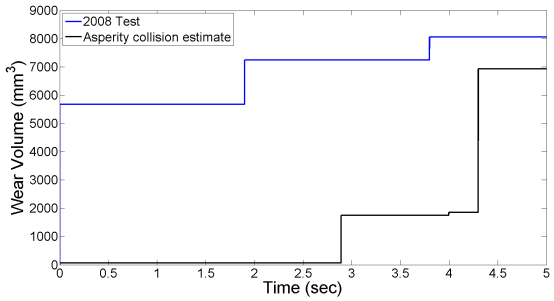

Figure 4.45: Wear Volumes - Time

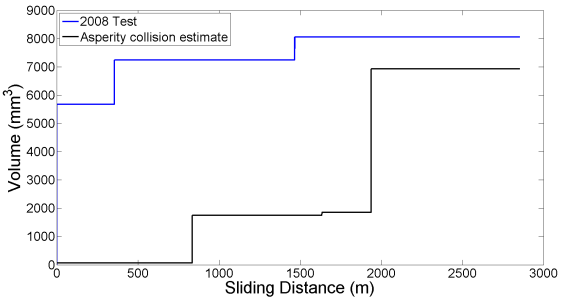

Figure 4.46: Wear Volumes - Distance

Summary of Wear estimate results

The relative wear volumes are of particular interest. The results of the FEM show minimal wear at the beginning of the run and a large growth in the second interval. The third interval again shows minimal wear and then the final interval shows a very large growth. In contrast the worn slipper seemed to show most wear during the first stage with less wear at the second stage and still less wear for the third stage. This disparity is at least partially due to the relative damage produced by the asperity collision. It can be seen in Table 4.6 that the higher the velocity of impact the greater the damage incurred by the slipper model.

This should be taken into account when considering using an asperity collision based FEM for high-speed wear estimates.

Numerous other studies have examined high velocity impacts through modeling. Material modeling is of utmost importance when microscale models are considered. Voyiadjis has done modeling at the micro and nano scale. That work included development of constitutive models based on dislocation theory as well as work determining length scales. Length scales are important when comparing micro and nano scale models to macro scale experiments. It was shown that size dependency of mechanical properties is dependent on increasing strain gradients due ultimately to dislocations [94]. Buentello showed decent results when using a microscale model to estimate the wear of the 2008 HHSTT scenario despite these considerations[18].

4.3 Heat Transfer Model

The results of the one-dimensional heat transfer model are presented below. The partition function will be discussed first as it was partially validated with data from a 2014 test at the Holloman High Speed Test Track. Then the results which were the main focus of this study are analyzed and discussed to include assumptions made as appropriate.

4.3.1 Partition function.

One of the primary drivers of the results from the heat transfer estimate, is the partition function. Previous work by Le [17] showed that a decaying exponential seemed to fit previous results from Wolfson [16]. During this study, an opportunity presented itself to obtain additional data to partially validate the partition function as discussed in Section 3.3.5.1. A test was conducted in 2014 that was comprised of a single stage rocket sled on a monorail. Figure 4.47 is a photo taken before the test was accomplished. Figure 4.48 is a closeup of the front slipper connecting the sled to the rail. The slipper wraps around the rail in a similar manner to the slipper from the 2008 test under study. However, it is apparent that the slipper is not as robust as the slipper under study.

Figure 4.47: 2014 Test Sled

Figure 4.48: 2014 Sled slipper

Figure 4.49 plots the velocities of the two tests as calculated by DADS. The slipper used in the 2014 test reached a maximum velocity of 1000 m/s versus the near 1500 m/s reached by the slipper in the 2008 test. The 2014 test was only a single stage but the reduced mass of the smaller sled allowed a faster acceleration and it reached maximum velocity quicker than the 2008 slipper. This could result in different wear rates however for this study the focus was on the partition function. A wear rate estimate and comparison could be done as part of a different study as discussed in Chapter 5.

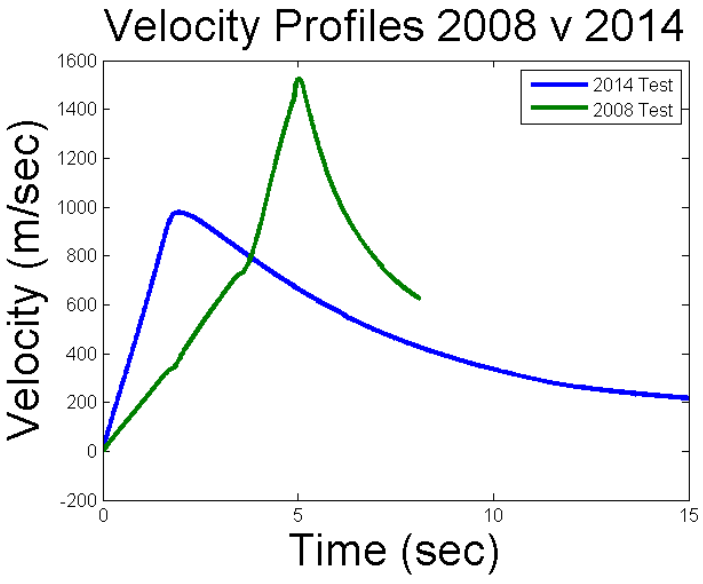

Figure 4.49: Velocity profiles

The slipper used in the 2014 test was outfitted with several thermocouples. The data output was shown in Section 3.3.5.1. That data was compared to the output from the one-dimensional heat transfer model. Note that the model incorporated material properties to correlate the slipper used in the 2014 test vice the 2008 test. The material this slipper was constructed of was AISI 4130 not the Vascomax 300 used in 2008. In addition, the contact area was not adjusted but rather kept constant as the full slipper. Finally, the material properties were not varied with temperature but rather they were kept constant as well. These simplified the model but recall that the goal was not an accurate melt wear estimate but rather a partial validation of the partition function.

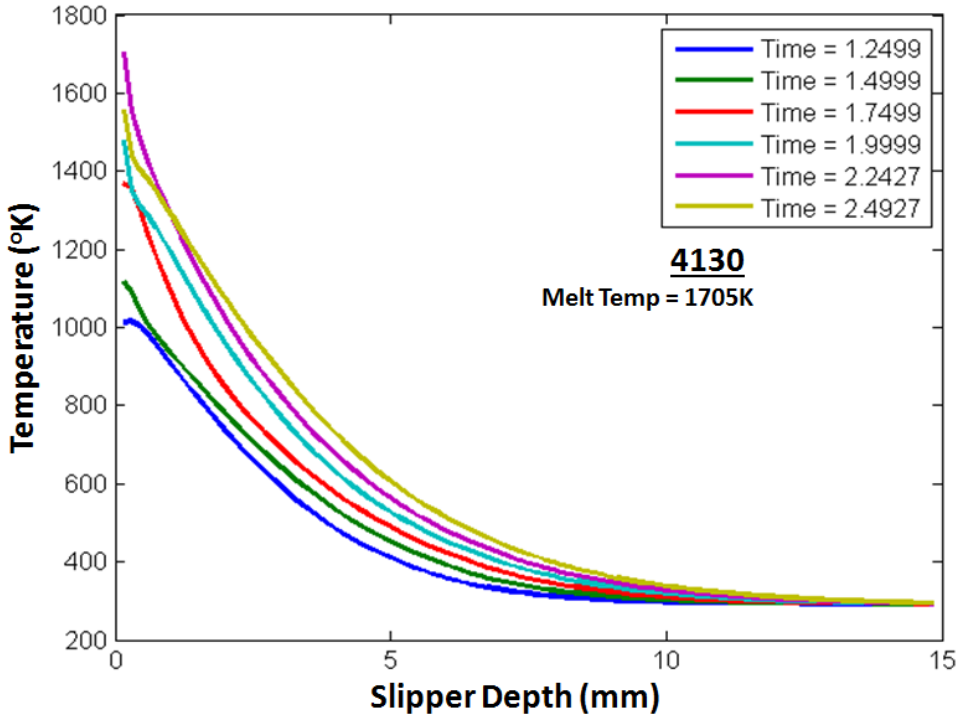

Figure 4.50: Temperatures through slipper depth.

Figure 4.50 plots the temperatures through the slipper depth for several time steps. Reviewing Figure 4.49 shows that the plotted times correspond with velocities approaching the maximum velocity of 1000 m/s. Note that the temperature does not exceed 1705°K due to the melt estimation technique discussed in Section 3.3.7.2.

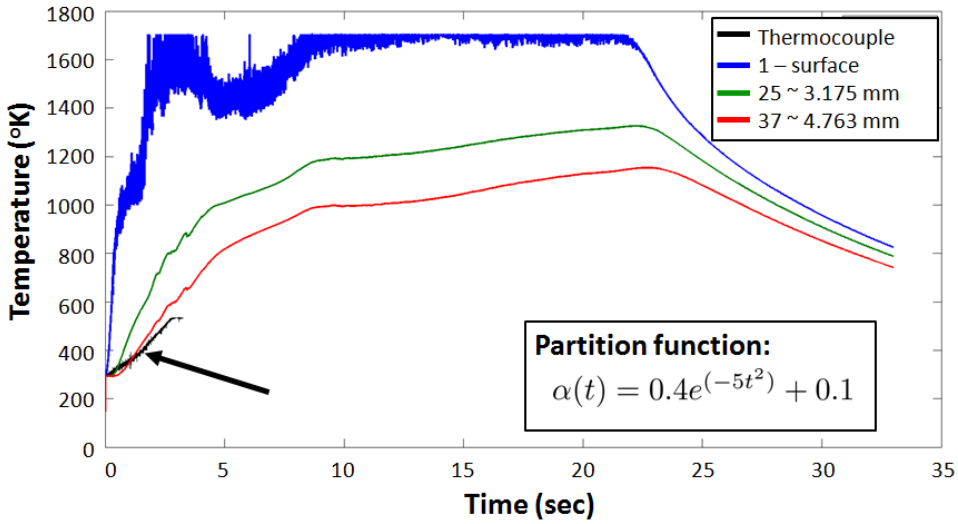

Figure 4.51: Thermocouple output versus calculated

The comparison between the output from the model and the recorded thermocouple data is shown in Figure 4.51. The blue line represents the temperatures calculated at the surface of the slipper in contact with the rail. They are higher than the temperatures recorded by the thermocouples. This is expected as Figure 4.50 shows that the temperatures fall as the distance from the surface increases. The green and red lines are the temperatures as calculated at different nodes for the duration of the run. Although the legend shows depths associated with each, it is noted that those locations are approximate. Recall that there are 100 nodes in the model situated through the thickness of the slipper. The entire length, that the nodes cover, is the diffusivity length as calculated considering the thermal conductivity and specific heat. In addition, the nodes move to account for any melt that occurs. This can be seen by the small rapid changes in temperature seen in the green and red lines near the 2.5 second mark.

The two thermocouples that captured temperature data were averaged as they were located toward the front of the slipper and the rear. It is noted that the temperatures were very similar for the time that they captured useful data. The nodes are located toward the front of the slipper per the aerodynamic assumptions made as discussed in Section 2.4.4.

The comparison, shown in Figure 4.51, provides a level of confidence that the partition function is a decent approximation. To further validate the partition function, additional data is required as discussed in Chapter 5.

4.3.2 Results.

Section 3.3 presented the approach to estimating the melt wear of the slipper used in the 2008 test. This section discusses the results from the model. With the Dynamic Analysis and Design System (DADS) data as an input, the one-dimensional heat transfer model outputs the temperature at the slipper surface as shown in Figure 4.52. The model was used to study the acceleration portion of the test run only. During the deceleration phase, the slipper traveled on a length of the rail that has a friction reducing coating which changes the friction estimation. Thus, the deceleration portion is not modeled in this work.

In this section, the results are presented and discussed. Those results include temperature data from a monorail test that occurred in 2014. The significance of this data is it was used as a partial validation of the partition function used in the heat transfer model. The next sections present the out put form the one-dimensional heat transfer model. This includes temperature estimates both at the bottom surface of the slipper and through the thickness of the slipper. Finally the melt wear estimate is analyzed and compared to the measured wear from the worn slipper used in the 2008 test.

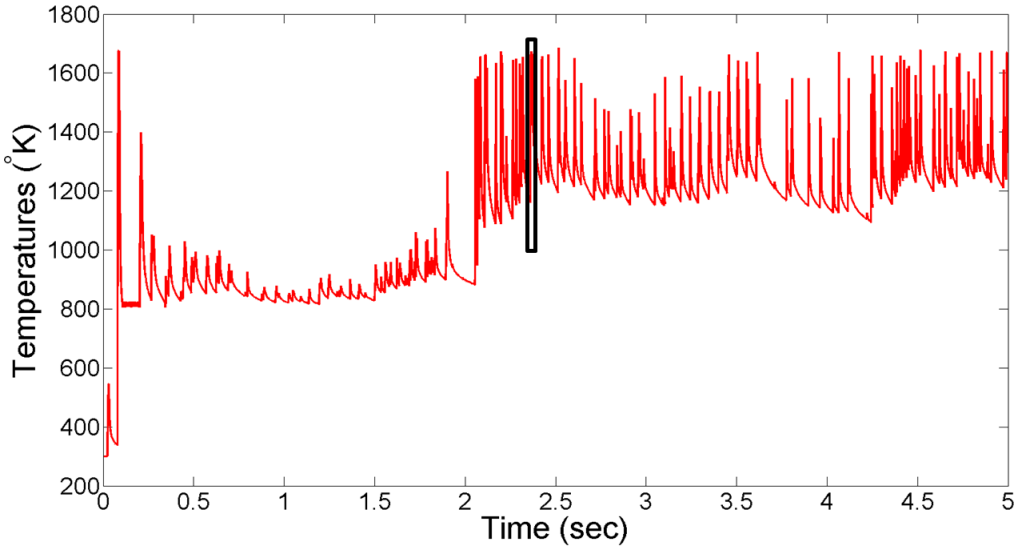

Figure 4.52: Temperatures at surface of Slipper

Figure 4.52 shows that the maximum temperature at the surface of the slipper is 1685°K. This is the melt temperature of Vascomax 300 and thus any time this temperature is exceeded the melt estimation portion of the simulation is performed as discussed in Section 3.3.7.2. As the temperatures exceed the melt temperature, the model adjusts by accounting for latent heat to simulate material removal. The melt temperature is not exceeded due to the computation of the melt depth in concert with material removal.

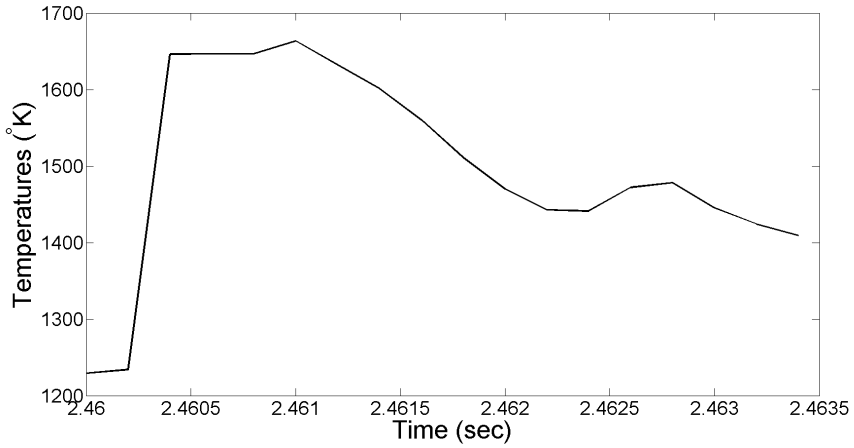

Figure 4.53: Temperatures over time interval

Figure 4.53 shows additional detail for an instance of slipper and rail contact, corresponding to the rectangular box in Figure 4.52 at approximately 2.4 seconds. The slipper bounce is reflected in the temperature behavior. The temperature rises sharply as the slipper initially makes contact with the rail. The temperature decays when the slipper is not in contact. The aerodynamic flow cools the surface of the slipper however, there is insufficient time for the slipper temperature to fall below the initial temperature from the previous contact. Figure 4.52 reflects this as it shows that the temperature does not return to the initial temperature of 300°K.

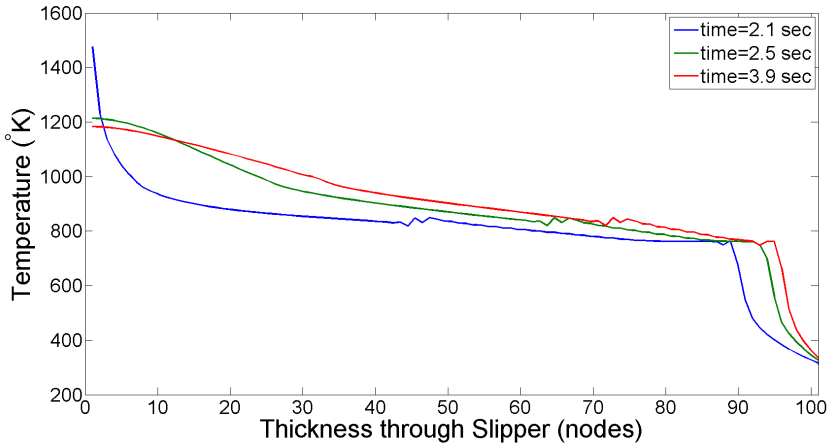

Figure 4.54: Temperatures through Slipper depth

Figure 4.54 plots the nodal temperatures as calculated for three different time increments. The temperatures at the bottom surface of the slipper are on the left with a boundary condition of 300°K imposed on the right. The results show the temperatures gradually decreasing as the distance increases from the bottom surface as one would expect. The first time selected was during contact between the slipper and the rail hence the elevated temperature relative to the other 2. It is noted that there are some deviations common to all three plots, occurring as the temperatures pass through approximately 800°K. This is due to the specific heat's nonlinear dependence on temperature as shown in Figure 3.15.

4.3.3 Comparison.

The temperature data shown in the previous section could not be compared to test data. This is due to the fact that typical slippers are not instrumented to collect temperatures. In addition, the temperatures shown above reflect the estimated temperatures at the bottom surface of the slipper. Thermocouples would quickly be rendered useless if the were placed at the surface of the slipper bottom. Measurements could in theory be taken using visual means although the distances involved would require many cameras and the resolution required would be difficult to achieve to say nothing of interfering structure. As such the only comparison that can be made is the melt wear and wear rate.

The melt wear was accumulated over the acceleration phase of the test run by the one-dimensional heat transfer model. The depth increases as melt occurs. This correlates with the 3 rocket stages increasing the velocity experienced by the slipper. The previously measured contact area was used to calculate the pressures that led to the temperature exceeding melt.

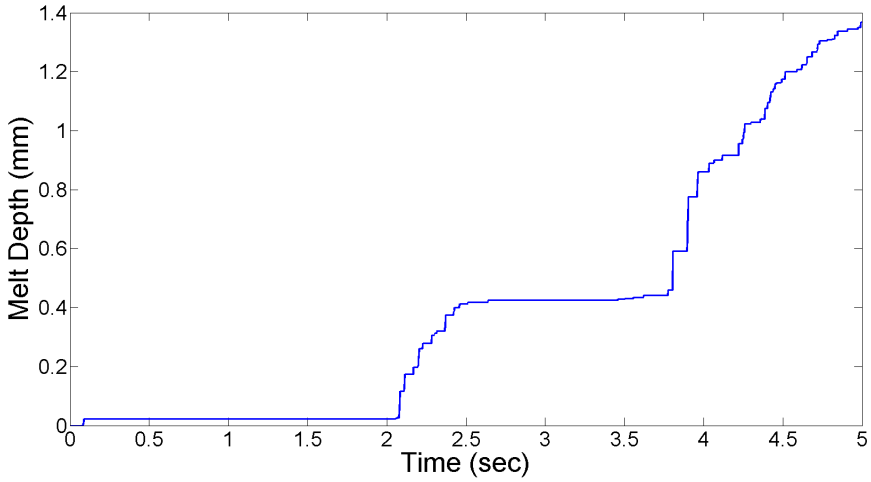

Figure 4.55: Melt depth, Finite Difference Model

The final overall depth as shown in Figure 4.55 is approximately 1.4 mm. This compares to the final depth as measured from the worn slipper of 1.8 mm as shown to the right of Figure 4.42. Since the heat transfer model calculated a melt depth at each time

increment an accumulated wear volume can be calculated. Figure 4.56 plots the results of the calculation. It is readily apparent that very little melt was calculated for the first stage. Stages 2 and 3 show clear melt wear occurring. The final wear volume is 3403 mm^3. This is compared to the final wear volume of 8100 mm^3 estimated from measurements taken from the worn slipper used at the 2008 test.

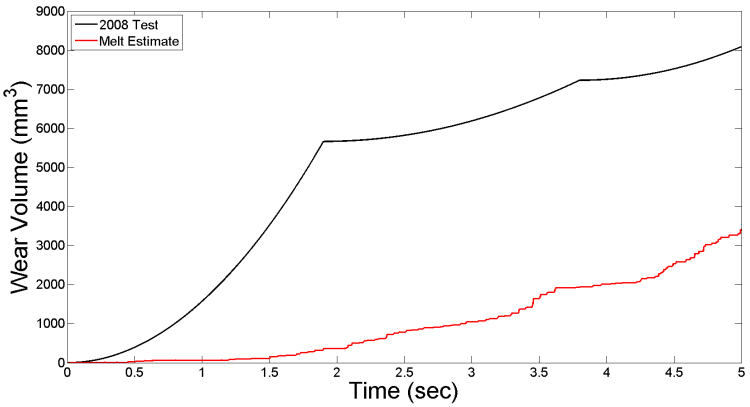

Figure 4.56: Heat Transfer compared to measurement

The failure to estimate any wear for the first stage as well as the non-conservative nature of the final wear volume would seem to indicate a very limited use for this model. However, the first stage results obscure the overall results of the model.

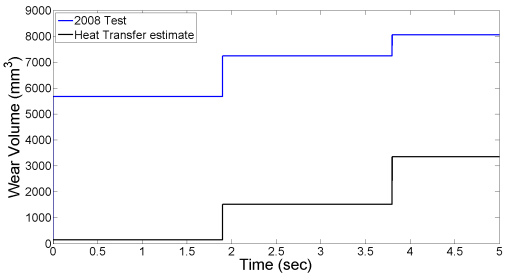

Figure 4.57: Wear Volumes - Time

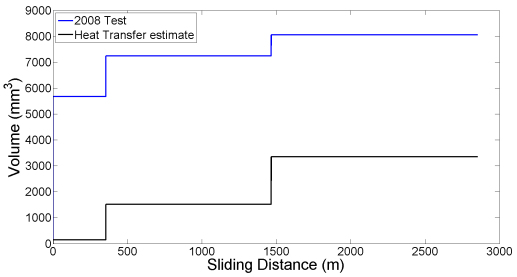

Figure 4.58: Wear Volumes - Distance

Figure 4.57 and Figure 4.58 are the maximum wear volumes, per stage, taken as constants. This was done to better compare to the measured results from the worn slipper. At each stage there is an increase in the wear volume. This is the accumulation of the maximum

wear volumes from the previous stages. The point of interest is the magnitude of the increments. The second and third increments as calculated from the Heat Transfer model are much closer to the measured values. These values are listed in Table 4.11.

Table 4.11: Comparison of wear rates.

Stage	Melt Wear Rate (mm^3)	Measured Wear Rate (mm^3)
1	107	5670
2	1984	1575
3	1419	855

The table lists the total wear estimated for the worn slipper from the 2008 test in column 3 and the melt wear as estimated from the one-dimensional heat transfer model in column 2. The heat transfer model shows a much smaller total wear value for the first rocket stage as previously mentioned. This seems reasonable as at lower velocity the wear being predominately of a mechanical nature and not wear due to melt. The second stage shows much better agreement with the model total wear volume only slightly greater than the measured. This says that the wear during this stage was predominately melt wear with only a small portion of the wear if any due to mechanical processes. The third stage shows a total melt wear that is much greater than the total measured wear. This is a conservative result for the third stage. Thus the total wear volume, as calculated from the one-dimensional heat transfer model, is conservative at higher velocities.

4.4 Combined Model

4.4.1 Overview.

This section concerns the Finite Element Model (FEM) that was used to model wear by combining the material modeling of the previously discussed FEM and the initial temperatures from the one-dimensional heat transfer model with inputs from the Dynamic Analysis and Design System (DADS). The model was scaled to model an entire contact

increment between the slipper and rail. The sizing of the slipper and rail was discussed in previous chapters. The FEM output will be presented and analyzed. A wear calculation will be presented and the results compared to the measurements taken from the worn slipper used in the 2008 test as before. A wear rate will also be estimated, a comparison made and an analysis performed. Figure 4.59 is a graphic representation of the output from ABAQUS [27] after simulating a slipper model traveling down a rail model with an imposed velocity of 40 m/s. The bottom of the slipper model displays the total damage that occurred after the simulation run. As the slipper model traveled down the rail model, the interaction between the bottom surface of the slipper model and the top surface of the rail model was dominated by friction as calculated with force inputs from DADS, the contact area as hypothesized by Buentello [18], and the curve fit developed by Hale [3]. The deleted elements provide a volume, that is assumed to be correlated to wear, that is the basis of the estimate for the total wear volume.

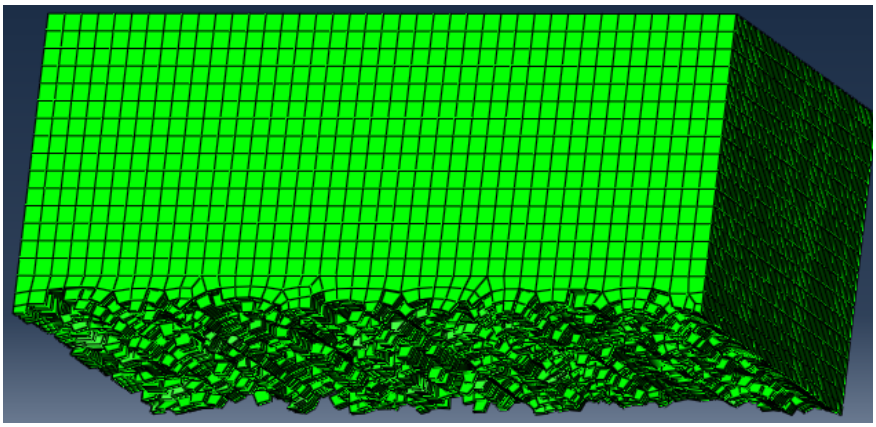

Figure 4.59: FEM Result - 40 m/s

4.4.2 Comparison.

4.4.2.1 Wear Measurements.

The wear calculation for the results from the FEM are different than for the worn slipper and for the one-dimensional heat transfer model. In those two cases the final wear depth per stage was known or could be inferred. In the case of the worn slipper,

a line (per stage) could be extrapolated based on the measurements shown in Figure 4.42. Where this line crossed the front slipper boundary was the estimated final wear depth for that stage. The one-dimensional heat transfer model accumulated the melt wear for the entire acceleration phase. Hence, the estimated wear at the end of each stage was readily available.

In the case of this FEM, the wear estimate was accomplished for three instances of slipper and rail contact. The elements that failed were deleted and this was defined as wear for this study. This wear only occurred for the time in contact modeled. Thus a total wear estimate per stage was unavailable. The data does provide enough information to calculate a wear rate. This rate was used to estimate a total wear accumulated per contact increments which is then compared to previous results.

4.4.2.2 Wear rate.

The wear rate can be calculated by taking the wear volume and dividing by the distance traveled. The slipper model was scaled as discussed in Section 2.5. Thus the wear volume as estimated by the FEM must be scaled to account for the entire slipper and then a wear rate estimate can be made.

Table 4.12 lists the values used in calculating the worn volumes. The volumes of the entire slipper model at the beginning and the end of the simulation were output by ABAQUS [27]. The difference, between the two, is the volume of elements that were deleted from the simulation due to the interaction between the slipper and rail models.

Table 4.12: Slipper Wear Volume Calculation.

Velocity (m/s)	Original Volume (mm^3)	End Volume (mm^3)	Deleted Volume (mm^3)
40	16.0167	13.5282	2.4885
500	40.3955	37.4988	2.8967
1100	66.7952	63.0317	3.7635

Table 4.13 lists the dimensions used to calculate the wear depth from the wear volume as estimated by the FEM. The length and width were discussed in Section 2.5. Figure 4.59 clearly shows the removed elements.

Table 4.13: FEM Wear Volume.

Velocity (m/s)	Deleted Elements (mm^3)	Length (mm)	Width (mm)	Wear Depth (mm)
40	2.4885	4.14	2.0	0.301
500	2.8967	10.1	2.0	0.144
1100	3.7635	16.70	2.0	0.1126

Table 4.14 lists the results of dividing the wear by the increments correlating with the time of contact for each simulation. For the first simulation the total wear depth is divided by 46. This is the number of increments, that DADS listed, when the slipper was in contact with the rail. This is necessary to obtain a total wear per stage. DADS reports the increments when the slipper and rail are in contact. By obtaining the wear depth per increment, summing the wear for every increment during contact results in total wear depth per stage.

Table 4.14: Wear Rate Calculation.

Velocity (m/s)	Wear Depth (mm)	# increments	Wear Rate (mm/inc)
40	0.301	46	6.54×10^3
500	0.144	12	12.0×10^3
1100	0.1126	8	14.1×10^3

To compare the total wear per stage from the FEM to the measured wear as in Figure 4.43, the wear rate per increment w_{r_I} needs to be multiplied by the contact length l_c and the contact width w_c at each increment in contact. Note that the wear rate changes per interval as shown in Table 4.14. This method does not require a percent in contact as it is taken care

of since only when contact occurs is the wear volume calculated. When there is no contact there is zero accumulation of wear volume at that increment. This is shown in Equation 4.4.

$$Vol_{Tot}(\mathrm{t}) = \frac{1}{2}(l_c(\mathrm{t}) \times w_{r_1}) \times w_c \times m(t) \tag{4.4}$$

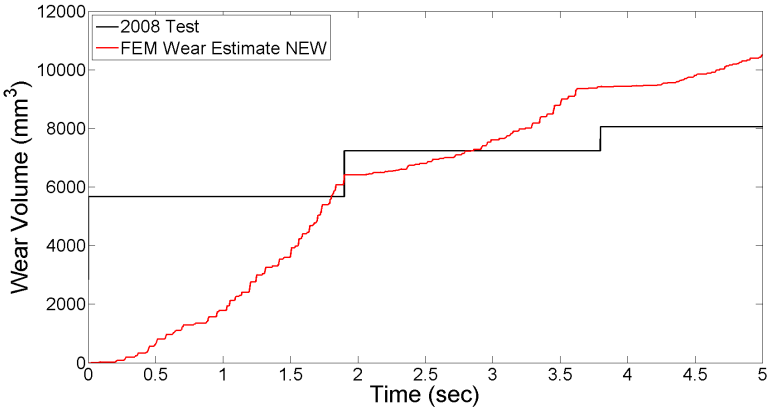

Figure 4.60: FEM compared to measurement

Figure 4.60 displays the results. It can be seen that the total wear volume, as estimated from the FEM, for the first stage is very nearly the same as the volume as measured from the worn slipper. At the end of the second stage the total wear volume from the FEM is greater than the measured wear. For the third stage the FEM results increase, but not as much as the second stage. The worn slipper had the greatest wear at the beginning of the test and the wear rate reduced at each stage. Of the three models used in this research these are the only results that showed a lower wear rate at each stage. The total wear volume as estimated by the FEM at the end of the acceleration phase (3 stages) is 10490 mm^3. This is a conservative value to the 8100 mm^3 measured from the worn slipper.

4.5 Summary

This Chapter presented the results of the different sections of this research. This included investigating an asperity collision FEM behavior in regards to modeling contact

and shock waves. The asperity collision FEM was also used to estimate wear for the HHSTT scenario.

The next item discussed was the one-dimensional heat transfer model. First the partial validation of the partition function was discussed and then the out put from the model was analyzed. The calculated melt wear was discussed and compared to the measured wear from the worn slipper. A wear rate was estimated and discussed as well.

Finally, the results from the three-dimensional combined FEM were presented and discussed. The method for estimating the wear was discussed and the wear rate was also shown. The results were compared to the measured wear from the worn slipper and the wear rate was presented alongside the wear rates calculated from the other models.

Figure 4.61 shows the comparison of the wear rates for the 3 techniques as well as the measured wear. The 2 FEM techniques bracket the measured wear. The heat transfer results are far below the other techniques when comparing total wear. However, as previously discussed the wear rates, as estimated from the heat transfer results, are conservative and close to the measured results for the stages 2 and 3. One other item to note is that the Combined model results are the ones that follow the wear pattern of the worn slipper. That is the wear of stage 1 is greater than the wear of stage 2 which is greater than the wear of stage 3, that is $W_{s1} > W_{s2} > W_{s3}$. Neither the asperity collision FEM nor the one-dimensional heat transfer model exhibit this behavior. The asperity collision model does add an additional increment but it does not change the overall assessment i.e there is a W_{s4}. The reason for this are due to the lower relative damage due to asperity collision at the lower velocities. The higher velocities resulted in greater damage as discussed in the summary of Section 4.2.2. The heat transfer model shows a very little wear in stage 1 (W_{s1}) but the results of stage 2 are greater than the wear results from stage 3. The first stage results are a possible result of little melt wear at the lower velocities. The other two results mirror the behavior of the worn slipper.

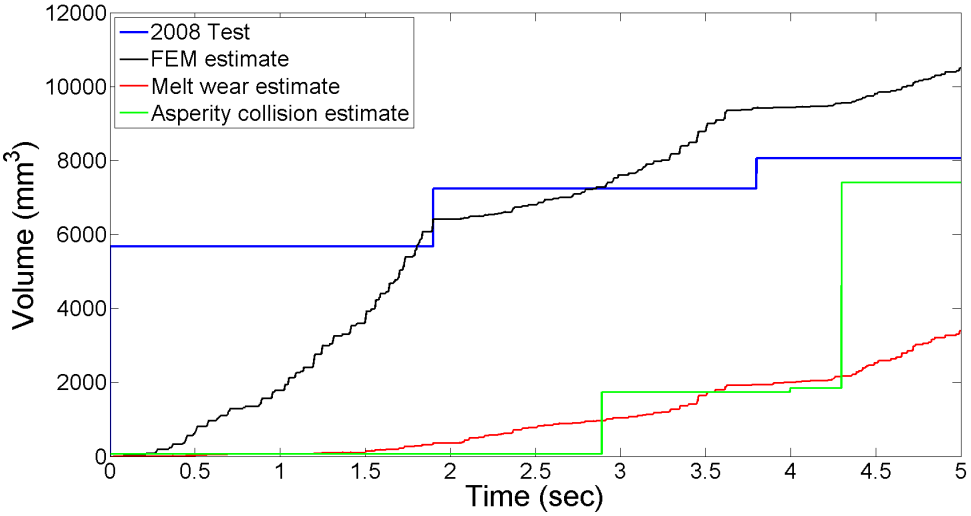

Figure 4.61: Comparison of wear volumes

The goal of the overall research, into the slipper-rail wear scenario at the Holloman High Speed Test Track, is predicting the wear rates to ensure that a slipper survives a test run. Of particular interest is expanding a chart as shown in Figure 4.62 to include the high velocities of interest. The results of the three models developed in this study are plotted along with actual data from the HHSTT design guide [1]. The lines shown are from actual test data. Note that the plot uses a logarithmic scale on the y-axis. The data points from the numerical models are different shapes loosely correlated with velocities. All of the data from the models used in this study modeled Vascomax 300. One of the challenges, in translating the model outputs to the charts, is that the scenario modeled is a sled accelerating down a track with constant bouncing. This leads to changing velocities and pressures. The three-dimensional model utilized simulations at constant velocity although the pressure did change per inputs from DADS. Hence, an average pressure over the distance was used.

The results from the three dimensional test are the three shapes (circle, triangle, and diamond) colored green. The circle is the result from the 40 m/s simulation run. It shows the highest wear rate on the chart. The second simulation result is shown as a green triangle. It shows a lower wear rate than the first output with a higher pressure again per DADS. The

third result is displayed as a green diamond. The wear rate is again lower than the second results as previously discussed in Section 4.4.2.2. The pressure is lower than the second stage ostensibly due to lift produced by aerodynamics at the higher velocity.

The one-dimensional heat transfer model results are all colored black. The model did not output any result of significance for the first stage and was thus omitted here. The model simulates the entire scenario from rest to the acceleration phase of the 2008 test. As such the velocity is constantly changing as well as the pressure, calculated based on the force input from DADS. To get data relevant to the chart an average of the velocity and the pressure, respectfully, was taken for a specific time in contact. As such, selecting a specific velocity can be problematic as it is not certain if the slipper was in contact with the rail at that particular point. The first result shown from the heat transfer model is designated by a black triangle. It is from approximately the same velocity as the three-dimensional second simulation. It is encouraging that they are almost identical lending confidence to the result. The second heat transfer model result is designated as a black +. It is the results from approximately $\sim$ 790 m/s ($\sim$ 2600 ft/s) in order to better compare with the previous data from tests at 2500 ft/s. The pressure, as calculated in the model, is far beyond any test data presented. It could be postulated that it fits into the trend displayed by 304 Stainless steel tested at 2500 ft/s or possibly the Molybdenum test at the same velocity. The third result from the heat transfer model is designated as a black diamond and is at a velocity far higher than the previous test data. The velocity matches the third result from the three-dimensional combined FEM result. The pressures are the same and that can be seen in the chart. The wear rates are different although not significantly so.

The asperity collision FEM results are several shapes of the color purple. The wear rates are from this work, however the pressures are more speculative as there was no pressure input from DADS for the asperity collision model. Of a similar nature, the measured results are included and shown in red. The velocities and pressures are averaged

and speculative by their nature. They are included for completeness but not meant to be authoritative.

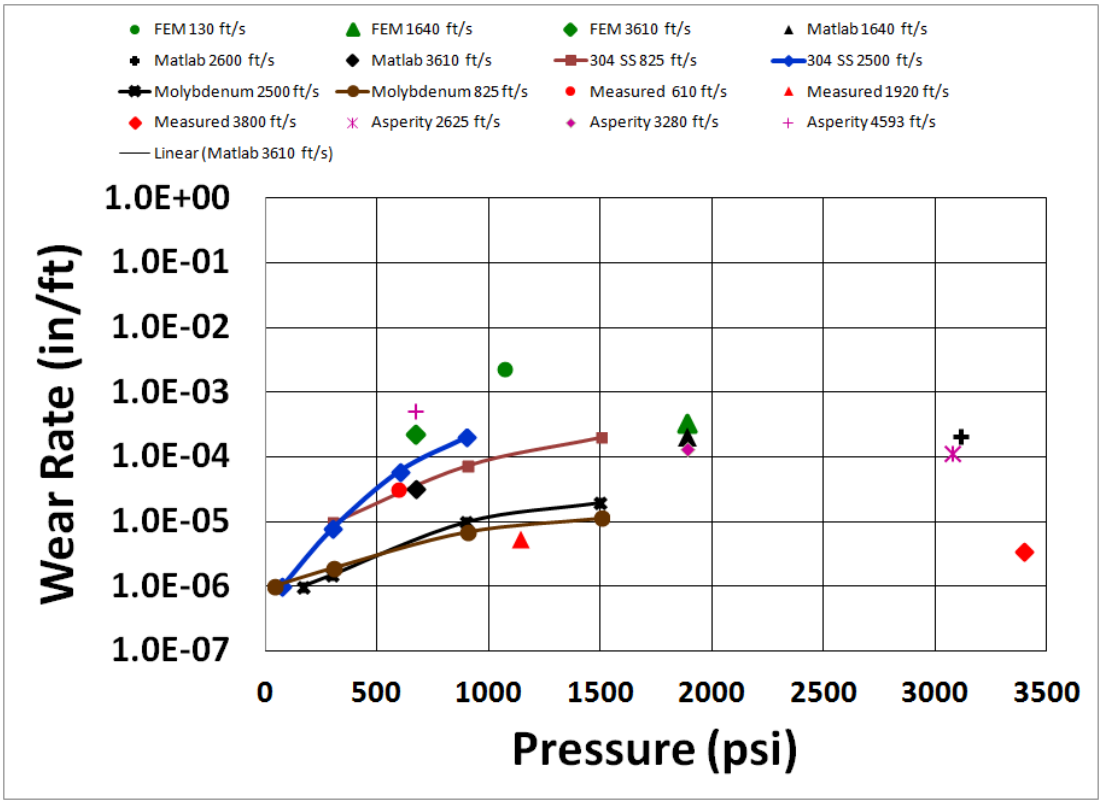

Figure 4.62: Wear Rates determined by multiple parameters

Figure 4.63 is based on work by Lim-Ashby wherein wear maps were developed based on an accumulation of wear research [95]. Of interest is the scenario at the HHSTT. To utilize the predictive nature of the map the DADS normalized pressure must be calculated. Equation 4.5 was used to do this for every time step as provided by DADS.

$$\tilde{F} = \frac{F(t)}{A(t) \cdot H_{VM}} \tag{4.5}$$

The force is input from DADS at the two top locations on the slipper and added together to account for the total force on the slipper. The slipper area in contact is from the slipper rotation hypothesis. These two variables are used to calculate pressure which in turn

allows a coefficient of friction to be calculated. For this investigation the coefficient of friction is not needed. The last variable in Equation 4.5 is the hardness coefficient (at room temperature). The slipper was constructed of Vascomax 300 and the hardness coefficient is listed below.

Table 4.15: VascoMax 300.

Hardness coefficient @ room temp
$1.8 \times 10^9 Nm^{-2}$

With the inputs available for the 2008 test, the results are plotted on a wear map. The overall results and trend are shown in Figure 4.63. To correlate with the scenario the velocities are followed. Hence, at the beginning of the test run the velocities are lower and the data points correlated with these lower velocities and were to the center-right of the wear map. The map includes very low velocities including experimental results from pin on disk experiments and other similar data sources. This explains the fact that the data from the test scenario at the HHSTT begins at a higher velocity to the right. As that velocity increased, the data begins to appear further to the right. Recall that the slipper bounces and hence the force is variable. The contact area also grows and then is reduced at each new stage and is always changing. Thus, at each time step, during the acceleration phase, of the test run a data point was created on the wear map and summarized here.

The overall trend is clear, as the velocity increases during the test run, the wear map predicts melt wear dominating the scenario. This is further validation of the results from the heat transfer model. Also of interest is the fact that the data overruns the map and enters areas where no clear description exists for that type of wear. The nearest types of seizure and melt wear would seem at odds with each other as there had been speculation that the slipper was reducing wear at higher velocities due to lubrication from melted material. These results may contradict that conjecture.

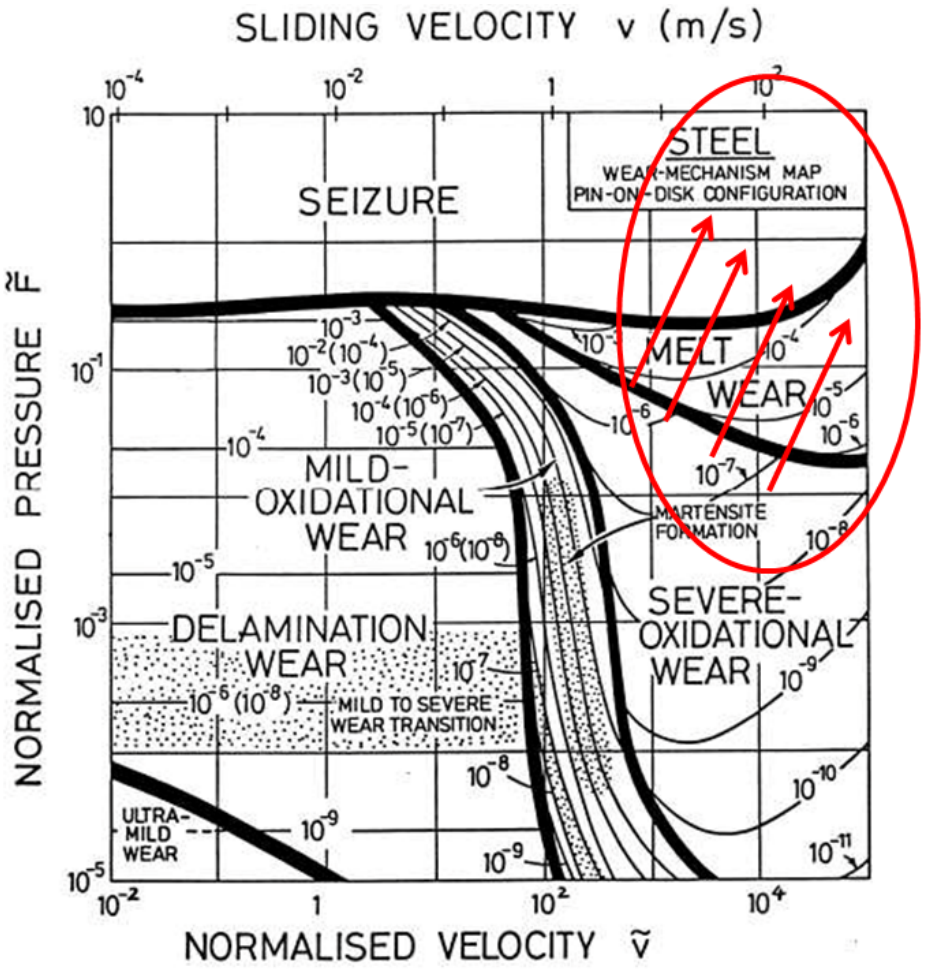

Figure 4.63: Scenario plotted on Lim-Ashby Wear Map

V. Conclusions and Recommendations

5.1 Conclusions

5.1.1 Contributions.

Several contributions were made in this study and will be discussed in this section. For the first time the one-dimensional heat transfer model was used to obtain a melt wear estimate. This included accounting for a varying slipper contact area as well as material properties that vary by temperature. In addition, a larger scale three-dimensional FEM was created. This model incorporated aspects of material modeling taken from the asperity collision model, the initial temperatures from the heat transfer model, and boundary conditions directly from DADS. This allowed a model that could be more appropriately compared to test data due to its scale.

This study has provided deeper insights into the slipper-rail interaction. This understanding included the postulate that increased contact are would lead to less wear due to the decreased pressure reducing material melt. This is a direct result of the work done with the one-dimensional heat transfer model. This model currently provides results for the entire acceleration portion of the test. There are ample opportunities to improve this model and those effort may provide fruitful on this quest to provide an accurate estimate for slipper wear prior to a test run.

5.1.2 Final Analysis.

The one-dimensional heat transfer model provided a melt wear estimate based on a melt temperature. The results provided an estimate of how much of the measured wear was due to melt. By comparing these with the measured wear from the slipper it can be concluded that there was correlation between the wear estimates and the measurements made from the worn slipper as presented in Section 4.3.

There were numerous assumptions and decisions made that could lead to different results if they were different as discussed in Section 3.3.2. The fact that the results correlate is very encouraging. Other than the first stage the results are conservative. This means that the model predicted more wear than what was actually measured for those two stages. In some respects this is logical. At the higher velocities material removal due to melt would be expected to increase. The model suggests that at those higher velocities this mechanism becomes the predominant reason for material removal. If that is the case, then the model is an excellent first order approximation (due to computational times) of estimating wear for the scenario at higher velocities but may be less useful at lower ones. This may necessitate a different method of estimating the wear at those lower velocities as it has been shown that the majority of wear takes place at the lower velocities.

The three-dimensional combined FEM incorporated aspects of the asperity collision model, the heat transfer model, and inputs from DADS to provide wear estimates for three specific instances of slipper-rail contact. The simulation produced realistic results for each rocket stage. In addition, modeling additional contact occurrences could produce a result that would be compared directly with worn slipper measurements as discussed in Section 4.4. The down side of using a three-dimensional FEM is the time associated with it. Thus, a FEM could not be used to predict slipper wear prior to test in a timely manner but it would be useful to help to validate the one-dimensional heat transfer model. In addition, the model once validated could assist in modeling material behavior at high velocity that would be impractical to test outside of the Holloman High Speed Test Track as discussed in Section 5.2.4

The wear comparisons, for the measured wear from the worn slipper and the three models used in this study, are shown in Chapter 4. In the final analysis some trends were observed. The asperity model is the most complicated and problematic of the models due to its scale spatially and temporally. The results were not as comprehensive as those done

by Buentello [18]. However, enough velocity intervals were modeled to show the intrinsic nature of the model in that relatively minor decisions play a huge role in the results as shown in Section 3.2.2.4. The model does serve to prove that the material modeling was successful in modeling impact damage which was scaled to develop total wear and a wear rate. Unfortunately, it would take a substantial number of simulations to enable at least a partial validation of the one-dimensional heat transfer model.

The heat transfer model, while needing additional validation, is the best model studied that could be used to estimate slipper wear in a timely manner. The method includes computational time that is orders of magnitude shorter than the FEMs. The time is less than half an hour on a laptop versus upwards of a week per simulation for either FEM, even utilizing a relatively powerful supercomputer. At the higher velocities, the results appeared to correlate very well with the measurements taken from the worn slipper. With additional work summarized in Section 5.2, this model could fit the needs at the Holloman High Speed Test Track as a first order approximation of the total wear volume.

The largest lesson learned in this work was that a simpler test should have been studied. Multiple slippers from a single stage monorail test would have been more appropriate to study. The complications from the multiple stages increased the uncertainty in the results and reduced the efficiency of the study by keeping the focus on something that did not add to the accuracy of the results. Simulating the slipper-rail interaction scenario from a single-stage sled would still present challenges but more focus could be spent addressing the underlying physics as opposed to the slipper rotations which are really low value added at this juncture of maturity for the models.

5.2 Recommendations

5.2.1 Partition function.

The partition function is problematic in that it was utilized without a derivation. Originally appearing in Paek's work [15], it is a simple decaying exponential that assumes

that the thermal energy flows evenly into the slipper and the rail when both are at the initial temperature of 300°K. It also assumes a smooth decrease of that flow into the slipper. This is based on the fact that as the slipper temperature rises the thermal energy would tend to flow into the cooler slipper due to the Second Law of Thermodynamics. The partition function development also assumed that after a certain amount of time has passed the thermal energy flow into the slipper would drop to 10% of the total.

There are two considerations that are not addressed by the current partition function. The partition function is dependent on time only, as shown in Equation 5.1.

$$\alpha(t) = 0.4e^{-5t^2} + 0.1 \tag{5.1}$$

The fact is that the flow of energy into the rail and slipper is dependent on temperature and material properties. In the case of the HHSTT slipper-rail scenario, the temperature is dependent on time and as a first order approximation is always rising during acceleration. The material properties are also dependent on temperature which as mentioned is always rising. It was shown that the specific heat for the slipper material is nonlinear with rest to temperature. This would have an affect on the flow of thermal energy into the slipper as it travels down the rail. As the specific heat rises for the slipper material it would further resist thermal energy flow into the slipper.

In addition to the material properties consideration, the slipper bouncing is problematic for this partition function. As currently constructed, there is no consideration to the cooling that occurs while the slipper bounces. Figure 4.53 shows the temperature change that occurs during contact and just before. During these temperature shifts there is little doubt that the thermal energy flow would change. By how much and in which direction is currently unknown.

The recommendation would include a re-derivation of the partition function to include dependence on these items. Recall that the current partition function does seem to approximate the thermal energy flow direction and timing based on the data from the 2014

monorail test. However, that data was very limited and as such additional data would be required to validate any newly obtained partition function as described. The preferable data would be from thermocouples embedded at multiple locations and depths in multiple slippers for multiple tests.

5.2.2 One-dimensional Heat Transfer Model.

The one-dimensional heat transfer model can simulate the entire acceleration phase of a test run at Holloman High Speed Test Track. In this study it was used to estimate the melt wear during the test. It did this by determining when the melt temperature was exceeded and removing material (energy) until the temperature did not exceed melt. It might be possible to modify this method to account for not just melted material but also failed material. This adjustment would be based on material failure considerations with respect to this particular scenario.

Several Finite Element Models have been created to study the HHSTT scenario. These models have utilized the Johnson-Cook plasticity model and the Johnson-Cook failure model to account for wear through element deletion as previously described in further detail. Both models are dependent on temperature. By analyzing the material behavior as elements failed, it is hypothesized that a common temperature could be identified that indicated imminent material failure during slipper-rail contact. This temperature could be substituted for the melt temperature currently used in the model to account for total wear as opposed to only melt wear.

Another area of consideration is the slipper contact area used to determine pressure which in turn is used to determine the coefficient of friction. For this study the contact area was known a priori from the wear pattern hypothesis from Buentello's work [18]. This contact area was input into the model and used to determine pressure etc. The model could determine the contact area through geometric considerations directly from wear depth estimations. Recall that the slipper rotation hypothesis postulates that the contact

area grows over time due to wear. Although the slipper is at an angle, that angle is very small. It should be possible to calculate a contact area for each time step when wear occurs. This contact area would be used in the subsequent step to calculate pressure etc. In this way the model becomes predictive of the entire wear volume as opposed to only the wear depth.

The FEM used in this study, that included DADS inputs, could be used to partially validate the one-dimensional heat transfer model. The wear estimated at particular contact situations could be compared directly with the output from the heat transfer model at the same times. Additional worn slippers would also be used to validate this model but they only provide the total wear at the end of a distance. The only way to obtain interim results would be through modeling.

5.2.3 Single stage.

One of the greater difficulties, in modeling the slipper rail interaction for the scenario at the HHSTT, is accounting for the multiple stages that occurred during the 2008 test. The worn slipper showed multiple wear patterns that were hypothesized to be due to the multiple stages [18]. The rapid change in contact area adds to the complexity in modeling the material due to the effects on the material properties. The bouncing and high velocities contribute to rapid changes in temperature. Adding stages serves to further complicate the underlying physics of interest.

The recommendation would be to model a single stage monorail test with the one-dimensional heat transfer model. To validate the model numerous worn slippers would be obtained and measurements taken using the same method utilized by Hale [3].

5.2.4 Design Manual Contribution.

Figure 5.1 displays data on several metals that assists in ensuring safe testing at the HHSTT. There are two issues with the figure as it currently stands. First is that the metals listed although similar to the materials that the slippers are formed from are not the same (i.e. VM300 and AISI 4130) and secondly, and perhaps more importantly, the highest

velocity listed is 2500 ft/s (~ 760 m/s). This is not half the velocity reached at stage three of the 2008 test and less than that for the fourth stage to say nothing of future testing. The challenges at testing materials at those velocities are many to include safety concerns due to possible failure under severe loadings. What this research posits is that the data required to account for wear rates at those higher velocities could be obtained through modeling. Data points were obtained and placed on the chart as seen in Section 4.5. These were models of the 2008 test. As such the pressure was ever changing as provided by DADS. This was done as the only data to compare was the worn slipper from the 2008 test. It is important to use additional slippers to validate the models. Note that the asperity collision model would give the least value for this effort as pressure is not a direct input into the model. The one-dimensional heat transfer model showed very good results at higher velocities and would provide results relatively quickly while the three-dimensional model accurately modeled the wear rate behavior of the worn slipper and provide, at the minimum, correlation with data from the one-dimensional model while taking relatively longer to provide results. Between the two models (once validated), confidence could be developed in the results to depend on them in test sled designs in the future.

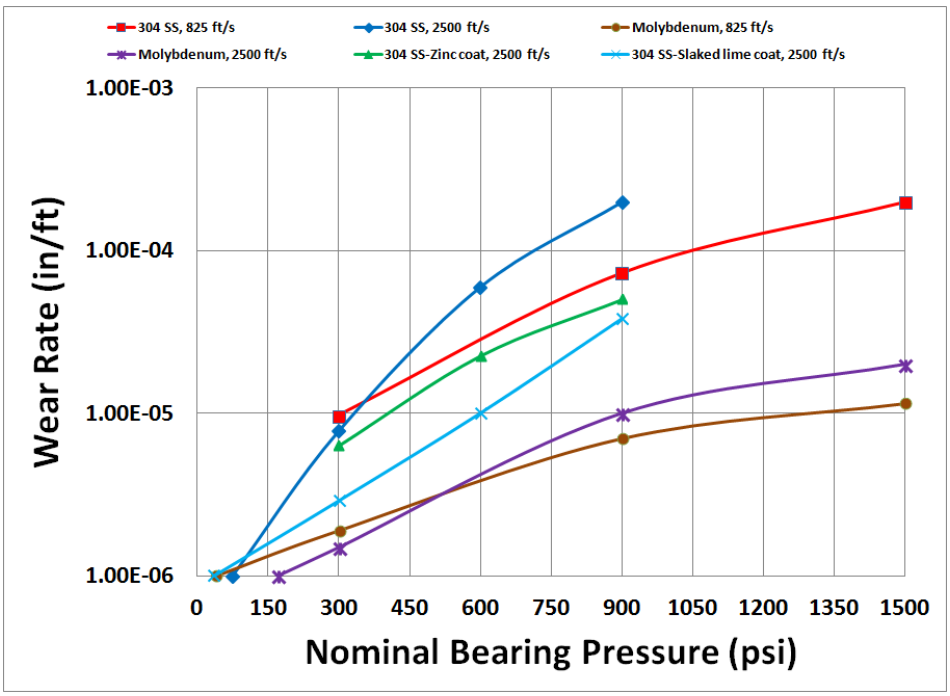

Figure 5.1: Wear Rates determined by multiple parameters

VI. Appendix A

A one-dimensional heat transfer was accomplished using a finite difference scheme that modeled the entire test run. The model consists of 100 nodes through the thickness of the slipper. The distance between each node was constant with the overall distance based on the diffusivity length of the slipper material. Wear is a system property and not an intrinsic property, meaning that the same materials wear differently depending on the system [96]. Thus importance must be paid to the parameters unique to the HHSTT. These are discussed in the following sections.

A cursory examination of the slipper wear pattern reveals several features of interest. First the underside of the slipper shows the most wear as opposed to the wrap around flange. Second the wear does not exceed the slipper depth but is rather a relatively small portion of it. Also, the wear is more pronounced at the leading edge versus the rear. These items occur in both slippers examined for this study and are in agreement with the experienced staff observations at the HHSTT. From this one can surmise that the heat flux occurs primarily in one direction and that the temperature distribution of interest is relatively similar across the width of the slipper. For these reasons, a one-dimensional heat equation was used in this study. The following derivation is based on the physical example of a rod.

Given a rod of distributed temperature, heat moves from high temperature to low temperature. We can express the heat (thermal energy) as

$$q = C_p m_s T \tag{6.1}$$

where q is heat energy, C_p is specific heat (with units of length, time, and temperature $L^2t^{-2}T^{-1}$) m_s is mass, and T is temperature.

From Fourier's law of heat transfer we have that the rate of heat transfer is proportional to

the negative temperature gradient,

$$\frac{\text{Rate of heat transfer}}{\text{Area}} = -k^{TC}\frac{\partial T}{\partial y} \tag{6.2}$$

where k^{TC} is the thermal conductivity (with units of mass, length, time, and temperature $mLt^{-3}T^{-1}$). This shows heat transfers from high temperatures to low temperatures.

If the rod is uniform then the density is constant as is the cross-sectional area. In this derivation we will assume that the specific heat C_p and the thermal conductivity k^{TC} are NOT constants, but rather remain dependent on temperature for reasons discussed below. In addition, assume that the rod is insulated except for the ends. In other words heat energy can only move in and out of the rod at the ends and not through the middle. Also assume that no heat source exists within the rod itself. If we consider an arbitrary slice of the rod of width Δy between y and $y + \Delta y$ with a temperature distribution of $T(y, t)$ we have,

$$q = C_p(T)\rho A \Delta y T \tag{6.3}$$

Invoking the conservation of energy and Fourier's Law gives us that,

$$C_p(T)\rho A\Delta y T(y, t + \Delta t) - C_p(T)\rho A\Delta y T(y, t) = \Delta t A\left(-k^{TC}(T)\frac{\partial T}{\partial y}\right)_y - \Delta t A\left(-k^{TC}(T)\frac{\partial T}{\partial y}\right)_{y+\Delta y} \tag{6.4}$$

This tells us that the heat heat that enters from one side of the arbitrary slice minus the heat exiting the other side of the arbitrary slice is equal to the change of heat energy in the arbitrary slice over time, Δt.

Rearranging yields the following,

$$\frac{T(y, t + \Delta t) - T(y, t)}{\Delta t} = \frac{k^{TC}(T)}{C_p(T)\rho}\left(\frac{\left(\frac{\partial T}{\partial y}\right)_{y+\Delta y} - \left(\frac{\partial T}{\partial y}\right)_y}{\Delta y}\right) \tag{6.5}$$

Taking the limit Δt as $\Delta y \rightarrow 0$ gives the one dimensional heat equation shown below.

$$\rho C_p(T)\frac{dT}{dt} = \frac{\partial}{\partial y}\left(k^{TC}(T)\frac{\partial T}{\partial y}\right) \tag{6.6}$$

also of note,

$$\kappa = \frac{k^{TC}(T)}{C_p(T)}\frac{1}{\rho} \tag{6.7}$$

with κ defined as the thermal diffusivity. Of particular note in this research is that the material properties are not taken as constants. This is due to the wide range of temperatures that the material experiences during the event. The temperatures rise from ambient up to and including melt temperatures. For example one of the materials commonly used to create slippers, Vascomax 300, has a strong temperature dependence for specific heat as well as thermal conductivity. Next, boundary conditions are required in order to solve the partial differential heat equation. The two boundary conditions come from the geometry of the slipper. In this instance they are located at the interface between the rail and the slipper where a thermal flux exists and at the other end of the diffusion length y^*. The diffusion length is based on thermal diffusivity and is further discussed below in the section on scaling.

For the boundary that is nearest the rail, two conditions can hold. One is that a heat flux due to conduction occurs, as indicated by

$$q''(t) = \alpha(t)\frac{\mu_k F(t)\mathrm{v}(t)}{A_c(t)} \tag{6.8}$$

where α is the partition function and is discussed in further detail below, μ is the frictional coefficient and is described below, F is the force discussed in the section on DADS, v is the velocity also discussed in the DADS section, and A_c is the area in contact discussed in the section on slipper geometry.

The other consideration is a heat flux due to convection which is expressed by

$$q''(t) = h(t)(T_{aw} - T_{surf}) \tag{6.9}$$

where h is the heat transfer coefficient as determined due to aerodynamic effects, T_{aw} is the adiabatic wall temperature, and T_{surf} is the slipper surface temperature.

Convection occurs when the bottom of the slipper is not in contact with the rail and is discussed in the section on contact.

If the maximum distance from the flux location is taken to be:

$$y_{max} = y^* + u_m(t)$$

The Boundary Condition at y^* is:

$$T(y^* + u_m(t), t) = T_a \tag{6.10}$$

This states that at the diffusion length away from the flux boundary, temperature is the ambient temperature. Recall that this boundary location is constantly changing due to the melt estimation. This is expressed by $u_m(t)$. This non linear behavior mirrors the wear that occurs as the slipper travels down the rail. As material melts it is removed and the geometry of the slipper changes.

The initial condition is the initial temperature distribution as described by:

$$T_{t=0}(y, 0) = T_0(y) \tag{6.11}$$

where

$$T_0(y) \to T_a \text{ as } y \to \infty$$

In addition, $\overline{T}_0$ is the initial temperature distribution through the thickness of the slipper. The temperature goes to ambient as the distance increases away from the contact location.

In previous sections the one dimensional heat transfer equation was discussed as were the boundary conditions and the initial condition. In this section scaling factors

are introduced. Scaling factors are used due to using numerical computations to solve the equations. In the case of interest physical variable would need to be assigned and tracked for each material used and the values are of different order which could lead to misinterpretation as the larger values possibly impact the solution to a greater degree than the more important values. Thus scaling the values leads to a greater understanding of the physical problem while also increasing the convenience and flexibility of the underlying model. Finally, scaling allows the use of dimensionless parameters.

The first scaling factor is based on the depth through the slipper. Since, the solution is based on a finite difference scheme, a distance must be used to attach boundary conditions. Distance can't be ∞ for T_a, per Equation 4.21, because it must be computed numerically (truncated domain). The distance between nodes must also remain fixed. This length through the thickness is based on the diffusivity length for the material used. Since the specific heat and the thermal conductivity are variable with respect to temperature, the max diffusion length, y^* is calculated below and shown in Figure 6.1.

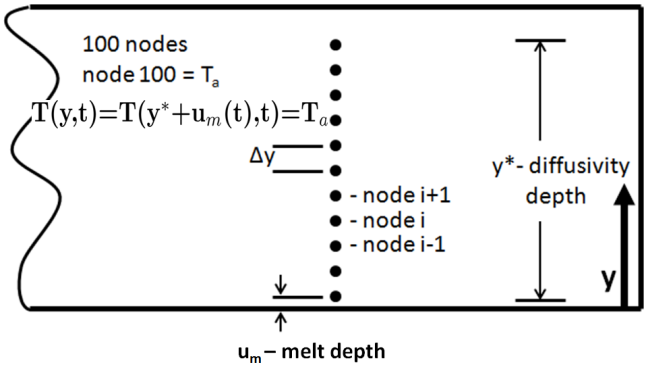

Figure 6.1: Diffusion Length

$$y^* = \max_{T_a<T<T_m} \sqrt{\frac{k^{TC}(T)}{\rho C_p(T)} t^*} \tag{6.12}$$

As previously stated in Section 2.4.1.3, this equation finds the maximum value for the diffusivity length over the time, t^*, of the entire test scenario with regard to temperature.

6.0.4.1 Scaling.

The equation is scaled in this section. This is done to prepare a numerical simulation of the slipper rail test event. Scaling allows dimensionless parameters and is useful when dealing with differing magnitudes of spatial and temporal quantities as in this case. Thus, a scaled coordinate system, ξ is introduced, which moves with the melt front.

$$\xi = \frac{y - u_m(t)}{y^*} \quad \text{so} \quad y = y^*\xi + u_m(t) \tag{6.13}$$

Equation 6.13 scales the coordinate system between 0 and 1. This coordinate system moves with the melt front. As material melts the melt depth increase but the coordinate system is always between 0 and 1 and always begins at the slipper-rail interface. The depth through the slipper y is the scaled diffusivity length plus any additional melt depth u_m.

The next scaling factor is used to scale temperatures. Physically the system under study experiences a wide range in temperatures from ambient, 300K to melt which can be upwards of close to 1700K. Considering the area of interest is on the order of millimeters, the temperature values are on a much larger order presenting possible numerical computation difficulties. The homologous temperature expresses the temperature as a fraction of the melting temperature using the Kelvin scale. Homologous temperature is defined as:

$$\omega(\xi, t) = \frac{T(y, t) - T_a}{(T_m - T_a)} \quad \text{from 0 to 1} \tag{6.14}$$

with

$$T(y, t) = T_a + (T_m - T_a)\,\omega(\xi, t) \tag{6.15}$$

These two scaling factors are the basis for a coordinate system of the one dimensional problem.

6.0.4.2 Initial Condition.

Initial Condition in this new coordinate system is:

$$\omega(\xi, 0) = \frac{T_o\,(y^*\xi + \sigma(0)) - T_a}{(T_m - T_a)} \equiv \phi(\xi) \tag{6.16}$$

In addition,

$$\omega(0, t) = \frac{T(u_m(t), t) - T_a}{(T_m - T_a)} = 1 \;\text{ because }\; T(u_m(t), t) = T_m \quad \text{when } \dot{u}_m(t) > 0 \tag{6.17}$$

6.0.4.3 Boundary conditions.

The boundary condition at the interface between the slipper and the rail changes depending on the contact/no contact condition as discussed in previous sections. The flux condition after scaling gives:

$$\begin{aligned} &\text{If } y = u_m(t) \;\text{ then }\; \xi = 0 \\ &-\frac{\partial \omega}{\partial \xi}(0, t) = \frac{y^*}{k^{TC}(T)\,(T_m - T_a)}\left[q'' - \rho l_h \dot{u}_m(t)\right] = Q(t) \end{aligned} \tag{6.18}$$

Furthermore, using Equation 6.10 and Equation 6.13 with $\xi = 1$ in Equation 6.14:

$$\omega(1, t) = \frac{T(y^* + u_m(t), t) - T_a}{(T_m - T_a)} = 0 \tag{6.19}$$

Also, using Equation 6.9 and Equation 6.13 with $\xi = 1$ in Equation 6.14.

$$\omega(1, t) = \frac{T(y^* + u_m(t), t) - T_a}{(T_m - T_a)} = 0 \tag{6.20}$$

Equation 6.20 represents the temperature at the boundary the diffusivity length away from the slipper-rail interface. When $\xi = 1$ the boundary is into the depth of the slipper. Recall $\omega = 0$ corresponds to ambient temperature.

6.0.4.4 Rescaled PDE.

In this section, the one-dimensional heat equation 6.6 will be rescaled by utilizing the scaling factors, the rescaled initial condition, and the rescaled boundary conditions. The

temperature differentials are rescaled below as they are also needed.

Differentiating Equation 6.14 wrt to y leaves:

$$\frac{\partial T}{\partial y} = (T_m - T_a)\frac{\partial \omega}{\partial \xi} \cdot \frac{\partial \xi}{\partial y} \tag{6.21}$$

as well as

$$\frac{\partial T}{\partial t} = \frac{\partial}{\partial t}\left[T_a + (T_m - T_a)\omega(\xi(t), t)\right] \tag{6.22}$$

and in addition,

$$\frac{\partial^2 T}{\partial y^2} = \frac{(T_m - T_a)}{y^{*2}}\frac{\partial^2 \omega}{\partial \xi^2} \tag{6.23}$$

Substituting the results of 6.21,6.22, and 6.23 into Equation 6.6:

$$\frac{\partial \omega}{\partial t} = \frac{k^{TC}}{\rho C_p}\frac{1}{y^{*2}}\frac{\partial^2 \omega}{\partial \xi^2} + \frac{k^{TC}}{\rho C_p}\frac{\frac{\partial k^{TC}}{\partial T}}{k^{TC}}\frac{T_m - T_a}{y^{*2}}\left(\frac{\partial \omega}{\partial \xi}\right)^2 + \frac{\dot{u}_m}{y^*}\frac{\partial \omega}{\partial \xi} \tag{6.24}$$

Furthermore one can define:

$$a(T) = \frac{k^{TC}(T)}{\rho C_p(T)}\frac{1}{y^{*2}} \tag{6.25}$$

It defines a ratio of thermal conductivity, specific heat, density, and diffusivity length.

$$s(t) = \frac{\dot{u}_m(t)}{y^*} \tag{6.26}$$

The variable s is a ratio of the speed of the melt front and the diffusivity length.

$$G(T) = (T_m - T_a)\frac{\frac{\partial k(T)}{\partial T}}{k(T)} \tag{6.27}$$

Variable G encapsulates the change that thermal conductivity undergoes as the temperature changes. It is noted that if the thermal conductivity were a constant then $G = 0$.

Remembering that T is given by 6.15, substituting 6.25, 6.26 and 6.27 simplifies Equation 6.24 leaving:

$$\frac{\partial \omega}{\partial t} = a(T)\frac{\partial^2 \omega}{\partial \xi^2} + a(T)G(T)\left(\frac{\partial \omega}{\partial \xi}\right)^2 + s(t)\frac{\partial \omega}{\partial \xi} \tag{6.28}$$

Note that taking thermal conductivity as a constant reduces the middle expression to 0.

6.0.4.5 Discretization.

The next step required to utilize the one-dimensional heat transfer equation in the numerical simulation is to replace spatial dimensions with discretization.

Set $\xi_i = (i-1)\Delta\xi \quad i = 1, 2, \ldots N+1$

this sets the node positions throughout the slipper thickness at even intervals.

Define $v_i(t) = \omega(\xi_i, t)$

with v_i as the vector containing the nodal temperatures, through the slipper thickness, at time t.

Then the rate of change of the temperature is:

$$\dot{v}_i(t) = \frac{d}{dt} v_i(t) = \frac{\partial \omega}{\partial t}(\dot{\xi}_i, t) \tag{6.29}$$

The spatial derivatives are now discretized using a central difference scheme. The temperature changes through the slipper thickness and the rate of change is important to this research.

$$\frac{\partial \omega}{\partial \xi}(\xi_i, t) = \frac{\omega(\xi_{i+1}, t) - \omega(\xi_{i-1}, t)}{2\Delta\xi} = \frac{v_{i+1} - v_{i-1}}{2\Delta\xi} \tag{6.30}$$

and the second derivative can similarly be expressed as:

$$\frac{\partial^2 \omega}{\partial \xi^2}(\xi_i, t) = \frac{v_{i+1} - 2v_i + v_{i-1}}{(\Delta\xi)^2} \tag{6.31}$$

$$\text{for } \; 2 \leq i \leq N$$

This holds for the nodes between the boundary conditions.

Substituting Equation 6.29, Equation 6.30, and Equation 6.31 in the scaled PDE (Equation 6.28) results in the following expression:

$$\begin{aligned} \dot{v}_i = a_i \frac{v_{i+1} - 2v_i + v_{i-1}}{(\Delta\xi)^2} + \frac{a_i G_i}{4\Delta\xi^2}(v_{i+1} - v_{i-1})^2 \\ + s(t)\left(\frac{v_{i+1} - v_{i-1}}{2\Delta\xi}\right) \end{aligned} \tag{6.32}$$

where the previous simplifying variables are scaled as follows:

$a_i = a(T(y^*\xi_i + \sigma(t), t))$

$G_i = G(T(y^*\xi_i + \sigma(t), t))$

for $2 \leq i \leq N$ This holds for the nodes between the boundary conditions. The two boundary conditions are discretized below. The first boundary condition corresponds to the Node at the slipper-rail interface.

Case $i = 1$

$$\begin{aligned}\dot{v}_1 = a_1 \frac{v_2 - 2v_1 + v_0}{(\Delta\xi)^2} + \frac{a_1 G_1}{4(\Delta\xi)^2}(v_2 - v_0)^2 \\ + s(t)\frac{v_2 - v_0}{2\Delta\xi}\end{aligned} \tag{6.33}$$

and v_0 is determined using Equation 6.30 while recalling Equation 6.9.

$$-\left.\frac{\partial\omega}{\partial\xi}\right|_{\xi=0} \approx \frac{v_2 - v_0}{2\Delta\xi} = Q(t) \tag{6.34}$$

$$\text{or} \quad v_0 = v_2 - 2\Delta\xi Q(t) \tag{6.35}$$

The second boundary condition corresponds with the Node farthest from the slipper-rail interface.

Case i=N+1

$$\begin{aligned}\dot{v}_{N+1} = a_{N+1}\frac{(v_{N+2} - 2v_{N+1} + v_N)}{(\Delta\xi)^2} + a_{N+1}G_{N+1}\frac{(v_{N+2} - v_N)^2}{4(\Delta\xi)^2} \\ + s(t)\frac{v_{N+2} - v_N}{2\Delta\xi}\end{aligned} \tag{6.36}$$

Recall from Equation 6.20 that the ambient temperature is scaled to 0 when $\xi = 1$ which corresponds to the boundary a distance from the slipper-rail interface or $\omega(1, t) = 0$, this corresponds to the end of the vector v or $v_{N+1}(t) = 0$ leaving

$$\dot{v}_{N+1} = \frac{-2v_N + v_{N-1}}{(\Delta\xi)^2} + 0 + \xi(t)\frac{-v_{N-1}}{2\Delta\xi} \tag{6.37}$$

By defining:

$$
\begin{aligned}
q(t) &= \frac{q''(t)y^*}{k^{TC}(T)(T_m - T_a)}, \quad b(T) = \frac{\rho l_h y^*}{k(T)(T_m - T_a)}, \\
\alpha(T) &= \frac{k^{TC}(T)}{(y^*)^2 \rho C_p(T)\Delta\xi^2}, \quad \beta(t) = \frac{\dot{u}_m(t)}{2y^*\Delta\xi}, \\
a(T) &= \alpha(T)\Delta\xi^2, \\
C_v(T) &= (2\alpha\Delta\xi - s)\frac{y^* h(t)}{k^{TC}(T)(T_m - T_a)}, \quad C_d = q(t) - b(T)\dot{u}_m(t)
\end{aligned}
\tag{6.38}
$$

Equations 6.29 (with Equation 6.28) and Equation 6.38 can be gathered into a matrix system as:

$$
\dot{\overline{\mathrm{v}}}(t) = \mathbf{A}(t, \overline{\mathrm{T}})\overline{\mathrm{v}}(t) + \mathbf{N}(\overline{\mathrm{v}}(t)) + \overline{f}(t) \tag{6.39}
$$

where

$$
\mathbf{A}(t) = \begin{bmatrix}
-2\alpha - (1-m)C_v & 2\alpha & 0 & \dots & 0 \\
\alpha - \beta & -2\alpha & \alpha + \beta & \dots & 0 \\
\vdots & \ddots & \ddots & \ddots & \vdots \\
0 & \dots & \alpha - \beta & -2\alpha & \alpha + \beta \\
0 & \dots & 0 & \alpha - \beta & -2\alpha
\end{bmatrix}
\tag{6.40}
$$

also

$$
\begin{aligned}
\overline{f}(t) =& m((a_1 G_1 C_d^2) + (2\alpha_1\Delta\xi - s)C_d) + \\
& (1-m)((2\alpha_1\Delta\xi - s)(C_v)\frac{T_{awb} - T_0}{T_m - T_0})\underline{e}_1
\end{aligned}
\tag{6.41}
$$

and

$$
\mathbf{N}(\overline{v}) = \begin{bmatrix}
(1-m)a_1 G_1 C_v^2 \frac{T_{awb} - T_a}{T_m - T_a} v_{i-1}^2 \\
\frac{a_i G_i}{4(\Delta\xi)^2}(v_{i+1} - v_{i-1})^2 \\
\vdots \\
0
\end{bmatrix}
\tag{6.42}
$$

$\underline{e}_1$ is the unit vector $e_1^T = [1, 0, 0, \cdots 0]$

However, the matrix implicitly depends on $\overline{v}$ through the determination of $\overline{\overline{T}}$. This nonlinear system utilizes a Runge-Kutta Order 4 solver to ensure stability as it arrives at a solution for each time step as discussed in Section 2.4.1.6.

NOTE: The switch, demarcating when the slipper is in contact versus no contact, is designated *m*. It has the value of 1 when in contact and 0 when not in contact.

Bibliography

[1] 846th Test Squadron, *Holloman High Speed Test Track Design Manual - 1 March 2005*. 2005.

[2] 846th Test Squadron, "Design manual technical report, holloman high speed test track, holloman afb, new mexico," tech. rep., 2004.

[3] C. S. Hale, *Consideration of Wear Rates at High Velocity*. PhD thesis, Air Force Institute of Technology, Wright-Patterson AFB, OH, 2009.

[4] A. Szmerekovsky and A. Palazotto, "Structural dynamic considerations for a hydrocode analysis of hypervelocity test sled impacts," *AIAA Journal*, vol. 44(6), pp. 1350–1359, 2006.

[5] R. Korkegi and R. Briggs, "The hypersonic slipper bearing - a test track problem.," *Journal of Spacecraft and Rockets*, vol. 6(2), pp. 210–212, 1969.

[6] A. J. Lofthouse, "Computational aerodynamic analysis of the flow field about a hypervelocity test sled," Master's thesis, Air Force Institute of Technology, Wright-Patterson AFB, OH, 2002.

[7] J. D. Cinnamon, *Analysis and Simulation of Hypervelocity Gouging Impacts*. PhD thesis, Air Force Institute of Technology, Wright-Patterson AFB, OH, 2006.

[8] S. Lim and M. Ashby, "Recent developments in wear mechanism maps," *Tribology International*, vol. 31(1-3), pp. 87–97, 1998.

[9] R. Montgomery, "Friction and wear at high sliding speeds," *Wear*, vol. 36(3), pp. 275–298, July 1976.

[10] G. J. Cameron, "An evaluation of high velocity wear," Master's thesis, Air Force Institute of Technology, Wright-Patterson AFB, OH, 2007.

[11] A. Chmiel, "Finite element simulation methods for dry sliding wear," Master's thesis, Air Force Institute of Technology, Wright-Patterson AFB, OH, 2008.

[12] C. Hale, A. Palazotto, G. Cameron, and A. Chmiel, "Consideration of wear at high velocities," in *Structural Dynamics and Materials Conference. AIAA, Schaumburg, IL*, pp. 7–10, April 2008.

[13] C. A. Burton and R. A. Brockman, "Frictional interactions in high-speed sliding contact.," in *Proceedings of the 50th AIAA/ASME/ASCE/AHS/ASC Structures, Structural Dynamics and Materials Conference.*, pp. 4–7, 2009.

[14] S. P. Meador, "Consideration of wear at high velocities," Master's thesis, Air Force Institute of Technology, Wright-Patterson AFB, OH, 2010.

[15] G. Paek-Spidell, *Analysis of Heat Partitioning During Sliding Contact at High Speed and Pressure*. PhD thesis, Air Force Institute of Technology, Wright-Patterson AFB, OH, 2014.

[16] M. R. Wolfson, "Solid lubrication, and bearing material investigation for high-speed track applications," tech. rep., Technical Report AFMDC-TR-60-7, Test Track Division, Air Force Missile Development Center, Holloman AFB, New Mexico, 1960.

[17] K. H. Le, "Study of the thermal environment developed by a traveling slipper at high velocity," Master's thesis, Air Force Institute of Technology, Wright-Patterson AFB, OH, 2013.

[18] R. G. Buentello, *3D Finite Element Modeling of Sliding Wear*. PhD thesis, Air Force Institute of Technology, Wright-Patterson AFB, OH, 2013.

[19] S. Philippon, G. Voyiadjis, L. Faure, A. Lodygowski, A. Rusinek, P. Chevrier, and E. Dossou, "A device enhancement for the dry sliding friction coefficient measurement between steel 1080 and vascomax with respect to surface roughness changes," *Experimental Mechanics*, vol. 51(3), pp. 337–358, March 2011.

[20] G. Voyiadjis, A. Lodygowski, and B. Deliktas, "Non-local coupling of friction and damage in high velocity wear.," tech. rep., Technical Report, Louisiana State University, Baton Rouge, Louisiana, 2009.

[21] G. Cavallaro, "A study of slipper and rail wear interaction at low speed," Master's thesis, Air Force Institute of Technology, Wright-Patterson AFB, OH, 2014.

[22] C. J. Alban, "Thermal and melt wear characterization of materials in sliding contact at high speed," Master's thesis, Air Force Institute of Technology, Wright-Patterson AFB, OH, 2014.

[23] C. Alban, A. Palazotto, and J. Rutledge, "Thermal considerations with respect to sliding contact at high speed," *Journal of Thermophysics and Heat Transfer*, vol. 30(1), pp. 1–8, June 2015.

[24] K. Thoma, U. Hornemann, M. Sauer, and E. Schneider, "Shock waves - phenomenology, experimental, and numerical simulation," *Meteoritics and Planetary Science*, vol. 40(9/10), pp. 1283–1298, 2005.

[25] M. A. Meyers, *Dynamic Behavior of Materials*. John Wiley and Sons, Inc., 1994.

[26] D. Grady, "Dynamic material properties of armor ceramics," tech. rep., Technical Report SAND 91-0147.4C-704, Sandia National Laboratories, Albuquerque, New Mexico, 1991.

[27] D. Syst‘emes., “Abaqus v6.11 analysis users manual. dassault syst‘emes, providence, rhode island,” 2011.

[28] M. Ashby, “Physical modeling of materials problems,” *Journal of Materials Science and Technology*, vol. 8, pp. 102–111, 1992.

[29] R. Lesar, *Computational Materials Science*. Cambridge University Press, 2013.

[30] ASM Handbook Committee, *ASM Handbook. Friction, Lubrication and Wear Technology*, vol. 18. ASM International, 2002.

[31] I. Hutchings, “The challenge of wear.,” *Wear -Materials, Mechanisms and Practice, Tribology in Practice Series*, pp. 1–7, 2005.

[32] C. Alban, A. Palazotto, and J. Rutledge, “Thermal considerations with respect to sliding contact at high speed.,” in *Proceedings of the 54th AIAA/ASME/ASCE/AHS/ASC Structures, Structural Dynamics and Materials Conference.*, pp. 4–7, 2013.

[33] D. W. Minto, “Recent increases in hypersonic test capabilities at the holloman high speed test track.,” in *Proceedings of the 38th AIAA Aerospace Sciences Meeting and Exhibit. AIAA, Reno, Nevada.*, pp. 10–13, January 2000.

[34] D. W. Minto, “The holloman high speed test track hypersonic upgrade program status.,” in *Proceedings of the 22nd AIAA Aerodynamic Measurement Technology and Ground Testing Conference. AIAA, Saint Louis, Missouri,*, pp. 24–26, June 2002.

[35] A. Szmerekovsky, *The Physical Undestanding of the Use of Coatings to Mitigate Hypervelocity Gouging Considering Real Test Sled Dimensions*. PhD thesis, Air Force Institute of Technology, Wright-Patterson AFB, OH, 2004.

[36] K. Kato, “Classification of wear mechanisms/models,” *Wear - Materials, Mechanisms and Practice, Tribology in Practice Series*, pp. 9–20, 2005.

[37] ASTM, *Standard Terminology Relating to Wear and Erosion, Annual Book of Standards*, vol. 03.02. 1987.

[38] D. J. Laird, *The Investigation of Hypervelocity Gouging*. PhD thesis, Air Force Institute of Technology, Wright-Patterson AFB, OH, 2002.

[39] MathWorks, “Matlab software,” 2012.

[40] P. Podra and S. Andersson, “Simulating sliding wear with finite element method,” *Tribology International*, vol. 32(2), p. 7181, January 1999.

[41] L. Barker, T. Trucano, and J. Munford, “Surface gouging by hypersonic sliding contact between metallic materials,” tech. rep., Sandia National Laboratories Report SAND87-1328-UC-34, 1987.

[42] R. Tachau, "An investigation of gouge initiation in high-velocity sliding contact," tech. rep., Sandia National Laboratories Report SAND91-1732-UC-706, 1991.

[43] D. Krupovage and H. Rassmussen, "Hypersonic rocket sled development.," tech. rep., Technical Report AD-TR-82-41, Test Track Division, 6585th Test Group, Holloman AFB, New Mexico, 1981.

[44] R. Korkegi and R. Briggs, "Compressible turbulent plane couette flow = Technical Report ARL 670223, Aerospace Research Laboratory, year = 1967," tech. rep.

[45] D. Laird and A. Palazotto, "Effect of temperature on the process of hypervelocity gouging," *AIAA Journal*, vol. 41(11), pp. 2251–2260, 2003.

[46] D. Laird and A. Palazotto, "Gouge development during hypervelocity sliding impact," *International Journal of Impact Engineering*, vol. 30(2), pp. 205–223, 2004.

[47] A. Szmerekovsky, A. Palazotto, and W. Baker, "Scaling numerical models for hypervelocity test sled slipper-rail impacts," *International Journal of Impact Engineering*, vol. 32, pp. 928–946, 2004.

[48] G. Johnson and W. Cook, "A constitutive model and data for metals subjected to large strains, high strain rates and high temperatures.," in *Proceedings of the 7th International Symposium on Ballistics.*, pp. 541–547, April 1983.

[49] G. Johnson and W. Cook, "Fracture characteristics of three metals subjected to various strains, strain rates, temperatures and pressures.," *Engineering Fracture Mechanics*, vol. 21(I), pp. 31–48, 1985.

[50] F. Zerilli and R. Armstrong, "Dislocation-mechanics-based constitutive relations for material dynamics calculations," *Journal of Applied Physics*, vol. 61(5), pp. 1816–1825, March 1987.

[51] J. Cinnamon, *Hypervelocity Gouging Impacts*. AIAA, 2009.

[52] S. Lim and M. Ashby, "Overview no. 55 wear-mechanism maps," *Acta Metallurgica*, vol. 35(1), pp. 1–24, January 1987.

[53] R. Montgomery, "Surface melting of rotating bands," *Wear*, vol. 38(2), pp. 235–243, March 1976.

[54] J. Archard and W. Hirst, "The wear of metals under unlubricated conditions," *Royal Society of London. Series A, Mathematical and Physical Sciences*, vol. 236, pp. 397–410, 1956.

[55] G. Cameron and A. Palazotto, "An evaluation of high velocity wear," *Wear Journal*, vol. 265(7), pp. 1066–1075, September 2008.

[56] R. Smith and E. Haug, *Multibody Systems Handbook*. Springer Berlin Heidelberg, 1990.

[57] M. Hooser and A. Schwing, "Validation of dynamic simulation techniques at the holloman high speed test track," in *Proceedings of the 38th AIAA Aerospace Sciences Meeting and Exhibit. AIAA, Reno, Nevada*, pp. 10–13, January 2000.

[58] C. Hale, A. Palazotto, and W. Baker, "Engineering approach for the evaluation of mechanical wear considering the experimental holloman high speed test track," *Journal of Engineering Mechanics*, vol. 138(9), pp. 1127–1140, September 2012.

[59] S. Meador and A. Palazotto, "Consideration of wear at high velocities using a hydrocode," *AIAA Journal*, vol. 50(3), pp. 746–751, March 2012.

[60] D. A. Huber, "The use of various failure criteria as applied to high speed wear," Master's thesis, Air Force Institute of Technology, Wright-Patterson AFB, OH, 2011.

[61] I. Polyzois, "Finite element modeling of the behavior of armor materials under high strain rates and large strains," Master's thesis, University of Manitoba, 2010.

[62] M. ElTobgy and et al., "Finite element modeling of erosive wear," *International Journal of Machine Tools & Manufacture*, vol. 45, pp. 1337–1346, January 2005.

[63] J. Dean, C. Dunleavy, P. Brown, and T. Clyne, "Energy absorption during projectile perforation of thin steel plates and the kinetic energy of ejected fragments," *International Journal of Impact Engineering*, pp. 1–9, 2009.

[64] G. Voyiadjis, B. Deliktas, A. Lodygowski, A. Palazotto, S. Philippon, A. Rusinek, L. Faure, and P. Chevrier, "High rate and frictional effects in wear of metals using strain gradient plasticity.," in *Proceedings of the International Workshop in Memory of J.R.R. Klepaczko.*, pp. 13–15, May 2009.

[65] R. Buentello, A. Palazotto, and K. Le, "3d finite element modeling of high-speed sliding wear," in *Structural Dynamics and Materials Conference. AIAA, Boston, MA*, pp. 1–20, April 2013.

[66] Z. Kennan, "Determination of the constitutive equations for 1080 steel and vascomax 300," Master's thesis, Air Force Institute of Technology, Wright-Patterson AFB, OH, 2005.

[67] T. Borvik, O. Hopperstad, M. Langseth, K. Labibes, and C. Albertini, "On the influence of stress triaxiality and strain rate on the behaviour of a structural steel part i, experiments," *European Journal of Mechanics A: Solids*, vol. 22, pp. 1–13, October 2002.

[68] T. Borvik, O. Hopperstad, and T. Berstad, "On the influence of stress triaxiality and strain rate on the behaviour of a structural steel part ii, numerical study," *European Journal of Mechanics A: Solids*, vol. 22, pp. 15–32, October 2002.

[69] L. Wuertemberger, *Evaluation and Correlation of Dynamic Flow, Failure, and Microstructural Properties of Heat-Treated 4130 Steel*. PhD thesis, Air Force Institute of Technology, Wright-Patterson AFB, OH, 2016.

[70] D. Grady, "Shock-wave properties of brittle solids," tech. rep., Technical Report SAND 95-0838C, Sandia National Laboratories, Albuquerque, New Mexico, 1995.

[71] J. Cinnamon, A. Palazotto, and Z. Kennan, "Material characterization and development of a constitutive relationship for hypervelocity impact of 1080 steel and vascomax 300," *Impact Enginering*, vol. 33, pp. 180–189, September 2006.

[72] W. Howard and J. Molitoris, "Modeling propagation of shock waves in metals," in *American Physical Society Topical Shock Compression of Condensed Matter Meeting., Baltimore, MD*, August 2005.

[73] J. Donea, A. Huerta, J.-P. Ponthot, and A. Rodriguez-Ferran, *Encyclopedia of Computational Mechanics*, vol. 1(15). Wiley, Dec 2004.

[74] D. Steinberg, S. Cochran, and M. Guinan, "A constitutive model for metals applicable at high-strain rate," *Journal of Applied Physics*, vol. 51(3), pp. 1498–1504, 1980.

[75] W. Davis, "The detonation of explosives," *Scientific American*, vol. 256(5), pp. 106–112, 1987.

[76] M. J. Vanderhyde, "Comparison of thermodynamic equilibrium and non-equilibrium representations of materials," Master's thesis, Air Force Institute of Technology, Wright-Patterson AFB, OH, 2007.

[77] N. Cristescu and I. Suliciu, *Viscoplasticity*. Martinus Nijhoff, 1976.

[78] L. Meyer, "Constitutive equations at high strain rates," in *Shock-wave and High-Strain Rate Phenomena in Materials. EXPLOMET90, San Diego, California,*, pp. 49–68, August 1990.

[79] A. N. Sissala, "Stress finite element analysis of a simple hy-80 steel tension specimen using progressive failure feature in abaqus," Master's thesis, Rensselaer Polytechnic Institute, Hartford, CT, 2012.

[80] A. Hillerborg, M. Modeer, and P. Petersson, "Analysis of crack formation and crack growth in concrete by means of fracture mechanics and finite elements," *Cement and Concrete Research*, vol. 6, pp. 773–782, 1976.

[81] C. Yeo, A. Palazotto, J. Song, and R. Buentello, "Evaluation of thermomechanical damage of a slipper and rail in a rocket sled system," *Journal of Testing and Evaluation*, vol. 44(4), pp. 1443–1453, July 2016.

[82] B. Boley and J. Weiner, *Theory of Thermal Stress*. John Wiley and Sons, Inc., 1960.

[83] M. Thirumaleshwar, *Fundamentals of heat and mass transfer*. New Delhi : Dorling Kindersley, 2009.

[84] J. R. Cannon, *One Dimensional Heat Equation, Encyclopedia of Mathematics and Its Applications(1st Edition)*. New York: Cambridge University Press, 1984.

[85] F. Incropera and W. DeWitt, *Fundamentals of Heat and Mass Transfer*. John Wiley and Sons, New York, 1996.

[86] J. Dormond and P. Prince, "A family of embedded runge-kutta formulae," *Journal of Computational and Applied Mathematics*, vol. 6, pp. 19–26, 1990.

[87] N. D. Institute, "18 per cent nickel maraging steels.," tech. rep., Publication No. 4419, INCO Europe Limited, 1976.

[88] A. Hall and C. Slunder, "The metallurgy, behavior, and application of the 18-percent nickel maraging steels.," tech. rep., Technical Report NASA SP-5051, National Aeronautics and Space Administration, Washington, D.C., 1968.

[89] R. Montgomery, "Muzzle wear of cannon," *Wear*, vol. 33(2), pp. 359–368, July 1975.

[90] W. Kays and M. Crawford, *Convective Heat and Mass Transfer*. McGraw Hill,New York, 1980.

[91] D. Flanagan and T. Belytschko, "A uniform strain hexahedron and quadrilateral with orthogonal hourglass control," *International Journal for Numerical Methods in Engineering*, vol. 17, pp. 679–706, 1981.

[92] B. Bhushan, *Introduction to Tribology*. John Wiley and Sons, Inc., 2002.

[93] O. E. C. D. research group on Wear of Engineering Materials, *Glossary of Terms and Definitions in the Field of Friction, Wear and Lubrication Tribology*. Paris OECD, 1969.

[94] G. Voyiadjis, D. Faghihi, and C. Zhang, "Analytical and experimental determination of rate and temperature-dependent length scales using nanoindention experiments," *Nanomechanics and Micromechanics*, vol. 1(1), pp. 24–40, March 2011.

[95] S. Lim, M. Ashby, and J. Brunton, "The effects of sliding conditions on the dry friction of metals," *Acta Metallurgica*, vol. 37(3), p. 767772, March 1989.

[96] S. Bahadur and I. Iskandar, "Effect of test variables on the friction and wear of alumina.," in *Symposium of Wear Testing of Advanced Materials, American Society for Testing and Materials.*, pp. 7–23, 1992.

REPORT DOCUMENTATION PAGE

Form Approved
OMB No. 0704–0188

1. REPORT DATE *(DD–MM–YYYY)*	2. REPORT TYPE	3. DATES COVERED *(From — To)*
22–03–2018	Doctoral Dissertation	Oct 2012–Mar 2018

4. TITLE AND SUBTITLE

INVESTIGATION of SEVERAL METHODS of EVALUATING WEAR in a HIGH-SPEED ENVIRONMENT

5a. CONTRACT NUMBER

5b. GRANT NUMBER

5c. PROGRAM ELEMENT NUMBER

6. AUTHOR(S)

DeLeon, Armando, Lt Col, USAF

5d. PROJECT NUMBER

5e. TASK NUMBER

5f. WORK UNIT NUMBER

7. PERFORMING ORGANIZATION NAME(S) AND ADDRESS(ES)

Air Force Institute of Technology
Graduate School of Engineering and Management (AFIT/EN)
2950 Hobson Way
WPAFB, OH 45433-7765

8. PERFORMING ORGANIZATION REPORT NUMBER

AFIT-ENY-DS-18-M-249

9. SPONSORING / MONITORING AGENCY NAME(S) AND ADDRESS(ES)

Air Force Office of Scientific Research
875 Randolph St, Suite 325, room 3112
Arlington, VA 22203

10. SPONSOR/MONITOR'S ACRONYM(S)

AFOSR

11. SPONSOR/MONITOR'S REPORT NUMBER(S)

12. DISTRIBUTION / AVAILABILITY STATEMENT

DISTRIBUTION STATEMENT A:
APPROVED FOR PUBLIC RELEASE; DISTRIBUTION UNLIMITED

13. SUPPLEMENTARY NOTES

14. ABSTRACT

The HHSTT located at Holloman Air Force Base conducts hypersonic testing in a unique way. Rather than perform cost prohibitive flight testing or hypersonic wind tunnel testing, a rocket-powered sled propels test articles down a track. This test setup has been used to test at speeds up to 2885 m/s (~Mach 8.6).

The sled is kept on the rails by utilizing slippers, fabricated to wrap around the rail[1]. This slipper design keeps the sled from separating from the rail during a test due to the airflow producing lift, in a designed effort to minimize the wear that occurs during the test run. Different sleds and rails are used at the HHSTT and thus different geometries exist [2]. The slipper material is carefully chosen in an attempt to minimize rail wear as well as to include a safety margin so that the slipper can maintain the designed load carrying capability despite material loss due to wear. Through the years, different materials were used as test velocities increased and a better understanding of the wear environment occurred. This research investigated the wear phenomenon using three different methods, incorporating finite element mechanical modeling as well as heat transfer thermal modeling. One of the methods incorporated a three-dimensional FEM consisting of a portion of the slipper colliding with micron sized asperities to simulate slipper-rail contact and included assumptions pertaining to that scale. The second method was a one-dimensional heat transfer model that simulated the entire time that a test run occurs. The third method was another three-dimensional FEM. As opposed to the previous FEM described, it used friction as the mechanism by which the slipper and rail interacted. These last two models were at a larger scale and their results, along with the asperity collision results, were compared to experimental data acquired from a worn slipper from an actual test at the HHSTT in 2008.

15. SUBJECT TERMS

High velocity, sliding, wear,Holloman High Speed Test Track (HHSTT), friction, finite element

16. SECURITY CLASSIFICATION OF:			17. LIMITATION OF ABSTRACT	18. NUMBER OF PAGES	19a. NAME OF RESPONSIBLE PERSON
a. REPORT	b. ABSTRACT	c. THIS PAGE			Dr. Anthony N. Palazotto (ENY)
U	U	U	UU	263	19b. TELEPHONE NUMBER *(include area code)* (937) 255-3636 x4599 anthony.palazotto@afit.edu